



UNIVERSITY OF LIÈGE

FACULTY OF SCIENCES

Department of Astrophysics, Geophysics and Oceanography

---

**Theoretical studies of gravitational  
lensing phenomena: the case of multiply  
imaged quasars**

---

**Olivier WERTZ**

Research Fellow, Belgian National Fund for Scientific Research (F.R.S.-FNRS)

*Supervisor:*

Prof. Jean SURDEJ

*A thesis submitted in fulfilment of the requirements  
for the degree of Doctor of Philosophy in Space Science*

*in the*

Extragalactic Astrophysics and Space Observations group  
Department of Astrophysics, Geophysics and Oceanography

March 2014

**Members of the Jury** — Prof. M.-A. Dupret (President, ULg)  
Prof. Maarten Baes (University of Gent)  
Prof. M. Bartelmann (Universität Heidelberg)  
Prof. A. Füzfa (Université de Namur)  
Dr. E. Gosset (ULg)  
Dr. D. Hutsemékers (ULg)  
Prof. P. Magain (ULg)  
Prof. J. Surdej (Supervisor, ULg)

*“Of course, there is not much hope of observing this phenomenon directly.”*

ALBERT EINSTEIN, 1936.





# THESIS ABSTRACT

In the early 1960s, gravitational lensing (GL) has received a special attention when S. Liebes and S. Refsdal have derived in detail some of the basic equations of the theory. While Liebes (1964) discussed the probability of detecting these GL effects and considered several astrophysical applications, Refsdal (1964) derived, inter alia, his famous relation which links the Hubble parameter ( $H_0$ ) to the expected time delays between pairs of lensed images. From that moment, the scientific community fully realized that gravitational lensing effects offer a new way of probing cosmology. However, an important fact has been to accept that the determination of  $H_0$  seems to be model dependent, not only on the universe model, but also on the mass distribution of the deflector. The main topic of the present thesis constitutes a straight continuation of this inquiry. We have been sounding parts of the mathematical lensing framework on two fronts. First, considering to first order a very small misalignment between the source, the lens and the observer, we have derived the expressions of the lensed image positions along with their amplification ratios, for the case of power-law axially symmetric mass distributions, the so-called  $\varepsilon-\gamma$  family of models (Wertz, Pelgrims & Surdej, 2012). Combining these results has allowed us to derive an expression for  $H_0$  independently of the model parameters. We have extended this study to the  $\varepsilon-\gamma$  family of models with external shear, as well as to the singular isothermal ellipsoid (SIE) models. For both these types of models, we have obtained an expression of  $H_0$  which is once again independent, to first order, of the model parameters. Furthermore, we have demonstrated the feasibility of analytically constraining to first order the model parameters by only using the astrometric positions of the lensed images. Therefore, for the case of a small misalignment between the source, the deflector and the observer, it is straightforward to determine whether the  $\varepsilon-\gamma$  or SIE family of models constitutes a judicious representation of the mass distribution of the deflector. It is conceivable that similar results can be deduced for other families of models. Secondly, we have developed a new analytical approach in order to determine the expression of the deflection angle, hereafter  $\hat{\alpha}$ . Since the latter depends on the deflector mass distribution, there exists no global explicit expression but only an implicit definition of  $\hat{\alpha}$ . Therefore, the analytical methods used to obtain the explicit expression differ for different types of mass distribution. However, using the Fourier transform theory, one may basically express  $\hat{\alpha}$  in terms of the Fourier transform of the surface mass density. Such a method allows us to approach any mass distribution in a unique way. As a first application, we have separately derived the expression of the two components of  $\hat{\alpha}$  for the case of homoeoidal symmetric lenses (Wertz & Surdej, 2013). This original result constitutes a first proof that the Fourier approach constitutes a promising alternative to the complex formalism introduced by Bourassa & Kantowski (1975, corrected by Bray 1984). A particular case of homoeoidal symmetric lenses lies in the non-singular isothermal ellipsoid (NSIE) family of models for which the analytical treatment has been somewhat limited (Kovner 1987a, Kormann & al. 1994, Keeton & Kochanek 1998). The use of the Fourier approach has made possible to derive a complete analytical treatment for the NSIE, i.e. the expressions of the deflection

angle, the deflection potential, and the critical and caustic curves even off the axis (Wertz & Surdej, submitted to MNRAS on 3rd of February 2014). This original result has allowed us to investigate and better understand the NSIE family of models. Furthermore, it is also of great interest for mass distribution modeling and to rigorously determine the expected time delays between pairs of lensed images. The previous analytical treatments mainly consisted of parametric models for the deflector. An alternative way to grasp lenses consists in modeling their mass distribution using non-parametric models. With this aim in mind, we have proceeded as follows: we tessellate the lens plane with squared pixels, and associate to each of them a constant surface mass density. Making use of the Fourier approach, we have derived the expression of the deflection angle for the whole grid. This result contains the main advantage of the non-parametric models, i.e. to model any type of mass distribution without any preconception, and the usefulness of handling quantities which can be described with analytical functions.

## RÉSUMÉ

Au début des années 1960, l'étude des mirages gravitationnels a connu un nouvel essor lorsque S. Liebes et S. Refsdal ont tous deux publié ce qui s'est avéré être les équations fondamentales de cette théorie. Tandis que Liebes (1964) discutait de la probabilité de détecter ce phénomène conjointement à l'étude de différentes applications astrophysiques, Refsdal (1964) déterminait sa célèbre relation exprimant le paramètre de Hubble ( $H_0$ ) comme une fonction des délais temporels mesurés à partir des courbes de lumières obtenues par l'observation des images multiples d'un quasar distant. A partir de cette période, la communauté scientifique a pleinement pris conscience de l'utilité que pouvait apporter l'étude des mirages gravitationnels pour l'estimation des paramètres fondamentaux de la cosmologie. La détermination de  $H_0$  semble toutefois dépendre profondément du modèle de défecteur en plus de celle du modèle d'univers adopté. Le sujet central de cette thèse est dans la continuité directe de cette réflexion. Nous avons investigué mathématiquement ce phénomène sur deux fronts. Premièrement, en considérant au premier ordre un petit désalignement entre la source, le défecteur et l'observateur, nous avons établi les équations donnant la position des images multiples ainsi que leurs rapports d'amplification pour le cas d'une distribution de masse à symétrie axiale obéissant à une loi de puissance (Wertz, Pelgrims & Surdej, 2012). En combinant ces résultats, nous avons déterminé une expression de  $H_0$  indépendante des paramètres du modèle. Nous avons étendu cette étude d'une part en perturbant le modèle précédent au moyen d'un cisaillement gravitationnel externe, puis en considérant le modèle ellipsoïde isotherme singulier (EIS). Pour ces deux types de modèles, nous avons obtenu au premier ordre une expression de  $H_0$  qui, une fois encore, s'exprime uniquement à partir de quantités observables. De plus, nous avons démontré qu'il était possible d'exprimer les différents paramètres du modèle en termes de la position des images multiples uniquement. En conséquence, dans le cas d'un petit désalignement entre la source, le défecteur et l'observateur, il devient immédiat de déterminer lequel de ces deux modèles permet de rendre compte le plus efficacement la distribution de masse du défecteur liée au mirage gravitationnel étudié. Il est tout à fait raisonnable de supposer que des relations équivalentes puissent être déduites pour d'autres familles de défecteurs. Deuxièmement, nous avons développé une nouvelle approche analytique permettant de déterminer l'expression explicite de l'angle de déflexion, noté ci-après  $\hat{\alpha}$ . Etant donné que ce dernier dépend inextricablement de l'expression de la distribution de masse, il n'existe aucune méthode générale permettant de déduire l'expression explicite de  $\hat{\alpha}$  mais uniquement une définition implicite. Par conséquent, les approches employées peuvent différer d'une famille de modèles à une autre. En utilisant la théorie des transformées de Fourier, il est possible d'exprimer  $\hat{\alpha}$  en termes de la transformée de Fourier de la densité surfacique de masse. Nous avons étudié, comme première application, le cas des défecteurs à symétrie homoéïdale et sommes parvenus à établir séparément l'expression des deux composantes de  $\hat{\alpha}$ . Ce résultat original constitue une première preuve de l'utilité de cette approche ce qui permet de nous convaincre qu'elle puisse être une alternative robuste au

formalisme complexe introduit par Bourassa & Kantowski (1975, corrigé par Bray 1984). Un cas particulier de défecteur à symétrie homoéïdale réside dans l'ellipsoïde isotherme non singulier (EINS) qui n'a jamais fait l'objet que d'un développement analytique assez restreint (Kovner 1987a, Kormann & al. 1994 et Keeton & Kochanek 1998). L'application des transformées de Fourier a permis de retrouver l'expression du potentiel de déflexion ainsi que celle de l'angle de déflexion sous une forme différente mais équivalente. De plus, nous avons apporté une solution analytique complète pour les expressions des caustiques et lignes critiques correspondantes (Wertz & Surdej, soumis à MNRAS le 3 février 2014). Les différents traitements analytiques cités précédemment s'attardent sur des modèles paramétriques. L'approche "Fourier" s'avère également utile dans l'étude des modèles non paramétriques. En considérant le plan du défecteur comme une mosaïque de pixels carrés auxquels sont associés une densité surfacique de masse constante, il est a priori possible de modéliser toutes distributions de masse, quelque'elles soient. En utilisant les transformées de Fourier, nous avons établi l'expression de l'angle de déflexion pour ce type de modèle. Nous sommes convaincus de l'utilité que va trouver cette expression analytique dans l'étude de la reconstruction de la distribution de masse des défecteurs.

*Dedicated to Olivier GARCET*



# CONTENTS

---

<b>Abstract</b>	<b>v</b>
<b>Résumé</b>	<b>vii</b>
<b>1 Introduction to the gravitational lensing theory</b>	<b>1</b>
1.1 General introduction . . . . .	1
1.2 Gravitational lensing theory hypotheses . . . . .	3
1.2.1 The geometrical optics approximation . . . . .	3
1.2.2 The FLRW universe and the weak-field approximation . . . . .	4
1.2.3 The transparent geometrically-thin lens approximation . . . . .	5
1.3 General relativity, cosmology and distances . . . . .	6
1.3.1 Foreword . . . . .	6
1.3.2 The FLRW metric . . . . .	7
1.3.3 The non-trivial concept of distances . . . . .	9
1.4 From general relativity to the deflection angle . . . . .	14
1.4.1 First derivation of the expression of the deflection angle . . . . .	14
1.4.2 Gravitational lens deflection angle . . . . .	17
1.4.3 The deflection potential . . . . .	19
1.5 The lens equation . . . . .	20
1.6 Time delays . . . . .	22
1.7 Lens equation in terms of dimensionless quantities . . . . .	26
1.8 Amplification, critical and caustic curves . . . . .	28
1.9 The mass-sheet degeneracy . . . . .	35
1.10 The simple case of axially symmetric lenses . . . . .	37
1.11 Elliptical symmetric lenses and complex representation . . . . .	42
<b>2 Asymptotic solutions for the case of power-law axially symmetric and sie gravitational lens models</b>	<b>49</b>
2.1 Introduction . . . . .	49
2.2 Paper I . . . . .	51
2.3 Derivation of Eqs. (96) and (97) proposed in Paper I . . . . .	67
2.3.1 Determination of $y_{c,m}$ for the case of $\varepsilon = 1$ (SIS) and $\omega = 0$ . . . . .	68
2.3.2 Determination of $y_{c,m}$ for the case $0 \leq \varepsilon \leq 1$ and $\omega = 0$ . . . . .	69
2.4 Paper II . . . . .	73

---

<b>3</b>	<b>Use of the Fourier transform to derive simple expressions for the gravitational lens deflection angle</b>	<b>87</b>
3.1	Introduction . . . . .	87
3.2	Paper III . . . . .	91
3.3	Deflection angle as the sum of two contributions . . . . .	99
3.4	The singular isothermal ellipsoid (SIE) lens models . . . . .	101
3.5	The uniform disk lens models . . . . .	105
3.6	Regular grid composed of square pixels . . . . .	107
3.6.1	Determination of the expression of the deflection angle . . . . .	108
3.6.2	Test of Eq. (3.62) for the case of the NSIS lens model . . . . .	112
3.7	Paper IV . . . . .	121
3.8	Illustration of the NSIE lens mapping . . . . .	135
<b>4</b>	<b>Conclusions</b>	<b>145</b>
	<b>Bibliography</b>	<b>149</b>
	<b>List of publications</b>	<b>153</b>
	<b>Acknowledgements</b>	<b>159</b>



# INTRODUCTION TO THE GRAVITATIONAL LENSING THEORY

---

## 1.1 General introduction

---

Since the emergence of the Einstein's general relativity theory (GR, Einstein 1916), our understanding and knowledge about the origin and evolution of the universe have been constantly improving. However, despite all efforts provided by several generations of scientists, there exists no definitive answer to the universe model's puzzle. To date, probing the cosmological parameters remains an open subject, so much that many present and future space missions have been proposed and selected to try answering these fundamental questions.

One of the most beautiful predictions of GR concerns the deflection of light rays which pass close or through a mass distribution. Such a phenomenon is known as gravitational lensing (GL) and has first been observed by D. Walsh, B. Carswell and R. Weymann in 1979. Currently, GL studies allow to investigate numerous fields of astrophysical research, e.g. exoplanet detection and characterization, dynamic of galaxies, distribution of dark matter inside galaxy clusters, or cosmography diagnosis. The use of GL phenomena as a cosmological tool constitutes a unique and independent way to probe the fundamental universe parameters such as  $H_0$ ,  $\Omega_m$  or  $\Omega_\Lambda$ . The GL phenomena can be approached according to two regimes : the strong lensing and the weak lensing. Based upon the same physical concepts, the first one includes GL which produces multiple lensed images or giant luminous arcs, while the second one includes small magnification and distortion which do not lead to the formation of multiple lensed images. Both of these regimes can be used as cosmological probes. The strong GL allows to observe multiple (de-)amplified lensed images of a background source. The foreground origin of the light bending may be due, for instance, to a galaxy or a cluster of galaxies. From the observation of the light curves of

the lensed images of a quasar (galaxy-quasar lensing), the time delays, together with the modeling of the deflector mass distribution, may reveal the value of  $H_0$  (Refsdal 1964 a and b). When the deflector is a galaxy cluster (cluster lensing), the lensed images of background galaxies may take the form of huge and twisted arcs. The study of their shapes allows to reconstruct the mass distribution of the cluster and then to constrain the dark matter inside the cluster. Furthermore, since the strength of lensing directly depends on the ratios between angular diameter distances between the source, the deflector and the observer, cluster lensing is sensitive, as well as galaxy-quasar lensing, to the value of the cosmological parameters.

Even though the study of the lensed images of a unique source can in principle provide a study of the geometry of the universe, the statistical approach of the GL phenomenon constitutes a more powerful and trustworthy tool to constrain the cosmological parameters. Indeed, Turner, Ostriker and Gott (1984) have first developed a formalism in order to calculate statistical quantities associated with GL of quasars in the framework of flat Friedmann-Lemaître-Robertson-Walker (FLRW) universes. In particular, the integrated probability for a quasar at a given redshift of being multiply imaged by a galaxy is sensitive to the cosmological parameters. This approach has already been investigated for different types of deflectors : the singular isothermal sphere (e.g. see Turner, Ostriker & Gott, 1984, Gott, Park & Lee, 1989, Surdej et al., 1993), the point-like deflector (e.g. Fukugita, Futamase & Kasai, 1990), or more recently the singular isothermal ellipsoid (Oguri et al., 2012). These statistical studies need of course a representative sample of lensed quasars at various redshifts. Such a lensed quasar distribution has already been obtained from the "sloan digital sky survey quasar lens search" (SQLS, see Oguri et al., 2012). In the foreseeable future, the international liquid mirror telescope (ILMT) will also provide an ideal tool in order to consistently detect and catalog lensed quasar candidates in a narrow strip of the sky (Borra et al. 2009). In addition, the recently launched Gaia mission should also provide a sample of bright lensed quasar candidates over the whole sky.

Since the galaxy shapes are intrinsically elliptic, the distillation of relevant information from an individual lensed image of a distant galaxy in the weak lensing regime turns out to be difficult. However, a statistical study of the shapes and orientations of a set of galaxies may lead to the reconstruction of the tidal gravitational field, the so-called shear (Bartelmann & Schneider, 2001). Actually, if the shear can be observed from image distortions, the distribution of mass can be directly deduced. As a consequence, weak lensing also constitutes a powerful tool to probe the nature and distribution of dark matter in galaxy clusters and large-scale structures. Finally, let us mention the impact of weak lensing on the cosmic microwave background (CMB). This relic radiation represents the signature of the decoupling between

photons and matter, approximately 300,000 years after the Big Bang ( $z \simeq 1000$ ). Since it travels over very long distances, this radiation is slightly deflected by the presence of matter which fills the universe. Furthermore, this matter acts mostly on the CMB as weak lensing. Therefore, together with the Planck observations, the study of the weak lensing effects on the CMB should lead to a better estimation of the cosmological parameters.

The present thesis focuses on strong gravitational lensing of point-like sources (e.g. quasars) from a mathematical and theoretical point of view. All the results presented in the following introduction come from the literature and can be mostly found in the excellent monograph "Gravitational Lenses" by Schneider, Ehlers & Falco (1992, hereafter SEF). Specific references will always be indicated. Our goal in this chapter consists of presenting these well-known results to the non-specialist readers.

## **1.2** Gravitational lensing theory hypotheses

---

The gravitational lens theory, alike any other theory, is based upon some assumptions which simplify the handling of the involved concepts but allow to quantitatively grasp the phenomenon. In this section, we present these fundamental assumptions, starting points for GL studies, and we discuss their range of validity. For more details about the gravitational lensing theory hypotheses, the reader is invited to consult "Singularity Theory and Gravitational Lensing", Petters, Levine & Wambsganss (2001), and "Aspects statistiques du phénomène de lentille gravitationnelle dans un échantillon de quasars très lumineux", Claeskens (1998).

### **1.2.1** The geometrical optics approximation

---

Light is commonly defined as an electromagnetic radiation which exhibits properties of both waves and particles, also called the wave-particle duality of the light. Wave optics constitutes a convincing approximation of an exact physical theory of light, which allows the studies of interference, diffraction and polarization phenomena, among others. However, since the "distortions" of spacetime studied in the framework of GL are much larger than the wavelength of light, the diffraction effects can be reasonably ignored. Light bundles from two or more lensed images could, in principle, show interference. However, since the time

delays between these lensed images are much larger than the coherence length of the light wave, interference effects can be ignored.

Consequently, the gravitational lensing phenomenon can be studied under the geometrical optics approximation which can be summarized by the three following statements (Misner, Thorne & Wheeler 1973, p. 571 - 583). First, light is propagating along null geodesics of spacetime which are called *light rays*. Furthermore, light rays lie in and are orthogonal to surfaces of constant phase. Secondly, A light ray's polarization vector is orthogonal to the ray and transported parallel along the ray. Thirdly, light obeys the law of photon conservation which states that the number of photons is always conserved. From the last statement, one deduces that the gravitational lensing phenomenon deforms the cross sectional area of light bundles, which affects the flux of unresolved lensed images.

For the case of a point-like source located on a caustic curve, the geometrical optics approximation leads to an infinite amplification factor, which is of course unphysical. As a consequence, a more rigorous way to study this case should be investigated using the wave optics approximation (see chapter 7 of SEF, 1992). Despite that, the geometrical optics approximation suffices for the majority of the lensing situations.

## **1.2.2** The FLRW universe and the weak-field approximation

---

Owing to its nature, the deflector constitutes an inhomogeneity lying in the universe. Therefore, a rigorous treatment of the gravitational lensing phenomenon should require an inhomogeneous description of the spacetime in the vicinity of the deflector. Unfortunately, there exists no exact solutions for the Einstein field equations in such a situation. With a view of analytically treating the gravitational lensing theory, a reasonable assumption consists in describing the spacetime geometry with the FLRW metric. The latter models describe matter dominated universes which can be considered homogeneous, isotropic and without pressure, at large scale. A light ray dealing with gravitational lensing will propagate during most of its travel through a FLRW universe for which the spacetime metric is given by (e.g. see Schutz 1985) :

$$ds^2 = -c^2 dt^2 + R^2(t) \left[ \frac{dr^2}{1 - kr^2} + r^2 (d\theta^2 + \sin^2 \theta d\phi^2) \right]. \quad (1.1)$$

The determination of the latter equation, the signification of all the terms and other basic results concerning FLRW universes can be found in section 1.3.2.

Since the shortest distance between the deflected light rays passing through the lensing galaxy and its center is at least of the order of kpc, the strength of the gravitational field can be considered very small. Indeed, by denoting  $\Phi$  the Newtonian gravitational potential and  $c$  the speed of light in vacuum, we have typically  $\Phi/c^2 \lesssim 10^{-5}$ . Therefore, the weak gravitational field approximation can be adopted and the deflection angle is sufficiently small to be associated with the value of its tangent. The geometry of spacetime in the lens plane can then be described by the well-known metric :

$$ds^2 = -\left(1 + \frac{2\Phi}{c^2}\right)c^2 dt^2 + \left(1 - \frac{2\Phi}{c^2}\right)dr^2, \quad (1.2)$$

which is an exact solution of the linearized Einstein field equations. The latter equation is used in section 1.4.1 in order to determine the expression of the deflection angle. For the case of a point-like deflector, e.g. a black hole, the weak-field approximation is no longer valid. Nevertheless, the latter spacetime metric together with the distribution theory allow to derive the expression of the deflection angle.

### 1.2.3 The transparent geometrically-thin lens approximation

The distances involved in the gravitational lensing theory are of the order of cosmological distances. Typically, the distance between the observer and the source (resp. the deflector), e.g. a quasar (resp. a galaxy), is often larger than one Gpc. Moreover, the distance along which the light ray is bent corresponds roughly to the thickness of the deflector, which is much smaller. We assume then that the change in direction of the light ray occurs instantaneously in a plane, the so-called *lens plane*, which is defined perpendicularly to the source-observer line-of-sight and includes the deflector gravity center. Let us therefore define the observer and source planes which are both perpendicular to the line-of-sight and include respectively the observer and the source. As a consequence, the light rays are regarded as propagating along straight lines and the 3D mass distribution density of the deflector represented by the volume  $\rho(\mathbf{b}, l)$  can be modeled by means of the projected surface mass density  $\Sigma(\mathbf{b})$  defined as :

$$\Sigma(\mathbf{b}) = \int_{\mathbb{R}} \rho(\mathbf{b}, l) dl, \quad (1.3)$$

where  $l$  corresponds to an affine parameter defined along the direction of light propagation. In addition, we assume that galactic and extragalactic extinction is negligible. This hypothesis

reflects more the a priori unknown extinction-law through the light travel than a quantitative and measured value of the extinction.

## 1.3 General relativity, cosmology and distances

---

### 1.3.1 Foreword

---

Cosmology, i.e. the study of the universe as a whole, raises some of the most fundamental questions of physics : how did the universe begin, how did the matter originate, where do the laws of physics come from ? Our ability to understand the origin and evolution of the universe essentially depends, at least until now, on the Einstein's theory of general relativity. This geometric theory of gravitation generalizes the special relativity theory and Newton's law of universal gravitation, providing in a very elegant way a unified description of gravity as due to the curvature of its spacetime. The relation between the energy-momentum contained in the universe and the curvature of spacetime is fully determined by the so-called Einstein field equations :

$$G_{\mu\nu} \equiv R_{\mu\nu} - \frac{g_{\mu\nu}}{2} R + g_{\mu\nu} \Lambda = \frac{8\pi G}{c^4} T_{\mu\nu}, \quad (1.4)$$

where  $R_{\mu\nu}$  represents the *Ricci tensor*,  $g_{\mu\nu}$  the metric tensor,  $R$  the curvature scalar,  $\Lambda$  the cosmological constant, and  $T_{\mu\nu}$ , the energy-momentum tensor. Behind its apparent simplicity lies a very powerful tool in order to quantitatively describe most parts of the observed phenomena in the universe. According to large-scale observations, the universe turns out to be highly *homogeneous* and *isotropic*. Indeed, on scales typically much larger than 10 Mpc, the uniformity of the universe is apparent in the average density, the types of galaxies and their chemical composition, for instance. Furthermore, since the speed of light is finite, looking far away results in looking back in the past. The observations lead to the conclusion that the early universe presents the same level of homogeneity. The isotropic property of the universe means that it looks the same, on average, in every direction, i.e. there exists no preferred direction. In addition, the expansion of the universe seems to be at the same rate in every direction we look at. As a consequence, galaxies seem to recede from us at a speed which is proportional to their distance. This feature can be expressed by the famous Hubble's relation  $v = Hd$ , where  $v$  represents the recession velocity of the galaxies,  $d$  their

distances from us, and  $H$ , the Hubble parameter which is time dependent. The actual value of  $H$  is denoted as  $H_0$  and is estimated to be  $67.3 \pm 1.2 \text{ km s}^{-1} \text{ Mpc}^{-1}$  (Planck Collaboration 2013). Let us note that the latter expression of the Hubble relation is *local*, i.e. applicable for  $v/c \ll 1$ . For the case of distances  $d \gtrsim 1 \text{ Gpc}$ , relativistic corrections have to be considered. Fortunately, 1 Gpc is large enough to maintain the homogeneous and isotropic features of the universe.

### 1.3.2 The FLRW metric

Let us now derive the cosmological metric which describes the geometry of an homogeneous and isotropic universe. The present approach follows Schutz (1985). Let us remind the two following assumptions. First, we consider the spacetime as a set of hypersurfaces of constant cosmic time  $t$ , also called *proper time*, which are perfectly homogeneous and isotropic. Therefore, any events which belong to such an hypersurface are considered as simultaneous. Secondly, the mean rest frame of the galaxies agrees with this definition of simultaneity. We denote  $x^i$  with  $i \in \{1, 2, 3\}$  the space coordinates and  $t$  the proper time associated to a galaxy. At one given moment denoted by  $t_0$ , the hypersurface of constant proper time  $t_0$  has the line element given by :

$$dl^2(t_0) = g_{ij}(t_0) dx^i dx^j, \quad (1.5)$$

where the components of the metric tensor  $g_{ij}$  are time dependent because of the expansion of the universe. At another time  $t_1 > t_0$ , the hypersurface with constant proper time  $t_1$  has the line element given by :

$$dl^2(t_1) = g_{ij}(t_1) dx^i dx^j, \quad (1.6)$$

where  $g_{ij}(t_1)$  can be represented as :

$$g_{ij}(t_1) = R^2(t_1, t_0) g_{ij}(t_0), \quad (1.7)$$

with  $R(t_1, t_0)$ , a function which guarantees that all the components of the metric tensor increase at the same rate, i.e. which convey the isotropy of the universe. This latter function can be scaled to equal 1 at  $t_0$  and be denoted by  $R(t)$ . In that form,  $R(t)$  is known as *the scale*

*factor*. The general form of Eq. (1.6) is then given by :

$$dl^2(t) = R^2(t) g_{ij} dx^i dx^j , \quad (1.8)$$

and the line element for the full spacetime takes the form :

$$ds^2 = -c^2 dt^2 + R^2(t) g_{ij} dx^i dx^j . \quad (1.9)$$

Under the isotropic assumption, the geometry of spacetime must be spherically symmetric with respect to the origin of the system coordinates. One can then demonstrate that the expression of the line element  $dl^2$  always takes the form (see Schutz 1985) :

$$dl^2 = e^{2\Lambda(r)} dr^2 + r^2 d\Omega^2 , \quad (1.10)$$

where  $d\Omega^2 = d\theta^2 + \sin^2 \theta d\phi^2$ , when adopting the spherical coordinates  $(r, \theta, \phi)$ . Let us insist on the fact that the latter equation results from geometrical considerations only. In order to take account of the homogeneity feature of the universe, a necessary and sufficient condition is that the curvature scalar  $R$  must have the same value at every point, By inference, the trace of the Einstein tensor  $G$ , whose components are defined by Eq. (1.4), must also be constant :

$$G = G_{ij} g^{ij} = -\frac{1}{r^2} \left[ 1 - \frac{d}{dr} \left( r e^{-2\Lambda(r)} \right) \right] \equiv K , \quad (1.11)$$

where  $K$  is a constant. After integrating the latter equation with respect to  $r$ , we obtain :

$$e^{2\Lambda(r)} \equiv g_{rr} = \frac{1}{1 + \frac{Kr^2}{3} - \frac{C}{r}} , \quad (1.12)$$

where  $C$  represents a constant of integration. Its value can be constrained by requiring that the geometry of spacetime has to be locally flat. Therefore,  $g_{rr}(r \rightarrow 0) = 1$  implies  $C = 0$ . Furthermore, by denoting the so-called *curvature constant*  $k = -K/3$  and scaling the coordinate  $r$  in such a way that  $k = -1, 0$  or  $1$ , the latter equation simply transforms into :

$$g_{rr} = \frac{1}{1 - kr^2} . \quad (1.13)$$

As a result, the spacetime geometry which meets the homogeneous and isotropic conditions



can be described by the metric :

$$ds^2 = -c^2 dt^2 + R^2(t) \left[ \frac{dr^2}{1 - kr^2} + r^2 d\Omega^2 \right], \quad (1.14)$$

which is called the *Friedmann - Lemaitre - Robertson - Walker metric*. Let us note that all the time dependence lies in the scale factor  $R(t)$  which explicit expression requires solving the Einstein field equations (1.4). Due to the chosen definition of  $k$ , the coordinate  $r$  is unitless and  $R(t)$  has units of length. We may deduce important consequences from the latter form of the FLRW metric.

### 1.3.3 The non-trivial concept of distances

At the human scale, the determination of the distance between two objects is rather intuitive. We can easily imagine to simply use a rigid ruler in order to count how many meters separate two objects. Since we need to measure the distance between two galaxies, the use of a ruler is, of course, no longer appropriate. Because of the expansion and the geometry of the universe, and the finite speed of light, there exist several definitions of the notion of distance between two events. Let us define several of them which are particularly relevant.

Let us first consider the so-called *comoving coordinate distance* between two events. By denoting O the observer located at the origin of the coordinate system  $(r, \theta, \phi)$ , the comoving coordinate distance  $\chi(r)$  between O and the event E characterized by  $(r, 0, 0)$  is given by :

$$\chi(r) = \int_0^r \frac{1}{\sqrt{1 - kr'^2}} dr' = \begin{cases} \arcsin(r) & \text{if } k = 1, \\ r & \text{if } k = 0, \\ \operatorname{arcsinh}(r) & \text{if } k = -1. \end{cases} \quad (1.15)$$

By definition, the comoving coordinate distance  $\chi(r)$  between two events does not depend on the time coordinate which indicates that  $\chi(r)$  remains constant and independent on the expansion of the universe. Of course, the possible proper motions are neglected since they are significantly smaller than the systematic expansion speed over cosmological distances. Therefore,  $\chi(r)$  may be useful in order to define the cosmological redshift of a distant event.

Let us consider two photons, each one emitted from a galaxy G characterized by  $(r, 0, 0)$ . The emission times are denoted by  $t_E$  and  $t_E + \Delta t_E$ , and the reception time by  $t_R$  and  $t_R + \Delta t_R$ .

Therefore, since the comoving coordinate distance  $\chi(r)$  is constant and from Eq. (1.14) remembering that  $ds^2 = 0$  for the case of a photon, we have :

$$\chi(r) = \int_{t_E}^{t_R} \frac{c dt}{R(t)} = \int_{t_E + \Delta t_E}^{t_R + \Delta t_R} \frac{c dt}{R(t)}. \quad (1.16)$$

In addition, we can reasonably assume that  $R(t)$  remains constant during the considered time scale. Therefore, Eq. (1.16) leads to :

$$\frac{\Delta t_R}{\Delta t_E} = \frac{R(t_R)}{R(t_E)} = \frac{\lambda_R}{\lambda_E} \equiv 1 + z, \quad (1.17)$$

where  $\lambda_E$  (resp.  $\lambda_R$ ) corresponds to the wavelength of the emitted photon (resp. received photon), and  $z$ , the redshift of the source emitting the photons.

Another method to define the distance between two events can be based on the use of the physical property of the considered astrophysical objects. Indeed, we can compare the proper size of a galaxy with respect to its angular size on the sky plane in order to determine its distance. Such a distance is called the *angular diameter distance*. Let us consider on one hand a galaxy characterized by its position  $(r, 0, 0)$ , a proper size  $l$  projected on the sky plane and an angular size  $\phi \ll 1$ , and, on the other hand, an observer located at the origin of the coordinate system. The angular diameter distance  $D_A(r)$  is simply defined by :

$$D_A(r) = \frac{l}{\phi}. \quad (1.18)$$

Using the angular part of Eq. (1.14) and assuming, without loss of generality, that the proper size  $l$  lies in the plane  $\theta = \pi/2$  and one of its extremity corresponds to  $\phi = 0$ , the expression of  $l$  takes the form :

$$l = \int_0^l dl' = R(t_E) r \int_0^\phi d\phi' = R(t_E) r \phi, \quad (1.19)$$

and then, using Eq. (1.17) the expression of the angular diameter distance transforms into :

$$D_A(r) = \frac{R_0 r}{1 + z}, \quad (1.20)$$

where  $R_0 \equiv R(t_R)$  represents the value of the scale parameter at the present reception time. In the framework of the gravitational lensing theory, the involved distances are angular diameter distances relative to a FLRW metric. Explicit expressions, in terms of cosmological

parameters, of the angular diameter distances between two events located respectively at redshifts  $z_1$  and  $z_2$  require to solve the Einstein field equations (1.4) for the FLRW metric.

First, we can express the components of the energy-momentum tensor for the case of a perfect fluid (Schutz 1985) :

$$T_{\mu\nu} = \text{diag} \left( \rho c^4, p \frac{R^2(t)}{1 - kr^2}, p R^2(t) r^2, p R^2(t) r^2 \sin^2 \theta \right), \quad (1.21)$$

where  $\text{diag}$  represents "the diagonal matrix components", and  $\rho$  denotes the mass density,  $p$  the pressure, both measured by a comoving observer. As a result, from Eqs. (1.4), (1.14) and (1.21), and since the FLRW universe has no pressure ( $p = 0$ ), we obtain the two following equations :

$$\left( \frac{\dot{R}}{R} \right)^2 = \frac{8\pi G\rho}{3} - \frac{kc^2}{R^2} + \frac{\Lambda c^2}{3}, \quad (1.22)$$

and

$$3 \frac{\ddot{R}}{R} = -4\pi G\rho + \Lambda c^2, \quad (1.23)$$

where the  $\cdot$  denotes the derivative with respect to the proper time  $t$ . We recall that  $R$  and  $\rho$  are both proper time dependent functions, and we denote by the subscript 0 the quantities evaluated at the proper time  $t_0$ , i.e. the current proper time. Let us define three cosmological parameters which can be, in principle, deduced from the observations. The *Hubble parameter*  $H(t)$ , the deceleration parameter  $q(t)$  and the density parameter  $\Omega(t)$  are respectively defined by :

$$H(t) = \frac{\dot{R}(t)}{R(t)}, \quad (1.24)$$

$$q(t) = - \frac{\ddot{R}(t)R(t)}{\dot{R}^2(t)}, \quad (1.25)$$

$$\Omega(t) = \frac{8\pi G\rho(t)}{3H^2(t)}, \quad (1.26)$$

with  $H_0$ ,  $q_0$  and  $\Omega_0$  representing current values of those parameters. After dividing by  $H_0^2$

both members of Eq. (1.22), the latter one and Eq. (1.23) transform into :

$$\frac{H^2}{H_0^2} = \Omega_0 \frac{\rho}{\rho_0} - \frac{kc^2}{R^2 H_0^2} + \frac{\Lambda c^2}{3H_0^2}, \quad (1.27)$$

and

$$H^2 q = \frac{H_0^2 \Omega_0}{2} \frac{\rho}{\rho_0} - \frac{\Lambda c^2}{3}, \quad (1.28)$$

which remain valid for any value of the proper time  $t$ , especially for  $t = t_0$ . Therefore, by defining the scaled cosmological constant  $\Omega_\Lambda = \Lambda c^2 / 3H_0^2$  and the curvature parameter  $\Omega_k = -kc^2 / R_0^2 H_0^2$ , we obtain from Eqs. (1.27) and (1.28) the two following relations :

$$\Omega_\Lambda = \frac{\Omega_0}{2} - q_0, \quad \text{and} \quad -\Omega_k = \Omega_0 + \Omega_\Lambda - 1. \quad (1.29)$$

For the case of matter-dominated cosmologies, the pressure  $p = 0$  and the equation of motion for matter,  $T^{\mu\nu}_{;\nu} = 0$ , together with the isotropy assumption lead to  $\rho R^3 = \text{constant}$ . Therefore, using Eq. (1.20), we have  $\rho/\rho_0 = (1+z)^3$  and Eq. (1.29) leads to the expression of the Hubble parameter in terms of observable quantities for the matter-dominated FLRW universe :

$$H^2(z) = H_0^2(z) \left[ \Omega_0 (1+z)^3 + \Omega_k (1+z)^2 + \Omega_\Lambda \right]. \quad (1.30)$$

From the FLRW metric (see Eq. (1.14)) and Eq. (1.17), the element of comoving coordinate distance  $d\chi$  is simply given by :

$$d\chi = c \frac{dt}{R} = -\frac{c}{R_0} \frac{dz}{H(z)}, \quad (1.31)$$

and from Eq. (1.30), the comoving coordinate distance  $\chi(z_1, z_2)$  between two events located at  $z_1$  and  $z_2$  is given by :

$$\chi(z_1, z_2) = \frac{c}{H_0 R_0} \int_{z_1}^{z_2} \frac{dz}{\sqrt{\Omega_0 (1+z)^3 + \Omega_k (1+z)^2 + \Omega_\Lambda}}. \quad (1.32)$$

The latter integral can only be solved for particular values of the cosmological parameters  $\Omega_0$ ,  $\Omega_k$  and  $\Omega_\Lambda$ . For the case of  $\Omega_\Lambda = 0$  and from Eq. (1.15), the comoving radial coordinate  $r(z_1, z_2)$  of an event located at  $z_2$  in the referential of an event located at  $z_1 < z_2$  is given, for

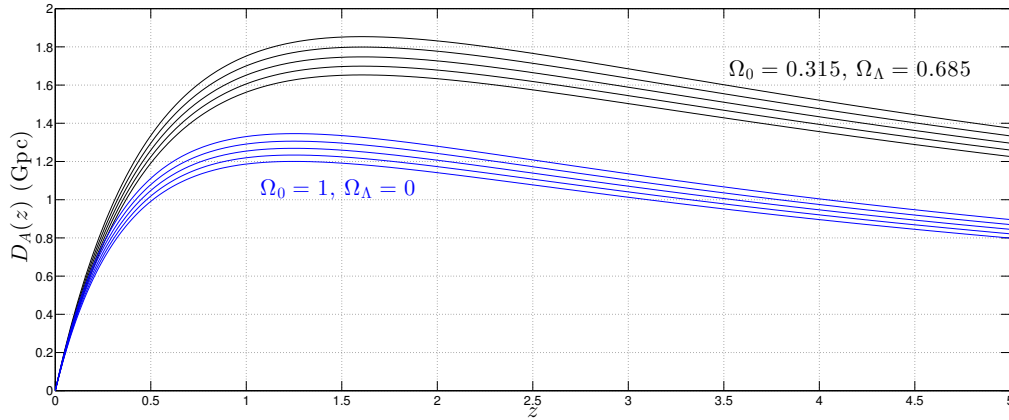


**Figure 1.1:** Illustration of the angular distance  $D_A(0, z)$  as a function of the redshift  $z$  for the two cases  $(\Omega_0, \Omega_\Lambda) = (1, 0)$  (red) and  $(\Omega_0, \Omega_\Lambda) = (0.315, 0.685)$  (black) for different values of the Hubble parameter [66, 68, 70, 72, 74]  $\text{km s}^{-1} \text{Mpc}^{-1}$ .

any values of  $k$ , i.e. whatever the sign of  $\Omega_0$ , by :

$$r(z_1, z_2) = \frac{2c}{H_0 R_0 \Omega_0^2 (1+z_1)(1+z_2)} \left[ (2 + \Omega_0(z_2 - 1)) \sqrt{\Omega_0 z_1 + 1} - (2 + \Omega_0(z_1 - 1)) \sqrt{\Omega_0 z_2 + 1} \right], \quad (1.33)$$

which is called the *generalized Mattig relation*. From Eqs. (1.20) and (1.33), we obtain the expression of the angular diameter distance  $D_A(z_1, z_2)$  for the case of the matter-dominated FLRW universe without cosmological constant :

$$D_A(z_1, z_2) = \frac{2c}{H_0 \Omega_0^2 (1+z_1)(1+z_2)^2} \left[ (2 + \Omega_0(z_2 - 1)) \sqrt{\Omega_0 z_1 + 1} - (2 + \Omega_0(z_1 - 1)) \sqrt{\Omega_0 z_2 + 1} \right], \quad (1.34)$$

which can be reduced, for the case  $z_1 = 0$ , i.e. with respect to an earth observer, to :

$$D_A(z) = \frac{2c}{H_0} \frac{\Omega_0 z + (\Omega_0 - 2) (\sqrt{\Omega_0 z + 1} - 1)}{\Omega_0^2 (1+z)^2}. \quad (1.35)$$

For the case of the so-called  $\Lambda$ CDM universe with  $\Omega_\Lambda = 0.685$ ,  $\Omega_0 = 0.315$ , hence  $k = 0$ , the angular diameter distance between the earth ( $z_1 = 0$ ) and an event located at  $z_2 \equiv z$  is implicitly given by :

$$D_A(z) = \frac{c}{H_0(1+z)} \int_0^z \frac{dz'}{\sqrt{\Omega_0(1+z')^3 + \Omega_\Lambda}}. \quad (1.36)$$

In Fig. 1.1, we have illustrated the dependence of the angular diameter distance  $D_A(z)$  as a function of the redshift  $z$  for the two previous cases.

**1.4** From general relativity to the deflection angle

---

In the present section, we derive the expression of the deflection angle of a light ray passing near or through a deflector. The present approach follows Van Drom (1989) and Schutz (1985).

**1.4.1** First derivation of the expression of the deflection angle

---

We adopt here the standard tensor notation. Greek and Roman subscripts refer respectively to spacetime and spatial coordinates or components. Furthermore, we use the Einstein summation convention.

Since the involved angles are very small (typically 1 arcsec), and the four-momentum vector  $\mathbf{p}$  of a photon points towards the direction of its propagation, we can always define the  $x$ -component of the deflection angle as the ratio between the  $z$ - and  $x$ -components of the deviated photon four-momentum :

$$\alpha^x = \frac{p^z}{p^x}, \quad (1.37)$$

where the system of coordinates is defined such as the components of the non-deviated photon four-momentum are given by  $\mathbf{p} = (0, 0, p^z)$ . Since the deflection angle remains small, the  $z$ -component of the four-momentum photon is assumed constant, while the  $x$ -component can be evaluated by the sum of all the infinitesimal contributions along the  $x$ -direction with respect to  $z$  :

$$p^x = \int_{\mathbb{R}} \frac{dp^x}{dz} dz. \quad (1.38)$$

The equation of motion for a photon is simply given by :

$$\nabla_{\mathbf{p}} \mathbf{p} \equiv p^\alpha p_{\beta;\alpha} = 0, \quad (1.39)$$

where the semi-colon symbol denotes the covariant derivative, and  $p_\beta$  the component of the one-form  $\tilde{p}$  (also called dual vector) associated to the vector  $\mathbf{p}$ . From the definition of the

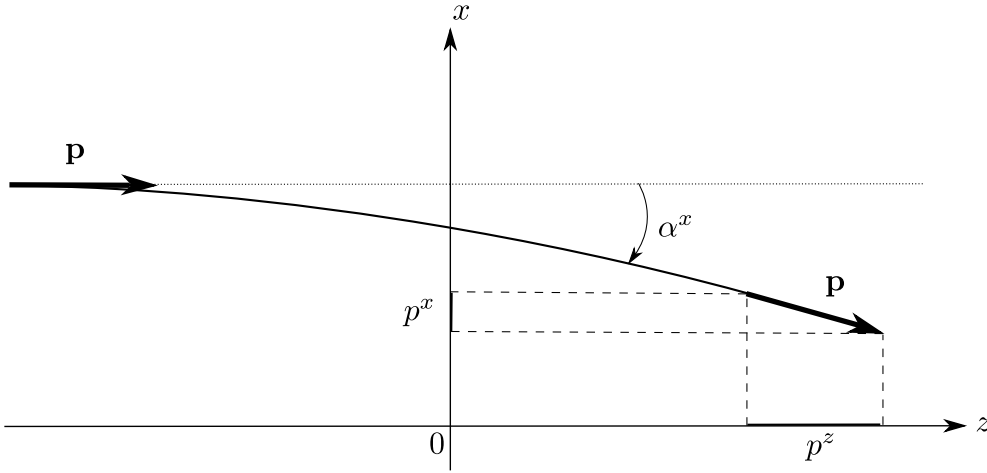


**Figure 1.2:** Illustration of the propagation of a deflected light ray along the direction of the four-momentum vector  $\mathbf{p}$ .

covariant derivative (e.g. see Weinberg 1972), the latter equation can be reduced to :

$$p^\alpha p_{\beta,\alpha} - \Gamma_{\beta\alpha}^\gamma p^\alpha p_\gamma = 0, \quad (1.40)$$

where the comma symbol followed by a subscript denotes the usual partial differentiation with respect to the coordinate labeled, and  $\Gamma_{\beta\alpha}^\gamma$  the connexion coefficients which can be expressed in terms of the metric tensor components  $g_{ij}$  :

$$\Gamma_{\beta\alpha}^\gamma = \frac{1}{2} g^{\mu\gamma} (g_{\mu\beta,\alpha} + g_{\mu\alpha,\beta} - g_{\beta\alpha,\mu}). \quad (1.41)$$

Therefore, by denoting  $\lambda$  an affine parameter (which could be chosen equal to  $\lambda = \tau/m$  for the case of a massive particle with a proper time  $\tau$ ), Eq. (1.40) can be reduced to :

$$p_{\beta,\lambda} = \frac{1}{2} g_{\alpha\mu,\beta} p^\alpha p^\mu. \quad (1.42)$$

In the framework of the gravitational lensing theory, gravitational fields are supposed to be weak. The components of the metric tensor can therefore be expressed by  $g_{\alpha\mu} = \eta_{\alpha\mu} + h_{\alpha\mu}$  where  $\eta_{\alpha\mu} = \text{diag}(-1, 1, 1, 1)$  represents the components of the Minkowski metric tensor, and  $|h_{\alpha\mu}| \ll 1$ , a first order perturbation. Let us recall that  $\eta_{\alpha\mu}$  is the metric which describes the geometry of a pseudo-Euclidean spacetime with four dimensions. As a result, the ordinary Newtonian potential  $\Phi$  completely determines the metric, which has, to first order and in agreement with Eq. (1.2), the following form :

$$ds^2 = -\left(1 + \frac{2\Phi}{c^2}\right) c^2 dt^2 + \left(1 - \frac{2\Phi}{c^2}\right) dr^2, \quad (1.43)$$

where the sign of  $\Phi$  is chosen negative, so that, far from a mass  $M$ , the Newtonian potential equals  $-GM/r$ . Under these assumptions, Eq. (1.42) simply reduces, to first order, to :

$$p_{\beta,\lambda} = \frac{1}{2} h_{\alpha\mu,\beta} p^\alpha p^\mu . \quad (1.44)$$

Furthermore, from Eq. (1.43), we easily deduce that  $h_{tt} = h_{xx} = h_{yy} = h_{zz} = -2\Phi/c^2$ . As a result, after reminding that  $p^x = p^y = 0$  at order 0, the  $x$ -component reduces to :

$$p_{x,\lambda} = \frac{1}{2} (h_{tt,x} p^t p^t + h_{zz,x} p^z p^z) , \quad (1.45)$$

$$= -\frac{2}{c^2} \Phi_{,x} p^z p^z , \quad (1.46)$$

where the last equality is deduced from the fact that, for the case of a photon, we have  $\eta_{\mu\nu} p^\mu p^\nu = 0$ , which implies that  $p^t = p^z$ . Since  $p^z$  remains essentially constant and by noticing that  $p^z = p_z = dz/d\lambda \simeq \text{constant}$  and  $p_x = p^x$ , Eq. (1.46) can be transformed into :

$$\frac{d}{dz} \left( \frac{p^x}{p^z} \right) = -\frac{2\Phi_{,x}}{c^2} . \quad (1.47)$$

Finally, from Eq. (1.37), the  $x$ -component of the deflection angle can be expressed by :

$$\alpha^x = -\frac{2}{c^2} \int_{\mathbb{R}} \frac{\partial\Phi}{\partial x} dz . \quad (1.48)$$

By following the same argument for the  $y$ -component and  $z$ -component, the deflection angle vector is finally given by :

$$\alpha = -\frac{2}{c^2} \int_{\mathbb{R}} \nabla_{\perp} \Phi dz , \quad (1.49)$$

where the vector  $\nabla_{\perp} \Phi$  lies in the plane perpendicular to the direction of the deflected light ray propagation. Since the deflection angle is assumed to be very small, we approximate the gradient operator  $\nabla_{\perp}$  with  $\nabla$  which lies in the lens plane. Furthermore, the integral is performed along the line-of-sight characterized by the affine parameter  $l$ . Consequently, Eq. (1.49) reduces to :

$$\alpha = -\frac{2}{c^2} \int_{\mathbb{R}} \nabla \Phi dl . \quad (1.50)$$



### 1.4.2 Gravitational lens deflection angle

Since in the framework of the gravitational lensing theory, we consider the geometrically-thin lens approximation, we assume that the deflection angle vector lies in the lens plane. Therefore, by denoting  $(b_x, b_y)$  the system of coordinates in the lens plane, and by assuming that the Newtonian potential  $\Phi$  vanishes in the source and observer planes, Eq. (1.50) can be transformed into :

$$\boldsymbol{\alpha}(\mathbf{b}) = -\frac{2}{c^2} \int_s^o \nabla \Phi(\mathbf{b}, l) dl, \quad (1.51)$$

where  $\mathbf{b} = (b_x, b_y)$  represents the light ray impact parameter in the lens plane. We note that the gradient operator  $\nabla$  now applies only on the  $b_x$  and  $b_y$  components. The latter equation can be expressed as :

$$\boldsymbol{\alpha}(\mathbf{b}) = -\nabla \psi(\mathbf{b}), \quad (1.52)$$

where  $\psi(\mathbf{b})$  is called the *deflection potential* and is defined by :

$$\psi(\mathbf{b}) = \frac{2}{c^2} \int_s^o \Phi(\mathbf{b}, l) dl. \quad (1.53)$$

From Eqs. (1.51) and (1.52), we deduce two interesting intermediate results. First, since the deflection angle can be expressed by the gradient of a scalar quantity, its curl vanishes :

$$\nabla \times \boldsymbol{\alpha}(\mathbf{b}) = 0. \quad (1.54)$$

The second result is obtained by taking the divergence of Eq. (1.51) :

$$\nabla \cdot \boldsymbol{\alpha}(\mathbf{b}) = -\frac{2}{c^2} \int_s^o \Delta \Phi(\mathbf{b}, l) dl, \quad (1.55)$$

where  $\Delta$  represents the Laplacian. By using the Poisson equation of the Newton gravitational theory  $\Delta \Phi = -4\pi G \rho(\mathbf{b}, l)$ , the latter equation reduces to :

$$\nabla \cdot \boldsymbol{\alpha}(\mathbf{b}) = \frac{8\pi G}{c^2} \Sigma(\mathbf{b}), \quad (1.56)$$

where we have defined the *surface mass density*  $\Sigma(\mathbf{b})$  by :

$$\Sigma(\mathbf{b}) = \int_s^o \rho(\mathbf{b}, l) dl, \quad (1.57)$$

in agreement with Eq. (1.3). From Eqs. (1.54) and (1.56), we easily deduce that :

$$\Delta \alpha(\mathbf{b}) = \frac{8\pi G}{c^2} \nabla \Sigma(\mathbf{b}). \quad (1.58)$$

Since the Laplacian  $\Delta$  is a linear differential operator, the solution  $\alpha(\mathbf{b})$  can be written as an integral over a distribution of sources given by the right member of the last equation :

$$\alpha(\mathbf{b}) = \frac{8\pi G}{c^2} \iint_{\mathbb{R}^2} G(\mathbf{b}, \mathbf{b}') \nabla \Sigma(\mathbf{b}') d\mathbf{b}', \quad (1.59)$$

where  $G(\mathbf{b}, \mathbf{b}')$  represents the Green's function for the Laplacian equation and is given by :

$$G(\mathbf{b}, \mathbf{b}') = -\frac{1}{2\pi} \frac{1}{|\mathbf{b} - \mathbf{b}'|}. \quad (1.60)$$

By substituting Eq. (1.60) into Eq. (1.59), the deflection angle expression reduces to :

$$\alpha(\mathbf{b}) = -\frac{4G}{c^2} \iint_{\mathbb{R}^2} \frac{\nabla \Sigma(\mathbf{b}')}{|\mathbf{b} - \mathbf{b}'|} d\mathbf{b}'. \quad (1.61)$$

Finally, assuming that  $\Sigma(\mathbf{b}) = 0$  at the integration limits, the integration by parts of the right member of the latter equation gives :

$$\alpha(\mathbf{b}) = -\frac{4G}{c^2} \iint_{\mathbb{R}^2} \frac{\Sigma(\mathbf{b}') (\mathbf{b} - \mathbf{b}')}{|\mathbf{b} - \mathbf{b}'|^2} d\mathbf{b}'. \quad (1.62)$$

The latter expression of the deflection angle constitutes a fundamental result of the gravitational lens theory. Indeed, this expression allows one to determine the deflection angle of a light ray which reaches the lens plane at a given impact parameter  $\mathbf{b}$ , for any mass distribution of the deflector. We note that Eq. (1.62) is independent of the frequency of the deflected light, which implies that the gravitational lensing phenomenon is achromatic.

We insist on the fact that Eq. (1.62) of the deflection angle has been derived for an asymptotically flat spacetime derived from the FLRW metric (see Eq. (1.43) and their related assumptions). For the case of a spheric ( $k = 1$ ) or hyperbolic ( $k = -1$ ) geometry of spacetime, the vicinity of the deflector can still be described by an asymptotically flat spacetime. Indeed, the cosmological model dependence of Eq. (1.62) is included in the scale factor  $R(t)$  through

the terms  $\mathbf{b}'$  (and of course  $\mathbf{b}$ ) which is very small in comparison with the involved distances between the source, the lens and the observer. Therefore, it is reasonable to assume that this expression holds for those cosmological models. One keeps in mind that further calculations will be performed, unless explicitly mentioned, for an asymptotically flat spacetime.

The possibility of analytically deriving the explicit expression of the deflection angle essentially depends on the expression of the surface mass density  $\Sigma(\mathbf{b})$ . For mass distributions characterized by a high level of symmetry, e.g. axially mass distributions (see Section 1.10),  $\Sigma(\mathbf{b})$  takes a very simple form which allows to calculate straightforwardly the integrals appearing in Eq. (1.62). For the case of the singular isothermal ellipsoid (SIE) models, the use of Eq. (1.62) turns out to be very difficult. By the way, the first derivation of the SIE deflection angle proposed by Kormann & al. (1994) makes use of the Green's function theory instead of Eq. (1.62). However, the Fourier transform theory allows to consider the determination of the expression of the deflection angle in a unique way (Wertz & Surdej, 2014). Such a method has been successfully used to derive a complete and original solution for the case of the non-singular isothermal ellipsoid (NSIE) family of models (Wertz and Surdej, submitted to MNRAS on 3rd February 2014).

### 1.4.3 The deflection potential

In section 1.4.2, we have defined the deflection potential  $\psi(\mathbf{b})$  (see Eq. (1.53)). From Eq. (1.62), we can derive the explicit expression of the deflection potential as follows. First, we have :

$$\nabla\psi(\mathbf{b}) = \frac{4G}{c^2} \iint_{\mathbb{R}^2} \frac{\Sigma(\mathbf{b}') (\mathbf{b} - \mathbf{b}')}{|\mathbf{b} - \mathbf{b}'|^2} d\mathbf{b}' . \quad (1.63)$$

Integrating both members with respect to  $\mathbf{b}$  over  $\mathbb{R}^2$ , we obtain, up to an additive constant :

$$\psi(\mathbf{b}) = \frac{4G}{c^2} \iint_{\mathbb{R}^2} \Sigma(\mathbf{b}') \left\{ \iint_{\mathbb{R}^2} \frac{(\mathbf{b} - \mathbf{b}')}{|\mathbf{b} - \mathbf{b}'|^2} d\mathbf{b} \right\} d\mathbf{b}' . \quad (1.64)$$

Noticing that  $\nabla \ln |\mathbf{b}| = \mathbf{b}/|\mathbf{b}|^2$ , the expression of the deflection angle reduces to :

$$\psi(\mathbf{b}) = \frac{4G}{c^2} \iint_{\mathbb{R}^2} \Sigma(\mathbf{b}') \ln |\mathbf{b} - \mathbf{b}'| d\mathbf{b}' . \quad (1.65)$$

Furthermore, the deflection potential is a solution of the Poisson equation. Indeed, by taking the Laplacian of the latter equation with respect to  $\mathbf{b}$ , we have :

$$\Delta\psi(\mathbf{b}) = \frac{4G}{c^2} \iint_{\mathbb{R}^2} \Sigma(\mathbf{b}') \Delta(\ln|\mathbf{b} - \mathbf{b}'|) d\mathbf{b}' , \quad (1.66)$$

$$= \frac{8\pi G}{c^2} \iint_{\mathbb{R}^2} \Sigma(\mathbf{b}') \delta^2(\mathbf{b} - \mathbf{b}') d\mathbf{b}' , \quad (1.67)$$

$$= \frac{8\pi G}{c^2} \Sigma(\mathbf{b}) , \quad (1.68)$$

where  $\delta^2$  represents the 2D Dirac delta function and the second equality comes from the theory of distributions (see example 2.3.2 from « Théorie des distributions », L. Schwartz 1950).

## 1.5 The lens equation

The fundamental equation of the gravitational lens theory consists in linking the positions of a point-like source to those of the lensed images, taking into account the deflection angle. This equation, the so-called *lens equation*, can be deduced in two distinct ways : the physical and the geometrical approach. The first one can be analytically derived from the application of the Fermat principle, while the second can be straightforwardly deduced from the geometric illustration of the gravitational lensing phenomenon.

First, we adopt the physical approach. Let us consider a light ray emitted by a point-like source S at time  $t = 0$ . We assume that the light path is composed of two straight line segments, SP and PO, in agreement with the transparent geometrically-thin lens approximation (see section 1.2.3). According to the metric of the weak gravitational field (see Eq. (1.43)) and recalling that  $ds^2 = 0$  for a photon, the arrival time  $t$  of this light ray is given, to first order, by :

$$t \simeq \frac{1}{c} \int_s^o \left( 1 - \frac{2\Phi(l)}{c^2} \right) dl , \quad (1.69)$$

$$= \frac{l}{c} - \frac{2}{c^3} \int_s^o \Phi(l) dl , \quad (1.70)$$

where  $l$  can be read into the curvilinear Euclidean length of the path S (the source) - P

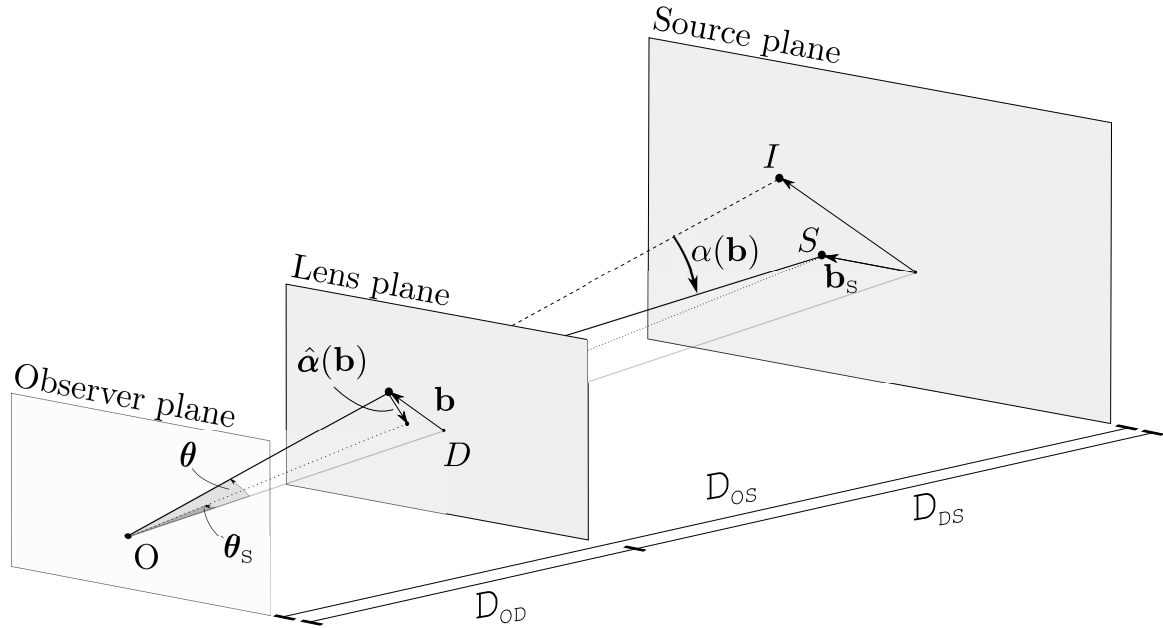


**Figure 1.3:** Illustration of the gravitational lensing phenomenon. The source  $S$  located at the position  $\mathbf{b}_s$  in the source plane emits light rays towards all directions. The light ray characterized by the impact parameter  $\mathbf{b}$  in the lens plane is deflected by the quantity  $\alpha$  and reaches the observer  $O$  in the observer plane.

(position of the lensed image in the lens plane) -  $O$  (the observer). We can evaluate the expression of  $l$  to first order as :

$$l = SP + PO, \quad (1.71)$$

$$= \sqrt{D_{DS}^2 + (\mathbf{b} - \mathbf{b}_s)^2} + \sqrt{D_{OD}^2 + \mathbf{b}^2}, \quad (1.72)$$

$$\simeq D_{DS} + D_{OD} + \frac{(\mathbf{b} - \mathbf{b}_s)^2}{2D_{DS}} + \frac{\mathbf{b}^2}{2D_{OD}}, \quad (1.73)$$

where  $\mathbf{b}_s$  represents the point-like source position in the source plane,  $D_{OD}$  (resp.  $D_{DS}$  and  $D_{OS}$ ) the angular diameter distance between the observer and the lens planes (resp. the lens and the source planes, the observer and the source planes). According to the Fermat's principle, the gravitationally lensed images appear at locations that correspond to extrema in the light travel time  $t(\mathbf{b}, \mathbf{b}_s)$ . Therefore, the lensed image positions  $\mathbf{b}$  of a point-like source located at  $\mathbf{b}_s$  in the source plane satisfy :

$$\nabla t(\mathbf{b}, \mathbf{b}_s) = 0, \quad (1.74)$$

where  $\nabla$  represents the gradient operator with respect to  $\mathbf{b}$ . After substituting Eqs. (1.70) and (1.73) into Eq. (1.74), and considering a stationary configuration, i.e. the involved distances

and mass distribution do not change during the considered time scale, we obtain

$$0 = \frac{1}{2D_{\text{DS}}} \nabla (\mathbf{b} - \mathbf{b}_s)^2 + \frac{1}{2D_{\text{OD}}} \nabla \mathbf{b}^2 - \nabla \psi(\mathbf{b}), \quad (1.75)$$

$$= \frac{D_{\text{OS}} \mathbf{b}}{D_{\text{OD}} D_{\text{DS}}} - \frac{\mathbf{b}_s}{D_{\text{DS}}} - \nabla \psi(\mathbf{b}), \quad (1.76)$$

where the deflection potential  $\psi(\mathbf{b})$  is defined by Eq. (1.65). The latter equation constitutes the lens equation, whose standard form, using Eq. (1.52), is given by :

$$\mathbf{b}_s = \frac{D_{\text{OS}}}{D_{\text{OD}}} \mathbf{b} + D_{\text{DS}} \alpha(\mathbf{b}). \quad (1.77)$$

For a given deflector, characterized by a mass distribution (information contained into  $\psi(\mathbf{b})$  and then  $\alpha(\mathbf{b})$ ), and a given cosmology (information contained into the distances  $D_{\text{OD}}$ ,  $D_{\text{DS}}$  and  $D_{\text{OS}}$ ), the lens equation gives the position  $\mathbf{b}$  of the gravitationally lensed images of a point-like source located at the position  $\mathbf{b}_s$ . The geometrical approach of determining the lens equation leads to the same expression as the one given in Eq. (1.77) (see Fig. 1.3). We note that the inversion of the lens equation can only be carried out analytically for simple mass distributions.

Finally, we can express the latter equation in terms of vectorial angle quantities. To that end, we define  $\boldsymbol{\theta}$  and  $\boldsymbol{\theta}_s$  as follows :

$$\boldsymbol{\theta} = \frac{\mathbf{b}}{D_{\text{OD}}}, \quad \text{and} \quad \boldsymbol{\theta}_s = \frac{\mathbf{b}_s}{D_{\text{OS}}}. \quad (1.78)$$

Therefore, Eq. (1.77) simply transforms into :

$$\boldsymbol{\theta}_s = \boldsymbol{\theta} + \frac{D_{\text{DS}}}{D_{\text{OS}}} \alpha(D_{\text{OD}} \boldsymbol{\theta}). \quad (1.79)$$

The advantage of this formulation of the lens equation resides in the fact that the involved vectorial quantities are no longer defined in different planes.

## 1.6 Time delays

Let us consider a background source, e.g. a quasar, which emits simultaneously two photons. We assume that these photons propagate towards two distinct lensed images of the source. Since the followed paths are not equal, the arrival time of these photons are different.

Consequently, since they are produced by the same background source, the corresponding observed light curves are shifted in time. This difference in arrival time is called the *time delay* and is denoted by  $\Delta t$ . Let us calculate  $\Delta t_{AB}$  between the light curves of two distinct lensed images of a point-like source.

First, we can define the *Fermat potential*  $\tau(\mathbf{b}, \mathbf{b}_s)$  as :

$$\tau(\mathbf{b}, \mathbf{b}_s) = \frac{D_{OD}D_{OS}}{2D_{DS}} \left( \frac{\mathbf{b}}{D_{OD}} - \frac{\mathbf{b}_s}{D_{OS}} \right)^2 - \psi(\mathbf{b}), \quad (1.80)$$

which satisfies the equation  $\nabla\tau(\mathbf{b}, \mathbf{b}_s) = 0 = \nabla t(\mathbf{b}, \mathbf{b}_s)$ . Then, we can interpret  $\tau$  as being the light travel time along the rays. The first term of the right member describes the deviation of the light ray compared to an unbent ray which crosses the lens plane at  $\mathbf{b} = \mathbf{b}_s D_{OD}/D_{OS}$ . On the other hand, the second term of the right member leads to the time delay that a ray experiences as it crosses the deflection potential  $\psi$  at the position  $\mathbf{b}$  in the lens plane. Furthermore, from Eqs. (1.70), (1.73) and (1.80), the relation between  $\tau(\mathbf{b}, \mathbf{b}_s)$  and  $t(\mathbf{b}, \mathbf{b}_s)$  can be expressed as :

$$ct(\mathbf{b}, \mathbf{b}_s) = \tau(\mathbf{b}, \mathbf{b}_s) + D_{OS} + \frac{\mathbf{b}_s^2}{2D_{OS}}. \quad (1.81)$$

In the latter equation, the second and third terms of the right member are constant, for a fixed configuration of source-deflector-observer and under the adopted assumptions. Therefore, those terms should not contribute to the total time delay.

By denoting with the subscript A (resp. B) the quantities relative to image A (resp. B), the time delay  $\Delta t_{AB}$  between the two light curves, deduced from observations, of the lensed images A and B is given by :

$$\begin{aligned} \Delta t_{AB}(\mathbf{b}_s) &= \frac{1}{c} \left( \tau(\mathbf{b}_B, \mathbf{b}_s) - \tau(\mathbf{b}_A, \mathbf{b}_s) \right), \quad (1.82) \\ &= \frac{1}{c} \frac{D_{OD}D_{OS}}{2D_{DS}} \left[ \left( \frac{\mathbf{b}_B}{D_{OD}} - \frac{\mathbf{b}_s}{D_{OS}} \right)^2 - \left( \frac{\mathbf{b}_A}{D_{OD}} - \frac{\mathbf{b}_s}{D_{OS}} \right)^2 \right] - \frac{1}{c} [\psi(\mathbf{b}_B) - \psi(\mathbf{b}_A)], \quad (1.83) \end{aligned}$$

or, identically, after inserting Eq. (1.78) into Eq. (1.83) :

$$\Delta t_{AB}(\boldsymbol{\theta}_s) = \frac{1}{c} \frac{D_{OD}D_{OS}}{2D_{DS}} \left[ (\boldsymbol{\theta}_B - \boldsymbol{\theta}_s)^2 - (\boldsymbol{\theta}_A - \boldsymbol{\theta}_s)^2 \right] - \frac{1}{c} [\psi(D_{OD}\boldsymbol{\theta}_B) - \psi(D_{OD}\boldsymbol{\theta}_A)], \quad (1.84)$$

where  $\mathbf{b}_A$  (resp.  $\mathbf{b}_B$ ) are deduced from Eq. (1.77), for a given source position  $\mathbf{b}_s$  and mass distribution of the deflector. We underline the fact that the derived time delay corresponds to the difference of the times at which the light rays reach the observer. In order to obtain the

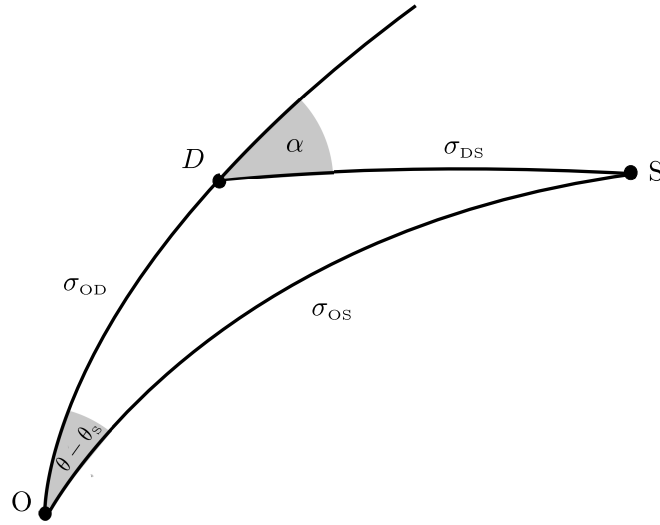


**Figure 1.4:** Illustration of the considered distances in a closed universe ( $k = 1$ ). The triangle  $O - S - D$  lies at the surface of a sphere.

proper time difference,  $\Delta t$  has to be multiplied by the time dilation factor  $1 + \Phi_0/c^2$ , where  $\Phi_0$  corresponds to the value of the gravitational potential at the observer position. For the case of the Earth, we have  $\Phi_0/c^2 \simeq 10^{-9}$ , which implies that this correction is unnecessary in applications of gravitational lensing.

We have derived the expression of the time delay (see Eq. (1.84)) for the case of asymptotically flat spacetimes. Unlike the deflection angle (see Eq. (1.62)), Eq. (1.83) does not remain exact for the case of FLRW cosmological models. The argument follows SEF 4.6, p. 143. In order to determine the time delay in such a case, we recall the expression of the FLRW metric :

$$ds^2 = -c^2 dt^2 + R^2(t) \left( \frac{dr^2}{1 - kr^2} + r^2 d\Omega^2 \right), \quad (1.85)$$

where  $d\Omega^2 = d\theta^2 + \sin^2 \theta d\phi^2$ . By denoting  $\eta$ , the so-called *conformal time*, defined as follows :

$$R(\eta) d\eta = c dt, \quad (1.86)$$

where  $R(\eta)$  represents the scale parameter  $R(t)$  expressed in terms of the conformal time, the FLRW metric transforms into :

$$ds^2 = -R^2(\eta) (d\eta^2 - d\sigma^2). \quad (1.87)$$

We assume the emission time to be  $\eta = 0$ . According to Eq. (1.85) and recalling that  $ds^2 = 0$



along light rays, the geometric contribution  $\eta_{\text{geo}}$  to the excess time delay relative to the case of no lensing is given by :

$$\eta_{\text{geo}} = \sigma_{\text{OD}} + \sigma_{\text{DS}} - \sigma_{\text{OS}} , \quad (1.88)$$

where the function  $\sigma$  represents distances measured by means of the metric  $ds^2$  given in Eq. (1.87). In order to evaluate the right member of the latter equation, we first assume  $k = 1$ . According to the law of cosines in spherical trigonometry applied to the spherical triangle O-S-D (see Fig. 1.4), and considering that  $\sigma_{\text{OS}} \simeq \sigma_{\text{OD}} + \sigma_{\text{DS}}$ , we obtain :

$$\eta_{\text{geo}} = \frac{\sin \sigma_{\text{DS}} \sin \sigma_{\text{OD}}}{2 \sin \sigma_{\text{OS}}} \alpha^2 , \quad (1.89)$$

where  $\alpha^4$ -terms have been neglected. Furthermore, by definition of the angular diameter distance (see Eq. (1.18)) and by denoting  $R_{\text{OS}}$  (resp.  $R_{\text{OD}}$ ) the value of the scale parameter for the source (resp. the deflector), we have :

$$D_{\text{OD}} = R_{\text{OD}} \sin \sigma_{\text{OD}} , \quad D_{\text{OS}} = R_{\text{OS}} \sin \sigma_{\text{OS}} , \quad D_{\text{DS}} = R_{\text{OS}} \sin \sigma_{\text{DS}} . \quad (1.90)$$

After inserting Eq. (1.90) into Eq. (1.89), we simply obtain :

$$\eta_{\text{geo}} = \frac{D_{\text{OD}} D_{\text{DS}}}{D_{\text{OS}}} \frac{\alpha^2}{2 R_{\text{OD}}} . \quad (1.91)$$

Since the time delay is small in comparison with the Hubble time  $H_0^{-1}$ , we have  $ct_{\text{geo}} = R_0 \eta_{\text{geo}}$  where  $R_0$  represents the actual value of the scale parameter. Furthermore, by definition of the redshift, we have  $1 + z_{\text{D}} = R_0 / R_{\text{OD}}$ . As a consequence, using the lens equation given in Eq. (1.79), the geometrical contribution to the arrival time compared to the unbent light ray is finally given by :

$$ct_{\text{geo}} = (1 + z_{\text{D}}) \frac{D_{\text{OD}} D_{\text{OS}}}{2 D_{\text{DS}}} (\theta - \theta_{\text{S}})^2 . \quad (1.92)$$

The latter result holds for  $k = -1$  or  $k = 0$ . Comparison between Eq. (1.92) and the geometrical contribution in Eq. (1.80) leads to the conclusion that taking into account the cosmology appears by simply “redshifting” the quantity  $ct_{\text{geo}}$ . The same conclusion can be deduced for the potential contribution to the time delay, to the extent that  $ct_{\text{pot}}$  is simply given by :

$$ct_{\text{pot}} = (1 + z_{\text{D}}) \psi(D_{\text{OD}} \theta) + \text{constant} , \quad (1.93)$$

where the constant remains the same for all light rays leaving the source plane and reaching the observer plane. As a conclusion, from Eqs. (1.92) and (1.93), the total time delay between the light curves of two lensed images can be expressed as :

$$\Delta t_{\text{AB}}(\boldsymbol{\theta}_s) = \frac{(1+z_D)}{c} \left( \frac{D_{\text{OD}} D_{\text{OS}}}{2D_{\text{DS}}} \left[ (\boldsymbol{\theta}_B - \boldsymbol{\theta}_s)^2 - (\boldsymbol{\theta}_A - \boldsymbol{\theta}_s)^2 \right] - [\psi(D_{\text{OD}}\boldsymbol{\theta}_B) - \psi(D_{\text{OD}}\boldsymbol{\theta}_A)] \right). \quad (1.94)$$

## 1.7 Lens equation in terms of dimensionless quantities

The inconvenience of the expression of the lens equation given by Eq. (1.77) resides in the fact that the different vectors are defined in different planes. Indeed,  $\mathbf{b}$  is defined in the lens plane,  $\mathbf{b}_s$ , in the source plane, while  $\boldsymbol{\alpha}(\mathbf{b})$  corresponds to a vectorial angle. However, both quantities  $\mathbf{b}D_{\text{OS}}/D_{\text{OD}}$  and  $D_{\text{DS}}\boldsymbol{\alpha}(\mathbf{b})$  lie in the source plane. Therefore, it is convenient to express the lens equation, as well as other quantities, in terms of vector quantities which all lie in the same plane (see Eq. (1.79)). In order to obtain further results in a canonical form, we introduce dimensionless quantities. First, we express the lens equation in terms of quantities defined in the lens plane :

$$\frac{D_{\text{OD}}}{D_{\text{OS}}} \mathbf{b}_s = \mathbf{b} + \frac{D_{\text{DS}} D_{\text{OD}}}{D_{\text{OS}}} \boldsymbol{\alpha}(\mathbf{b}). \quad (1.95)$$

Let us define a length scale  $b_0$  in the lens plane. Then, we define the dimensionless vectors  $\mathbf{x}$ ,  $\mathbf{y}$  and  $\hat{\boldsymbol{\alpha}}(\mathbf{x})$  such as :

$$\mathbf{x} = \frac{\mathbf{b}}{b_0}, \quad \mathbf{y} = \frac{D_{\text{OD}}}{D_{\text{OS}}} \frac{\mathbf{b}_s}{b_0}, \quad \hat{\boldsymbol{\alpha}}(\mathbf{x}) = \frac{D_{\text{DS}} D_{\text{OD}}}{D_{\text{OS}} b_0} \boldsymbol{\alpha}(b_0\mathbf{x}). \quad (1.96)$$

We note that all these vectors lie in the lens plane. As a consequence, after inserting Eq. (1.96) into Eq. (1.95), the lens equation in terms of dimensionless quantities takes the simple form :

$$\mathbf{y} = \mathbf{x} + \hat{\boldsymbol{\alpha}}(\mathbf{x}). \quad (1.97)$$

From Eqs. (1.62), (1.96), and after noticing that the jacobian of the 2D variable change  $\mathbf{b} \rightarrow \mathbf{x}$  is equal to  $b_0^2$ , we deduce that the expression of the dimensionless deflection angle

defined in the lens plane can be express as :

$$\hat{\alpha}(\mathbf{x}) = -\frac{4G D_{\text{DS}} D_{\text{OD}}}{c^2 D_{\text{OS}}} \iint_{\mathbb{R}^2} \Sigma(b_0 \mathbf{x}') \frac{\mathbf{x} - \mathbf{x}'}{|\mathbf{x} - \mathbf{x}'|^2} d\mathbf{x}' , \quad (1.98)$$

$$= -\frac{1}{\pi} \iint_{\mathbb{R}^2} \kappa(\mathbf{x}') \frac{\mathbf{x} - \mathbf{x}'}{|\mathbf{x} - \mathbf{x}'|^2} d\mathbf{x}' , \quad (1.99)$$

where we have defined the dimensionless surface mass density  $\kappa(\mathbf{x})$  by :

$$\kappa(\mathbf{x}) = \frac{\Sigma(b_0 \mathbf{x})}{\Sigma_{\text{cr}}} , \quad (1.100)$$

where the critical surface mass density  $\Sigma_{\text{cr}}$  is given by :

$$\Sigma_{\text{cr}} = \frac{c^2}{4\pi G} \frac{D_{\text{OS}}}{D_{\text{DS}} D_{\text{OD}}} . \quad (1.101)$$

From Eqs. (1.65) and (1.96), the dimensionless deflection potential, defined up to an additive constant, is given by :

$$\hat{\psi}(\mathbf{x}) = \frac{D_{\text{DS}} D_{\text{OD}}}{D_{\text{OS}} b_0^2} \psi(b_0 \mathbf{x}) , \quad (1.102)$$

$$= \frac{4G D_{\text{DS}} D_{\text{OD}}}{c^2 D_{\text{OS}}} \iint_{\mathbb{R}^2} \Sigma(b_0 \mathbf{x}') \ln |\mathbf{x} - \mathbf{x}'| d\mathbf{x}' , \quad (1.103)$$

$$= \frac{1}{\pi} \iint_{\mathbb{R}^2} \kappa(\mathbf{x}') \ln |\mathbf{x} - \mathbf{x}'| d\mathbf{x}' . \quad (1.104)$$

From Eq. (1.68), the dimensionless Poisson equation takes the simple form :

$$\Delta \hat{\psi}(\mathbf{x}) = \frac{D_{\text{DS}} D_{\text{OD}}}{D_{\text{OS}} b_0^2} \Delta \psi(b_0 \mathbf{x}) , \quad (1.105)$$

$$= 2 \kappa(\mathbf{x}) . \quad (1.106)$$

The dimensionless Fermat potential is simply given by :

$$\tau(\mathbf{x}, \mathbf{y}) = \frac{1}{2} (\mathbf{x} - \mathbf{y})^2 - \hat{\psi}(\mathbf{x}) . \quad (1.107)$$

From Eqs. (1.78), (1.94) and (1.96), the dimensionless expression of the time delay between the light curves of two lensed images can be expressed as :

$$\Delta t_{\text{AB}}(\mathbf{y}) = \frac{(1 + z_{\text{D}})}{c} \left\{ \frac{D_{\text{OD}} D_{\text{OS}}}{2D_{\text{DS}}} \left[ \left( \frac{b_0 \mathbf{x}_{\text{B}}}{D_{\text{OD}}} - \frac{b_0 \mathbf{y}_{\text{B}}}{D_{\text{OD}}} \right)^2 - \left( \frac{b_0 \mathbf{x}_{\text{A}}}{D_{\text{OD}}} - \frac{b_0 \mathbf{y}_{\text{A}}}{D_{\text{OD}}} \right)^2 \right] - \frac{D_{\text{OS}} b_0^2}{D_{\text{OD}} D_{\text{DS}}} \left[ \hat{\psi}(\mathbf{x}_{\text{B}}) - \hat{\psi}(\mathbf{x}_{\text{A}}) \right] \right\} , \quad (1.108)$$

which leads, after some trivial simplifications, to :

$$\Delta t_{AB}(\mathbf{y}) = \frac{(1 + z_D)}{c} \frac{D_{OS}}{D_{OD}D_{DS}} b_0^2 \left( \tau(\mathbf{x}_B, \mathbf{y}) - \tau(\mathbf{x}_A, \mathbf{y}) \right). \quad (1.109)$$

Let us summarize the main results of this section :

$$\mathbf{y} = \mathbf{x} + \hat{\alpha}(\mathbf{x}), \quad (1.110)$$

$$\hat{\alpha}(\mathbf{x}) = -\frac{1}{\pi} \iint_{\mathbb{R}^2} \kappa(\mathbf{x}') \frac{\mathbf{x} - \mathbf{x}'}{|\mathbf{x} - \mathbf{x}'|^2} d\mathbf{x}', \quad (1.111)$$

$$\hat{\psi}(\mathbf{x}) = \frac{1}{\pi} \iint_{\mathbb{R}^2} \kappa(\mathbf{x}') \ln |\mathbf{x} - \mathbf{x}'| d\mathbf{x}', \quad (1.112)$$

$$\hat{\alpha}(\mathbf{x}) = -\nabla \hat{\psi}(\mathbf{x}), \quad (1.113)$$

$$\Delta t_{AB}(\mathbf{y}) = \frac{(1 + z_D)}{c} \frac{D_{OS}}{D_{OD}D_{DS}} b_0^2 \left( \tau(\mathbf{x}_B, \mathbf{y}) - \tau(\mathbf{x}_A, \mathbf{y}) \right), \quad (1.114)$$

$$\tau(\mathbf{x}, \mathbf{y}) = \frac{1}{2} (\mathbf{x} - \mathbf{y})^2 - \hat{\psi}(\mathbf{x}). \quad (1.115)$$

It is important to notice that we assume that  $\kappa$  is non-negative and smooth, although in specific models, we may admit some singularities, e.g. the Chang-Refsdal lens (Chang & Refsdal 1984, An & Evans 2006). Furthermore, the integrals which appear in Eqs. (1.111) and (1.112) hold if  $\kappa$  decreases at infinity faster than  $|\mathbf{x}|^{-2}$ .

## 1.8 Amplification, critical and caustic curves

In addition to produce multiple lensed images of a background source, the gravitational lensing phenomenon affects their observed flux. Indeed, the differential deflection across a light bundle distorts its cross-sectional area. Therefore, since the photon number is preserved (Etherington 1933), the flux of a lensed image is simply determined by its area in the lens plane.

Let us consider an undeflected infinitesimal source with a constant surface brightness  $I$  which subtends a solid angle  $d\Omega_s$  on the sky plane. Since the gravitational lensing phenomenon is achromatic, we do not specify the observed frequency of the source flux. The observed flux  $F_s$  of the unbent image of the source is given by :

$$F_s = I d\Omega_s. \quad (1.116)$$

Let us now consider a mass distribution located along the line-of-sight of the emitting light source which produce several lensed images. The solid angle  $d\Omega_i$  of a particular lensed image differs from  $d\Omega_s$  and the observed flux of this image is given by :

$$F_i = I d\Omega_i . \quad (1.117)$$

As a consequence, the *amplification factor*  $\mu$  which affects the lensed image is defined by :

$$|\mu| = \frac{F_i}{F_s} = \frac{d\Omega_i}{d\Omega_s} . \quad (1.118)$$

Since the lens equation (see Eq. (1.110)) represents a surjective mapping  $\mathbf{x} \rightarrow \mathbf{y}$ , the amplification factor is obtained from the Jacobian determinant of this lens mapping. The Jacobian matrix for Eq. (1.110), also called the *amplification matrix*, is given by :

$$A(\mathbf{x}) = \frac{\partial \mathbf{y}}{\partial \mathbf{x}} , \quad (1.119)$$

and the amplification factor  $\mu$  takes the form :

$$\mu(\mathbf{x}) = \frac{1}{\det A(\mathbf{x})} . \quad (1.120)$$

The flux of a lensed image located at the position  $\mathbf{x}$  of an infinitesimally small source located at  $\mathbf{y}$ , both lying in the lens plane, is scaled by the factor  $|\mu(\mathbf{x})|$ . For the case  $|\mu(\mathbf{x})| > 1$ , the lensed image is brighter than the unbent image of the source, while for  $|\mu(\mathbf{x})| < 1$ , it is fainter. We note that  $\mu(\mathbf{x})$  can be positive or negative, and the corresponding images are said to have *positive* or *negative parity*. In addition, we can construct the *amplification map* corresponding to a given lens mapping  $\mathbf{x} \rightarrow \mathbf{y}$  by associating to any position  $\mathbf{y}$  in the source plane the value of the corresponding modulus of the amplification factor in the lens plane. We have illustrated in Fig. 1.5 the amplification map associated with different mappings.

Using Eqs. (1.110) and (1.113), the amplification matrix  $A(\mathbf{x})$  takes the form :

$$A(\mathbf{x}) = \begin{pmatrix} 1 - \frac{\partial^2 \hat{\psi}}{\partial x_1^2} & -\frac{\partial^2 \hat{\psi}}{\partial x_1 \partial x_2} \\ -\frac{\partial^2 \hat{\psi}}{\partial x_1 \partial x_2} & 1 - \frac{\partial^2 \hat{\psi}}{\partial x_2^2} \end{pmatrix} . \quad (1.121)$$

Furthermore, from Eq. (1.106), we have :

$$\kappa(\mathbf{x}) = \frac{1}{2} \left( \frac{\partial^2 \hat{\psi}}{\partial x_1^2} + \frac{\partial^2 \hat{\psi}}{\partial x_2^2} \right) , \quad (1.122)$$

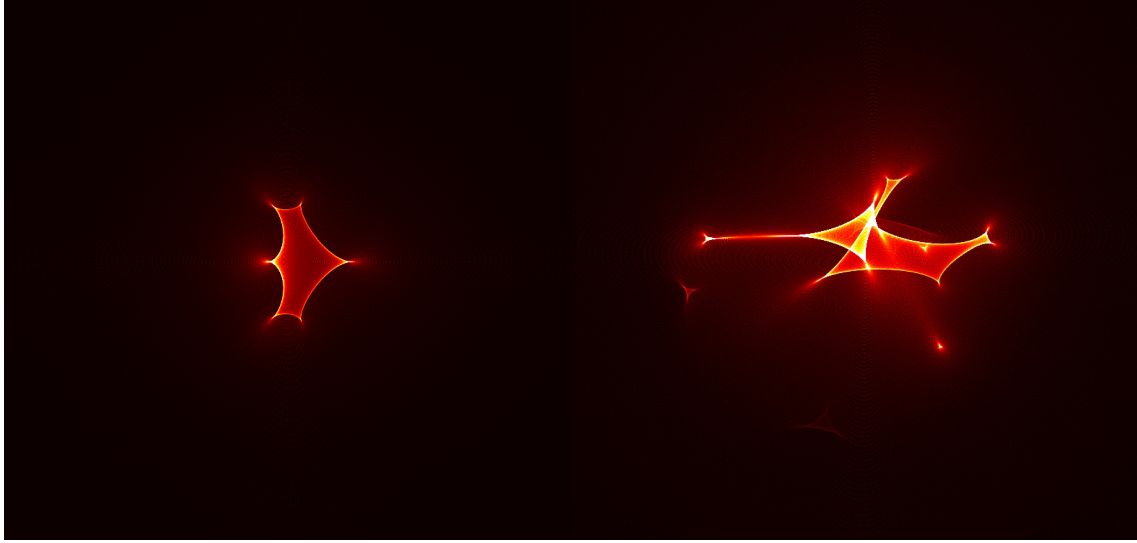


**Figure 1.5:** Illustration of two amplification maps (AM). The left panel represents the AM for two point-like lenses characterized by  $M_1 = 2M_2$  where  $M_i$  corresponds to their masses. The right panel represents the AM for a cluster of point-like lenses characterized by different masses. One clearly distinguishes different zones for which the amplification factor tends towards infinity. Those curves are called caustic curves (more informations are given in the text).

which, combined with Eq. (1.121), leads to :

$$A(\mathbf{x}) = \begin{pmatrix} 1 - \kappa - \gamma_1 & -\gamma_2 \\ -\gamma_2 & 1 - \kappa + \gamma_1 \end{pmatrix}, \quad (1.123)$$

where  $\gamma_1$  and  $\gamma_2$  are defined by :

$$\gamma_1 = \frac{1}{2} \left( \frac{\partial^2 \hat{\psi}}{\partial x_1^2} - \frac{\partial^2 \hat{\psi}}{\partial x_2^2} \right), \quad \text{and} \quad \gamma_2 = \frac{\partial^2 \hat{\psi}}{\partial x_1 \partial x_2}. \quad (1.124)$$

Therefore, the determinant of the amplification matrix  $A(\mathbf{x})$  is simply given by :

$$\det A(\mathbf{x}) = (1 - \kappa)^2 - \gamma^2, \quad (1.125)$$

where  $\kappa$ , which is responsible for the isotropically increase of the image size, is here called *the convergence*, while  $\gamma = \sqrt{\gamma_1^2 + \gamma_2^2}$ , which is responsible for the stretches of the image tangentially around the lens, is called *the shear*. Of course, both are functions of  $\mathbf{x}$ . Since the amplification matrix is real and symmetric, it may be expressed as a diagonal matrix formed by the eigenvalues  $\lambda_1$  and  $\lambda_2$  which can be derived when solving the equation  $\det(A(\mathbf{x}) - \lambda_i I_2) = 0$ , where  $I_2$  represents the identity matrix of size 2. Therefore, the

amplification matrix takes the form :

$$A(\mathbf{x}) = \begin{pmatrix} \lambda_1 & 0 \\ 0 & \lambda_2 \end{pmatrix} = \begin{pmatrix} 1 - \kappa - \gamma & 0 \\ 0 & 1 - \kappa + \gamma \end{pmatrix}. \quad (1.126)$$

The amplification matrix is strongly linked to the Fermat potential given in Eq. (1.107). Indeed,  $A(\mathbf{x})$  corresponds to the Hessian matrix of  $\tau(\mathbf{x}, \mathbf{y})$ . Such a relation can be easily deduced by noticing the fact that the Hessian matrix  $H$  of any real-valued function  $f$  for which all second partial derivatives exist, is related to the Jacobian matrix  $J$  by :

$$H[f(\mathbf{x})] = J[\nabla f(\mathbf{x})]. \quad (1.127)$$

Hence, since  $A(\mathbf{x}) = J[\nabla \tau(\mathbf{x}, \mathbf{y})]$  where  $\nabla$  denotes the gradient operator with respect to  $\mathbf{x}$ , we have :

$$A(\mathbf{x}) = H[\tau(\mathbf{x}, \mathbf{y})]. \quad (1.128)$$

Since the lensed image positions  $\mathbf{x}^{(i)}$  are those for which  $\nabla \tau(\mathbf{x}^{(i)}, \mathbf{y}) = 0$ , and making use of the Hessian matrix properties, we may deduce three different types of lensed images. First, for the case of  $A(\mathbf{x})$  being a positive-definite matrix, i.e.  $\lambda_1 > 0$  and  $\lambda_2 > 0$ , or identically  $\det A(\mathbf{x}) > 0$  and  $\text{tr} A(\mathbf{x}) > 0$ , the lensed image position  $\mathbf{x}^{(i)}$  corresponds to a minimum of  $\tau(\mathbf{x}^{(i)}, \mathbf{y})$ . Such a lensed image  $\mathbf{x}_1^{(i)}$  is denoted as Type I. We deduce from Eq. (1.126) that  $\lambda_1 > 0$  implies  $\gamma < 1 - \kappa$ , which combined with  $\lambda_2 > 0$  implies  $0 < \kappa < 1$ , hence  $0 < 1 - \kappa < 1$ . Therefore, it follows that  $0 < \lambda_1 < 1$ , hence  $0 < (1 - \kappa)^2 - \gamma^2 < 1$ , and finally  $\mu(\mathbf{x}_1) \geq 1$ . As a result, the flux of a Type I lensed image is always amplified or unaltered (in the very special case  $\kappa = 0 = \gamma$ ). In addition, for smooth mass distributions with a finite total mass, there always exists at least one Type I lensed image (Schneider 1984).

Secondly, for the case  $\lambda_1 < 0 < \lambda_2$ , i.e.  $\det A(\mathbf{x}) < 0$ , the lensed image position  $\mathbf{x}^{(i)}$  corresponds to a saddle point of the iso-density contours of  $\tau(\mathbf{x}^{(i)}, \mathbf{y})$ . Such a lensed image is denoted as Type II. We deduce that  $\gamma^2 > (1 - \kappa)^2$  and  $\mu(\mathbf{x}_{\text{II}}) < 0$ . As a result, Type II lensed images have always a negative parity.

Thirdly, for the case of  $A(\mathbf{x})$  being a negative-definite matrix, i.e.  $\lambda_1 < 0$  and  $\lambda_2 < 0$ , or identically  $\det A(\mathbf{x}) > 0$  and  $\text{tr} A(\mathbf{x}) < 0$ , the lensed image position  $\mathbf{x}^{(i)}$  corresponds to a maximum of  $\tau(\mathbf{x}^{(i)}, \mathbf{y})$ . Such a lensed image is denoted as Type III. Since  $\lambda_1 \leq \lambda_2$ , there is no possibility to consider the fourth case  $\lambda_2 < 0 < \lambda_1$ . We deduce that  $\lambda_1 < 0$  implies  $1 - \kappa < \gamma$ , which combined with  $\lambda_2 < 0$  implies  $\kappa > 1$ . Therefore, it follows that  $\gamma^2 < (1 - \kappa)^2$ , and finally  $\mu(\mathbf{x}_{\text{III}}) > 0$ . As a result, Type III lensed images have always a positive parity. We have

**Table 1.1:** Summary of the lensed image features for types I, II and III.

	$\lambda_i$	$\det A(\mathbf{x})$	$\text{tr } A(\mathbf{x})$	$\kappa(\mathbf{x})$	$\mu(\mathbf{x})$
Type I	$\lambda_i > 0$	$> 0$	$> 0$	$0 < \kappa < 1$	$\geq 1$
Type II	$\lambda_1 < 0 < \lambda_2$	$< 0$	$-$	$(1 - \kappa)^2 < \gamma^2$	$< 0$
Type III	$\lambda_i < 0$	$> 0$	$< 0$	$\kappa > 1$	$> 0$

*Remark :* For the case of Type II lensed images, the values of  $\lambda_i$  do not allow a direct determination of the sign of  $\text{tr } A(\mathbf{x})$ .

summarized those lensed image characteristics in Table 1.1.

For very special values of  $\mathbf{x}$  we may have  $\lambda_1 = 0$  and/or  $\lambda_2 = 0$ , hence  $\det A(\mathbf{x}) = 0$ . For such specific values of  $\mathbf{x}$ , the so-called *critical points*, the amplification factor formally diverges :  $\mu(\mathbf{x}) \rightarrow \infty$ . The geometrical locus in the lens plane at which the amplification factor tends towards infinity are called *critical curves*. Of course, any elements of a critical curve constitute critical points. Moreover, the source point located at the position  $\mathbf{y}$  which leads to a critical point from the lens mapping is called a *caustic point*. A curve for which all points consist of caustic points is called a *caustic curve*. For any caustic curve, we may associate, using the lens mapping, a critical curve which can sometimes degenerate into a single point. For the case of several lens mass distributions and a point-like source, we have illustrated in Fig. 1.6 the corresponding lensed image positions, the critical and caustic curves and selected iso-density contours of the Fermat potential. For the case of a diamond-shape caustic curve, we define two types of special caustic points. First, the set of caustic points  $\mathbf{y}_{\text{fold}}$  which constitute a branch of the caustic curve is called a *fold*. From the lens equation, we may deduce the lensed image points  $\mathbf{x}_{\text{fold}}$  of the fold points  $\mathbf{y}_{\text{fold}}$ . Such points  $\mathbf{x}_{\text{fold}}$  are those for which  $A(\mathbf{x}_{\text{fold}}) \cdot \mathbf{T}(\mathbf{x}_{\text{fold}}, \mathbf{y}_{\text{fold}}) \neq 0$  where  $\mathbf{T}$  represents the tangential vector to the critical curve at the position  $\mathbf{x}_{\text{fold}}$ . Secondly, the intersection point of two folds is located at  $\mathbf{x}_{\text{cusp}}$  and is called a *cusp*. Such a point  $\mathbf{x}_{\text{cusp}}$  is one for which  $A(\mathbf{x}_{\text{cusp}}) \cdot \mathbf{T}(\mathbf{x}_{\text{cusp}}, \mathbf{y}_{\text{cusp}}) = 0$ . Furthermore, all lenses produce always an even number of cusps (A. Weiss, p. 213).

For the case of a source crossing a fold (resp. a cusp), we note that two (resp. three) lensed images merge (see Fig. 1.7). Due to the lensed image characteristics (see Table 1.1), the parities of two lensed images on either side of a critical curve are opposite. For the case of the source crossing a cusp, two lensed images share the same parity while the third one has an opposite parity. Therefore, for a smooth mass distribution, one may link the amplification factor of such lensed images. Indeed, the *fold relation* states that  $\mu_1 + \mu_2 = 0$  where  $\mu_i$  corresponds to the amplification factor of two nearly merging lensed images of a source which is infinitely close to a fold. In addition, the *cusp relation* states that  $\mu_1 + \mu_2 + \mu_3 = 0$  where  $\mu_i$  corresponds to the amplification factor of three nearly merging lensed images of a



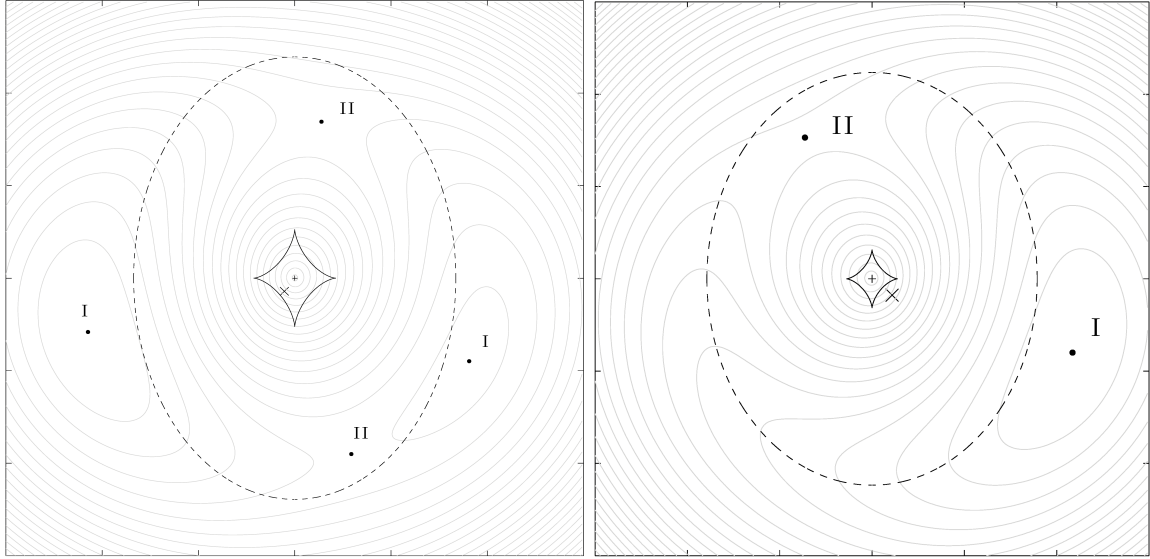


**Figure 1.6:** For the SIE lens model, we have represented the position of a point-like source (cross  $\times$ ), the associated lensed images (dots  $\bullet$ ), the critical curves (dashed lines), the caustic curves (solid black lines) and iso-contours of the Fermat potential (gray solid lines). The cross  $+$  denotes the central position of the deflector and the roman numbers refer to the type of lensed images.

source which is infinitely close to a cusp.

Given a smooth normalized surface mass density  $\kappa(\mathbf{x})$  which decreases faster than  $|\mathbf{x}|^{-2}$  for the case  $|\mathbf{x}| \rightarrow \infty$ , the gravitational lens has a finite total mass and the deflection angle  $\hat{\alpha}(\mathbf{x})$  is a bounded continuous function of  $\mathbf{x}$ . Under these assumptions and by denoting  $\mathbf{y}$  the position of a point-like source not located on a caustic, we have the following results (SEF, 1992) :

$$n_I \geq 1, \quad (1.129)$$

$$n < \infty, \quad (1.130)$$

$$n_I + n_{III} = 1 + n_{II}, \quad (1.131)$$

$$n = n_I = 1 \quad \text{for sufficiently large values of } |\mathbf{y}|, \quad (1.132)$$

where  $n_I$  (resp.  $n_{II}$  or  $n_{III}$ ) denotes the number of lensed images of type I (resp. II or III) of the point-like source located at  $\mathbf{y}$ , and  $n = n_I + n_{II} + n_{III}$ . Furthermore, from the latter equation and Eq. (1.131), we easily deduce that :

$$n = 1 + 2n_{II}. \quad (1.133)$$

Therefore, the total number of lensed images is always an odd number. Such a result is known as the *odd-number theorem*. These results may be used to derive a necessary and

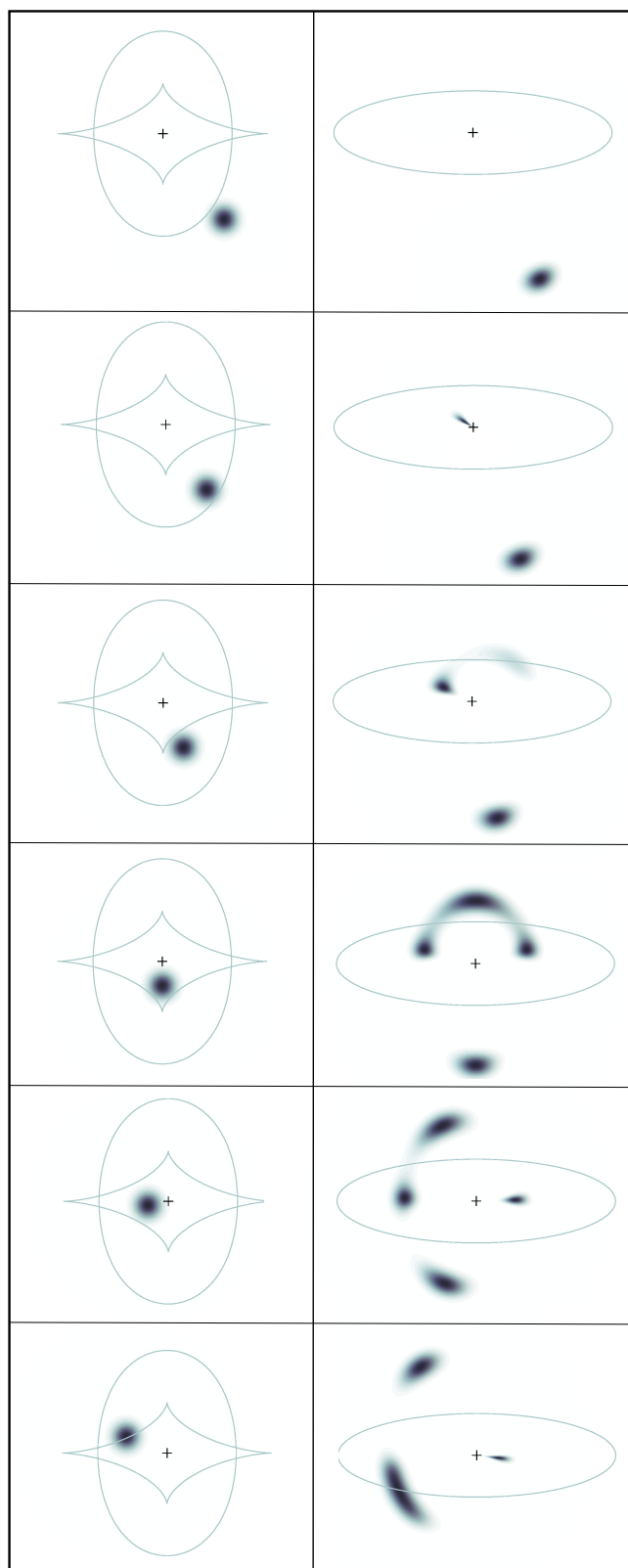


**Figure 1.7:** Illustration of lensed image configurations for the case of a circular source which passes through a SIE lens. The left panels represent the position of the source with respect to the tangential caustic curve (diamond-like shaped solid line) and the so-called *cut*. The right panels represent stretched and twisted lensed images. When the source crosses the caustic line, several lensed images merge on the corresponding critical line (right panel, solid lines).

sufficient condition to cause multiple lensed images of a source. Let us consider an isolated transparent gravitational lens and a point-like source, both respectively located at distance  $D_{\text{OD}}$  and  $D_{\text{OS}}$  from an observer  $O$ . The lens produces multiple lensed images if, and only if, there exists a point  $\mathbf{x}$  in the lens plane for which  $\det A(\mathbf{x}) < 0$ . On one hand, the condition is necessary. Indeed, if  $\det A(\mathbf{x}) > 0$  for all  $\mathbf{x}$  in the lens plane, then the amplification matrix  $A(\mathbf{x})$  is globally invertible and either  $\lambda_i > 0$  or  $\lambda_i < 0$ , with  $i = 1$  or  $2$ . Therefore, according to Table 1.1, there exist only Type I or Type III lensed images, hence  $n_{\text{II}} = 0$ . As a consequence, from Eq. (1.133), the total number of lensed images is 1, which means that no multiple imaging occurs. On the other hand, the condition is sufficient. Indeed, let us consider  $\mathbf{x}_0$  for which  $\det A(\mathbf{x}_0) < 0$ , from Eq. (1.131), there must be at least two additional lensed images of Type I or III. Let us note that there exists another sufficient (but not necessary) condition for possible multiple lensed images. The latter occurs if there exists  $\mathbf{x}$  in the lens plane for which  $\kappa(\mathbf{x}) > 1$ . Indeed, according to Table 1.1, there exists at least a Type III lensed image. However, under the considered assumptions, there must exist at least one Type I lensed image (Schneider 1984). Therefore,  $\kappa(\mathbf{x}) > 1$  implies that there exists at least two lensed images. The latter condition is not necessary since we may consider the case of  $\mathbf{x}_I$ ,  $\mathbf{x}'_I$  and  $\mathbf{x}_{\text{II}}$  which are three lensed images of respectively Type I, Type I and Type II, and  $\kappa(\mathbf{x}_{\text{II}}) < 1$ .

Finally, we underline the fact that the divergence of the amplification factor, which appears when an infinitesimally small source crosses a caustic line, only indicates that the approximation of geometric optics fails. In such a situation, the wave optics should be applied, although it does not lead to any relevant correction. For more details about wave optics in gravitational lensing, the reader may consult the chapter 7 of SEF (p 217).

## 1.9 The mass-sheet degeneracy

Let us consider a lens mass distribution characterized by its surface mass density  $\kappa(\mathbf{x})$  which is linked to the deflection potential  $\hat{\psi}(\mathbf{x})$  by  $\Delta\hat{\psi}(\mathbf{x}) = 2\kappa(\mathbf{x})$ . We assume that this lens produces multiple lensed images  $\mathbf{x}^{(i)}$  of a background source located in the lens plane at  $\mathbf{y}$ . Let us now consider the following transformation of the deflection potential :

$$\hat{\psi}_\nu(\mathbf{x}) = \frac{\nu}{2} |\mathbf{x}|^2 + \mathbf{s} \cdot \mathbf{x} + (1 - \nu) \hat{\psi}(\mathbf{x}) + K, \quad (1.134)$$

where  $0 < \nu < 1$  is a real number,  $\mathbf{s} \cdot \mathbf{x}$  corresponds to an unobservable constant shift in the source plane, and  $K$  is a constant which fixes the zero point of the deflection potential.

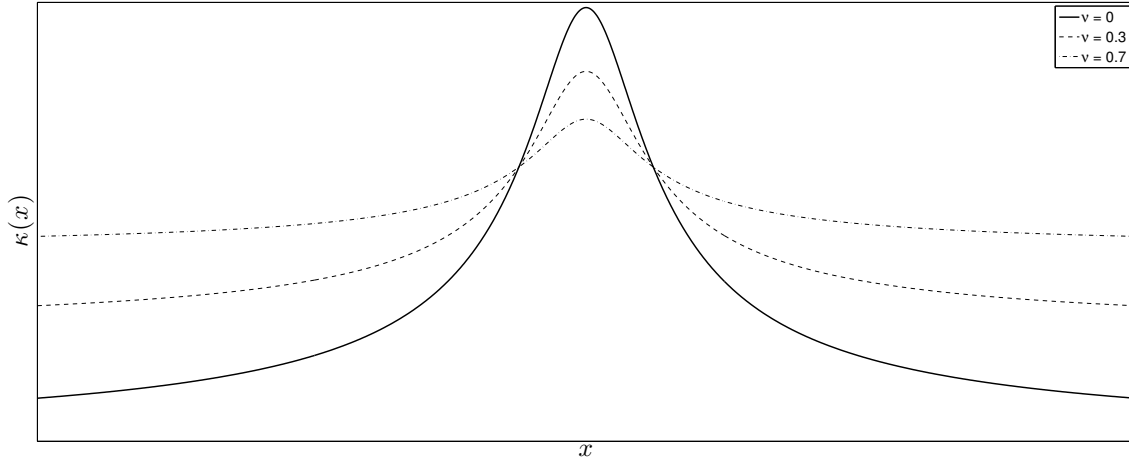


**Figure 1.8:** Illustration of different surface mass density profiles for the case of the NSIE lens model and for  $\nu = 0$ ,  $\nu = 0.3$ , and  $\nu = 0.7$ , respectively.

From Eq. (1.134), we may define the corresponding deflection angle  $\hat{\alpha}_\nu(\mathbf{x})$  and surface mass density  $\kappa_\nu(\mathbf{x})$  such as :

$$\hat{\alpha}_\nu(\mathbf{x}) = -\nabla\hat{\psi}_\nu(\mathbf{x}), \quad (1.135)$$

$$= -\nu \mathbf{x} - \mathbf{s} - (1 - \nu) \nabla\hat{\psi}(\mathbf{x}), \quad (1.136)$$

and

$$\kappa_\nu(\mathbf{x}) = \Delta\hat{\psi}_\nu(\mathbf{x}), \quad (1.137)$$

$$= \nu + (1 - \nu) \kappa(\mathbf{x}). \quad (1.138)$$

From the latter equation, the considered transformation can be understood as corresponding to the addition of a circular disk of uniform surface mass density  $\nu$  centered at  $\mathbf{x} = 0$ . Furthermore, the original surface mass distribution  $\kappa(\mathbf{x})$  is scaled by the factor  $(1 - \nu)$ . We have illustrated in Fig. 1.8 different surface mass density profiles for the case of the NSIE lens ( $f = 0.4$  and  $\rho_0 = 0.2$ ) model and for different values of  $\nu$ . From Eq. (1.136), the lens equation takes the form :

$$\mathbf{y}_\nu = \mathbf{x} + \hat{\alpha}_\nu(\mathbf{x}), \quad (1.139)$$

$$= (1 - \nu) \mathbf{x} - \mathbf{s} + (1 - \nu) \hat{\alpha}(\mathbf{x}), \quad (1.140)$$

which can be expressed as :

$$\frac{\mathbf{y}_\nu}{1-\nu} + \frac{\mathbf{s}}{1-\nu} \equiv \mathbf{y} = \mathbf{x} + \hat{\alpha}(\mathbf{x}) . \quad (1.141)$$

Therefore, for any value of  $0 < \nu < 1$ , the surface mass densities  $\kappa(\mathbf{x})$  and  $\kappa_\nu(\mathbf{x})$  exactly provide the same dimensionless quantities, i.e. lensed image positions and shapes, amplification ratios between a pair of lensed images. From Eq. (1.141), one may not distinguish between the source position  $\mathbf{y}$  and the scaled and shifted source position  $\mathbf{y}_\nu$ , which both effects remain unobservable. This effect is called the *mass-sheet degeneracy* and has first been pointed out by Falco & al. (1985).

From Eqs. (1.107), (1.134) and (1.141), the Fermat potential  $\tau_\nu(\mathbf{x}, \mathbf{y}_\nu)$  is given by :

$$\tau_\nu(\mathbf{x}, \mathbf{y}_\nu) = (1-\nu) \tau(\mathbf{x}, \mathbf{y}) + \text{constant} . \quad (1.142)$$

Therefore, the mass-sheet degeneracy has a significative impact on the cosmography.

## 1.10 The simple case of axially symmetric lenses

A mass distribution for which the surface mass density  $\kappa(\mathbf{x})$  depends only on the radial coordinate of the impact parameter is called an *axially symmetric* lens. Owing to their simplicity, these models of deflectors represent an interesting class of models, both from the mathematical and physical point of view. Indeed, the analytical treatment of such particular deflectors allows the use of scalar quantities instead of the vector formalism. In this section, we present the main results regarding axially symmetric lenses. Since the surface mass density only depends on the radial coordinate, we have of course  $b = |\mathbf{b}|$ . Then, without loss of generality, we can set the orientation of the system of polar coordinates such as  $\mathbf{b} = (b, 0)$ . Therefore, the expression of the deflection angle can be reduced to :

$$\alpha(b) = -\frac{4G}{c^2} \int_0^{+\infty} \int_0^{2\pi} \Sigma(b') \frac{b' (b - b' \cos \varphi')}{(b - b' \cos \varphi')^2 + (-b' \sin \varphi')^2} d\varphi' db' , \quad (1.143)$$

$$= -\frac{4G}{c^2} \int_0^{+\infty} \Sigma(b') b' \left\{ \int_0^{2\pi} \frac{b - b' \cos \varphi'}{b^2 + b'^2 - 2 b b' \cos \varphi'} d\varphi' \right\} db' . \quad (1.144)$$

After successively applying Eqs. (2.554 - 2) and (2.553 - 3) from Gradshteyn & Tyzhik (2007), the  $\varphi$ -integral equals  $2\pi/b$  if  $b' < b$  and vanishes otherwise. Consequently, the expression of the deflection angle reduces to :

$$\alpha(b) = -\frac{8\pi G}{bc^2} \int_0^b \Sigma(b') b' db' . \quad (1.145)$$

From the latter equation, we can define the projected mass  $M(b)$  within a circle of radius  $b$  by :

$$M(b) = 2\pi \int_0^b \Sigma(b') b' db' . \quad (1.146)$$

In vectorial notation, the expression of the deflection angle for the case of a symmetric mass distribution is simply given by :

$$\alpha(\mathbf{b}) = -\frac{4G}{b^2 c^2} M(b) \mathbf{b} . \quad (1.147)$$

From the use of the dimensionless quantities, the latter equation can then be expressed as :

$$\hat{\alpha}(\mathbf{x}) = -\frac{m(x)}{x^2} \mathbf{x} , \quad (1.148)$$

where  $x = |\mathbf{x}|$  and the dimensionless projected mass  $m(x) \geq 0$  is defined by :

$$m(x) = 2 \int_0^x x' \kappa(x') dx' . \quad (1.149)$$

The scalar expression of Eq. (1.148) is simply given by :

$$\hat{\alpha}(x) = -\frac{m(x)}{x} . \quad (1.150)$$

From Eqs. (1.110) and (1.148), we may establish the lens equation for the case of axially symmetric lenses :

$$\mathbf{y} = \left(1 - \frac{m(x)}{x^2}\right) \mathbf{x} , \quad (1.151)$$

which indicates that the source position, the center of the symmetric mass distribution and the lensed image positions are collinear. The scalar form of the lens equation is simply given

by :

$$y = x - \frac{m(x)}{x} . \quad (1.152)$$

Let us underline the fact that  $x$  and  $y$ , which appear in the scalar form of the deflection angle definition and lens equation, are always positive or null :  $x \geq 0$  and  $y \geq 0$ . However, the components  $x_1$ ,  $x_2$ ,  $y_1$  and  $y_2$ , which appear in the vectorial form of the mentioned quantities may be positive, null or negative.

From Eq. (1.112) and making use of the polar system of coordinates, we may deduce the expression of the deflection potential  $\hat{\psi}(x)$  :

$$\hat{\psi}(x) = \frac{1}{2\pi} \int_0^{+\infty} x' \kappa(x') \left\{ \int_0^{2\pi} \ln(x^2 + x'^2 - 2xx' \cos \varphi) d\varphi \right\} dx' , \quad (1.153)$$

$$= \frac{1}{2\pi} \int_0^{+\infty} x' \kappa(x') \left\{ 4\pi \ln(\max[x, x']) \right\} dx' , \quad (1.154)$$

$$= 2 \ln(x) \int_0^x x' \kappa(x') dx' + 2 \int_x^{+\infty} x' \kappa(x') \ln(x') dx' . \quad (1.155)$$

Since the deflection potential is determined only up to an additive constant, we can add to the latter equation any term which is independent of  $x$ . Therefore by adding to Eq. (1.155) the term :

$$K = -2 \int_0^{+\infty} x' \kappa(x') \ln(x') dx' , \quad (1.156)$$

the deflection potential transforms into :

$$\hat{\psi}(x) = 2 \ln(x) \int_0^x x' \kappa(x') dx' - 2 \int_0^x x' \kappa(x') \ln(x') dx' , \quad (1.157)$$

$$= 2 \int_0^x x' \kappa(x') \ln\left(\frac{x}{x'}\right) dx' . \quad (1.158)$$

Of course, it is straightforward to deduce from the latter equation that  $\hat{\alpha}(x) = -\nabla \hat{\psi}(x)$  and  $\hat{\alpha}(x) = -d\hat{\psi}/dx$ .

Due to the symmetry of the considered mass distribution and using polar coordinates, we

may significantly simplify the expression of the amplification matrix (see Eq. (1.123)) :

$$A(x) = \begin{pmatrix} 1 + \frac{d\hat{a}(x)}{dx} & 0 \\ 0 & 1 + \frac{\hat{a}(x)}{x} \end{pmatrix}, \quad (1.159)$$

$$= \begin{pmatrix} 1 + \frac{m(x)}{x^2} - 2\kappa(x) & 0 \\ 0 & 1 - \frac{m(x)}{x^2} \end{pmatrix}, \quad (1.160)$$

$$= \begin{pmatrix} 1 + \bar{\kappa}(x) - 2\kappa(x) & 0 \\ 0 & 1 - \bar{\kappa}(x) \end{pmatrix}, \quad (1.161)$$

where we have used the relation  $dm(x)/dx = 2x\kappa(x)$  for the second equality, and we have defined the *mean surface mass density*  $\bar{\kappa}(x) = m(x)/x^2 \geq 0$ . As a result, the amplification factor takes the form :

$$\mu(x) = \frac{1}{(1 - \bar{\kappa}(x))(1 + \bar{\kappa}(x) - 2\kappa(x))}. \quad (1.162)$$

As a consequence, for the case of axially symmetric lenses, the critical curves are simply circles which radii can be determined from the latter equation. First, solving the previous equation for  $\bar{\kappa}(x_t) = 1$  with respect to  $x_t$  leads to the determination of the radii of the *tangential* critical curve. Secondly, the solution  $1 + \bar{\kappa}(x_r) - 2\kappa(x_r) = 0$  with respect to  $x_r$  leads to the determination of the radii of the *radial* critical curve. The distinction between tangential and radial results from the way two lensed images merge when a point-like source crosses the corresponding tangential or radial caustic curves. Such curves are simply given by the mapping of  $x_t$  and  $x_r$ , respectively. From Eq. (1.152), we deduce that the tangential caustic curve simply reduces to the point  $y_t = 0$ . In addition, let us notice that all axially symmetric lenses do not necessarily lead to two critical curves.

To conclude this section, we may summarize some general properties of axially symmetric lenses. First, let us note that the scalar form of the lens equation (see Eq. (1.152)) may not rigorously lead to the determination of all lensed image positions. For instance, for the case of the singular isothermal sphere (SIS) mass distribution, the surface mass density is given by  $\kappa(x) = 1/(2x)$ . Therefore, from Eq. (1.149), the projected mass  $m(x)$  corresponds to  $m(x) = x$ . By substituting the latter equation into the lens equation (1.152), we obtain  $x = y + 1$  which seems to indicate the existence of only one solution. By considering the vectorial form of the lens equation (see Eq. (1.151)), we obtain the following system of two



equations to be solved :

$$\begin{cases} y_1 = x_1 - \frac{x_1}{\sqrt{x_1^2 + x_2^2}}, \\ y_2 = x_2 - \frac{x_2}{\sqrt{x_1^2 + x_2^2}}, \end{cases} \quad (1.163)$$

which leads to :

$$\begin{cases} x_1 = \frac{y_1}{y} (1 \pm y), \\ x_2 = \frac{y_2}{y} (1 \pm y). \end{cases} \quad (1.164)$$

Therefore, remembering that  $x = \sqrt{x_1^2 + x_2^2}$ , the radial coordinate of the lensed image positions is given by :

$$x = 1 \pm y. \quad (1.165)$$

Furthermore, from the latter equation and since the radial coordinate  $x \geq 0$ , we deduce that for the case  $y > 1$ , the second solution  $x = 1 - y$  has to be rejected. As a conclusion, only the use of the vectorial form of the lens equation allows to determine all solutions.

Secondly, for a source position  $y_1 > 0$  (resp.  $y_1 < 0$ ), any image with  $x_1 > 0$  (resp.  $x_1 < 0$ ) leads to  $x \geq y$ . Furthermore, for sufficiently large values of the source position  $y$ , there only exists one lensed image. Finally, since the general condition to obtain multiple lensed images is  $A(x) < 0$  for, at least, one point  $x$  located in the lens plane, we may consider the two following cases :  $1 + \bar{\kappa}(x) - 2\kappa(x) < 0$  and  $1 - \bar{\kappa}(x) > 0$ , or,  $1 + \bar{\kappa}(x) - 2\kappa(x) > 0$  and  $1 - \bar{\kappa}(x) < 0$ . However, since  $1 + \bar{\kappa}(x) - 2\kappa(x) = dy(x)/dx$ , the second case produces no multiple lensed images since  $y(x)$  increases monotonically. Therefore, any axially symmetric lenses produce multiple lensed images if, and only if,  $1 + \bar{\kappa}(x) - 2\kappa(x) < 0$ . Furthermore, from the last inequation, we deduce that :

$$\kappa(x) > \frac{1 + \bar{\kappa}(x)}{2} \geq \frac{1}{2}, \quad (1.166)$$

where the last inequality is deduced from  $\bar{\kappa}(x) \geq 0$ . As a result, a necessary condition to produce multiple lensed images is  $\kappa(x) > 1/2$ , for at least one point.

## 1.11 Elliptical symmetric lenses and complex representation

Since many galaxies appear to have elliptical-shape isophotes, elliptical mass distributions seem to be more appropriate than axially symmetric ones in order to model gravitational lenses. However, there is no guarantee that the light distribution of an observed galaxy matches the distribution of matter. Such a family of deflectors has been studied in detail although rather difficult to handle. One of them is the singular isothermal ellipsoid (SIE) family of models. The explicit analytical treatment of the SIE has been first proposed by Kormann & al. (1994). Let us summarize some general results. After having adopted the polar coordinate system, the SIE dimensionless surface mass density can be expressed as :

$$\kappa(r, \varphi) = \frac{\sqrt{f}}{2 r \sqrt{\cos^2 \varphi + f^2 \sin^2 \varphi}}, \quad (1.167)$$

where  $r \cos \varphi = x_1$ ,  $r \sin \varphi = x_2$ , and  $f$  represents the axis ratio of the elliptical iso-density contours. Let us note that the abscissa axis points towards the minor axis of the ellipse. From the expression of  $\kappa(r, \varphi)$  and Eq. (1.106), the Poisson equation takes the form :

$$\frac{1}{r} \frac{\partial}{\partial r} \left( r \frac{\partial \hat{\psi}(r, \varphi)}{\partial r} \right) + \frac{1}{r} \frac{\partial^2 \hat{\psi}(r, \varphi)}{\partial \varphi^2} = \frac{\sqrt{f}}{r \sqrt{\cos^2 \varphi + f^2 \sin^2 \varphi}}. \quad (1.168)$$

Assuming that the deflection potential  $\hat{\psi}(r, \varphi)$  can be expressed with separated variables, i.e.  $\hat{\psi}(r, \varphi) = r \tilde{\psi}(\varphi)$ , Eq. (1.168) reduces to :

$$\tilde{\psi}(\varphi) + \frac{d^2 \tilde{\psi}(\varphi)}{d\varphi^2} = \frac{\sqrt{f}}{\sqrt{\cos^2 \varphi + f^2 \sin^2 \varphi}}. \quad (1.169)$$

The latter equation can be resolved using the Green's function method. As a result, the deflection potential is then given by :

$$\hat{\psi}_{\text{SIE}}(r, \varphi) = \frac{\sqrt{f} r}{f'} \left[ \sin \varphi \arcsin(f' \sin \varphi) + \cos \varphi \operatorname{arcsinh} \left( \frac{f'}{f} \cos \varphi \right) \right], \quad (1.170)$$

where  $f' = \sqrt{1 - f^2}$ . From the latter equation and Eq. (1.113), the deflection angle takes the form :

$$\hat{\alpha}_{\text{SIE}}(\mathbf{x}) = -\frac{\sqrt{f}}{f'} \left[ \operatorname{arcsinh} \left( \frac{f'}{f} \cos \varphi \right) \mathbf{e}_1 + \arcsin (f' \sin \varphi) \mathbf{e}_2 \right], \quad (1.171)$$

where the unit vector  $\mathbf{e}_i$  points towards  $x_i$ . Afterwards, the amplification matrix :

$$A(r, \varphi) = \begin{pmatrix} 1 - 2\kappa \sin^2 \varphi & \kappa \sin 2\varphi \\ \kappa \sin 2\varphi & 1 - 2\kappa \cos^2 \varphi \end{pmatrix}, \quad (1.172)$$

leads to the determination of the amplification factor :

$$\mu(r, \varphi) = \frac{1}{1 - 2\kappa(r, \varphi)}. \quad (1.173)$$

The determination of the critical curve results from the solution of  $\det A(r, \varphi) = 0 = 1 - 2\kappa(r, \varphi)$ . Therefore, the simple solution  $\kappa = 1/2$  leads to the following expression of the critical curve :

$$r_{\text{cri}} = \frac{\sqrt{f}}{\sqrt{\cos^2 \varphi_{\text{cri}} + f^2 \sin^2 \varphi_{\text{cri}}}}. \quad (1.174)$$

By substituting the latter equation into the lens equation, we obtain a parametrized equation for the corresponding caustic curve :

$$y_1 = \frac{\sqrt{f}}{\sqrt{\cos^2 \varphi + f^2 \sin^2 \varphi}} \cos \varphi - \frac{\sqrt{f}}{f'} \operatorname{arcsinh} \left( \frac{f'}{f} \cos \varphi \right), \quad (1.175)$$

and

$$y_2 = \frac{\sqrt{f}}{\sqrt{\cos^2 \varphi + f^2 \sin^2 \varphi}} \sin \varphi - \frac{\sqrt{f}}{f'} \arcsin (f' \sin \varphi). \quad (1.176)$$

Due to the singularity of the SIE surface mass density at the center  $\mathbf{x} = 0$ , there exists a region in the source plane for which a source produce multiple lensed images but which is not surrounded by a caustic curve. One of these lensed images is infinitely faint and located at  $\mathbf{x} = 0$ . This region is surrounded by a curve, the so-called *cut* (Kovner 1987a), for which

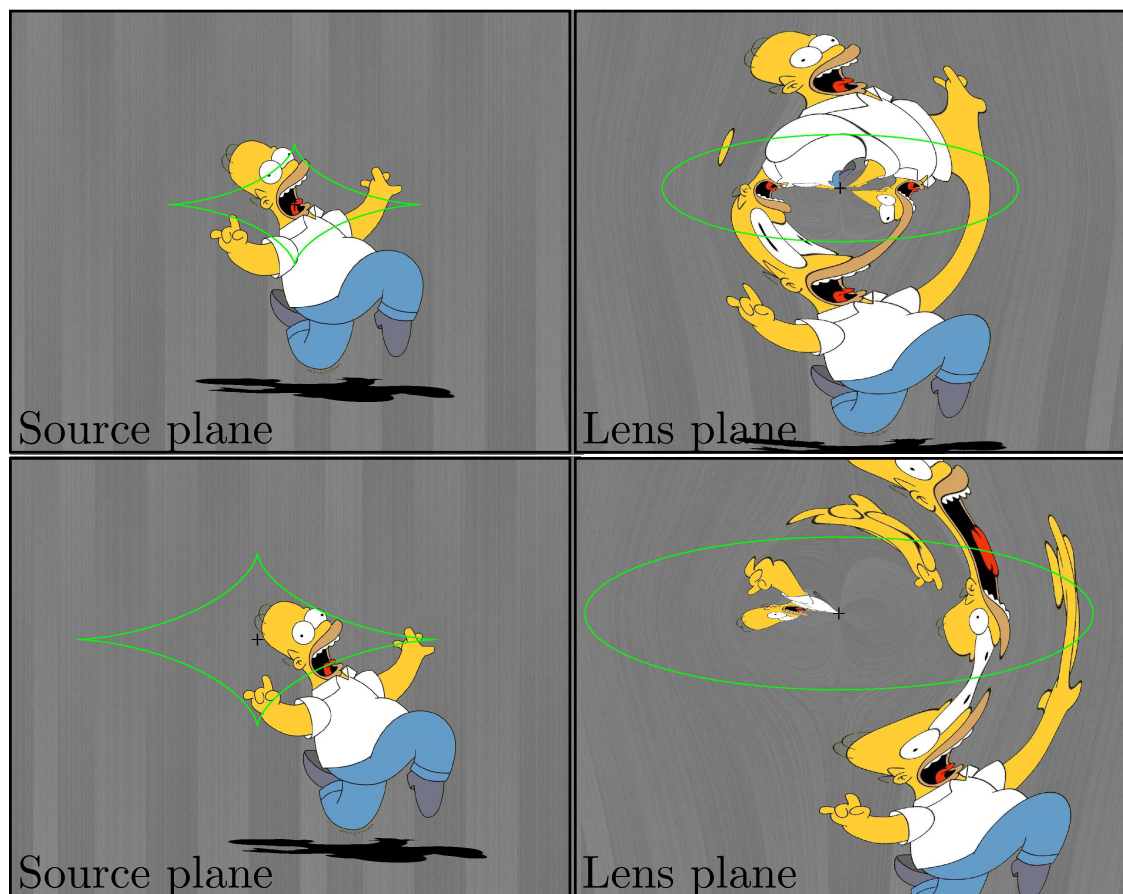


**Figure 1.9:** Illustration of gravitational lensing deformations due to a SIE deflector. The green lines correspond respectively to the caustic curves (left panel) and to the critical lines (right panel).

the analytical expression can be simply deduced from  $\mathbf{y}(\varphi) = \lim_{r \rightarrow 0} \mathbf{y}(r, \varphi)$ , hence :

$$\mathbf{y}(\varphi) = -\frac{\sqrt{f}}{f'} \left[ \operatorname{arcsinh} \left( \frac{f'}{f} \cos \varphi \right) \mathbf{e}_1 + \arcsin (f' \sin \varphi) \mathbf{e}_2 \right]. \quad (1.177)$$

In order to visualize the different features of the SIE lens mapping, we have illustrated in Fig. 1.9 the lensed images of Homer Simpson in two different situations. For instance, such an illustration allows to easily recognize the parities of the different lensed images of a particular part of the source (e.g. Homer's head).

The SIE is a particular case of a more general family of lenses for which the deflection potential obeys the relation :

$$\hat{\psi}(r, \varphi) = r \frac{\partial \hat{\psi}(r, \varphi)}{\partial r}, \quad (1.178)$$

whose general solution for the deflection potential is :

$$\hat{\psi}(r, \varphi) = r F(\varphi) , \quad (1.179)$$

where  $F(\varphi)$  represents a function of  $\varphi$  only. For the case of this family of models, in particular SIE lenses, Witt & al. (2000) have proposed a very simple expression for the time delay between a pair of two lensed images :

$$\Delta t_{i,j} = \frac{1 + z_D}{2c} \frac{D_{OD} D_{OS}}{D_{DS}} (r_j^2 - r_i^2) . \quad (1.180)$$

The main advantage of the latter equation is that the determination of the time delays does not require to know the lens orientation, nor the need to search for the best-fit model parameters. However, the use of the latter equation still requires to assume that the considered mass distribution can be described by the SIE family of models. For the case of a small misalignment between the source, the deflector and the observer, one can retrieve all the model parameters using only the lensed image positions (Wertz & Surdej, submitted to MNRAS on February 2014). Such an approach allows to conclude, without requiring any numerical simulations, whether the SIE family of models constitutes a relevant choice. The same approach has been first applied to axially symmetric mass distributions which obey a power-law, as well as the latter perturbed with an external shear (Wertz, Pelgrims & Surdej, 2012).

As already mentioned, the analytical treatment of those families of models is difficult. When the determination of the deflection angle is non-trivial and when complex integration theory can lead to analytical handling, the lens theory can be usefully formulated in terms of complex quantities. Such a complex representation of the gravitational lens theory has been first proposed by Bourassa & Kantowski (1973, 1975), corrected by Bray (1984). Let us summarize some general results of this approach. First, we may express the deflection angle, the source and the lensed image positions in terms of complex numbers :  $y_c = y_1 + \iota y_2$ ,  $x_c = x_1 + \iota x_2$  and  $I_c(x_c) = \alpha_1(x_1, x_2) + \iota \alpha_2(x_1, x_2)$ , where  $\iota$  represents the imaginary unit and  $I_c(x_c)$  is called the *complex scattering function*. From the latter equations and from Eq. (1.111), the expression of  $I_c(x_c)$  can be expressed as :

$$I_c(x_c) = -\frac{1}{\pi} \int_{\mathcal{C}} \frac{\kappa(x'_c)}{x_c - x'_c} dx'_c . \quad (1.181)$$

Adopting these notations, the lens equation in terms of complex quantities transforms into :

$$y_c = x_c - I_c^*(x_c) , \quad (1.182)$$

where the asterisk denotes complex conjugation. For the case of elliptical isodensity curve lenses, also called *homoeoidal symmetric lenses*, we can define the coordinates  $\rho$  and  $\phi$  in the lens plane such as :

$$x_1 = \rho \cos \phi, \quad x_2 = \frac{\rho}{f} \sin \phi, \quad (1.183)$$

which allow to express the surface mass density in the simple form  $\kappa(r, \phi) \equiv \kappa(\rho)$ . After substituting the coordinates  $(\rho, \phi)$  into Eq. (1.181), the complex scattering function takes the form :

$$I_c(x_c) = -\frac{1}{f\pi} \int_0^{+\infty} \rho' \kappa(\rho') \left\{ \int_0^{2\pi} \frac{d\phi}{x_c - \rho' \cos \phi - \iota \frac{\rho'}{f} \sin \phi} \right\} d\rho'. \quad (1.184)$$

The  $\phi$ -integral, hereafter  $I_\phi$ , can be evaluated by making use of the complex integration theory. First, reminding that  $\cos \phi = (e^{i\phi} + e^{-i\phi})/2$  and  $\sin \phi = (e^{i\phi} - e^{-i\phi})/2i$ , and defining the variable  $z = e^{i\phi}$ , the integral  $I_\phi$  becomes :

$$I_\phi = \iota \int_C \frac{1}{\frac{\rho'}{2} \left(1 + \frac{1}{f}\right) z^2 - x_c z + \frac{\rho'}{2} \left(1 - \frac{1}{f}\right)} dz, \quad (1.185)$$

where  $C$  denotes a rectifiable closed curve element of the set  $U$ . The latter set  $U$  is defined such as the integrand exists and is holomorphic (with the exception of the singular points denoted by  $z_k$ ), and does not meet any of the  $z_k$ . The singular points  $z_k$  of the integrand are simply given by :

$$z_{1,2} = \frac{f x_c \pm \sqrt{f^2 x_c^2 + \rho'^2 f'^2}}{\rho' (1 + f)}. \quad (1.186)$$

Therefore, the integral  $I_\phi$  takes the form :

$$I_\phi = \frac{2f\iota}{\rho'(1+f)} \int_C \frac{1}{(z - z_1)(z - z_2)} dz. \quad (1.187)$$

Making use of the Residue theorem and noticing that  $|z_1| > 1$ , the latter equation leads to :

$$I_\phi = \frac{2f\iota}{\rho'(1+f)} \frac{2\pi}{(z_2 - z_1)}, \quad (1.188)$$

$$= \frac{2\pi}{\sqrt{x_c^2 + \rho'^2 \frac{f'^2}{f^2}}}. \quad (1.189)$$

As a result, from Eq. (1.189) and noticing that the inner integral of Eq. (1.184) vanishes for

$\rho' > \rho$ , the complex scattering function reduces to :

$$I_c(x_c) = -\frac{2}{f} \text{sign}(x_c) \int_0^\rho \frac{\rho' \kappa(\rho')}{\sqrt{x_c^2 + \rho'^2 \frac{f'^2}{f^2}}} d\rho' . \quad (1.190)$$

In the literature, the axis ratio  $f$  is sometimes expressed as  $\cos\beta = 1/f$ . By taking account of this notation, the latter equation transforms into :

$$I_c(x_c) = -2 \text{sign}(x_c) \cos\beta \int_0^\rho \frac{\rho' \kappa(\rho')}{\sqrt{x_c^2 + \rho'^2 \sin^2\beta}} d\rho' . \quad (1.191)$$

It turns out that separating the deflection angle into real and imaginary parts is extremely difficult, and has not been published until recently. Therefore, we have proposed to use the Fourier formalism in order to analytically determine the deflection angle for homoeoidal symmetric lenses (Wertz & Surdej, 2014).





# 2

## ASYMPTOTIC SOLUTIONS FOR THE CASE OF POWER-LAW AXIALLY SYMMETRIC AND SIE GRAVITATIONAL LENS MODELS

---

### 2.1 Introduction

---

Determination of the Hubble parameter  $H_0$ , based upon the gravitational lensing theory, can be performed in different ways. Such a determination seems to be highly sensitive to the nature of the deflector mass distribution. Indeed, from Eq. (1.94), the expression of the time delays between pairs of lensed images directly depends on the deflection potential produced by the deflector mass distribution. A first possible approach consists in obtaining a statistical estimate of  $H_0$  from the determination of time delays between the light curves of the lensed images of selected multiply imaged quasars. Let us mention the COSMOGRAIL (COSmological Monitoring of GRAvitational Lenses) collaboration which has adopted such an approach for about thirty lensed quasars. For each of the selected gravitational lens systems, a precise lens model parameter fitting is required together with an efficient data reduction procedure based on the MCS algorithm (Magain & al., 1998). Some results obtained in this framework can be found, for instance, in papers by Eigenbrod & al. (2005, 2006, 2007), Saha & al. (2006), Vuissoz & al. (2007, 2008), Chantry & al. (2010), Courbin & al. (2011), Sluse & al. (2012), Eulaers & (2013), Rathna Kumar & al. (2013) and Tewes & al. (2013).

A second approach is dictated by the following questioning : might it be possible to find a lensing regime or lensed image configurations for which the determination of  $H_0$  only depends very slightly, for a given family of models, on the lens parameters ? We are convinced that the answer is yes. For the case of a nearly perfect alignment between the source, the deflector and the observer, the lensed image configurations are very symmetric and, then,

the involved time delays between pairs of lensed images are very small. Considering the lensed image positions as first order perturbations of the ones resulting from the perfect alignment, we have shown the possibility of deriving  $H_0$  from the observable quantities only, irrespective of the lens model parameters. The strength of this method consists, inter alia, in obtaining analytical expressions which link the astrometric positions of the lensed images to the model parameters. As a consequence, besides deriving  $H_0$  without any numerical model fitting, it is straightforward to determine whether the considered family of models constitutes a judicious representation of the lens mass distribution.

We have performed this study, as a first step, for a power-law axially symmetric family of models characterized by mass distributions obeying the relation  $M(\leq |\mathbf{x}|) = |\mathbf{x}|^\epsilon$  where  $\mathbf{x}$  represents the normalized angular impact parameter in the lens plane. Furthermore, we have considered both cases with and without external shear. The major results of this study have been summarized in the paper entitled "*Asymptotic solutions for the case of nearly symmetric gravitational lens systems*" and published in the peer reviewed journal Monthly Notices of the Royal Astronomical Society (MNRAS) 424, 1543-1555, 2012. The full content of this paper, referred in the remainder as to Paper I, is presented in the next Section 2.2. Several additional calculations are presented in Section 2.3.

Following up on the promising results obtained for the power-law axially symmetric family of models, we have investigated, as a second step, the case of the SIE family of models. Again, we have demonstrated the possibility of expressing  $H_0$  as a function of observable quantities only. Furthermore, we have applied such an approach to the multiply imaged quasar Q2237+0305 for which the choice of the SIE family of models turns out to be particularly appropriate. In order to confirm the relevance of the analytical results, we have performed both SIE and NSIE numerical fitting. Although the numerically modeled image positions are more accurate, the model parameters obtained immediately from the first order equations are very close to the ones obtained from intensive calculations. The major results of this study have been summarized in the paper entitled "*Asymptotic solutions for the case of SIE lens models and application to the quadruply imaged quasar Q2237+0305*", recently submitted to the peer reviewed journal MNRAS for publication. The full content of this paper, referred in the remainder as to Paper II, is presented in Section 2.4.

# **Asymptotic solutions for the case of nearly symmetric gravitational lens systems**

**O. Wertz, V. Pelgrims and J. Surdej**

*Monthly Notices of the Royal Astronomical Society*, 2012, **424**, 1543-1555.



# Asymptotic solutions for the case of nearly symmetric gravitational lens systems

O. Wertz,<sup>★†</sup> V. Pelgrims<sup>★‡</sup> and J. Surdej<sup>★§</sup>

*Institut d'Astrophysique et de Géophysique de l'Université de Liège, Allée du 6 Août 17, Sart Tilman, Bât. B5c, 4000 Liège, Belgium*

Accepted 2012 May 21. Received 2012 April 27; in original form 2011 November 30

## ABSTRACT

Gravitational lensing provides a powerful tool to determine the Hubble parameter  $H_0$  from the measurement of the time delay  $\Delta t$  between two lensed images of a background variable source. Nevertheless, knowledge of the deflector mass distribution constitutes a hurdle. We propose in the present work interesting solutions for the case of nearly symmetric gravitational lens systems. For the case of a small misalignment between the source, the deflector and the observer, we first consider power-law ( $\varepsilon$ ) axially symmetric models for which we derive an analytical relation between the amplification ratio and source position which is independent of the power-law slope  $\varepsilon$ . According to this relation, we deduce an expression for  $H_0$  also irrespective of the value  $\varepsilon$ . Secondly, we consider the power-law axially symmetric lens models with an external large-scale gravitational field, the shear  $\gamma$ , resulting in the so-called  $\varepsilon - \gamma$  models, for which we deduce simple first-order equations linking the model parameters and the lensed image positions, the latter being observable quantities. We also deduce simple relations between  $H_0$  and observable quantities only. From these equations, we may estimate the value of the Hubble parameter in a robust way. Nevertheless, comparison between the  $\varepsilon - \gamma$  and singular isothermal ellipsoid (SIE) models leads to the conclusion that these models remain most often distinct. Therefore, even for the case of a small misalignment, use of the first-order equations and precise astrometric measurements of the positions of the lensed images with respect to the centre of the deflector enables one to discriminate between these two families of models. Finally, we confront the models with numerical simulations to evaluate the intrinsic error of the first-order expressions used when deriving the model parameters under the assumption of a quasi-alignment between the source, the deflector and the observer. From these same simulations, we estimate for the case of the  $\varepsilon - \gamma$  family of models that the standard deviation affecting  $H_0$  is  $\sigma_{H_0} = 2 \text{ km s}^{-1} \text{ Mpc}^{-1}$  which merely reflects the adopted astrometric uncertainties on the relative image positions, typically  $\sigma_{\theta(i)} = 0.003 \text{ arcsec}$ . In conclusions, we stress the importance of getting very accurate measurements of the relative positions of the multiple lensed images and of the time delays for the case of nearly symmetric gravitational lens systems, in order to derive robust and precise values of the Hubble parameter.

**Key words:** gravitational lensing: strong – cosmological parameters.

## 1 INTRODUCTION

In 1964, Refsdal (1964a,b) has first proposed to determine the value of the Hubble parameter  $H_0$  from the observed time delay between two lensed images of an intrinsically variable distant source. Un-

fortunately, such a determination turns out to be lens model dependent. For the case of general isothermal models, Witt, Mao & Keeton (2000) have derived a common and surprisingly simple expression of the time delay between two lensed images involving only the observed image positions. Furthermore, Witt has analysed deviations from the isothermal profile by considering a deflection potential that obeys a power law. He concluded that when the model is not isothermal, he could not eliminate the dependence of the mass distribution from the time delay expression (Witt et al. 2000).

Our aim in this paper is to possibly identify gravitational lens image configurations for which the determination of  $H_0$  is not, or is very little, model dependent. For instance, in the case of

<sup>★</sup>E-mail: wertz@astro.ulg.ac.be (OW); pelgrims@astro.ulg.ac.be (VP); surdej@astro.ulg.ac.be (JS)

<sup>†</sup>Aspirant du F.R.S. – FNRS.

<sup>‡</sup>IFPA, AGO Department, University of Liège.

<sup>§</sup>Also Directeur de Recherche honoraire du FNRS.

a perfect alignment between a background point-like source, a foreground axially symmetric deflector and an observer, the resulting lensed images consist of a ring, the so-called Einstein ring, irrespective of the lens model. The time delays measured between different regions of the ring are equal to zero, also independently of the adopted axially symmetric lens model. If the source is very slightly misaligned, the Einstein ring breaks into two lensed images which expressions of the flux ratio and time delay turn out to be model independent of the power-law slope  $\varepsilon$  (cf. Section 2). Therefore, such cosmic image configurations naturally offer in principle the possibility of deriving robust estimates of  $H_0$ .

The main idea of this paper is to investigate for the case of more complex mass distributions whether different observable quantities such as the lensed image and deflector positions, the flux ratios and time delays may be used to determine the Hubble parameter irrespective of the lens model. Let us insist that we exclude here the additional mass sheet degeneracy problem which has been originally discussed by Falco, Gorenstein & Shapiro (1985).

In order to reproduce the general features of gravitational arcs, Alard (2007) has already developed a singular perturbative method for which he considers simultaneously two types of same order perturbations of a point-like source perfectly aligned in a circularly symmetric potential: first, the alignment may not be perfect and secondly, the potential may not be perfectly circular. In the same way, we have chosen to consider the perturbation of the alignment between the point-like source, the axially symmetric deflector and the observer but on the contrary, we consider axially symmetric deflectors to which we add an external perturbation, the shear, without any restriction on its strength. Since the range of values of the shear intensity is not restricted, the perturbation of the alignment and the one of the potential, i.e. the shear, are not necessarily of the same order.

In Section 2, we recall the basic gravitational lens, astrometric and amplification equations for the case of axially symmetric deflectors which mass distributions obey a power-law dependence with respect to the impact parameter. We also assume that the lensed images are not resolved individually. Assuming a very small misalignment between the source, the lens and the observer, we then derive first-order expressions for the lensed image positions, flux ratios and time delays.

In Section 3, we consider more realistic gravitational lens mass distributions by adding an external shear which may account for the formation of more complex gravitational lens image configurations (up to five lensed images). Still for the case of a very small misalignment between the source, the lens and the observer, we show how it is possible to infer the value of the Hubble parameter from the linearized astrometric and time delay expressions, irrespective of the values of  $\varepsilon$  and  $\gamma$ . In Section 4, we test the validity of the astrometric equations as well as the robustness of the inferred values of  $H_0$  versus the degree of misalignment between the source, the lens and the observer, and the gravitational lens model parameters. Some general conclusions form the last section.

## 2 AXIALLY SYMMETRIC LENSES

### 2.1 Mass distributions and lens equation

Owing to their simplicity, axially symmetric lenses represent an interesting class of models to probe asymptotic solutions which may turn out to be of practical interest. To this end, we characterize

axially symmetric mass distributions as follows:

$$M(\leq |\mathbf{x}|) = |\mathbf{x}|^\varepsilon, \quad (1)$$

where  $\mathbf{x} = \boldsymbol{\theta}/\theta_E$  represents the normalized angular impact parameter  $\boldsymbol{\theta}$  in the lens plane,  $\varepsilon \in [0, 2[$  the mass distribution power-law slope and  $\theta_E$  the value of the Einstein ring angular radius in the case of a perfect alignment between the source, the lens and the observer. The case  $\varepsilon = 0$  corresponds to the point mass and  $\varepsilon = 1$  corresponds to the singular isothermal sphere lens model. Furthermore,  $M = 1$  corresponds to the normalized mass of the deflector located inside the Einstein ring. In the case of axially symmetric lens models, the deflection angle at the normalized impact parameter  $\mathbf{x}$  can be expressed as a two-dimensional vector (Schneider 1984)

$$\hat{\alpha}(\mathbf{x}) = -\frac{M(|\mathbf{x}|)}{|\mathbf{x}|^2} \mathbf{x} = -\nabla_{\mathbf{x}} \hat{\psi}(\mathbf{x}), \quad (2)$$

where  $\hat{\psi}(\mathbf{x})$  represents the normalized deflection potential. After introducing the expression of the axially symmetric mass distributions (see equation 1), equation (2) becomes

$$\hat{\alpha}(\mathbf{x}) = -|\mathbf{x}|^{\varepsilon-2} \mathbf{x}. \quad (3)$$

Considering a typical source, deflector and observer configuration, the lens equation links the position of the source, the impact parameter and the deflection angle (Schneider 1984)

$$\mathbf{y} = \mathbf{x} + \hat{\alpha}(\mathbf{x}), \quad (4)$$

where  $\mathbf{y} = \boldsymbol{\theta}_S/\theta_E$  is the normalized angular point-like source position  $\boldsymbol{\theta}_S$  projected in the lens plane and the normalized impact parameter  $\mathbf{x}$  refers to the image positions in the lens plane. After introducing the expression of the deflection angle (equation 3), equation (4) becomes

$$\mathbf{y} = (1 - |\mathbf{x}|^{\varepsilon-2}) \mathbf{x}. \quad (5)$$

In Fig. 1, we have represented the modulus of the deflection angle  $\hat{\alpha}(\mathbf{x})$  as a function of the modulus of the normalized image position  $\mathbf{x}$  for several values of the parameter  $\varepsilon$ .

Given the symmetry of the deflector, it is appropriate to use a system of polar coordinates. Assuming an arbitrarily oriented coordinate system which is centred on the deflector's gravity centre, the lens equation reduces to

$$\begin{pmatrix} y_1 \\ y_2 \end{pmatrix} = y \begin{pmatrix} \cos \theta \\ \sin \theta \end{pmatrix} = [1 - (r^{(i)})^{\varepsilon-2}] r^{(i)} \begin{pmatrix} \cos \varphi^{(i)} \\ \sin \varphi^{(i)} \end{pmatrix}, \quad (6)$$

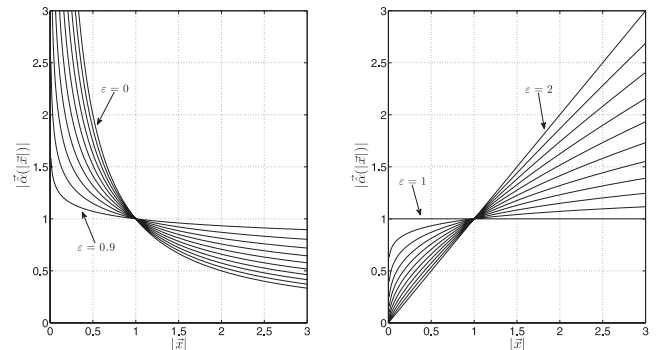


**Figure 1.** The modulus of the deflection angle  $|\hat{\alpha}(\mathbf{x})|$  is represented as a function of the modulus of the impact parameter  $|\mathbf{x}|$ . The left-hand panel illustrates the deflection angle for values of  $\varepsilon$  in the range  $[0, 1[$  by steps of 0.1 and the right-hand panel illustrates the deflection angle for values of  $\varepsilon$  in the range  $[1, 2]$ . The cases  $\varepsilon = 0, 1$  and  $2$  correspond to the point mass, the singular isothermal sphere and the uniform disc lens models, respectively.

where  $i$  refers to the  $i$ th image,  $y = \sqrt{y_1^2 + y_2^2} = |\theta_S|/\theta_E$  and

$$r^{(i)} = |\theta^{(i)}|/\theta_E = |\mathbf{x}^{(i)}| \geq 0 \quad (7)$$

is the normalized image radial coordinate. Furthermore,  $\theta$  and  $\varphi^{(i)}$  represent the source and image angular coordinates. According to the lens equation (see equation 5), the image positions  $(r^{(i)}; \varphi^{(i)})$  are located along the same direction as the source-deflector direction  $(y; \theta)$  and we have thus  $\varphi^{(i)} = \theta$  or  $\varphi^{(i)} = \theta + \pi$ . The analytical resolution of equation (6) is only possible for several integer values of  $\varepsilon$ . As a consequence, a numerical resolution is mandatory for most values of  $\varepsilon$ . Depending on the model parameters, equation (6) leads to one, two or three lensed image solutions. In the remainder, we shall concentrate on the properties of the two brightest lensed images. The three model parameters are thus  $\theta_S$ ,  $\theta_E$  and  $\varepsilon$ .

## 2.2 The amplification ratios

Since gravitational lensing preserves the surface brightness of the source and only changes the cross-section of the ray bundles (Etherington 1933), the amplification  $\mu$  of a lensed image is given by the determinant of the jacobian matrix of the surjective lens mapping  $\mathbf{x} \rightarrow \mathbf{y}$  (Schneider, Ehlers & Falco 1992)

$$\mu = \left| \frac{\partial \mathbf{y}}{\partial \mathbf{x}} \right|^{-1}. \quad (8)$$

From equations (6) and (8), we easily deduce the analytical expression of the amplification factor, in polar coordinates:

$$\mu^{(i)} = [1 - \varepsilon (r^{(i)})^{\varepsilon-2} + (\varepsilon - 1) (r^{(i)})^{2(\varepsilon-2)}]^{-1}. \quad (9)$$

The amplification factor diverges (i.e.  $1/\mu^{(i)}$  vanishes) for a lensed image located on the so-called *critical curve* and all points located on such a curve are termed *critical points*.<sup>1</sup> Denoting  $r_c \geq 0$  the radial coordinate of a critical point, equation (9) reduces to

$$[1 - (\varepsilon - 1) (r_c)^{\varepsilon-2}] [1 - (r_c)^{(\varepsilon-2)}] = 0, \quad (10)$$

and leads to the single solution  $r_{c,t} = 1$ , for  $\varepsilon \leq 1$ , and to the two solutions  $r_{c,t} = 1$  and  $r_{c,r} = (\varepsilon - 1)^{1/(2-\varepsilon)}$ , for  $\varepsilon > 1$ . As a result, the first critical curve, the so-called *tangential critical curve*, reduces to a unit radius circle and is the region of the lens plane where two lensed images merge tangentially into an Einstein ring as the source gets perfectly aligned with respect to the lens and the observer. The second critical curve, the so-called *radial critical curve*, reduces to a circle whose radius is  $r_{c,r}$  and is the region of the lens plane where two of the three lensed images merge along the radial direction. The images of the critical curves in the projected source plane, under the lens mapping, are called *caustics* (Erdl 1992). Since  $y_c$  is the radial coordinate of the caustic points, equation (5) leads to  $y_{c,t} = 0$  for any value of  $\varepsilon$  and the so-called *tangential caustic* reduces to a point. Similarly, equation (5) leads to  $y_{c,r} = (2 - \varepsilon) (\varepsilon - 1)^{(\varepsilon-1)/(2-\varepsilon)}$  if  $\varepsilon > 1$  and the so-called *radial caustic* reduces to a circle whose radius is  $y_{c,r}$ .

Since the real source cannot be directly observed, its original flux cannot be estimated either. Therefore, the only relevant observable quantity is the amplification ratio  $(\mu^{(1)}/\mu^{(2)})$  between the two main images 1 and 2 which can be simply measured from their image flux ratio. First of all, we can reduce the amplification factor defined by equation (9) while substituting  $(r^{(1)})^{\varepsilon-2}$  by  $1 - (y/r^{(1)})$  and

<sup>1</sup> For more details about lensing near critical points, see Schneider et al. (1992).

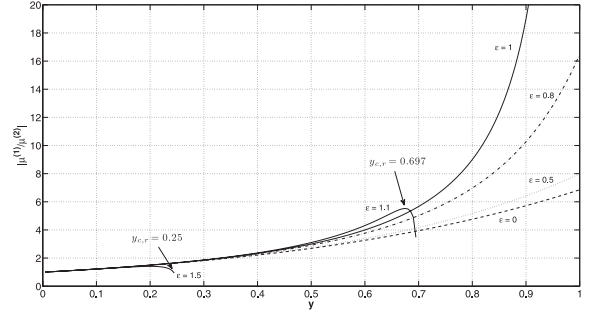


**Figure 2.** The amplification ratio  $|\mu^{(1)}/\mu^{(2)}|$  is plotted as a function of  $y$  for various values of the power-law slope ( $\varepsilon$ ). For a small misalignment (typically  $y < 0.15$ ), the amplification ratio is found to be nearly independent on the lens model ( $\varepsilon$ ).

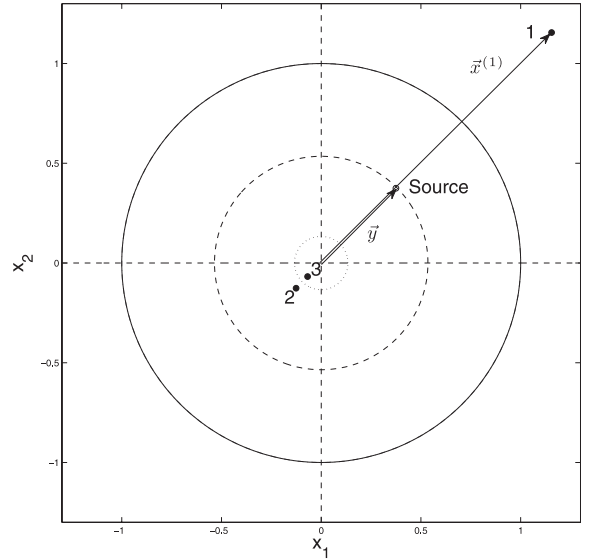


**Figure 3.** Image configuration in the lens plane for  $\varepsilon = 1.2$  and  $(y; \theta) = (0.53; \pi/4)$ . The projected point-like source is closed to the radial caustics (dashed line circle) and the lensed images 2 and 3 radially merge along the radial critical curve (dotted line circle). In the case of a perfect alignment between the source, the observer and the lens, the highly distorted images 1 and 2 merge along the tangential critical curve (solid line circle).

$(r^{(2)})^{\varepsilon-2}$  by  $1 + (y/r^{(2)})$  from equation (6). Therefore, with no loss of generality, the expression of the amplification ratio becomes

$$\frac{\mu^{(1)}}{\mu^{(2)}} = \frac{r^{(1)}}{r^{(2)}} \left[ \frac{(\varepsilon - 2) + (\varepsilon - 1) \frac{y}{r^{(2)}}}{(2 - \varepsilon) + (\varepsilon - 1) \frac{y}{r^{(1)}}} \right]. \quad (11)$$

First, the amplification ratio increases with  $y$ , for all values of  $\varepsilon \in [0, 2[$  (see Fig. 2). Although there are always two images for lens models characterized by  $\varepsilon < 1$  when  $y \neq 0$ , a third image may appear for  $\varepsilon > 1$  and the latter merges with image 2 when the source crosses the radial caustics (see Fig. 3). This situation occurs when  $y = y_{c,r}$  (see Fig. 2) and the amplification ratio decreases until the two merging lensed images vanish.

Secondly, the amplification ratio is independent on the lens model when typically  $y < 0.15$  (see Fig. 2), i.e. in the case of a quasi-perfect alignment between the source, the lens and the observer. This very interesting property highlights the strong link between the amplification ratio  $(\mu^{(1)}/\mu^{(2)})$  and the source position ( $y$ ) which can now be estimated irrespective of the power-law slope  $\varepsilon$ . This property can be explained from equation (11) when considering the



case of an infinitesimal misalignment between the source, the lens and the observer, typically  $y < 0.15$ .

### 2.3 First-order equations and solutions

To first order and in accordance with Alard (2007), we can write

$$(r^{(i)})^{(\varepsilon-2)} = 1 + (\varepsilon - 2)(r^{(i)} - 1). \quad (12)$$

After substituting equation (12) into equation (5), the latter can be rewritten as

$$(r^{(i)})^2(2 - \varepsilon) - r^{(i)}(2 - \varepsilon) + (-1)^i y = 0, \quad (13)$$

where  $(i) = 1$  and  $(i) = 2$  refer to the two brightest lensed images. Resolution of this quadratic equation gives the radial coordinate of the images to first order as a function of the radial coordinate of the source ( $y$ ) and of the lens model ( $\varepsilon$ ):

$$r^{(1)} = 1 + \frac{y}{2 - \varepsilon} + \mathcal{O}(y^2), \quad (14)$$

$$r^{(2)} = 1 - \frac{y}{2 - \varepsilon} + \mathcal{O}(y^2). \quad (15)$$

After substituting equations (14), (15) and  $y/r^{(i)}$  with their first-order development terms into equation (11), the amplification ratio between the two brightest lensed images becomes

$$\frac{\mu^{(1)}}{\mu^{(2)}} = -\frac{(2 - \varepsilon)^3 + (2 - \varepsilon)^3 y + 2(2 - \varepsilon)(1 - \varepsilon)y^2 + (1 - \varepsilon)y^3}{(2 - \varepsilon)^3 - (2 - \varepsilon)^3 y + 2(2 - \varepsilon)(1 - \varepsilon)y^2 - (1 - \varepsilon)y^3}, \quad (16)$$

To first order, it is clear that the amplification ratio merely reduces to

$$\frac{\mu^{(1)}}{\mu^{(2)}} = -\frac{1 + y}{1 - y}, \quad (17)$$

that is to say the flux ratio between the two brightest lensed images is only a function of the source position ( $y$ ). We note that for the case  $\varepsilon = 1$ , equation (17) turns out to be perfectly exact. This property arises from equations (14) and (15), where  $\mathcal{O}(y^2) = 0$  for the case  $\varepsilon = 1$ . As a result, for a small misalignment between the source, the axially symmetric deflector and the observer, the amplification ratio between the two brightest lensed images is independent of the power-law slope  $\varepsilon$  and is equal to the one defined by the singular isothermal sphere (SIS) model.

One could have hoped that equation (17) remains valid for more general axially symmetric lens models. Considering the most general axially symmetric deflection potential  $\hat{\psi} = \hat{\psi}(r)$ , the amplification ratio  $\mu^{(1)}/\mu^{(2)}$  can be expressed (see equations 2, 4 and 8) as

$$\frac{\mu^{(1)}}{\mu^{(2)}} = -\frac{1 + \frac{1 - K_2 + K_3}{(1 - K_2)^2} y}{1 - \frac{1 - K_2 + K_3}{(1 - K_2)^2} y}, \quad (18)$$

where  $K_n = (d\hat{\psi}(r)/dr)_{r=1}$  depends on the deflector model ( $\varepsilon$ ) only. In this way, the independency of the amplification ratio versus the analytical form of the deflection potential implies the following condition:

$$\frac{1 - K_2 + K_3}{(1 - K_2)^2} = 1. \quad (19)$$

This condition is generally not satisfied. Indeed, considering for instance the family of axially symmetric deflection potentials proposed by Alard (2007)

$$\hat{\psi}(r) = \frac{1}{\varepsilon} r^{\varepsilon [1 + \beta(r-1)]}, \quad (20)$$

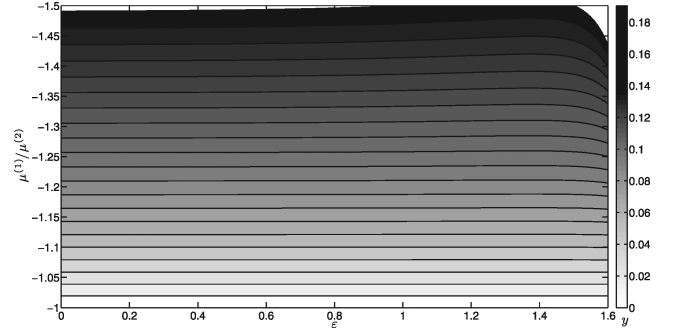


**Figure 4.** Contour plot diagram of the amplification ratio as a function of the lens model ( $\varepsilon$ ) and source position ( $y$ ). Each curve has been established for a fixed value of the source position, i.e.  $y$ . The maximum value of  $\varepsilon$  along the abscissa is less than 2 because for  $\varepsilon > 1$ , the radius of the radial caustics ( $y_{c,r}$ ) decreases when  $\varepsilon$  increases. As a result, there remains only one image for  $y > y_{c,r}$ .

and after substituting this deflection potential into the expression of  $K_n$ , we deduce

$$\frac{1 - K_2 + K_3}{(1 - K_2)^2} = \frac{(1 - K_2 + K_3)}{(1 - K_2 + K_3) + \beta(4\beta - 2\varepsilon - 3)}. \quad (21)$$

From equations (18), (19) and (21), we find that the amplification ratio between the two brightest lensed images is only a function of the source position, if and only if  $\beta = (2\varepsilon + 3)/4$  or  $\beta = 0$ . The latter case, i.e.  $\hat{\psi}(r) = r^\varepsilon/\varepsilon$ , corresponds to the lens models previously used.

From equation (17), we may express the normalized source position  $y$  as a function of the amplification ratio  $\mu^{(1)}/\mu^{(2)}$  and we find

$$y = \frac{\theta_S}{\theta_E} = -\frac{1 + \mu^{(1/2)}}{1 - \mu^{(1/2)}}, \quad (22)$$

where  $\mu^{(1/2)} = \mu^{(1)}/\mu^{(2)}$  and  $\theta_S = |\theta_S|$ . It is very convenient to represent equation (16) by means of a contour plot diagram (see Fig. 4) where each curve of  $\mu^{(1)}/\mu^{(2)}$  corresponds to a fixed value of the source position, i.e.  $y$ , as a function of  $\varepsilon$  in the range of 0–1.6. As we see, the amplification ratio is found to be independent on the power-law slope  $\varepsilon$  for small values of the source position ( $y$ ); this results in nearly horizontal curves for typically  $y < 0.15$ . Furthermore, the relative error  $\Delta\mu^{(1/2)}$  between the exact and the first-order expression of the amplification ratio (resp. equations 11 and 17) is maximum for the case  $\varepsilon = 0$ . Assuming  $y = 0.15$ ,  $\Delta\mu^{(1/2)}$  is then found to be  $\sim 0.0025$ , which corresponds to an absolute error on the value of  $\theta_S$  of  $\sigma_{\theta_S} = 0.001 \theta_E$ . We note that closer is the value of  $\varepsilon$  to 1, more accurate is equation (17). In addition, we can determine  $\theta_S$  from equation (22) insofar as we know the Einstein ring angular radius  $\theta_E$ . To this end, the sum of equations (14) and (15) simply leads to first order to

$$\theta_E = \frac{1}{2} (\theta^{(1)} + \theta^{(2)}), \quad (23)$$

and their difference to

$$y = \left( \frac{2 - \varepsilon}{2} \right) \frac{(\theta^{(1)} - \theta^{(2)})}{\theta_E}, \quad (24)$$

where  $\theta^{(i)} = |\theta^{(i)}|$  represents the radial coordinate of the  $i$ th image. Note that this latter equation had been established empirically by Refsdal & Surdej (1994). As a result, the source position  $\theta_S$  is given by

$$\theta_S = -\frac{1}{2} \left( \frac{1 + \mu^{(1/2)}}{1 - \mu^{(1/2)}} \right) (\theta^{(1)} + \theta^{(2)}), \quad (25)$$



and from equations (22) and (24), we can determine  $\varepsilon$  which is given by

$$\varepsilon = \left( \frac{\theta^{(1)} + \theta^{(2)}}{\theta^{(1)} - \theta^{(2)}} \right) \left( \frac{1 + \mu^{(1/2)}}{1 - \mu^{(1/2)}} \right) + 2. \quad (26)$$

Thus, for a small misalignment between the source, the deflector and the observer, we can in principle derive all values of the lens model parameters ( $\theta_S$ ,  $\theta_E$  and  $\varepsilon$ ) from the astrometric and amplification ratio equations.

## 2.4 Time delay and the Hubble parameter

A very interesting cosmological application of gravitational lensing consists in the determination of the Hubble parameter  $H_0$  from the measurement of the time delay  $\Delta t$  between two lensed image light curves (Refsdal 1964a,b). According to the wavefront method, Refsdal & Surdej (1994) have established for the case of small redshifts and of an axially symmetric lens model the analytical expression<sup>2</sup> for  $\Delta t$ :

$$\Delta t = \left( \frac{1 + z_1}{c} \right) \left( \frac{D_{OL} D_{OS}}{D_{LS}} \right) \theta_S (\theta^{(1)} + \theta^{(2)}), \quad (27)$$

and  $H_0$

$$H_0^{-1} = \left( \frac{1}{1 + z_1} \right) \left( \frac{z_s - z_1}{z_1 z_s} \right) \frac{\Delta t}{\theta_S (\theta^{(1)} + \theta^{(2)})}, \quad (28)$$

where  $D_{OL}$ ,  $D_{OS}$  and  $D_{LS}$  represent the angular-diameter distances between the observer and the lens, the observer and the source, and the lens and the source;  $z_s$  and  $z_1$  are the redshifts of the source and the lens, respectively and  $\Delta t$  is the time delay between the two brightest lensed images. From equation (24) and for the case  $\varepsilon = 1$ , i.e. for the SIS model, we note that equation (27) reduces to

$$\Delta t = \left( \frac{1 + z_1}{2c} \right) \left( \frac{D_{OL} D_{OS}}{D_{LS}} \right) [(\theta^{(1)})^2 - (\theta^{(2)})^2]. \quad (29)$$

The latter equation holds for more general isothermal lens models whose associated deflection potentials are assumed to obey the relation  $\hat{\psi} = r \mathcal{F}(\varphi)$ , where  $\mathcal{F}(\varphi)$  is an arbitrary function of  $\varphi$  (Witt et al. 2000, their equation 12). These authors also consider potentials of the form  $\hat{\psi} = r^\varepsilon \mathcal{F}(\varphi)$  which include our power-law models for the particular case  $\mathcal{F} = 1/\varepsilon$ . However, for these cases, Witt et al. (2000, see their equation 25) could not eliminate the dependence of the mass distribution, i.e.  $\varepsilon$ , from the time delay expression. As we have just previously shown,  $\theta_S$  can be estimated from the amplification ratio between the two lensed images and their angular positions (see equation 25). For a small misalignment between the source, the deflector and the observer, the expression of  $\Delta t$  thus reduces to

$$\Delta t = \left( \frac{1 + z_1}{2c} \right) \left( \frac{D_{OL} D_{OS}}{D_{LS}} \right) \left( \frac{\mu^{(1/2)} + 1}{\mu^{(1/2)} - 1} \right) (\theta^{(1)} + \theta^{(2)})^2, \quad (30)$$

and the Hubble parameter

$$H_0^{-1} = \left( \frac{1}{1 + z_1} \right) \left( \frac{z_s - z_1}{z_1 z_s} \right) \left( \frac{\mu^{(1/2)} - 1}{\mu^{(1/2)} + 1} \right) \frac{2\Delta t}{(\theta^{(1)} + \theta^{(2)})^2}. \quad (31)$$

As a consequence,  $H_0$  can be deduced from observable quantities irrespective of the power-law slope  $\varepsilon$ . Let us remind that we do not consider here the additional mass sheet degeneracy problem that has been first pointed out and discussed by Falco et al. (1985).

<sup>2</sup> In their paper,  $\theta^{(i)}$  is the angular distance of the  $i$ th image from the deflector's gravity centre and  $\theta^{(2)}$  was chosen negative.

For the case of a flat universe with  $\Omega_M = 0.3$ ,  $\Omega_\Lambda = 0.7$  and cosmological values for the lens and source redshifts (Perlmutter et al. 1999), equation (31) should be replaced by

$$H_0^{-1} = \left( \frac{1}{1 + z_1} \right) \left( \frac{z_s - z_1}{z_1 z_s} \right) \left( \frac{F(z_s - z_1)}{F(z_1) F(z_s)} \right) \times \left( \frac{\mu^{(1/2)} - 1}{\mu^{(1/2)} + 1} \right) \frac{2\Delta t}{(\theta^{(1)} + \theta^{(2)})^2}, \quad (32)$$

where  $F(z)$  is defined to first order by (Peebles 1993)

$$F(z) = \frac{1}{(1 + z)} - [\Omega_M + 2(1 - \Omega_\Lambda)] \frac{z}{4(1 + z)}, \quad (33)$$

$$= \frac{1}{(1 + z)} \left( 1 - \frac{9z}{40} \right). \quad (34)$$

As a result, for the case of a small misalignment between the source, the lens and the observer, the Hubble parameter may be estimated from only observable quantities of the gravitational lens system, namely the redshifts of the lens and of the source, the time delay, the relative positions and the amplification ratio between the two brightest lensed images.

## 2.5 Mass estimation of the deflector

In addition, it is interesting to note that we can derive an expression for the mass  $M(\leq \theta_E)$  of the deflector inside the Einstein radius  $\theta_E$  from the expression of the time delay (Borgeest 1985). Indeed, from equations (22), (23), (27) and using the following equation (Refsdal & Surdej 1994)

$$\theta_E^2 = \frac{4G}{c^2} \left( \frac{D_{LS}}{D_{OL} D_{OS}} \right) M(\leq \theta_E), \quad (35)$$

the mass of the deflector  $M(\leq \theta_E)$  may be expressed as

$$M(\leq \theta_E) = \frac{c^3}{8G(1 + z_1)} \left( \frac{\mu^{(1/2)} - 1}{\mu^{(1/2)} + 1} \right) \Delta t. \quad (36)$$

The latter can thus be derived irrespective of  $\varepsilon$  and of  $H_0$  for the case of a small misalignment between the source, the lens and the observer. The corresponding gravitational lens systems always then consist of two symmetric lensed images, almost equally bright.

## 3 AXIALLY SYMMETRIC LENSES WITH SHEAR

### 3.1 General equations

Most of observed gravitational lens systems actually consist of more than two lensed images. Therefore, it seems wise to consider lenses with a somewhat perturbed symmetry. Such a perturbation can be represented by the tidal field caused by an external large-scale gravitational field, the so-called *shear*. The whole system is then described by the general lens equation:

$$\mathbf{y} = \mathbf{x} + \hat{\alpha}_{\text{gen}}(\mathbf{x}) = \mathbf{x} + \hat{\alpha}_{\text{iso}}(\mathbf{x}) + \hat{\alpha}_{\text{aniso}}(\mathbf{x}), \quad (37)$$

where the general deflection angle is split into two parts. The first part, the isotropic contribution, represents the light deflection of the beam due to the axially symmetric lens (see equation 3), whereas the second part, the anisotropic contribution, represents the shear influence which can be expressed as (Kovner 1987)

$$\hat{\alpha}_{\text{aniso}}(\mathbf{x}) = \gamma \begin{pmatrix} \cos 2\omega & \sin 2\omega \\ \sin 2\omega & -\cos 2\omega \end{pmatrix} \begin{pmatrix} x_1 \\ x_2 \end{pmatrix}, \quad (38)$$

where  $\gamma \geq 0$  is the shear intensity and  $\omega \in [0; 2\pi]$  represents the shear orientation measured from the same oriented coordinate system centred on the deflector's gravity centre as the one used to measure the lensed image positions. In the remainder, these models will be labelled  $\varepsilon - \gamma$ . Given the symmetry of the central deflector, it is again appropriate to use a system of polar coordinates. Using the same notation as in equation (6), the lens equation (37) becomes

$$y \cos \theta = [1 - (r^{(i)})^{\varepsilon-2}] r^{(i)} \cos \varphi^{(i)} + \gamma r^{(i)} \cos (2\omega - \varphi^{(i)}), \quad (39)$$

$$y \sin \theta = [1 - (r^{(i)})^{\varepsilon-2}] r^{(i)} \sin \varphi^{(i)} + \gamma r^{(i)} \sin (2\omega - \varphi^{(i)}). \quad (40)$$

Note that for  $\gamma = 0$ , i.e. without the external large-scale gravitational field, we recover the axially symmetric lens equation (6). Given several image positions  $(r^{(i)}; \varphi^{(i)})$ , equations (39) and (40) should allow us to retrieve all the model parameters  $\theta_S, \theta, \theta_E, \varepsilon, \gamma$  and  $\omega$ .

The amplification  $\mu$  of a lensed image is derived combining equation (8) and equations (39) and (40). The analytical expression of the amplification factor, in polar coordinates, is then found to be

$$\mu^{(i)} = \left\{ (1 - \gamma^2) + (r^{(i)})^{\varepsilon-2} [(2 - \varepsilon)(1 - \gamma \cos(2\omega - \varphi^{(i)})) - 2] + (\varepsilon - 1)(r^{(i)})^{2(\varepsilon-2)} \right\}^{-1}. \quad (41)$$

The critical curves are simply deduced from the condition  $1/\mu^{(i)} = 0$  using equation (41). Denoting  $r_c$  the radial coordinate of a critical point which depends on the angular coordinate  $\varphi_c \in [0; 2\pi]$ , and using the variable  $\rho(r_c; \varepsilon) = r_c^{2-\varepsilon}$  with  $\varepsilon < 2$ , equation (41) becomes

$$(1 - \gamma^2) \rho^2 + \rho [(2 - \varepsilon)(1 - \gamma \cos(2\omega - \varphi_c)) - 2] + (\varepsilon - 1) = 0, \quad (42)$$

which is simply a quadratic equation of the variable  $\rho$ .

Denoting  $\Gamma(\varphi_c) = [(2 - \varepsilon)(1 - \gamma \cos(2\omega - \varphi_c)) - 2]$  in equation (42) and after some trivial algebraic calculus, the resolution of this quadratic equation leads to two solutions which represent the equations of the critical curves in a system of polar coordinates and are given by

$$r_{c,1}(\varphi_c) = \left[ \frac{-\Gamma(\varphi_c) + \sqrt{\Gamma(\varphi_c)^2 - 4(1 - \gamma^2)(\varepsilon - 1)}}{2(1 - \gamma^2)} \right]^{\left(\frac{1}{2-\varepsilon}\right)}, \quad (43)$$

$$r_{c,2}(\varphi_c) = \left[ \frac{-\Gamma(\varphi_c) - \sqrt{\Gamma(\varphi_c)^2 - 4(1 - \gamma^2)(\varepsilon - 1)}}{2(1 - \gamma^2)} \right]^{\left(\frac{1}{2-\varepsilon}\right)}. \quad (44)$$

We note that for  $0 \leq \varepsilon < 1$  and  $\gamma < 1$ , we have  $r_{c,1}(\varphi_c) \in \mathbb{R}^+$  and  $r_{c,2}(\varphi_c) \in \mathbb{C}$  for any value of  $\varphi_c$  which indicates that there is only one critical curve,  $r_{c,1}(\varphi_c)$ . For  $\varepsilon \geq 1$  and  $\gamma < 1$ , we have  $r_{c,1}(\varphi_c) \in \mathbb{R}^+$  and  $r_{c,2}(\varphi_c) \in \mathbb{R}^+$  for any value of  $\varphi_c$  which indicates that there are two critical curves. For  $0 \leq \varepsilon < 1$  and  $\gamma > 1$ , a set of values of  $r_{c,1}(\varphi_{c,p})$  and  $r_{c,2}(\varphi_{c,q})$  show a non-null imaginary part. Otherwise, all the other real values constitute two mirror-symmetric curves. For  $\varepsilon > 1$  (excepted  $\varepsilon = 3/2$ ) and  $\gamma > 1$ , we have  $r_{c,2}(\varphi_c) \in \mathbb{R}^+$  and  $r_{c,1}(\varphi_c) \in \mathbb{C}$  for any value of  $\varphi_c$  which indicates that there is only one critical curve,  $r_{c,2}(\varphi_c)$ . For  $\varepsilon = 3/2$ , we have again two critical curves. All the related caustic curves  $(y_{c,j}; \theta_{c,j})$  can be simply deduced by either substituting  $r_{c,1}$  or  $r_{c,2}$  in the lens equations (39)

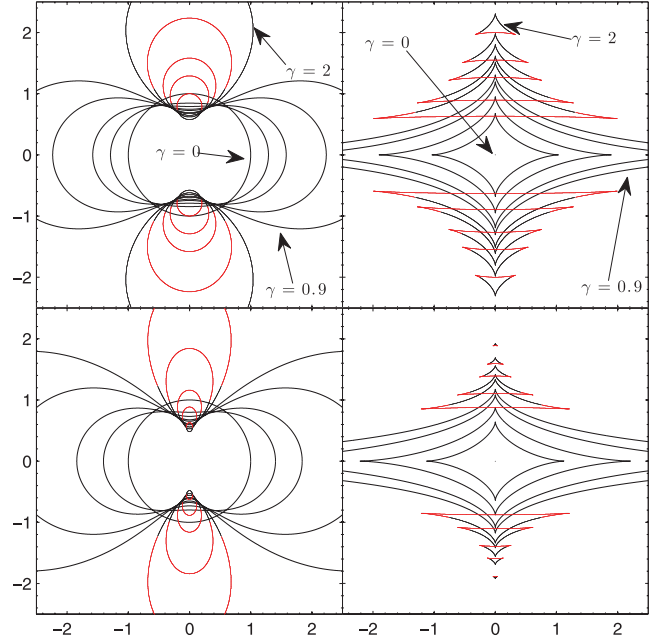


**Figure 5.** Critical curves (in the lens plane) and their associated caustic curves (projected in the lens plane) for different values of the lens model parameters ( $\varepsilon \in \{0, 0.5\}$ ,  $\gamma \in [0; 2]$  and  $\omega = 0$ ). The top panels are for  $\varepsilon = 0$  (the so-called Chang–Refsdal lens model; Chang & Refsdal 1984) and the bottom panels are for  $\varepsilon = 0.5$ . The left-hand panels illustrate the critical curves and the right-hand ones illustrate the corresponding caustics.

and (40) and become

$$y_{c,j} \begin{pmatrix} \cos \theta_{c,j} \\ \sin \theta_{c,j} \end{pmatrix} = [1 - (r_{c,j})^{\varepsilon-2}] r_{c,j} \begin{pmatrix} \cos \varphi_c \\ \sin \varphi_c \end{pmatrix} + \gamma r_{c,j} \begin{pmatrix} \cos (2\omega - \varphi_c) \\ \sin (2\omega - \varphi_c) \end{pmatrix}, \quad (45)$$

where  $j \in \{1, 2\}$  and  $(y_{c,j}; \theta_{c,j})$  represents the polar coordinates of the caustic points. Examples of critical curves and their associated caustic curves are shown in Fig. 5 for several values of  $\varepsilon$  and  $\gamma$ .

### 3.2 First-order equations and asymptotic solutions

For the case of a perfect alignment between the source, the lens and the observer, i.e. for  $y = 0$ , we may deduce from the lens equations (39) and (40) the exact positions  $(r_0^{(i)}; \varphi_0^{(i)})$  of the lensed images. On one hand, equation (39)  $\times \sin \varphi^{(i)}$ –equation (40)  $\times \cos \varphi^{(i)}$  leads to

$$y \sin(\varphi^{(i)} - \theta) = r^{(i)} \gamma \sin[2(\varphi^{(i)} - \omega)], \quad (46)$$

and from the latter equation and for  $y = 0$ , the exact image angular coordinates are found to be

$$\varphi_0^{(i)} = \omega + i \frac{\pi}{2}, \quad (47)$$

where  $i \in \{0, 1, 2, 3\}$  indicates that there are four lensed images. On the other hand, equation (39)  $\times \cos \varphi^{(i)}$  + equation (40)  $\times \sin \varphi^{(i)}$  leads to

$$y \cos(\varphi^{(i)} - \theta) = r^{(i)} [(1 - (r^{(i)})^{\varepsilon-2}) + \gamma \cos[2(\varphi^{(i)} - \omega)]], \quad (48)$$

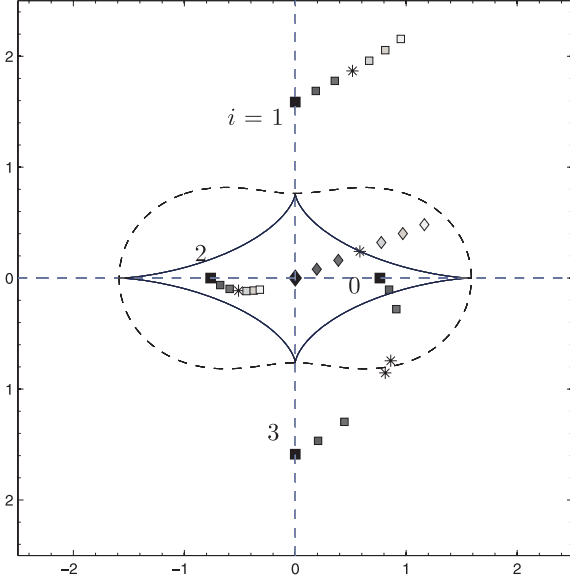


**Figure 6.** Illustration of different image configurations for the case of a point-like source and the lens model  $\varepsilon = 0.5$  with a shear intensity  $\gamma = 0.5$  and a shear orientation  $\omega = 0$ . When the source (asterisk) crosses the caustics (solid line), images 0 and 3 (asterisks) merge on the critical curve (dashed line).

and from the latter equation and for  $y = 0$ , the exact image radial coordinates are expressed as

$$r_0^{(i)} = (1 + (-1)^i \gamma)^{1/(\varepsilon-2)}. \quad (49)$$

We infer that images 0 and 2 (resp. 1 and 3) are located at the same angular distance on opposite sides with respect to the lens gravity centre and along the same direction as the shear (resp. along a perpendicular direction to that of the shear; see Fig. 6).

Considering a small misalignment between the source, the lens and the observer, the resulting image positions only slightly deviate from the perfect alignment case. Thus, the  $i$ th image position ( $r^{(i)}$ ;  $\varphi^{(i)}$ ) can be expressed as

$$r^{(i)} = r_0^{(i)} + \Delta r^{(i)}, \quad (50)$$

and

$$\varphi^{(i)} = \varphi_0^{(i)} + \Delta \varphi^{(i)}, \quad (51)$$

where  $\Delta r^{(i)}$  and  $\Delta \varphi^{(i)}$  represent small variations of the image polar coordinates, i.e.  $|\Delta r^{(i)}| \ll 1$  and  $|\Delta \varphi^{(i)}| \ll 1$ .

For the case of a small misalignment between the source, the lens and the observer, we shall now demonstrate how we can retrieve all the model parameters from the astrometric equations only developed to first order.

On one hand, from equations (46), (50) and (51), the expression of  $\Delta \varphi^{(i)}$  reduces to

$$\Delta \varphi^{(i)} = \frac{y \sin(\omega - \theta + i\pi/2)}{2(-1)^i \gamma r_0^{(i)}}. \quad (52)$$

We note that for  $\theta = \omega$  or  $\theta = \omega + \pi$ , we have  $\Delta \varphi^{(0)} = \Delta \varphi^{(2)} = 0$ , and for  $\theta = \omega + \pi/2$  or  $\theta = \omega + 3\pi/2$ , we have  $\Delta \varphi^{(1)} = \Delta \varphi^{(3)} = 0$ , whatever the value of  $y$ .

On the other hand, from equations (7), (48), (50) and (51), the expression of  $\Delta \theta^{(i)} = \theta_E \Delta r^{(i)}$  reduces to

$$\Delta \theta^{(i)} = \frac{y \theta_E \cos(\omega - \theta + i\pi/2)}{(2 - \varepsilon)(1 + (-1)^i \gamma)}. \quad (53)$$

We note that for  $\theta = \omega$  or  $\theta = \omega + \pi$ , we have  $\Delta \theta^{(1)} = \Delta \theta^{(3)} = 0$ , and for  $\theta = \omega + \pi/2$  or  $\theta = \omega + 3\pi/2$ , we have  $\Delta \theta^{(0)} = \Delta \theta^{(2)} = 0$ , whatever the value of  $y$ .

Equations (52) and (53) compose a set of eight independent equations for six model parameters ( $\theta_S$ ,  $\theta$ ,  $\theta_E$ ,  $\varepsilon$ ,  $\gamma$  and  $\omega$ ). Furthermore, we note that  $\Delta \varphi^{(0)} = -\Delta \varphi^{(2)}$ ,  $\Delta \varphi^{(1)} = -\Delta \varphi^{(3)}$ ,  $\Delta \theta^{(0)} = -\Delta \theta^{(2)}$  and  $\Delta \theta^{(1)} = -\Delta \theta^{(3)}$ .

### 3.2.1 The $\varepsilon - \gamma$ model parameters

Given that  $\Delta \varphi^{(0)} + \Delta \varphi^{(2)} + \Delta \varphi^{(1)} + \Delta \varphi^{(3)} = 0$  and using equations (47) and (51), the expression of the shear orientation  $\omega$  merely reduces to

$$\omega = \frac{1}{4} (\varphi^{(0)} + \varphi^{(1)} + \varphi^{(2)} + \varphi^{(3)} - 3\pi). \quad (54)$$

From equations (49) and (50) and given that  $\Delta \theta^{(1)} + \Delta \theta^{(3)} = 0$  and  $\Delta \theta^{(0)} + \Delta \theta^{(2)} = 0$ , we have

$$\theta^{(1)} + \theta^{(3)} = 2 \theta_E (1 - \gamma)^{1/(\varepsilon-2)}, \quad (55)$$

and

$$\theta^{(0)} + \theta^{(2)} = 2 \theta_E (1 + \gamma)^{1/(\varepsilon-2)}. \quad (56)$$

Furthermore, dividing equation (55) by equation (56) simply leads to

$$\frac{\theta^{(1)} + \theta^{(3)}}{\theta^{(0)} + \theta^{(2)}} = \left( \frac{1 - \gamma}{1 + \gamma} \right)^{\frac{1}{\varepsilon-2}}. \quad (57)$$

Before determining  $\varepsilon$  and  $\gamma$ , it is appropriate to determine the angular coordinate of the source, i.e.  $\theta$ . To this end, from equations (47), (51) and (52), we have

$$\Delta \varphi^{(1)} - \Delta \varphi^{(3)} = \varphi^{(1)} - \varphi^{(3)} + \pi = \varphi^{(1,3)} = -\frac{y \cos(\omega - \theta)}{\gamma(1 - \gamma)^{1/(\varepsilon-2)}}, \quad (58)$$

and

$$\Delta \varphi^{(0)} - \Delta \varphi^{(2)} = \varphi^{(0)} - \varphi^{(2)} + \pi = \varphi^{(0,2)} = \frac{y \sin(\omega - \theta)}{\gamma(1 + \gamma)^{1/(\varepsilon-2)}}, \quad (59)$$

where  $\varphi^{(i,i+2)} = (\varphi^{(i)} - \varphi^{(i+2)} + \pi)$ . We note that for the case  $i = 2$ , we have  $\varphi^{(2,4)} = -\varphi^{(0,2)}$  by virtue of  $\varphi^{(4)} = \varphi^{(0)} + 2\pi$  since  $i = 4$  corresponds in fact to  $i = 0$ . Dividing equation (59) by equation (58) and from equation (57), the relative angular coordinate  $\theta$  of the point-like source is found to be

$$\tan(\theta - \omega) = \left( \frac{\varphi^{(0,2)}}{\varphi^{(1,3)}} \right) \left( \frac{\theta^{(0)} + \theta^{(2)}}{\theta^{(1)} + \theta^{(3)}} \right). \quad (60)$$

Up to now, we have thus determined the values of  $\omega$  and  $\theta$  from the only astrometric positions of the lensed images. We shall now proceed with the determination of the remaining model parameters ( $\gamma$ ,  $\varepsilon$ ,  $\theta_E$  and  $\theta_S$ ) in terms of the same observable quantities. To this end, from equations (49), (50) and (53), we have

$$\frac{\theta^{(0)} - \theta^{(1)} + \theta^{(3)} - \theta^{(2)}}{\theta^{(0)} + \theta^{(1)} - \theta^{(3)} - \theta^{(2)}} = \frac{(1 - \gamma) \cos(\omega - \theta) + (1 + \gamma) \sin(\omega - \theta)}{(1 - \gamma) \cos(\omega - \theta) - (1 + \gamma) \sin(\omega - \theta)}. \quad (61)$$

Furthermore, combining equations (55) with (58) and (56) with (59) to express  $\cos(\omega - \theta)$  and  $\sin(\omega - \theta)$  as a function of observable quantities, the value of the shear intensity  $\gamma$  derived from equation (61) takes the form

$$\gamma = \frac{\varphi^{(1,3)} \theta^{(1,3)} - \varphi^{(0,2)} \theta^{(0,2)}}{\varphi^{(1,3)} \theta^{(1,3)} + \varphi^{(0,2)} \theta^{(0,2)}}. \quad (62)$$

where  $\theta^{(i,i+2)} = (\theta^{(i)})^2 - (\theta^{(i+2)})^2$ . From equations (57) and (62), the value of the lens model parameter  $\varepsilon$  is then found to be

$$\varepsilon = \frac{\log\left(\frac{\varphi^{(0,2)}\theta^{(0,2)}}{\varphi^{(1,3)}\theta^{(1,3)}}\right)}{\log\left(\frac{\theta^{(1)}+\theta^{(3)}}{\theta^{(0)}+\theta^{(2)}}\right)} + 2. \quad (63)$$

From equations (55) and (56), the value of the Einstein ring angular radius is given by

$$\theta_E = \frac{1}{2} (\theta^{(i)} + \theta^{(i+2)}) \left\{ \frac{1}{2} \left[ 1 + \left( \frac{\varphi^{(0,2)}\theta^{(0,2)}}{\varphi^{(1,3)}\theta^{(1,3)}} \right)^{(-1)^i} \right] \right\}^{\log\left(\frac{\theta^{(1)}+\theta^{(3)}}{\theta^{(0)}+\theta^{(2)}}\right) / \log\left(\frac{\varphi^{(0,2)}\theta^{(0,2)}}{\varphi^{(1,3)}\theta^{(1,3)}}\right)}, \quad (64)$$

where  $i = 0$  or  $1$ . Finally, from equations (58), (59) and using equations (55) and (56), the radial coordinate of the point-like source turns out to be

$$\theta_S = \frac{1}{2} \left( \frac{\varphi^{(1,3)}\theta^{(1,3)} - \varphi^{(0,2)}\theta^{(0,2)}}{\varphi^{(1,3)}\theta^{(1,3)} + \varphi^{(0,2)}\theta^{(0,2)}} \right) \left[ (\varphi^{(0,2)})^2 (\theta^{(0)} + \theta^{(2)})^2 + (\varphi^{(1,3)})^2 (\theta^{(1)} + \theta^{(3)})^2 \right]^{1/2}. \quad (65)$$

Furthermore, we note that from equations (55), (56), (58), (59) and (62), we have

$$\theta_S \cos\left(\omega - \theta + \frac{i\pi}{2}\right) = (-1)^i \varphi^{(i+1,i+3)} \left( \frac{\varphi^{(0,2)}\theta^{(0,2)} - \varphi^{(1,3)}\theta^{(1,3)}}{\varphi^{(0,2)}\theta^{(0,2)} + \varphi^{(1,3)}\theta^{(1,3)}} \right) \left( \frac{\theta^{(i+1)} + \theta^{(i+3)}}{2} \right). \quad (66)$$

In summary, all model parameters ( $\theta_S$ ,  $\theta$ ,  $\theta_E$ ,  $\varepsilon$ ,  $\gamma$  and  $\omega$ ) can be expressed as functions of the observable quantities  $\theta^{(i)}$  and  $\varphi^{(i)}$ , derived from the only first-order astrometric equations.

### 3.2.2 The amplification ratios

We shall now investigate the amplification relations. Alike for the case of axially symmetric lens models, the relevant observable is also here the amplification ratio  $|\mu^{(i)}/\mu^{(j)}|$  between pairs of lensed images. Considering a four image configuration, we only have three independent amplification ratios which can be expressed as a function of the source position, i.e.  $y$ . We have chosen to show two series of typical curves for the amplification ratio:  $|\mu^{(3)}/\mu^{(2)}|$  (see Fig. 7) and  $|\mu^{(0)}/\mu^{(2)}|$  (see Fig. 8).

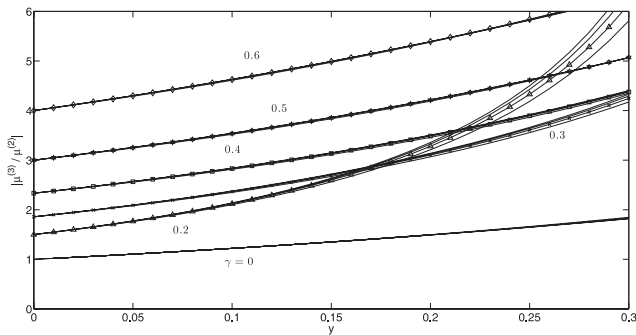


**Figure 7.** The amplification ratio  $|\mu^{(3)}/\mu^{(2)}|$  is plotted as a function of  $y$  for various values of the shear intensity ( $\gamma \in [0, 0.6]$ ) and for various lens models ( $\varepsilon \in \{0, 0.3, 0.6, 0.9\}$ ) with  $\omega = 0$  and  $\theta = \pi/8$ . The various plotted symbols refer to the  $\varepsilon = 0.6$  curve.

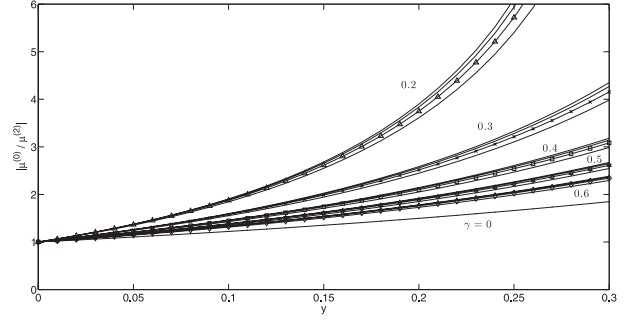


**Figure 8.** The amplification ratio  $|\mu^{(0)}/\mu^{(2)}|$  is plotted as a function of  $y$  for various values of the shear intensity ( $\gamma \in [0, 0.6]$ ) and for various lens models ( $\varepsilon \in \{0, 0.3, 0.6, 0.9\}$ ) with  $\omega = 0$  and  $\theta = \pi/8$ . The various plotted symbols refer to the  $\varepsilon = 0.6$  curve.

First, we observe that the amplification ratio is almost independent on the lens model (i.e. upon  $\varepsilon$ ) when typically  $y < 0.15$ . On the other hand, the former is dependent on the shear intensity  $\gamma$ . In the case of a perfect alignment between the source, the lens and the observer, i.e. for  $y = 0$ , the amplification ratio  $|\mu^{(3)}/\mu^{(2)}|$  evidently depends on the shear intensity ( $\gamma$ ), whereas  $|\mu^{(0)}/\mu^{(2)}| = 1$  for all values of  $\gamma$ . These properties can simply be accounted for from equation (41) where we substitute  $r_0^{(i)}$  and  $\varphi_0^{(i)}$  from equations (47) and (49). That is, the amplification factor for the  $i$ th lensed image reduces to

$$\left(\mu_0^{(i)}\right)^{-1} = 2\gamma(\varepsilon - 2)(\gamma + (-1)^i), \quad (67)$$

and thus the amplification ratio becomes

$$\frac{\mu_0^{(i)}}{\mu_0^{(j)}} = \frac{\gamma + (-1)^i}{\gamma + (-1)^j}, \quad (68)$$

where  $i \in \{0, 1, 2, 3\}$  and  $j \in \{0, 1, 2, 3\}$ . Therefore, for  $y = 0$ , the amplification ratio becomes  $|\mu^{(0)}/\mu^{(2)}| = |\mu^{(1)}/\mu^{(3)}| = 1$  and  $|\mu^{(3)}/\mu^{(2)}| = |\mu^{(1)}/\mu^{(2)}| = |\mu^{(3)}/\mu^{(0)}| = |\mu^{(1)}/\mu^{(0)}| = |(\gamma + 1)/(\gamma - 1)|$  as confirmed from Figs 7 and 8.

In order to express the amplification ratios to first order, it is useful to consider the amplification factor to second order. First, from equation (48) we express the term  $(r^{(i)})^{\varepsilon-2}$  to first order as

$$(r^{(i)})^{\varepsilon-2} = 1 + (-1)^i \gamma - \frac{y}{r_0^{(i)}} \left[ \left( 1 - \frac{\Delta r^{(i)}}{r_0^{(i)}} \right) \cos\left(\omega - \theta + \frac{i\pi}{2}\right) - \sin\left(\omega - \theta + \frac{i\pi}{2}\right) \Delta\varphi^{(i)} \right], \quad (69)$$

where  $\cos[2(\omega - \varphi^{(i)})] \simeq (-1)^i$ ,  $\Delta\varphi^{(i)}$  being defined by equation (52) and  $\Delta r^{(i)}$  by equation (53). On the other hand, after inserting equation (69) into equation (41) and after some obvious simplifications, the amplification factor reduces to

$$\begin{aligned} (\mu^{(i)})^{-1} &= \left(\mu_0^{(i)}\right)^{-1} - \frac{y}{r_0^{(i)}} \left( 1 - \frac{\Delta r^{(i)}}{r_0^{(i)}} \right) \left[ \cos\left(\omega - \theta + \frac{i\pi}{2}\right) \right. \\ &\quad \left. - \sin\left(\omega - \theta + \frac{i\pi}{2}\right) \Delta\varphi^{(i)} \right] \left[ A^{(i)}(\gamma, \varepsilon) - (\varepsilon - 1) \frac{y}{r_0^{(i)}} \right. \\ &\quad \left. \left( 1 - \frac{\Delta r^{(i)}}{r_0^{(i)}} \right) \left[ \cos\left(\omega - \theta + \frac{i\pi}{2}\right) - \sin\left(\omega - \theta + \frac{i\pi}{2}\right) \Delta\varphi^{(i)} \right] \right], \end{aligned} \quad (70)$$

where we denote  $A^{(i)}(\gamma, \varepsilon) = (\varepsilon - 2) + (-1)^i \gamma (3\varepsilon - 4)$ , a function of  $\varepsilon$  and  $\gamma$ . After inserting equations (52) and (53) into equation (70) and considering up to second-order terms only, the amplification factor reduces to

$$\begin{aligned} (\mu^{(i)})^{-1} &= (\mu_0^{(i)})^{-1} - \frac{y}{r_0^{(i)}} A^{(i)} \cos\left(\omega - \theta + \frac{i\pi}{2}\right) + \left(\frac{y}{r_0^{(i)}}\right)^2 \\ &\left[ (\varepsilon - 1) \cos^2\left(\omega - \theta + \frac{i\pi}{2}\right) + A^{(i)} \left( \frac{\cos^2\left(\omega - \theta + \frac{i\pi}{2}\right)}{(2 - \varepsilon)(1 + (-1)^i \gamma)} \right. \right. \\ &\left. \left. + \frac{\sin^2\left(\omega - \theta + \frac{i\pi}{2}\right)}{2\gamma(-1)^i} \right) \right]. \end{aligned} \quad (71)$$

It is interesting to note that for the case of models without shear, i.e.  $\gamma = 0$ , we recover from equation (71) the amplification ratio previously established (see equation 17). Indeed, for  $\gamma = 0$ , it is easy to prove that  $r_0^{(i)} = 1$ ,  $1/\mu_0^{(i)} = 0$  and  $A^{(i)} = \varepsilon - 2$ . Furthermore, from equations (14), (15) and (53), the indices corresponding to the two brightest lensed images are  $i = 0$  and  $2$ , and we assume  $\omega = \theta$ . That is, the amplification factor of images  $i = 0$  and  $2$  simply reduces to

$$(\mu^{(0)})^{-1} = -y(\varepsilon - 2)(1 - y), \quad (72)$$

$$(\mu^{(2)})^{-1} = y(\varepsilon - 2)(1 + y), \quad (73)$$

and the amplification ratio between the two brightest lensed images becomes

$$\frac{\mu^{(0)}}{\mu^{(2)}} = -\frac{1 + y}{1 - y}, \quad (74)$$

the latter corresponding to equation (17).

For the case of models with shear and from equation (71), we deduce three independent amplification ratios given to first order by

$$\begin{aligned} \frac{\mu^{(1)}}{\mu^{(0)}} &= -\left(\frac{1 + \gamma}{1 - \gamma}\right) \\ &\times \left[ 1 - y \left( \sin(\omega - \theta) \frac{A^{(1)}}{r_0^{(1)}} \mu_0^{(1)} + \cos(\omega - \theta) \frac{A^{(0)}}{r_0^{(0)}} \mu_0^{(0)} \right) \right], \end{aligned} \quad (75)$$

$$\frac{\mu^{(2)}}{\mu^{(0)}} = 1 - y \cos(\omega - \theta) \frac{A^{(0)}}{\gamma(\varepsilon - 2)(1 + \gamma)r_0^{(0)}}, \quad (76)$$

$$\begin{aligned} \frac{\mu^{(3)}}{\mu^{(0)}} &= -\left(\frac{1 + \gamma}{1 - \gamma}\right) \\ &\times \left[ 1 + y \left( \sin(\omega - \theta) \frac{A^{(3)}}{r_0^{(3)}} \mu_0^{(3)} - \cos(\omega - \theta) \frac{A^{(0)}}{r_0^{(0)}} \mu_0^{(0)} \right) \right]. \end{aligned} \quad (77)$$

For the case of a perfect alignment between the source, the lens and the observer, i.e.  $y = 0$ , we recover the amplification ratios given by equation (68). For the general case of a small misalignment between the observer, the lens and the source, the amplification ratio remains a complex function involving all model parameters (see equations 75–77). Unlike for the case of the  $\varepsilon$  family lens models (see equation 17), the expressions of the amplification ratios derived for more complex deflectors turn out to be very model dependent.

### 3.2.3 Time delays and the Hubble parameter

Let us now consider the determination of the value of the Hubble parameter  $H_0$  from the measurement of the time delay  $\Delta t$  between

two lensed image light curves for the case of axially symmetric power-law lens models with an external shear. The time delay is split up into two parts with the first one being the well-known geometrical part  $\Delta t_{\text{geo}}$  and the second one the potential part  $\Delta t_{\text{pot}}$  due to the retardation of the deflected rays caused by the gravitational field of the lens, the so-called *Shapiro effect*. Adopting the same notation for the source and image positions as previously, the time-delay function  $t(x)$  for the  $i$ th image is given by (Narayan & Bartelmann 1996)

$$t(x^{(i)}) = \left(\frac{1 + z_1}{c}\right) \left(\frac{D_{\text{OL}} D_{\text{OS}}}{D_{\text{LS}}}\right) \theta_{\text{E}}^2 \left[ \frac{1}{2} (\mathbf{x} - \mathbf{y})^2 - \hat{\psi}_{\text{tot}}(\mathbf{x}) \right], \quad (78)$$

where  $z_1$  represents the redshift of the lens,  $D_{\text{OL}}$ ,  $D_{\text{OS}}$  and  $D_{\text{LS}}$  represent the usual angular-diameter distances,  $c$  is the speed of light in vacuum and  $\hat{\psi}_{\text{tot}}$  is the total lensing potential, which gradient corresponds to the general deflection angle, apart from an irrelevant constant

$$\hat{\alpha}_{\text{gen}}(\mathbf{x}) = -\nabla_{\mathbf{x}} \hat{\psi}_{\text{tot}} = -\nabla_{\mathbf{x}} \hat{\psi}_{\text{iso}} - \nabla_{\mathbf{x}} \hat{\psi}_{\text{aniso}}. \quad (79)$$

The time delay between images  $i$  and  $j$  is therefore given by

$$\begin{aligned} \Delta t_{i,j} &= \left(\frac{1 + z_1}{c}\right) \left(\frac{D_{\text{OL}} D_{\text{OS}}}{D_{\text{LS}}}\right) \theta_{\text{E}}^2 \left[ \frac{1}{2} (\mathbf{x}^{(j)} - \mathbf{y})^2 - \frac{1}{2} (\mathbf{x}^{(i)} - \mathbf{y})^2 \right. \\ &\left. - \hat{\psi}_{\text{tot}}(r^{(j)}; \varphi^{(j)}) + \hat{\psi}_{\text{tot}}(r^{(i)}; \varphi^{(i)}) \right]. \end{aligned} \quad (80)$$

Since  $\hat{\alpha}_{\text{iso}}(\mathbf{x})$  is independent on the angular coordinate, we deduce  $\nabla_{\mathbf{x}} \hat{\psi}_{\text{iso}} = (\partial \hat{\psi}_{\text{iso}} / \partial r, 0)$  and the expression of the isotropic lensing potential becomes

$$\hat{\psi}_{\text{iso}}(r^{(i)}) = \frac{(r^{(i)})^\varepsilon}{\varepsilon}, \quad (81)$$

for  $\varepsilon \neq 0$  and

$$\hat{\psi}_{\text{iso}}(r^{(i)}) = \ln(r^{(i)}), \quad (82)$$

for  $\varepsilon = 0$ . Since  $\hat{\alpha}_{\text{aniso}}(\mathbf{x}) = -\nabla_{\mathbf{x}} \hat{\psi}_{\text{aniso}}$ , the expression of the anisotropic lensing potential becomes (see equation 38)

$$\hat{\psi}_{\text{aniso}}(r^{(i)}; \varphi^{(i)}) = -\gamma \frac{(r^{(i)})^2}{2} \cos[2(\omega - \varphi^{(i)})]. \quad (83)$$

Furthermore, we note that

$$\begin{aligned} \frac{1}{2} (\mathbf{x}^{(j)} - \mathbf{y})^2 - \frac{1}{2} (\mathbf{x}^{(i)} - \mathbf{y})^2 &= \frac{1}{2} [(r^{(j)})^2 - (r^{(i)})^2] \\ &- y [r^{(j)} \cos(\varphi^{(j)} - \theta) - r^{(i)} \cos(\varphi^{(i)} - \theta)]. \end{aligned} \quad (84)$$

For a small misalignment between the source, the lens and the observer, the position of the  $i$ th image is given by  $r^{(i)} = r_0^{(i)} + \Delta r^{(i)}$  and  $\varphi^{(i)} = \varphi_0^{(i)} + \Delta \varphi^{(i)}$ , where  $r_0^{(i)}$  is defined by equation (49),  $\Delta r^{(i)} = \Delta \theta^{(i)} / \theta_{\text{E}}$  by equation (53),  $\varphi_0^{(i)}$  by equation (47) and  $\Delta \varphi^{(i)}$  by equation (52). For  $\varepsilon \neq 0$  and combining equations (80), (81) and (84) to first order, the time delay between images  $i$  and  $j$  becomes

$$\begin{aligned} \Delta t_{i,j} &= \left(\frac{1 + z_1}{c}\right) \left(\frac{D_{\text{OL}} D_{\text{OS}}}{D_{\text{LS}}}\right) \theta_{\text{E}}^2 \left\{ \left(\frac{\varepsilon - 2}{2\varepsilon}\right) [(r_0^{(j)})^\varepsilon - (r_0^{(i)})^\varepsilon] \right. \\ &\left. - y \left[ r_0^{(j)} \cos(\omega - \theta + j\pi/2) - r_0^{(i)} \cos(\omega - \theta + i\pi/2) \right] \right\}. \end{aligned} \quad (85)$$

It is interesting to note that for images  $i$  and  $i + 2$ , i.e. 0 and 2 or 1 and 3, the time delay simply reduces to

$$\begin{aligned} \Delta t_{i,i+2} &= \left(\frac{1 + z_1}{c}\right) \left(\frac{D_{\text{OL}} D_{\text{OS}}}{D_{\text{LS}}}\right) \theta_{\text{S}} \\ &\times (\theta^{(i)} + \theta^{(i+2)}) \cos(\omega - \theta + i\pi/2). \end{aligned} \quad (86)$$



The latter expression is a simple function of the model parameters which may be retrieved from the linearized astrometric equations. For  $\varepsilon = 0$  corresponding to the point-like mass distribution, and combining equations (80), (82) and (84) to first order, the time delay between images  $i$  and  $j$  becomes

$$\Delta t_{i,j} = \left( \frac{1+z_1}{c} \right) \left( \frac{D_{OL} D_{OS}}{D_{LS}} \right) \theta_E^2 \left[ -\frac{1}{2} \ln \left( \frac{1+(-1)^i \gamma}{1+(-1)^j \gamma} \right) - y \left( r_0^{(j)} \cos(\omega - \theta + j\pi/2) - r_0^{(i)} \cos(\omega - \theta + i\pi/2) \right) \right]. \quad (87)$$

For images  $i$  and  $i+2$ , i.e. 0 and 2 or 1 and 3, the time delay simply reduces to equation (86) as for the case  $\varepsilon \neq 0$ . From the value of the time delay observed between two such lensed images, we may thus deduce the value of the Hubble parameter  $H_0$  in a robust way with the values of  $\theta$ ,  $\gamma$ ,  $\varepsilon$ ,  $\theta_E$  and  $\omega - \theta$  given by equations (60), (62), (63), (64) and (65), respectively.

For the case of a flat universe with  $\Omega_M = 0.3$ ,  $\Omega_\Lambda = 0.7$  and cosmological values for the lens and source redshifts, and from equation (66), equation (86) transforms into

$$H_0 = (1+z_1) \left( \frac{z_s z_1}{z_s - z_1} \right) \left( \frac{F(z_1) F(z_s)}{F(z_s - z_1)} \right) \frac{(-1)^j \varphi^{(i+1, i+3)}}{2 \Delta t_{i, i+2}} (\theta^{(0)} + \theta^{(2)}) \times (\theta^{(1)} + \theta^{(3)}) \left( \frac{\varphi^{(0,2)} \theta^{(0,2)} - \varphi^{(1,3)} \theta^{(1,3)}}{\varphi^{(0,2)} \theta^{(0,2)} + \varphi^{(1,3)} \theta^{(1,3)}} \right), \quad (88)$$

where  $F(z_1)$ ,  $F(z_s)$  and  $F(z_s - z_1)$  have been defined by equation (34).

As a final result, in the case of a small misalignment between the observer, the lens and the source, the Hubble parameter  $H_0$  may be directly and robustly derived from the following observable quantities: the redshifts of the lens and of the source, the time delays and the astrometric positions of the four lensed images with respect to the centre of the gravitational lens.

### 3.2.4 Mass estimation of the deflector

Alike for the case of axially symmetric lens models, we derive a simple expression for the mass  $M(\leq \theta_E)$  of the deflector inside the radius  $\theta_E$  from the expression of the time delays  $\Delta t_{0,2}$  and  $\Delta t_{1,3}$ . From equations (35), (55), (56), (58), (59) and (86), the mass  $M(\leq \theta_E)$  may be expressed as

$$M(\leq \theta_E) = \frac{c^3 \Delta t_{i, i+2}}{8 G (1+z_1)} \frac{(-1)^{(i+1)}}{\varphi^{(i+1, i+3)}} \left( \frac{\varphi^{(1,3)} \theta^{(1,3)} + \varphi^{(0,2)} \theta^{(0,2)}}{\varphi^{(1,3)} \theta^{(1,3)} - \varphi^{(0,2)} \theta^{(0,2)}} \right) \times \left[ \frac{1}{4} \left( 1 + \frac{\varphi^{(0,2)} \theta^{(0,2)}}{\varphi^{(1,3)} \theta^{(1,3)}} \right) \times \left( 1 + \frac{\varphi^{(1,3)} \theta^{(1,3)}}{\varphi^{(0,2)} \theta^{(0,2)}} \right) \right]^{\log \left( \frac{\theta^{(1)} + \theta^{(3)}}{\theta^{(0)} + \theta^{(2)}} \right) / \log \left( \frac{\varphi^{(0,2)} \theta^{(0,2)}}{\varphi^{(1,3)} \theta^{(1,3)}} \right)}. \quad (89)$$

### 3.3 Comparison between the $\varepsilon - \gamma$ and SIE families of models

Another interesting way to investigate four lensed image configuration systems is to study intrinsically elliptical deflectors, in particular the singular isothermal ellipsoid (SIE) (Kormann, Schneider & Bartelmann 1994). Even for the case of a small misalignment between the source, the deflector and the observer, comparison between the SIE and the  $\varepsilon - \gamma$  families of models leads to the conclusion that these models remain strictly distinct, excepted when the alignment is perfect or when the SIE reduces to the SIS model without any shear.

In order to demonstrate the clear distinction between these two families of models, we have used the singular perturbative theory developed by Alard (2007, 2008, 2010) accounting for a small external perturbation, i.e.  $0 < \gamma \ll 1$  and  $0 < f \ll 1$ , where  $f$  represents the axis ratio of the deflection potential isodensity contours. Within that formalism, equation (37) may be expressed to first order as

$$\mathbf{y} = (\kappa_2 dr + \gamma \cos(2\varphi)) \mathbf{u}_r - \gamma \sin(2\varphi) \mathbf{u}_\varphi, \quad (90)$$

for the  $\varepsilon - \gamma$  models, and

$$\mathbf{y} = \left( \kappa_2 dr - \frac{1-f^2}{4} \cos(2\varphi) \right) \mathbf{u}_r + \frac{1-f^2}{2} \sin(2\varphi) \mathbf{u}_\varphi, \quad (91)$$

for the SIE models, where  $\mathbf{u}_r$  and  $\mathbf{u}_\varphi$  represent, respectively, the radial and orthoradial direction in polar coordinates, and  $\kappa_2 = 2 - 2\kappa$ , with  $\kappa$  standing for the lensing convergence of the unperturbed symmetrical mass distribution. A straightforward comparison between equations (90) and (91) shows that because both the  $(1-f^2)/4$  and  $(1-f^2)/2$  factors appear in equation (91),  $\gamma$  cannot be merely associated with  $(1-f^2)/4$  and the two families of models are thus shown to be very distinct, even for a small misalignment between the source, the deflector and the observer, and for small values of  $\gamma$  and  $f$ .

Alike for the  $\varepsilon - \gamma$  models, we have derived, for the SIE models, simple relations linking all model parameters and positions of the lensed images, for the case of a small misalignment. Furthermore, from equation (80), the time delay between images  $i$  and  $j$  derived for the case of the SIE models reduces to

$$\Delta t_{i, i+2} = \left( \frac{1+z_1}{c} \right) \left( \frac{D_{OL} D_{OS}}{D_{LS}} \right) \times \theta_S (\theta^{(i)} + \theta^{(i+2)}) \cos(\omega - \theta + i\pi/2), \quad (92)$$

which is identical to equation (86). As a consequence, despite of the difference between these two classes of models, we have derived the same expression for the time delay which is only a function of observable quantities and source position. However, still for a small misalignment and for the case of SIE models, we easily deduce that

$$\theta_S \cos(\omega - \theta + i\pi/2) = \frac{1}{2} (\theta^{(i)} - \theta^{(i+2)}). \quad (93)$$

After substituting equation (93) into equation (92), the time delay between images  $i$  and  $i+2$  becomes

$$\Delta t_{i, i+2} = \left( \frac{1+z_1}{2c} \right) \left( \frac{D_{OL} D_{OS}}{D_{LS}} \right) [(\theta^{(i)})^2 - (\theta^{(i+2)})^2]. \quad (94)$$

First, the latter equation, which is equivalent to equation (29), holds for more general isothermal models (Witt et al. 2000) as we have previously discussed in Section 2. Secondly, since equations (66) and (93) remain very distinct, the determination of  $\theta_S \cos(\omega - \theta + i\pi/2)$  essentially depends on the considered family of models. Although equation (92) seems to be valid irrespective of the considered models, the determination of the value of the Hubble parameter, by use of observable quantities only, depends on the adopted family of models. Therefore, we should always clearly distinguish the class of models that shows the best agreement with the observed gravitational lens systems, even for a small misalignment between the source, the deflector and the observer. For this purpose, the fitting of models to observational data consists in making use of equations (54), (60), (62), (63), (64) and (65), and similar corresponding equations for SIE lens models. This procedure is more straightforward than numerical fitting (e.g. see Evans & Witt 2003) but requires very well selected gravitational lens systems, i.e. nearly symmetric lensed image configurations.

## 4 VALIDITY RANGE OF THE METHOD

### 4.1 Errors caused by the first-order equations

We first propose in this section to test the validity range of the approximation  $r^{(i)} = r_0^{(i)} + \Delta r^{(i)}$  and  $\varphi^{(i)} = \varphi_0^{(i)} + \Delta\varphi^{(i)}$  while using equations (52) and (53). For the case  $y = 0$ , i.e. for a perfect alignment between the source, the deflector and the observer, the astrometric errors of the model are equal to zero. As soon as the source is no more perfectly aligned, we introduce errors in the determination of the lensed image positions due to the use of the first-order solutions, as compared with the exact solutions. These errors become very large as the source gets closer to the tangential caustic curve. Consequently, we may estimate the validity range of equations (50) and (51) from the derivation of the expression of the smallest acceptable distance between the source and the tangential caustic curve. We denote  $(y_{c,m}; \theta_{c,m})$  the polar coordinates of the tangential caustic point which is the closest to the centre of the coordinate system, in the first quadrant (see Fig. 9). Moreover, from equation (45), we deduce

$$y_c^2 = r_c^2 \left\{ [1 - (r_c)^{\varepsilon-2}]^2 + \gamma^2 + 2\gamma [1 - (r_c)^{\varepsilon-2}] \cos [2(\varphi_c - \omega)] \right\}. \quad (95)$$

The critical point coordinates  $(r_{c,m}; \varphi_{c,m})$  associated with  $(y_{c,m}; \theta_{c,m})$  are obtained by deriving equation (95) with respect to  $\varphi_c$  and determining the extremum of  $y_c^2$ . We find that

$$(r_{c,m}; \varphi_{c,m}) = \left( 1; -\frac{1}{2} \arccos \left[ \frac{\gamma}{\varepsilon - 2} \right] + \omega \right). \quad (96)$$

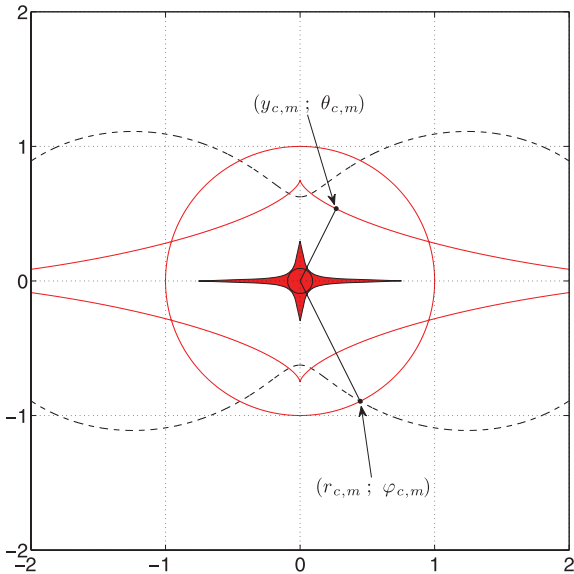


**Figure 9.** Illustration of the shaded source area projected in the lens plane across which the corresponding astrometric errors induced by the use of the first-order equations remain smaller or equal to  $\sigma_{\theta^{(i)}}$ . The small circle embedded inside this area has its radius equal to  $0.15\gamma$  and delimits the most restrictive region of the projected source position for which our method works well. The diamond-shaped solid line represents the tangential caustic curve and the peanut-shaped dashed line represents its associated critical curve. The solid circle (radius equals 1) represents the radial caustic curve, whereas its associated critical curve corresponds to a point located at  $(0, 0)$ . The illustrated model refers to the following parameters:  $\varepsilon = 1$ ,  $\gamma = 0.6$ ,  $\omega = 0$  and  $\theta_E = 1.0$  arcsec.

After substituting equation (96) into equations (45) and (95), the coordinates of the tangential caustic point  $(y_{c,m}; \theta_{c,m})$  are found to be

$$(y_{c,m}; \theta_{c,m}) = \left( \gamma; \frac{1}{2} \arccos \left[ \frac{\gamma}{\varepsilon - 2} \right] - \omega \right), \quad (97)$$

Hence, the smallest distance between the tangential caustic curve and the lens centre is equal to  $\gamma$ , as shown in Fig. 9. Furthermore, we note that for a fixed value of  $y$ , the distance from the tangential curve is always the smallest for  $\theta = \theta_{c,m}$ . As a consequence, the most restrictive condition on the source position, which can be expressed irrespective of  $\theta$  and  $\varepsilon$ , takes the form  $0 \leq y < \zeta\gamma$ , where  $\zeta \in \mathbb{R}^+$  has to be determined in order to account for realistic errors on the positions of the lensed images. The relative astrometric positions of the lensed images are usually known with a very high accuracy. According to recent *Hubble Space Telescope* data, the absolute error in the relative astrometry is of the order of  $\sim 0.0005$  arcsec (e.g. Courbin et al. 2011). However, the system of coordinates used in this paper is centred on the deflector’s gravity centre, usually not better precisely known than  $\sim 0.003$  arcsec. Indeed, the photometric centre and the gravity centre may not correspond exactly. Hence, we assume a perfect position of the deflector centre and a relevant error of  $\sigma_{\theta^{(i)}} \simeq 0.003$  arcsec on the positions of the lensed images. Finally, the numerically derived value of  $\zeta$  for which the astrometric errors induced from the use of the first-order model are smaller or equal to  $\sigma_{\theta^{(i)}}$  is found to be equal to  $\zeta = 0.15$ . In conclusion, a simple condition on  $y$  which validates the approximation defined by equations (52) and (53) is given by

$$0 \leq y < 0.15\gamma. \quad (98)$$

Since the tangential caustic curve is not a circle but a diamond-shaped curve, we can simulate a less restrictive condition on  $y$  which depends on the angular coordinate, i.e.  $\theta$ . We have illustrated this condition for the case of the SIS model, i.e.  $\varepsilon = 1$ , in Fig. 9 see the shaded area.

### 4.2 Corresponding errors on the Hubble parameter

For the case of a small misalignment between the source, the lens and the observer, we have derived in the previous section a simple equation (see equation 88) for the Hubble parameter in terms of observable quantities: the redshifts of the lens and the source, the time delays between images  $i$  and  $i + 2$ , and the astrometric positions  $(\theta^{(i)}, \varphi^{(i)})$  of the four lensed images. We propose in the remainder of this section to test the validity range of equation (88) when deriving the value of the Hubble parameter. For this purpose, we find from equation (80) that the exact value of the Hubble parameter is

$$H_0 = \Xi(z, \Delta t_{i,i+2}) \theta_E^2 \left[ \frac{1}{2} (\mathbf{x}^{(j)} - \mathbf{y})^2 - \frac{1}{2} (\mathbf{x}^{(i)} - \mathbf{y})^2 - \hat{\psi}_{\text{tot}}(r^{(j)}; \varphi^{(j)}) + \hat{\psi}_{\text{tot}}(r^{(i)}; \varphi^{(i)}) \right], \quad (99)$$

where

$$\Xi(z, \Delta t_{i,i+2}) = \frac{1 + z_1}{\Delta t_{i,i+2}} \left( \frac{z_s z_1}{z_s - z_1} \right) \left( \frac{F(z_1)F(z_s)}{F(z_s - z_1)} \right). \quad (100)$$

We have then calculated for various positions of the source with respect to the source caustics the relative error affecting  $H_0$ . This relative error corresponds to the absolute value of the difference between the value of  $H_0$  estimated from our first-order relations (see equation 88) and that given by equation (99), divided by the latter value. For an easy to understand visualization, we have represented

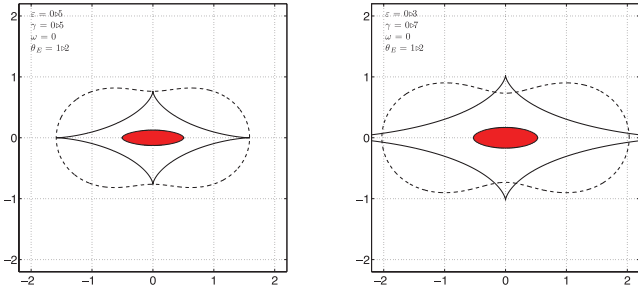


**Figure 10.** Illustration of the shaded source area projected in the deflector plane across which the relative error on  $H_0$  due to the use of first-order equations is smaller or equal to 1 per cent from the correct value. The left-hand panel corresponds to the following model parameters:  $\varepsilon = 0.5$ ,  $\gamma = 0.5$ ,  $\omega = 0$  and  $\theta_E = 1.2$  arcsec, whereas on the right-hand panel:  $\varepsilon = 0.3$ ,  $\gamma = 0.7$ ,  $\omega = 0$  and  $\theta_E = 1.2$  arcsec. The dashed lines represent the critical curves and the solid lines represent their associated caustic curves.

in Fig. 10 the area of the caustics projected in the deflector plane across which the error is smaller or equal to 1 per cent for two different sets of model parameters. We naturally conclude that this way of proceeding allows us to quantify the acceptable range of slight misalignment between the source, the lens and the observer.

Furthermore, considering that our first-order equations are applicable, we have estimated the errors affecting the value of  $H_0$  due to measurement uncertainties on the observed lensed image positions and that of the deflector. For this purpose, we have assumed a set of model parameters ( $\varepsilon$ ,  $\gamma$ ,  $\omega$ ,  $\theta_S$ ,  $\theta$  and  $\theta_E$ ) which we used to generate exact image positions  $(\theta^{(i)}, \varphi^{(i)})$ . Afterwards, using a Monte Carlo method with Gaussian distributed pseudo-random numbers around the exact image positions and deflector gravity centre with a  $\sigma_{\theta^{(i)}} = 0.003$  arcsec standard deviation, we have retrieved all model parameters at each step from equations (54), (60), (62), (63), (64) and (65). Note that at each step, we have searched the best deflector gravity centre by covering a 0.001 arcsec grid step size around the theoretical gravity centre position. In Fig. 11, we illustrate the distributions of the derived parameter values considering 50 000 simulations. In order to evaluate the error affecting the derived parameter values, we have fitted with a Gaussian model all the observed distributions. The fitting results are shown in Table 1. From the model parameter fit results and from equation (88), we have estimated the standard deviation affecting the Hubble parameter determination, assuming  $z_l = 0.4546$ ,  $z_s = 1.689$ ,  $\Delta t_{0.2} = 6.4 \pm 0.0$  d,  $\Omega_\Lambda = 0.7$  and  $\Omega_M = 0.3$ . In conclusion, we find that the Hubble parameter could be determined with a mean standard deviation equal to  $\sigma_{H_0} = 1.3 \text{ km s}^{-1} \text{ Mpc}^{-1}$  which merely reflects the adopted astrometric uncertainties (see Fig. 12).

## 5 CONCLUSIONS

We have shown in this paper that for the case of relatively symmetric lensed image configuration systems, corresponding to power-law axially symmetric deflector models and to a very small misalignment between the background source, the foreground lens and the observer, it is possible to determine the Hubble parameter value irrespectively of the power-law slope  $\varepsilon$ . First, for the case of axially symmetric deflectors, we have derived two straightforward linear equations linking the source position  $\theta_S$ , the power-law slope  $\varepsilon$ , the Einstein ring angular radius  $\theta_E$ , and the lensed image positions  $\theta^{(1)}$  and  $\theta^{(2)}$  (see equations 23 and 24). Furthermore, we

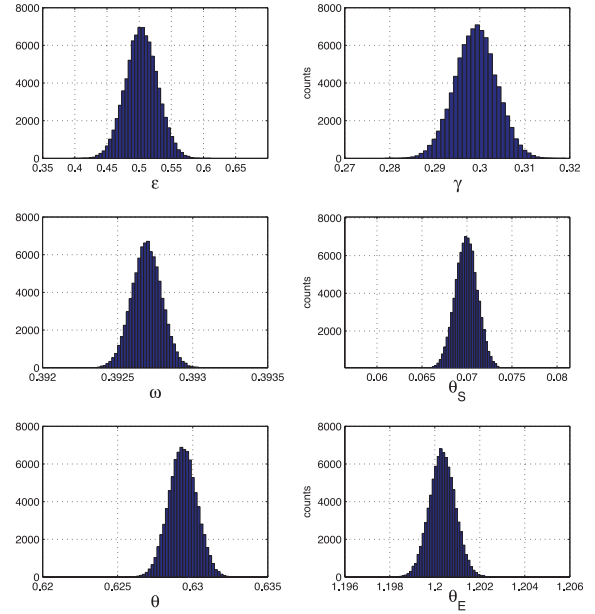


**Figure 11.** Distributions of the model parameter values determined using the first-order equations applied to 50 000 Monte Carlo gravitational lens simulations. These bell-shaped distributions can be fitted with a normal distribution which central values represent the values of the model parameters. The exact values of the parameters used to generate the exact image positions of the simulated gravitational lens systems were in this case  $\varepsilon = 0.5$ ,  $\gamma = 0.3$ ,  $\omega = \pi/8$ ,  $\theta_S = 0.07$ ,  $\theta = \pi/5$  and  $\theta_E = 1.2$  arcsec. The fitting results are shown in Table 1.

**Table 1.** Fit results.

Parameter	Value	Fit value	$\sigma$
$\varepsilon$	0.5	0.5037	0.0247
$\gamma$	0.3	0.2991	0.0046
$\omega$	$\pi/8$	0.3927	0.0001
$\theta_S$	0.07	0.0699	0.0012
$\theta$	$\pi/5$	0.6293	0.0009
$\theta_E$	1.2	1.2000	0.0009

have shown that the amplification ratio  $\mu^{(1)}/\mu^{(2)}$  is only a function of the normalized source position  $\theta_S/\theta_E$ , irrespectively of  $\varepsilon$ . As a result, for such symmetric lensed image configurations, there exists a straightforward relation between  $H_0$  and  $\Delta t$  that only involves the observable quantities  $\theta^{(1)}$ ,  $\theta^{(2)}$ ,  $\mu^{(1)}/\mu^{(2)}$ , and the lens and source redshifts, irrespectively of the value of the power-law slope  $\varepsilon$ .

For more realistic lens mass distributions with shear, the so-called  $\varepsilon - \gamma$  models, and for the case of a nearly perfect alignment between the observer, the deflector and the point-like source, all lens model parameters can be directly derived from the first-order astrometric equations. In the case of a small misalignment, typically  $y < 0.15\gamma$ , the astrometric equations lead to eight linear equations from which we can deduce all values of the lens model parameters. The expression of the time delay leads to three additional independent linear equations which only depend on the source position and on the lens model parameters. In particular, two of these three equations lead to a very simple dependence of the Hubble parameter



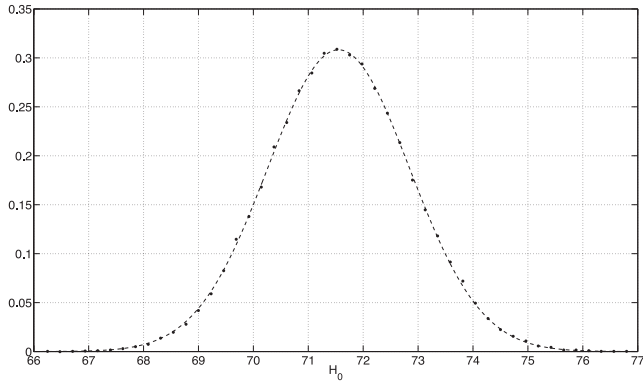


**Figure 12.** Probability distribution of the Hubble parameter  $H_0$  evaluated from equation (88) and from the derived lens model parameters (see Table 1). The mean value of  $H_0$  essentially depends on the exact value of the time delay between the two lensed images. In this case, the standard deviation obtained is  $\sigma_{H_0} = 1.3 \text{ km s}^{-1} \text{ Mpc}^{-1}$  and essentially reflects the adopted astrometric uncertainties on the image positions, i.e.  $\sigma_{\theta(i)} = 0.003 \text{ arcsec}$ .

versus the observed time delay (see equation 86). However, comparison between the  $\varepsilon - \gamma$  and SIE families of models leads to the conclusion that these models remain most often distinct. From this observation, we should succeed in retrieving which family of lens models shows the best agreement with the observed gravitational lens systems. Indeed, even if equation (86) holds for both families of models ( $\varepsilon - \gamma$ , SIE), the determination of  $\theta_S \cos(\omega - \theta + i\pi/2)$  from the observed positions of the lensed images critically depends on the correctly identified lens model (see equations 66 and 93). In Section 4, we have tested the robustness of the determination of the value of  $H_0$  as a function of the degree of misalignment between the source, the lens and the observer and the  $\varepsilon - \gamma$  gravitational lens model parameters. Assuming a flawless determination of the time delay between two lensed images, i.e.  $\sigma_{\Delta t} = 0$ , the standard deviation found is  $\sigma_{H_0} = 1.3 \text{ km s}^{-1} \text{ Mpc}^{-1}$  and only reflects the adopted astrometric uncertainties, i.e.  $\sigma_{\theta(i)} = 0.003 \text{ arcsec}$ . In the near future, we intend to model known gravitational lens systems which look nearly symmetric with the two families of deflectors ( $\varepsilon - \gamma$ , SIE) discussed in this paper. We shall select the best ones

in order to derive the value of  $H_0$  using the relative lensed image positions and the measured time delays.

## ACKNOWLEDGMENTS

OW thanks the Belgian National Fund for Scientific Research (FNRS). JS and OW acknowledge support from the Communauté française de Belgique – Actions de recherche concertées – Académie universitaire Wallonie-Europe, from the ESA PRODEX Programme ‘Gaia’, and from the Belgian Federal Science Policy Office.

## REFERENCES

- Alard C., 2007, MNRAS, 382, 58  
 Alard C., 2008, MNRAS, 388, 375  
 Alard C., 2010, A&A, 513, A39  
 Borgeest U., 1985, MPA Rep., 215, 13  
 Chang K., Refsdal S., 1984, A&A, 132, 168  
 Courbin F. et al., 2011, A&A, 536, A53  
 Erdl H., 1992, in Kayser R., Schramm T., Nieser L., eds, Lecture Notes in Physics, Vol. 406, Gravitational Lenses. Springer-Verlag, Berlin, p. 368  
 Etherington I. M. H., 1933, Philosophical Magazine, 15, 761  
 Evans W. N., Witt H. J., 2003, MNRAS, 345, 1351  
 Falco E. E., Gorenstein M. V., Shapiro I. I., 1985, ApJ, 289, L1  
 Kormann R., Schneider P., Bartelmann M., 1994, A&A, 284, 285  
 Kovner I., 1987, ApJ, 312, 22  
 Narayan R., Bartelmann M., 1996, preprint (arXiv:astro-ph/9606001)  
 Peebles P. J. E., 1993, Principles of Physical Cosmology. Princeton Univ. Press, Princeton  
 Perlmutter S. et al., 1999, ApJ, 517, 565  
 Refsdal S., 1964a, MNRAS, 128, 295  
 Refsdal S., 1964b, MNRAS, 128, 307  
 Refsdal S., Surdej J., 1994, Rep. Progress Phys., 57, 117  
 Schneider P., 1984, A&A, 140, 119  
 Schneider P., Ehlers J., Falco E. E., 1992, Gravitational Lenses. Springer-Verlag, Berlin  
 Witt H. J., Mao S., Keeton C. R., 2000, ApJ, 544, 98

This paper has been typeset from a  $\text{\TeX}/\text{\LaTeX}$  file prepared by the author.



## 2.3 Derivation of Eqs. (96) and (97) proposed in Paper I

In the present section, we derive in details the expression of the polar coordinates  $(y_{c,m}; \theta_{c,m})$  of the tangential caustic point which is the closest to the center of the coordinate system. To this end, we also derive its associated critical point located at  $(r_{c,m}; \varphi_{c,m})$ . These results correspond to Eqs. (96) and (97) in Paper I. The value of  $y_{c,m}$  corresponds to the smallest distance between the tangential caustic curve and the center of the deflector. To start with, we recall that :

$$y_c^2 = r_c^2 \left\{ \left[ 1 - (r_c)^{\varepsilon-2} \right]^2 + \gamma^2 + 2\gamma \left[ 1 - (r_c)^{\varepsilon-2} \right] \cos [2(\varphi_c - \omega)] \right\}, \quad (2.1)$$

where  $r_c$  is defined by :

$$r_c(\varphi_c) = \left[ \frac{-\Gamma(\varphi_c) \pm \sqrt{\Gamma(\varphi_c)^2 - 4(1 - \gamma^2)(\varepsilon - 1)}}{2(1 - \gamma^2)} \right]^{\left(\frac{1}{2-\varepsilon}\right)}, \quad (2.2)$$

and  $\Gamma(\varphi_c)$  :

$$\Gamma(\varphi_c) = (2 - \varepsilon) (1 - \gamma \cos [2(\omega - \varphi_c)]) - 2. \quad (2.3)$$

The approach is the following. We first deduce the expression of  $r_{c,m}(\varphi_c)$  in terms of  $\varphi_c$  by setting the derivative of Eq. (2.1) with respect to  $r_c$  equal to zero. Let us denote this term by  $r_{c,m}^{(\varphi)} \equiv r_{c,m}(\varphi_c)$ . Then, we insert the expression of  $r_{c,m}^{(\varphi)}$  into Eq. (2.1) which, after having been derivated with respect to  $\varphi_c$  and set equal to zero, leads to the determination of  $\varphi_{c,m}$  in terms of the model parameters  $\varepsilon$  and  $\gamma$ . Finally, we obtain successively the expressions of  $r_{c,m}$ ,  $y_{c,m}$  and  $\theta_{c,m}$ .

The derivative of Eq. (2.1) with respect to  $r_c$  leads to :

$$\frac{d(y_c^2)}{dr_c} = (\varepsilon - 1) r_c^{2(\varepsilon-2)} - \varepsilon A(\varphi_c) r_c^{\varepsilon-2} + B(\varphi_c), \quad (2.4)$$

where the functions  $A(\varphi_c)$  and  $B(\varphi_c)$  are defined by :

$$\begin{cases} A(\varphi_c) = 1 + \gamma \cos(\tilde{\varphi}), \\ B(\varphi_c) = 1 + \gamma^2 + 2\gamma \cos(\tilde{\varphi}), \end{cases} \quad (2.5)$$

where we have adopted the notation  $\tilde{\varphi} = 2(\varphi_c - \omega)$ . The expression of  $r_{c,m}^{(\varphi)}$  can then be deduced from Eq. (2.4) after having solved the following equation :

$$(\varepsilon - 1) \left( r_{c,m}^{(\varphi)} \right)^{2(\varepsilon-2)} - \varepsilon A(\varphi_c) \left( r_{c,m}^{(\varphi)} \right)^{(\varepsilon-2)} + B(\varphi_c) = 0 . \quad (2.6)$$

From the latter equation, the expression of  $r_{c,m}^{(\varphi)}$  can be simply expressed as :

$$r_{c,m}^{(\varphi)} = \left( \frac{\varepsilon A(\varphi_c) \pm \sqrt{\varepsilon^2 A^2(\varphi_c) - 4B(\varphi_c)(\varepsilon - 1)}}{2B(\varphi_c)} \right)^{1/(2-\varepsilon)} . \quad (2.7)$$

As a first step, we consider the particular case  $\varepsilon = 1$  which corresponds to the SIS family of models. For such a value of  $\varepsilon$ , the expression of  $r_{c,m}^{(\varphi)}$  takes a very simple form which allows to straightforwardly derive the expression of  $y_{c,m}$ . Without loss of generality, we fix the orientation of the system of coordinates to  $\omega = 0$ .

### 2.3.1 Determination of $y_{c,m}$ for the case of $\varepsilon = 1$ (SIS) and $\omega = 0$

For the case of  $\varepsilon = 1$ , Eq. (2.7) simply reduces to  $r_{c,m}^{(\varphi)} = A(\varphi_c)/B(\varphi_c)$ , which constitutes the unique non-trivial solution. After substituting the latter equation into Eq. (2.1), the expression of  $y_{c,m}$  as a function of  $\varphi_c$  takes the form :

$$y_c^2 = \frac{\gamma^2 \sin^2(2\varphi_c)}{B(\varphi_c)} . \quad (2.8)$$

The derivative of the latter equation with respect to  $\varphi_c$  leads to :

$$\frac{d(y_c^2)}{d\varphi_c} = \frac{\gamma \cos^2(2\varphi_c) + (1 + \gamma^2) \cos(2\varphi_c) + \gamma}{B^2(\varphi_c)} . \quad (2.9)$$

After setting equal to zero the latter equation, we deduce the expression of  $\varphi_{c,m}$  :

$$\cos(2\varphi_{c,m}) = -\gamma . \quad (2.10)$$

As a result, after inserting the value of  $\varphi_{c,m}$  from the latter equation respectively into Eqs. (2.7) and (2.1), we obtain :

$$\begin{cases} r_{c,m} = 1 , \\ y_{c,m} = \gamma . \end{cases} \quad (2.11)$$

Making use of Eq. (45) from Paper I together with Eq. (2.11), the angular coordinate  $\theta_{c,m}$  is simply given by  $\theta_{c,m} = -\varphi_{c,m}$ .

### 2.3.2 Determination of $y_{c,m}$ for the case $0 \leq \varepsilon \leq 1$ and $\omega = 0$

Let us first define the variable  $\rho = r_c^{2-\varepsilon}$ . Making use of the definition of  $\rho$ , the expression of  $y_c^2$  transforms into :

$$y_c^2 = \rho^{\frac{2(\varepsilon-1)}{2-\varepsilon}} \left( B(\varphi_c) \rho^2 - 2 A(\varphi_c) \rho + 1 \right) . \quad (2.12)$$

After inserting Eq. (2.7) into the term in brackets of the latter equation, we obtain :

$$y_c^2 = \rho^{\frac{2(\varepsilon-1)}{2-\varepsilon}} \left( \frac{\varepsilon - 2}{B} \right) \left( \frac{\varepsilon A^2}{2} - B + \frac{A}{2} \sqrt{\varepsilon^2 A^2 - 4(\varepsilon - 1)B} \right) , \quad (2.13)$$

$$\equiv \rho^{\frac{2(\varepsilon-1)}{2-\varepsilon}} \Omega(\varphi_c) , \quad (2.14)$$

where we have adopted the notation  $A(\varphi_c) \equiv A$  and  $B(\varphi_c) \equiv B$ . The next step consists in taking the derivative of the latter equation with respect to  $\varphi_c$  and setting the result equal to zero. Such a calculus leads to :

$$2 \left( \frac{\varepsilon - 1}{2 - \varepsilon} \right) \frac{d\rho(\varphi_{c,m})}{d\varphi_c} \Omega(\varphi_{c,m}) + \rho(\varphi_{c,m}) \frac{d\Omega(\varphi_{c,m})}{d\varphi_c} = 0 , \quad (2.15)$$

which solution leads to the determination of  $\varphi_{c,m}$ . Let us enumerate some intermediate results.

We have :

$$\frac{d\rho(\varphi_{c,m})}{d\varphi_c} = -\frac{\gamma \sin(2\varphi_{c,m})}{B^2} \left[ \varepsilon (\gamma^2 - 1) + \frac{1}{\sqrt{K}} \left( \varepsilon^2 A (\gamma^2 - 1) + 4(\varepsilon - 1)B \right) \right] , \quad (2.16)$$

and

$$\frac{d\Omega(\varphi_{c,m})}{d\varphi_c} = -\frac{2\gamma \sin(2\varphi_{c,m})}{B^2} \left( \frac{\varepsilon - 2}{2} \right) \left[ 2 \varepsilon A(B - A) + \sqrt{K}(\gamma^2 - 1) + \frac{AB}{\sqrt{K}} \left( \varepsilon^2 A - 4(\varepsilon - 1) \right) \right] , \quad (2.17)$$

where the function  $K \equiv K(\varphi_{c,m})$  is defined by :

$$K = \varepsilon^2 A^2 - 4 B (\varepsilon - 1) . \quad (2.18)$$

Let us notice that the definition of  $K$  implies that the expression of  $\Omega(\varphi_c)$  reduces to :

$$\Omega(\varphi_c) = \frac{\varepsilon A^2}{2} - B + \frac{A}{2} \sqrt{K}. \quad (2.19)$$

Substituting Eqs. (2.16) and (2.17) into Eq. (2.15), we obtain :

$$\begin{aligned} T^3 (\gamma^2 - 1)(2 - \varepsilon) + 2T^2 \varepsilon A \left[ B (\varepsilon - 1) - A (3\varepsilon - 4) \right] - 16 (\varepsilon - 1)^2 B^2 \\ + 4TB (\varepsilon - 1) \left[ \varepsilon (3A - B) + 2A (\varepsilon - 2) \right] = 0, \end{aligned} \quad (2.20)$$

where we have defined the function  $T = \varepsilon A + \sqrt{K}$ . The latter equation constitutes a polynomial of the third order in terms of  $T$ . We may use the Bézout's method which states that solutions of the third order polynomial equation  $\beta_0 + \beta_1 T + \beta_2 T^2 + \beta_3 T^3$  can be expressed as linear combinations of the cube root of unity, denoted by :

$$J = -\frac{1}{2} + \frac{\sqrt{3}}{2} \iota, \quad (2.21)$$

where  $\iota$  corresponds to the imaginary unit. Let us denote by  $\tilde{T}$  one particular solution of Eq. (2.20), we then have :

$$\tilde{T} = \alpha_0 + \alpha_1 J + \alpha_2 J^2, \quad (2.22)$$

where the coefficients  $\alpha_i$  are, of course, functions of  $\varphi_{c,m}$ . According to the Bézout's method which gives mathematical relationships between the coefficients  $\alpha_i$  and  $\beta_i$ , we obtain the system of linear equations :

$$\left\{ \begin{aligned} \frac{2\varepsilon A \left[ B (\varepsilon - 1) - A (3\varepsilon - 4) \right]}{(\gamma^2 - 1)(2 - \varepsilon)} &= -3\alpha_0, \\ \frac{4B (\varepsilon - 1) \left[ \varepsilon (3A - B) + 2A (\varepsilon - 2) \right]}{(\gamma^2 - 1)(2 - \varepsilon)} &= 3\alpha_0^2 - 3\alpha_1\alpha_2, \\ -\frac{16 (\varepsilon - 1)^2 B^2}{(\gamma^2 - 1)(2 - \varepsilon)} &= 3\alpha_0\alpha_1\alpha_2 - (\alpha_0^3 + \alpha_1^3 + \alpha_2^3). \end{aligned} \right. \quad (2.23)$$

The inversion of these equations leads to the expression of  $\alpha_i$  in terms of  $A$  and  $B$ , hence of  $\varphi_{c,m}$  implicitly :

$$\begin{cases} \alpha_0 = -\frac{2\varepsilon A [B(\varepsilon - 1) - A(3\varepsilon - 4)]}{3(\gamma^2 - 1)(2 - \varepsilon)}, \\ \alpha_1 = \delta_1 - \delta_2 \iota, \\ \alpha_2 = \delta_1 + \delta_2 \iota, \end{cases} \quad (2.24)$$

where the function  $\delta_i$  is given in such a way that the following equality is satisfied :

$$-\delta_1 + \delta_2 \sqrt{3} = \frac{2}{3} \left( -A + 3B - \frac{2A}{\varepsilon - 2} + \frac{\varepsilon A(B - 3A)}{1 - \gamma^2} \right). \quad (2.25)$$

After substituting Eq. (2.24) into Eq. (2.22) and noticing that  $(\delta_1 - \delta_2 \iota) J + (\delta_1 - \delta_2 \iota) J^2 = -\delta_1 + \delta_2 \sqrt{3}$ , the solution  $\tilde{T}$  of Eq. (2.20) simply reduces to :

$$\tilde{T} = -\frac{2\varepsilon A [B(\varepsilon - 1) - A(3\varepsilon - 4)]}{3(\gamma^2 - 1)(2 - \varepsilon)} + \frac{2}{3} \left( -A + 3B - \frac{2A}{\varepsilon - 2} + \frac{\varepsilon A(B - 3A)}{1 - \gamma^2} \right), \quad (2.26)$$

$$= \frac{2}{3(2 - \varepsilon)(\gamma^2 - 1)} (6AB(\varepsilon - 2) + 3B^2(2 - \varepsilon)), \quad (2.27)$$

$$= 2B. \quad (2.28)$$

Reminding that  $T = \varepsilon A + \sqrt{K}$ , together with Eq. (2.28), the next step consists in the determination of the solution of the equation

$$2B = \varepsilon A + \sqrt{\varepsilon^2 A^2 - 4(\varepsilon - 1)B}, \quad (2.29)$$

with respect to  $\varphi_{c,m}$ . Therefore, we obtain the expression of  $\varphi_{c,m}$  as a function of  $\varepsilon$  and  $\gamma$  :

$$\cos(2\varphi_{c,m}) = \frac{\gamma}{\varepsilon - 2}. \quad (2.30)$$

For the case  $\varepsilon = 1$ , i.e. for the SIS lens model, we retrieve the solution derived in Eq. (2.10). As a result, after substituting Eq. (2.30) respectively into Eqs. (2.7) and (2.1), we obtain :

$$\begin{cases} r_{c,m} = 1, \\ y_{c,m} = \gamma. \end{cases} \quad (2.31)$$

We note that from Eq. (2.29) and the definition of  $\rho$ , we straightforwardly deduce that  $r_{c,m} = 1$ . Finally, making use of Eq. (45) from Paper I together with Eq. (2.31), the angular coordinate  $\theta_{c,m}$  is simply given by  $\theta_{c,m} = -\varphi_{c,m}$ .





**2.4** Paper II

---

# **Asymptotic solutions for the case of SIE lens models and application to the quadruply imaged quasar Q2237+0305**

O. Wertz and J. Surdej

*Monthly Notices of the Royal Astronomical Society*, 2014, submitted.

**Asymptotic solutions for the case of SIE lens models and application to the quadruply imaged quasar Q2237+0305**

Journal:	<i>Monthly Notices of the Royal Astronomical Society</i>
Manuscript ID:	Draft
Manuscript type:	Main Journal
Date Submitted by the Author:	n/a
Complete List of Authors:	Wertz, Olivier; Université de Liège, Extragalactic Astrophysics and Space Observations Surdej, Jean; Université de Liège, Extragalactic Astrophysics and Space Observations
Keywords:	gravitational lensing: strong < Physical Data and Processes, (cosmology:) cosmological parameters < Cosmology

# Asymptotic solutions for the case of SIE lens models and application to the quadruply imaged quasar Q2237+0305

O. Wertz<sup>1\*</sup> and J. Surdej<sup>1\*†</sup>

<sup>1</sup>*Institut d'Astrophysique et de Géophysique, Université de Liège, Allée du 6 Août 17, Sart Tilman, Bât. B5c, 4000 Liège, Belgique*

Accepted — Received —; in original form —

## ABSTRACT

For the case of a small misalignment between a point-like source, a singular isothermal ellipsoid deflector and an observer, we derive to first order simple relations between the model parameters and the lensed image positions, and an expression for the time delay between pairs of opposed images which is analog to the one previously derived for the case of  $\varepsilon - \gamma$  models (Wertz, Pelgrims & Surdej, 2012). Combined with the first order astrometric relations, we retrieve a simple expression for time delays, already derived by Witt et al. (2000) for the SIE model, which solely depends on the lensed image positions. The real advantage of using the first order equations when dealing with symmetric gravitational lens systems is to directly test the validity of the adopted lens model without having to perform any accurate numerical fit. In this paper, we present in details the calculations which lead to those relations between the SIE lens model parameters and the lensed image positions. In addition, we model the well-known gravitational lens system Q2237+0305, the so-called Einstein cross, with three families of models :  $\varepsilon - \gamma$ , SIE and NSIE + shear, using a genetic algorithm from the Qubist Optimization Toolbox (Fiege, 2010). We conclude that although the NSIE + shear model shows the best agreement between the calculated and the observed image positions ( $\langle \Delta x \rangle = 0.0026$  arcsec), the more simple SIE also leads to quite satisfactory and acceptable results ( $\langle \Delta x \rangle = 0.0059$  arcsec). Furthermore, direct use of the SIE first order equations allows one to nearly recover the same model parameters (relative deviation better than 2%), which indicates that those relations are very useful and fully coherent. A comparison with previous studies is reported.

**Key words:** gravitational lensing : strong – cosmology : cosmological parameters.

## 1 INTRODUCTION

According to Refsdal (1964 a, b), the gravitational lens phenomenon provides a powerful tool to derive the values of several cosmological parameters, i.e.  $H_0$ ,  $\Omega_1$ , as well as to deduce the absolute mass of the lensing object, independently on the distance ladder. Unfortunately, such a determination turns out to be model dependent. However, for the case of a small misalignment between the source, the deflector and the observer, Wertz et al. (2012) have recently shown that a first order perturbative approach applied to the lensed image positions may lead to the determination of the Hubble parameter using observable quantities only (Wertz, Pelgrims & Surdej, 2012). Let us note that a similar kind of approach has been developed by Alard (2007) but his singular perturbative method proves to be more restrictive.

The main idea of the present paper is to investigate for the case of the singular isothermal ellipsoid (SIE) model whether we can derive first order equations linking the model parameters to the lensed image positions only. These equations are then used in

order to derive model independent expressions for the time delays between lensed images and the Hubble parameter. Let us note that the derived expressions of  $H_0$  are consistent with the ones already presented by Witt et al. (2000).

The outline of the present paper is as follows. In Section 2, we recall the basic gravitational lens and astrometric equations for the case of the singular isothermal ellipsoid (SIE). We also assume that the lensed images are not resolved individually. Assuming a very small misalignment between the source, the deflector and the observer, we then derive, in Section 3, first-order expressions which link the image positions to the model parameters, as well as the possibility to infer from only observable quantities the value of the Hubble parameter from the linearized astrometric and time delay expressions. Afterwards, we discuss the apparent problem of the degeneracy in determining the value of the parameter  $\varpi$  which represents the a priori unknown orientation of the elliptic-shape isodensity contours, and we propose to test the validity range of the astrometric equations. In Section 4, we test the first order equations for the case of the well-known quadruply imaged quasar : Q2237+0305. We compare the first order model parameters obtained with those determined numerically using a sophisticated genetic algorithm, called *Ferret* (Fiege et al. 2004), which is a com-

\* Aspirant du F.R.S. - FNRS.

† Also Directeur de Recherche honoraire du F.R.S. -FNRS.

## 2 *O. Wertz and J. Surdej*

ponent of the Qubist Global Optimization Toolbox (Fiege 2010). Some general conclusions form the last section.

### 2 THE SINGULAR ISOTHERMAL ELLIPSOID MODEL

The singular isothermal ellipsoid model (SIE) represents a particular case of more general models with elliptical mass distributions (Bourassa et al. 1973, Bourassa & Kantowski 1975, corrected by Bray 1984, Kormann & al. 1994). It can be described by its normalized surface mass density  $\kappa(\rho)$  defined as :

$$\kappa(\rho) = \frac{\sqrt{f}}{2\rho}, \quad (1)$$

where  $f$  represents the axis ratio and  $\rho = \sqrt{x_1^2 + f^2 x_2^2}$  with  $x_i$  the normalized cartesian coordinates of the impact parameter  $\mathbf{x}$ . The associated normalized deflection angle  $\hat{\alpha}(\mathbf{x})$  is given by :

$$\hat{\alpha}(\mathbf{x}) = -\frac{\sqrt{f}}{f'} \left[ \operatorname{arcsinh} \left( \frac{f'}{f} \cos(\varphi) \right) \mathbf{e}_1 + \operatorname{arcsin} (f' \sin(\varphi)) \mathbf{e}_2 \right], \quad (2)$$

where  $\mathbf{e}_i$  represents the unit vector along the direction  $x_i$ ,  $\varphi$  the angular coordinate of the impact parameter, and  $f' = \sqrt{1-f^2}$ . Accounting for the notation defined by Kormann & al. (1994), the  $\mathbf{e}_1$  direction corresponds to the semi-minor axis direction of the iso-density contours. Therefore, the coordinate system adopted in that paper is *not* arbitrarily oriented. Considering now an arbitrarily oriented coordinate system for which the abscissa axis form an angle  $\varpi$  with the semi-minor axis (see Fig. 1), the expression of the two components of the lens equation can be expressed as :

$$y \cos(\theta + \varpi) = r^{(i)} \cos(\varphi^{(i)} + \varpi) - \frac{\sqrt{f}}{f'} \operatorname{arcsinh} \left( \frac{f'}{f} \cos(\varphi^{(i)} + \varpi) \right), \quad (3)$$

$$y \sin(\theta + \varpi) = r^{(i)} \sin(\varphi^{(i)} + \varpi) - \frac{\sqrt{f}}{f'} \operatorname{arcsin} (f' \sin(\varphi^{(i)} + \varpi)), \quad (4)$$

where  $(r^{(i)}, \varphi^{(i)})$  represent the normalized polar coordinates of the position of the image  $i$ ,  $(y, \theta)$ , the normalized polar coordinates of the point-like source and where  $\theta$  and  $\varphi^{(i)}$  are now measured from the arbitrarily oriented coordinate system.

### 3 FIRST ORDER EQUATIONS AND SOLUTIONS

#### 3.1 Small deviations from the perfect alignment

For the case of a perfect alignment between the source, the deflector and the observer, i.e.  $y = 0$ , we may deduce from Eqs. (3) and (4) the exact positions  $(r_0^{(i)}; \varphi_0^{(i)})$  of the lensed images. On one hand, Eq. (3)  $\times \sin(\varphi^{(i)} + \varpi)$  - Eq. (4)  $\times \cos(\varphi^{(i)} + \varpi)$  leads to :

$$y \sin(\varphi^{(i)} - \theta) = \frac{\sqrt{f}}{f'} \left[ \operatorname{arcsin} (f' \sin(\varphi^{(i)} + \varpi)) \cos(\varphi^{(i)} + \varpi) - \operatorname{arcsinh} (f' \cos(\varphi^{(i)} + \varpi) / f) \sin(\varphi^{(i)} + \varpi) \right], \quad (5)$$

and from the latter equation and for  $y = 0$ , the exact image angular coordinates are expressed as :

$$\varphi_0^{(i)} = \frac{i\pi}{2} - \varpi, \quad (6)$$

where  $i \in [0, 1, 2, 3]$  indicates that there are up to four lensed images. On the other hand, Eq. (3)  $\times \cos(\varphi^{(i)} + \varpi)$  + Eq. (4)

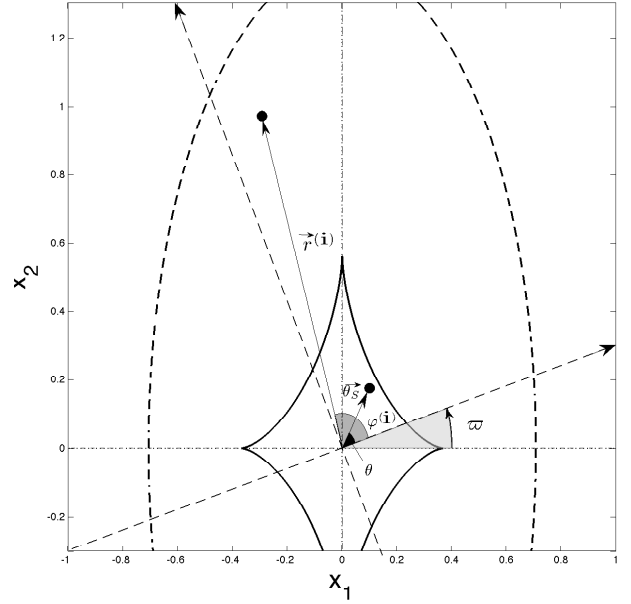


**Figure 1.** Illustration of the arbitrarily oriented coordinate system which abscissa axis form an angle  $\varpi$  with the semi-minor axis of the iso-density elliptic contours.

$\times \sin(\varphi^{(i)} + \varpi)$  leads to :

$$y \cos(\varphi^{(i)} - \theta) = r^{(i)} - \frac{1}{r^{(i)}} \hat{\psi}(r^{(i)}, \varphi^{(i)} + \varpi), \quad (7)$$

where  $\hat{\psi}(r, \varphi)$  represents the normalized deflection potential defined by :

$$\hat{\psi}(r, \varphi) = \frac{\sqrt{f}}{f'} r \left[ \sin(\varphi) \operatorname{arcsin} (f' \sin(\varphi)) + \cos(\varphi) \operatorname{arcsinh} \left( \frac{f'}{f} \cos(\varphi) \right) \right]. \quad (8)$$

From Eq. (7) and for  $y = 0$ , the exact image radial coordinates are expressed as :

$$r_0^{(0)} = r_0^{(2)} = \frac{\sqrt{f}}{f'} \operatorname{arcsinh} \left( \frac{f'}{f} \right), \quad (9)$$

and

$$r_0^{(1)} = r_0^{(3)} = \frac{\sqrt{f}}{f'} \operatorname{arcsin} (f'). \quad (10)$$

When considering a small misalignment between the source, the lens and the observer, the resulting image positions only slightly deviate from the perfect alignment case. Thus, the  $i$ -th image position  $(r^{(i)}; \varphi^{(i)})$  can be expressed as :

$$r^{(i)} = r_0^{(i)} + \Delta r^{(i)}, \quad (11)$$

and

$$\varphi^{(i)} = \varphi_0^{(i)} + \Delta \varphi^{(i)}, \quad (12)$$

where  $\Delta r^{(i)}$  and  $\Delta \varphi^{(i)}$  represent small variations of the image polar coordinates, i.e.  $|\Delta r^{(i)}| \ll 1$  and  $|\Delta \varphi^{(i)}| \ll 1$ . To first order, and after

substituting Eqs. (11) and (12) into Eq. (5), the latter becomes :

$$y \left[ \sin\left(\frac{i\pi}{2} - \theta - \varpi\right) + \cos\left(\frac{i\pi}{2} - \theta - \varpi\right) \Delta\varphi^{(i)} \right] = -\frac{\sqrt{f'}}{f'} \left[ \operatorname{arcsinh}\left(\frac{f'}{f} \mathcal{S}^{(i)}\right) \mathcal{C}^{(i)} - \operatorname{arcsin}\left(f' \mathcal{C}^{(i)}\right) \mathcal{S}^{(i)} \right] \quad (13)$$

where  $\mathcal{S}^{(i)} = \cos(i\pi/2) - \sin(i\pi/2) \Delta\varphi^{(i)}$  and  $\mathcal{C}^{(i)} = \sin(i\pi/2) + \cos(i\pi/2) \Delta\varphi^{(i)}$ . To first order, we find that  $\operatorname{arcsin}\left((-1)^{i/2} f' \Delta\varphi^{(i)}\right) \simeq (-1)^{i/2} f' \Delta\varphi^{(i)}$  for  $i \in \{0, 2\}$  and  $\operatorname{arcsinh}\left((-1)^{(3-i)/2} f' \Delta\varphi^{(i)}/f\right) \simeq (-1)^{(3-i)/2} f' \Delta\varphi^{(i)}/f$  for  $i \in \{1, 3\}$ . As a result, for  $i \in \{0, 1, 2, 3\}$ , Eq. (13) takes the form :

$$\Delta\varphi^{(0)} = -\Delta\varphi^{(2)} = \frac{y \sin(\theta + \varpi)}{\sqrt{f'} \left[ \frac{1}{f'} \operatorname{arcsinh}\left(\frac{f'}{f}\right) - 1 \right]}, \quad (14)$$

and

$$\Delta\varphi^{(1)} = -\Delta\varphi^{(3)} = \frac{y \cos(\theta + \varpi)}{\sqrt{f'} \left[ \frac{1}{f'} - \frac{1}{f'} \operatorname{arcsin}\left(f'\right) \right]}. \quad (15)$$

To first order, and after substituting Eqs. (11) and (12) into Eq. (7), the latter becomes :

$$y \left[ \cos\left(\theta + \varpi - \frac{i\pi}{2}\right) + \sin\left(\theta + \varpi - \frac{i\pi}{2}\right) \Delta\varphi^{(i)} \right] = r_0^{(i)} + \Delta r^{(i)} - \frac{\sqrt{f'}}{f'} \left[ \operatorname{arcsinh}\left(\frac{f'}{f} \mathcal{S}^{(i)}\right) \mathcal{S}^{(i)} + \operatorname{arcsin}\left(f' \mathcal{C}^{(i)}\right) \mathcal{C}^{(i)} \right]. \quad (16)$$

As a result, from Eqs. (9), (10) and for  $i \in \{0, 1, 2, 3\}$ , Eq. (16) reduces to :

$$\Delta r^{(0)} = -\Delta r^{(2)} = y \cos(\theta + \varpi), \quad (17)$$

and

$$\Delta r^{(1)} = -\Delta r^{(3)} = y \sin(\theta + \varpi). \quad (18)$$

We note that the small azimuthal and radial variations of the lensed image polar coordinates only depend on the source position compared to the semi-minor axis direction of the iso-density contours.

### 3.2 The SIE lens model parameters

In this section, we will recover all lens model parameters from Eqs. (6), (9), (10), (14), (15), (17) and (18). First of all, we need to be careful with the handling of the measured image angular coordinates  $\varphi^{(i)}$ . As a reminder, these coordinates are measured from the arbitrarily oriented coordinate system, which implies that  $\varphi^{(i)} \in [0, 2\pi]$ . However, according to the value of  $\varpi$  and  $\theta$ , we may have  $\varphi_0^{(i)} + \Delta\varphi^{(i)} = i\pi/2 - \varpi + \Delta\varphi^{(i)} < 0$  with  $i \in \{0, 1, 2, 3\}$ . Therefore, for  $(\theta + \varpi) \in [0, \pi]$  and  $\varpi \in [0, \Delta\varphi^{(0)}]$ , we have, to first order,  $\varphi^{(i)} = i\pi/2 - \varpi + \Delta\varphi^{(i)}$ ; but for  $(\theta + \varpi) \in [0, 2\pi]$  and  $\varpi \in [\varphi^{(i)}, \varphi^{(i+1)}]$  with  $\varphi$  representing the image angular coordinate measured from the semi-minor axis direction of the iso-density contours, we have  $\varphi^{(k)} = k\pi/2 - \varpi + \Delta\varphi^{(k)}$  with  $k \in \{i+1, \dots, 3\}$  and  $\varphi^{(l)} \neq i\pi/2 - \varpi + \Delta\varphi^{(l)}$  with  $l \in \{0, \dots, i\}$ . In the latter equation, since the angular quantities are cyclic, the two members are equivalent but not equal. In fact, we have  $\varphi^{(l)} = i\pi/2 - \varpi + \Delta\varphi^{(l)} \bmod 2\pi$ , where mod represents the modulo operation. In the remainder of this section, we will take into account these properties, in particular for the determination of the parameter  $\varpi$ .

From Eqs. (14) and (15), we note that  $\Delta\varphi^{(0)} + \Delta\varphi^{(1)} + \Delta\varphi^{(2)} +$

$\Delta\varphi^{(3)} = 0$ . Therefore, we have :

$$\sum_{j=0}^3 (\varphi_0^{(j)} + \Delta\varphi^{(j)}) = 3\pi - 4\varpi. \quad (19)$$

As a consequence, from the latter equation, the expression of  $\varpi$  can be retrieved :

$$\varpi = \frac{1}{4} \left( 3\pi - \sum_{j=0}^3 \varphi^{(j)} \right) + \frac{l\pi}{2} \equiv \varpi_0 + \frac{l\pi}{2}, \quad (20)$$

where  $l \in \{0, 1, 2, 3, 4\}$  such as  $\varpi \in [\varphi^{(l-1)}, \varphi^{(l)}]$  with  $\varphi^{(-1)} = 0$  and  $\varphi^{(4)} = \varphi^{(0)}$ . Although we are not able to determine  $l$  unequivocally from the lensed image positions, we can reduce the degeneracy to only two values :  $\varpi_{\text{real}}$  and  $\varpi_{\text{real}} + \pi$ , which lead to two equivalent SIE models. The latter property is shown in the next section.

From Eqs. (9), (10), (11), (17) and (18), we note that  $r^{(0)} - r^{(2)} = \Delta r^{(0)} - \Delta r^{(2)} = 2y \cos(\theta + \varpi)$ , and  $r^{(1)} - r^{(3)} = \Delta r^{(1)} - \Delta r^{(3)} = 2y \sin(\theta + \varpi)$ . Therefore, we have :

$$\theta^{(0)} - \theta^{(2)} = 2\theta_s \cos(\theta + \varpi), \quad (21)$$

and

$$\theta^{(1)} - \theta^{(3)} = 2\theta_s \sin(\theta + \varpi). \quad (22)$$

Dividing Eq. (22) by Eq. (21), the relative angular coordinate  $\theta$  of the point-like source can be deduced from :

$$\tan(\theta + \varpi) = \frac{\theta^{(1)} - \theta^{(3)}}{\theta^{(0)} - \theta^{(2)}}. \quad (23)$$

Since the determination of  $\theta$  depends on the value of  $\varpi$ , the latter parameter seems to be also degenerated. In fact, we show in the next section that the value of  $\theta$  can be derived unequivocally.

From Eqs. (21) and (22), the relative radial coordinate  $\theta_s$  of the point-like source can be expressed as :

$$\theta_s = \frac{1}{2} \sqrt{(\theta^{(0)} - \theta^{(2)})^2 + (\theta^{(1)} - \theta^{(3)})^2}. \quad (24)$$

From Eq. (17), we note that  $r^{(0)} + r^{(2)} = 2r_0^{(0)}$ . In addition, from Eq. (18), we note that  $r^{(1)} + r^{(3)} = 2r_0^{(1)}$ . Therefore, we have :

$$\theta^{(0)} + \theta^{(2)} = 2\theta_E \frac{\sqrt{f'}}{f'} \operatorname{arcsinh}\left(\frac{f'}{f}\right), \quad (25)$$

and

$$\theta^{(1)} + \theta^{(3)} = 2\theta_E \frac{\sqrt{f'}}{f'} \operatorname{arcsin}\left(f'\right). \quad (26)$$

Dividing Eq. (25) by Eq. (26), the axis ratio  $f$  is found to be :

$$\frac{\operatorname{arcsinh}\left(f'/f\right)}{\operatorname{arcsin}\left(f'\right)} = \frac{\theta^{(0)} + \theta^{(2)}}{\theta^{(1)} + \theta^{(3)}}, \quad (27)$$

the latter equation consisting of an implicit definition of  $f$ . From Eqs. (25) and (26), the value of the Einstein ring angular radius is given by :

$$\theta_E = \frac{f'}{2\sqrt{f'}} \frac{\theta^{(0)} + \theta^{(2)}}{\operatorname{arcsinh}\left(f'/f\right)} = \frac{f'}{2\sqrt{f'}} \frac{\theta^{(1)} + \theta^{(3)}}{\operatorname{arcsin}\left(f'\right)}, \quad (28)$$

where the axis ratio  $f$  is retrieved from Eq. (27).

As a result, we have thus determined the values of  $f$ ,  $\theta_s$ ,  $\theta$ ,  $\varpi$  and  $\theta_E$  from the only astrometric positions of the lensed images. In addition, we note that the index of the lensed images  $i = \{0, 1, 2, 3\}$  is in principle unknown. However, only four possible combinations remain since the index values have to be consecutive. Furthermore,

## 4 *O. Wertz and J. Surdej*

due to the symmetries in the relations between all model parameters and the lensed image positions (see Eqs. (20), (23), (24), (27) and (28)), we note that the inversion between the index of two opposed lensed images does not have any impact on their determination :  $0 \leftrightarrow 2$  and  $1 \leftrightarrow 3$ . In order to differentiate the two remaining combinations ( $02 \leftrightarrow 13$ ), we only need to calculate the value of  $f$  from Eq. (27). Indeed, one combination leads to  $f < 1$  while the other one to  $f > 1$ , which points towards a non-physical situation of having the minor axis larger than the major one.

### 3.3 The degeneracy affecting the value of $\varpi$

As shown in the previous section, the parameter  $\varpi$  can only take four possible values in accordance with the relation  $\varpi_l = \varpi_0 + l\pi/2$  for  $l \in \{0, 1, 2, 3\}$ . Furthermore, from Eq. (23) and after substituting the different values of  $\varpi$ , the different possible angular coordinates  $\theta$  of the source can be expressed as :

$$\theta_{lk} = \text{atan} \left( \frac{\theta^{(1)} - \theta^{(3)}}{\theta^{(0)} - \theta^{(2)}} \right) - \left( \varpi_0 + \frac{l\pi}{2} \right) + k\pi, \quad (29)$$

with  $k \in \{0, 1\}$ . From the latter equation, we may deduce 8 different combinations for the pair of parameters  $(\varpi_l, \theta_{lk})$ .

For each pair of these parameters and the already determined values of  $f$ ,  $\theta_s$  and  $\theta_E$ , we derive 8 sets of four lensed image positions. By comparison with the real lensed image positions, there only remain two pairs of parameters : the real one  $(\varpi_{\text{real}}, \theta_{\text{real}})$  and another one which leads to the same lensed image positions. Due to the symmetry of the SIE lens models which leads to a diamond-shape tangential caustic curve, and for fixed values of  $f$ ,  $\theta_s$  and  $\theta_E$ , the two pairs of parameters  $(\varpi, \theta)$  and  $(\varpi + \pi, \theta)$  rigorously lead to the same lensed image positions. As a consequence, among the 8 different remaining combinations of parameter pairs  $(\varpi_l, \theta_{lk})$ , the only valid ones are  $(\varpi_{\text{real}}, \theta_{\text{real}})$  and  $(\varpi_{\text{real}} + \pi, \theta_{\text{real}})$ . We thus find that the parameter  $\theta_{\text{real}}$  is unequivocally determined.

### 3.4 Time delays and the Hubble parameter

Let us now consider the determination of the value of the Hubble parameter  $H_0$  from the measurement of the time delay  $\Delta t$  between two lensed image light curves for the case of the SIE lens model. The time-delay function  $t(\mathbf{x})$  for the  $i$ -th image is given by (Narayan & Bartelmann 1996) :

$$t(\mathbf{x}^{(i)}) = \left( \frac{1+z_l}{c} \right) \left( \frac{D_{\text{OL}} D_{\text{OS}}}{D_{\text{LS}}} \right) \theta_E^2 \left[ \frac{1}{2} (\mathbf{x} - \mathbf{y})^2 - \hat{\psi}_{\text{tot}}(\mathbf{x}) \right], \quad (30)$$

where  $z_l$  represents the redshift of the lens,  $D_{\text{OL}}$ ,  $D_{\text{OS}}$  and  $D_{\text{LS}}$  represent the usual angular-diameter distances between the observer, lens and source,  $c$  the speed of light in vacuum and  $\hat{\psi}_{\text{tot}}$  the total lensing potential, which gradient corresponds to the general deflection angle, apart from an irrelevant constant :

$$\hat{\boldsymbol{\alpha}}_{\text{gen}}(\mathbf{x}) = -\nabla_{\mathbf{x}} \hat{\psi}_{\text{tot}}. \quad (31)$$

For the case of the SIE lens model, the time delay between the lensed images  $i$  and  $j$  is therefore given by :

$$\Delta t_{i,j} = \left( \frac{1+z_l}{c} \right) \left( \frac{D_{\text{OL}} D_{\text{OS}}}{D_{\text{LS}}} \right) \theta_E^2 \left[ \frac{1}{2} (\mathbf{x}^{(j)} - \mathbf{y})^2 - \frac{1}{2} (\mathbf{x}^{(i)} - \mathbf{y})^2 - \hat{\psi}_{\text{SIE}}(r^{(j)}; \varphi^{(j)}) + \hat{\psi}_{\text{SIE}}(r^{(i)}; \varphi^{(i)}) \right], \quad (32)$$

where  $\hat{\psi}_{\text{SIE}}$  is defined by Eq. (8). To first order, the expression of the lensing potential can be simplified as follows. Considering the

image  $i$ , from Eqs. (11) and (12) we have respectively  $r^{(i)} = r_0^{(i)} + \Delta r^{(i)}$  and  $\varphi^{(i)} = i\pi/2 + \Delta\varphi^{(i)} - \varpi$ . After substituting the latter results into Eq. (8), the expression of the deflection potential for the lensed image  $i$  reduces, to first order, to :

$$\hat{\psi}_{\text{SIE}}(r^{(i)}; \varphi^{(i)}) = r_0^{(i)} (r_0^{(i)} + \Delta r^{(i)}), \quad (33)$$

where  $r_0^{(i)}$  is defined by Eqs. (9) and (10), and  $\Delta r^{(i)}$  by Eqs. (17) and (18). Therefore, from Eqs. (32) and (33), the time delay between the lensed images  $i$  and  $j$  can be expressed as :

$$\Delta t_{i,j} = \left( \frac{1+z_l}{c} \right) \left( \frac{D_{\text{OL}} D_{\text{OS}}}{D_{\text{LS}}} \right) \left[ \frac{1}{2} \left( (\theta_0^{(i)})^2 - (\theta_0^{(j)})^2 \right) - \theta_s \left[ \theta^{(j)} \cos(\varphi_0^{(j)} - \theta) - \theta^{(i)} \cos(\varphi_0^{(i)} - \theta) - \theta_0^{(j)} \Delta\varphi^{(j)} \sin(\varphi_0^{(j)} - \theta) + \theta_0^{(i)} \Delta\varphi^{(i)} \sin(\varphi_0^{(i)} - \theta) \right] \right]. \quad (34)$$

Since there are three independent time delays for a four-lensed gravitational lens system, we only specify  $\Delta t_{i,i+1}$  and  $\Delta t_{i,i+2}$ . The expression : of  $\Delta t_{i,i+1}$  reduces to

$$\Delta t_{i,i+1} = \left( \frac{1+z_l}{c} \right) \left( \frac{D_{\text{OL}} D_{\text{OS}}}{D_{\text{LS}}} \right) \left[ \frac{1}{2} \left( (\theta_0^{(i)})^2 - (\theta_0^{(i+1)})^2 \right) + \theta_s \left[ \cos\left(\frac{i\pi}{2} - \varpi - \theta\right) (\theta^{(i)} + \theta_0^{(i+1)} \Delta\varphi^{(i+1)}) + \sin\left(\frac{i\pi}{2} - \varpi - \theta\right) (\theta^{(i+1)} - \theta_0^{(i)} \Delta\varphi^{(i)}) \right] \right], \quad (35)$$

while  $\Delta t_{i,i+2}$  simply reduces to :

$$\Delta t_{i,i+2} = \left( \frac{1+z_l}{c} \right) \left( \frac{D_{\text{OL}} D_{\text{OS}}}{D_{\text{LS}}} \right) \theta_s (\theta^{(i)} + \theta^{(i+2)}) \cos(\varpi + \theta - i\pi/2). \quad (36)$$

The latter equation is identical to the one already derived for a power-law axially symmetric lens model with an external large-scale gravitational field (the shear ; see Eq. (92) in Wertz, Pelgrims & Surdej, 2012). In the latter paper, the authors had already demonstrated that these two families of models remain strictly distinct, even at the first order, except when the alignment between the source, the lens and the observer is perfect or when the SIE reduces to the SIS model without any shear. Furthermore, from Eqs. (21) and (22), we easily deduce that :

$$\theta_s \cos(\varpi + \theta - i\pi/2) = \frac{1}{2} (\theta^{(i)} - \theta^{(i+2)}). \quad (37)$$

After substituting Eq. (37) into Eq. (36), the time delay between two opposed lensed images  $i$  and  $i+2$  becomes

$$\Delta t_{i,i+2} = \left( \frac{1+z_l}{2c} \right) \left( \frac{D_{\text{OL}} D_{\text{OS}}}{D_{\text{LS}}} \right) \left( (\theta^{(i)})^2 - (\theta^{(i+2)})^2 \right). \quad (38)$$

So we have retrieved the same expression for the time delays between two lensed images as the one already derived by Witt et al. (2000). According to them, Eq. (38) remains valid irrespective of the degree of misalignment. This implies that Eq. (36) derived from the first order astrometric equations is rigorously identical to the one derived without any approximation.

For completeness, we retrieve the expression of the Hubble parameter for the case of the SIE lens model. From Eq. (38),  $H_0$  can be expressed as :

$$H_0 = \frac{1+z_l}{2 \Delta t_{i,i+2}} \left( \frac{z_l z_s}{z_s - z_l} \right) \left( \frac{F(z_l) F(z_s)}{F(z_s - z_l)} \right) \left[ (\theta^{(i)})^2 - (\theta^{(i+2)})^2 \right], \quad (39)$$

where  $F(z)$  is given to first order (Peebles 1993) by :

$$F(z) = \frac{1}{1+z} - [\Omega_M + 2(1 - \Omega_\Lambda)] \frac{z}{4(1+z)}. \quad (40)$$

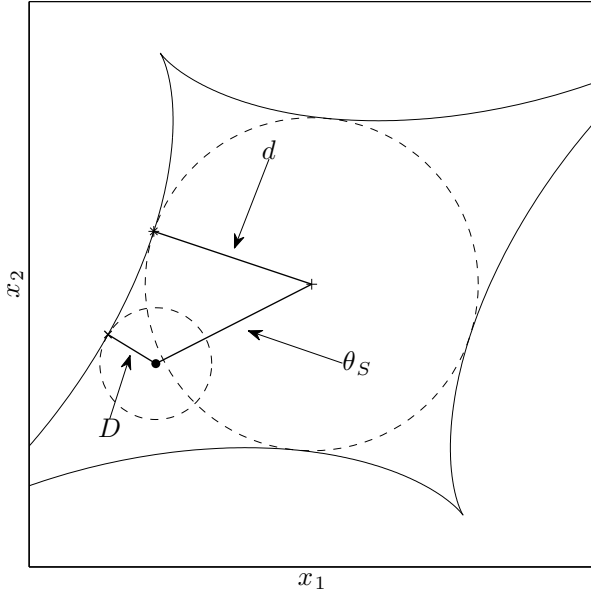


**Figure 2.** Illustration of the different angular sizes involved in the test of the validity range of the first order equations (see text).

### 3.5 Validity range of the first order equations

We propose to test the validity range of the first order Eqs. (20), (23), (24), (27) and (28). It is clear that the accuracy of these latter equations is directly dependent on the accuracy of the two Eqs. (11) and (12). Indeed, for the case of a perfect alignment between the source, the lens and the observer, the differences between the real SIE lensed image positions and those derived from the first order equations should be equal to zero. As soon as the source is no longer perfectly aligned, the first order determination of the lensed image positions loses some accuracy. Furthermore, these differences become larger as the point-like source gets closer to the tangential caustic curve. As a consequence, we can deduce a first estimation of the validity range of the first order equations by illustrating the distribution of the mean error  $\bar{E}$  between the exact lensed image positions and the derived first order ones as a function of the smallest distance  $D$  between the point-like source and the tangential caustic curve (see Fig. 2) :

$$\bar{E} = \frac{1}{4} \sum_{j=0}^3 \sqrt{(x_1^{(j)} - \underline{x}_1^{(j)})^2 + (x_2^{(j)} - \underline{x}_2^{(j)})^2}, \quad (41)$$

where  $\underline{x}_i$  represents the first order lensed image positions derived from the numerical inversion of the lens equation characterized by the model parameters deduced from Eqs. (20), (23), (24), (27) and (28). The angular diameter distance  $D$  is illustrated in Fig. 2. As shown in Fig. 3, from a set of 1000 model parameters randomly chosen, the mean error  $\bar{E}$  increases with the degree of misalignment between the source, the lens and the deflector, the latter being represented by small values of the angular distance  $D$  between the point-like source and the nearest point of the tangential caustic curve. For any value of  $f$ , we notice that the condition  $D \geq 0.1$  is sufficient to obtain  $\bar{E} \leq 0.05$  arcsec, but not necessarily. Indeed, we note that even for small values of  $D$ , we can have small mean error values of  $\bar{E}$ . This occurs when the two following conditions are being fulfilled : the misalignment is very small and the intrinsic size of the tangential caustic curve is small, i.e. for large values of  $f \leq 1$ . Thus, even if the source is intrinsically close to the tangential

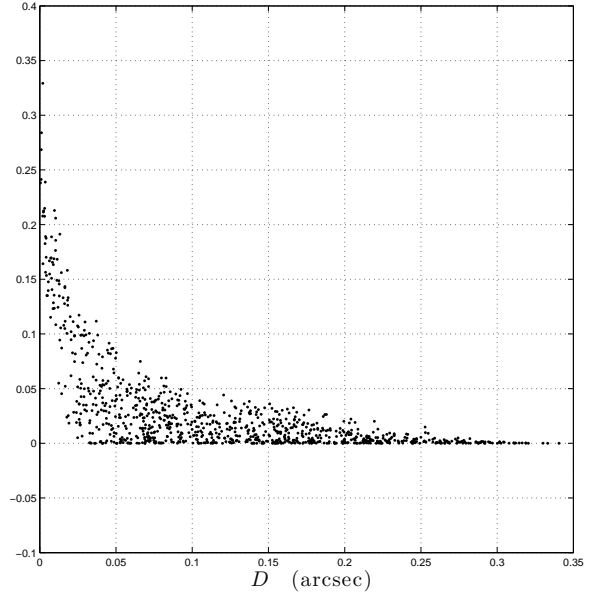


**Figure 3.** For a set of 1000 model parameters randomly chosen, we have represented the distribution of the mean error  $\bar{E}$  between the exact lensed image positions and the derived first order ones as a function of the distance between the point-like source and the tangential caustic curve.

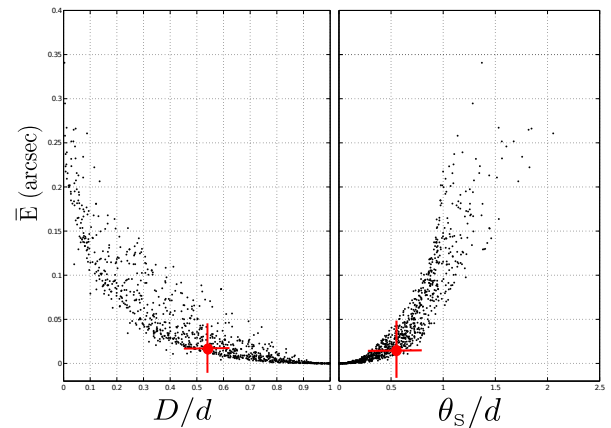


**Figure 4.** For the same set of 1000 model parameters randomly chosen (see Fig. 3), we have represented the distribution of the mean error  $\bar{E}$  between the exact lensed image positions and the derived first order ones as a function of the normalized distance  $D/d$  between the point-like source and the tangential caustic curve (left panel) and as a function of the point-like source radial coordinate  $\theta_s$  divided by the smallest distance between the tangential caustic curve and the center of the lens (right panel). The red crosses correspond to the case of the multiply imaged quasar Q2237+0305.

caustic curve, the quantities  $\Delta r^{(i)}$  and  $\Delta \varphi^{(i)}$  remain small compared to  $r_0^{(i)}$  and  $\varphi_0^{(i)}$ .

In order to further investigate this, we have represented  $\bar{E}$  as a function of the distance  $D$  (or  $\theta_s$  since these two quantities are correlated) divided by the smallest angular distance  $d$  between the tangential caustic curve and the center of the lens (see Fig. 4). The angular diameter distance  $d$  is illustrated in Fig. 2. As shown in Fig. 4, from the same set of the 1000 previous model parameters, a more precise condition on the alignment can be derived. For the case of a perfect alignment, i.e.  $D/d = 1$  and  $\theta_s/d = 0$ , the mean

6 *O. Wertz and J. Surdej*

**Table 1.** Real and first order lens parameters for the twelve SIE models represented respectively in Fig. 5. For each lens model denoted by # i, we have reported the real model parameters (first line) and the retrieved first order ones (second line).

Real	$f$	$\varpi$	$\theta_s$	$\theta$	$\theta_E$	$\theta_s/d$
First order						
#1	0.0875	0	0.0871	0.0616	0.9807	0.1876
	0.0865	0.0006	0.0871	0.0610	0.9829	
#2	0.6401	0.3307	0.0189	5.2981	0.8911	0.1459
	0.6386	0.3300	0.0189	5.2988	0.8912	
#3	0.1806	0.6614	0.0661	5.7952	1.1218	0.1379
	0.1796	0.6621	0.0661	5.7944	1.1226	
#4	0.0451	0.9921	0.0807	4.8440	1.1944	0.1459
	0.0447	0.9896	0.0806	4.8461	1.1982	
#5	0.7232	1.3228	0.0111	0.2680	0.8120	0.1280
	0.7222	1.3228	0.0111	0.2680	0.8123	
#6	0.3474	1.6535	0.0066	2.3762	1.0143	0.0206
	0.3474	1.6535	0.0066	2.3762	1.0143	
#7	0.6606	1.9842	0.0204	4.4255	0.8348	0.1799
	0.6585	1.9845	0.0204	4.4249	0.8346	
#8	0.3839	2.3149	0.0808	4.5837	1.1208	0.2490
	0.3786	2.3189	0.0805	4.5805	1.1228	
#9	0.6273	2.6456	0.0161	1.4092	1.1957	0.0886
	0.6267	2.6459	0.0161	1.4092	1.1958	
#10	0.0216	2.9762	0.0841	1.6905	0.8268	0.2428
	0.0201	2.9770	0.0841	1.6905	0.8561	
#11	0.9106	3.3069	0.0032	4.2288	1.1758	0.0866
	0.9104	0.1653	0.0032	4.2290	1.1758	
#12	0.8006	3.6376	0.0132	3.0002	0.8073	0.2216
	0.7985	0.4965	0.0132	2.9984	0.8071	

error  $\bar{E}$  equals zero, as expected. Furthermore, for  $\theta_s/d < 0.13$ , the mean error is always such as  $\bar{E} < 0.003$  arcsec which typically corresponds to the error on the observed positions of the lensed images of Q2237+0305. Since the value of  $d$  is correlated with the value of  $f$ , the latter validity range takes the form  $\theta_s < 0.13 d(f)$  where the analytical function  $d(f)$  has not yet been determined but could be numerically evaluated.

Furthermore, we have represented respectively in Figs. 5, 6 and 7 the lensed images, the point-like source, the tangential critical and caustic curves for twelve SIE models and their associated first order ones characterized by  $\theta_s/d \in [0.0, 0.25]$ ,  $\theta_s/d \in [0.25, 0.50]$  and  $\theta_s/d \in [0.50, 1.25]$ , respectively. The model parameters related to those SIE models are given in Tables 1, 2 and 3. We notice that as  $\theta_s/d$  increases, the accuracy of the first order SIE model decreases.

Finally, we have determined exact and first order time delays, between pairs of lensed images for all the simulated models represented in Figs. 5, 6 and 7. For this purpose, we have assumed a spatially-flat  $\Lambda$ CDM cosmology with a value  $H_0 = 67.3 \pm 1.2$  km  $s^{-1}$  Mpc $^{-1}$  for the Hubble parameter and the matter density parameter  $\Omega_m = 0.315 \pm 0.017$  (Planck Collaboration 2013). We have fixed the redshifts of the simulated sources and lenses according to realistic cases of expected multiply imaged quasars as in Finet (2013). From the normalised redshift distribution of the sources that are de-

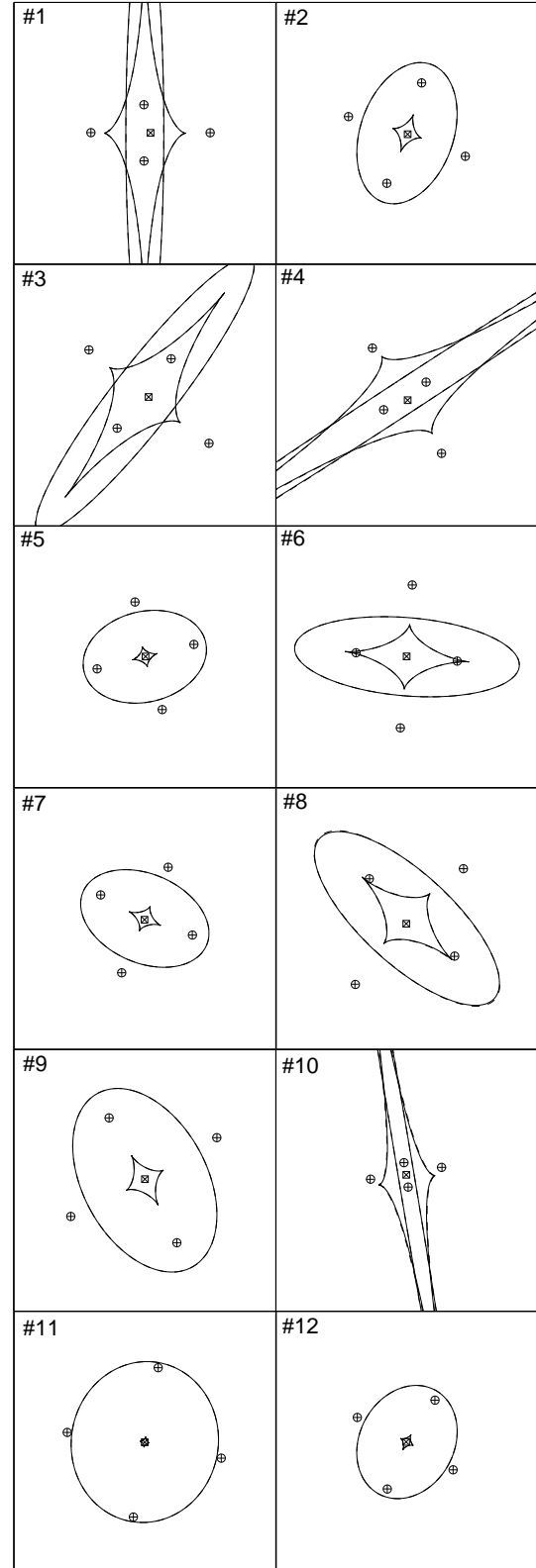


**Figure 5.** Illustration of different lensed image configurations corresponding to the SIE lens model (open circles  $\circ$ ) and the SIE first order one (crosses  $\times$ ). The source positions associated with the SIE lens model (open square  $\square$ ) and the SIE first order one (cross  $\times$ ) are also represented. The lens model parameters were randomly chosen such as  $\theta_s/d(f) \in [0, 0.25]$ . The solid lines correspond to the tangential critical and caustic curves deduced from the SIE lens model, whereas the dashed lines correspond to the SIE first order ones.



**Table 2.** Real and first order lens parameters for the twelve SIE models represented respectively in Fig. 6. For each lens model denoted by # i, we have reported the real model parameters (first line) and the retrieved first order ones (second line).

Real	$f$	$\varpi$	$\theta_s$	$\theta$	$\theta_E$	$\theta_s/d$
First order						
#1	0.0991	0	0.2414	5.5107	1.1990	0.4278
	0.0900	3.1177	0.2381	5.5227	1.2407	
#2	0.4898	0.3307	0.1029	2.2189	1.1246	0.4061
	0.4760	0.3227	0.1019	2.2266	1.1272	
#3	0.1932	0.6614	0.1655	2.8239	0.9943	0.3977
	0.1835	0.6723	0.1647	2.8129	1.0023	
#4	0.8959	0.9921	0.0176	6.0540	1.1578	0.4151
	0.8916	0.9935	0.0174	6.0528	1.1579	
#5	0.0991	1.3228	0.1054	0.2658	0.8550	0.2619
	0.0946	1.3225	0.1054	0.2658	0.8729	
#6	0.0442	1.6535	0.1491	6.1133	0.9560	0.3372
	0.0397	1.6563	0.1491	6.1134	1.0058	
#7	0.5573	1.9842	0.0798	1.1888	1.1709	0.3628
	0.5475	1.9846	0.0798	1.1881	1.1696	
#8	0.7725	2.3149	0.0309	4.1916	1.1670	0.3102
	0.7679	2.3157	0.0309	4.1888	1.1663	
#9	0.3119	2.6456	0.1569	3.6847	1.0854	0.4288
	0.2983	2.6470	0.1569	3.6828	1.0872	
#10	0.1790	2.9762	0.2080	4.2419	1.0473	0.4640
	0.1630	2.9980	0.2052	4.2355	1.0807	
#11	0.3390	3.3069	0.0958	2.2684	0.9373	0.3204
	0.3301	0.1577	0.0952	2.2732	0.9418	
#12	0.2101	3.6376	0.2070	3.8973	1.1744	0.4328
	0.1940	0.5068	0.2061	3.8979	1.2098	

tected as multiply imaged, we have selected the most likely redshift of the sources for  $\Omega_m = 0.315$  as well as both values corresponding to the half maxima of the distribution. For each source redshift, we have calculated the differential contribution to the lensing optical depth as a function of the deflector redshift. We have then selected the most likely deflector redshift corresponding to the maximum of this distribution, as well as those corresponding to half of its maxima. Added to this, we have considered the source and lens redshifts of Q2237+0305. The values of the corresponding time delays are summarized in Tables 4, 5 and 6. As expected, we note that the first order time delays for a pair of opposed lensed images are identical to the exact time delays.

#### 4 APPLICATION TO A REAL CASE : Q2237+0305

The gravitational lens Q2237+0305 consists of a quadruply imaged QSO at  $z = 1.695$ , discovered by Huchra et al. (1985) in the CfA Redshift Survey of Galaxies. The deflector which leads to the formation of the lensed images is a nearby 15 mag face-on spiral galaxy, at  $z = 0.0394$  (e.g. Schmidt et al. 1998). Due to its proximity, the lensing galaxy has already been explored in details. Different approaches have been applied to model this system, e.g. a constant mass-to-light ratio (Schneider et al. 1988; Rix et al. 1992;

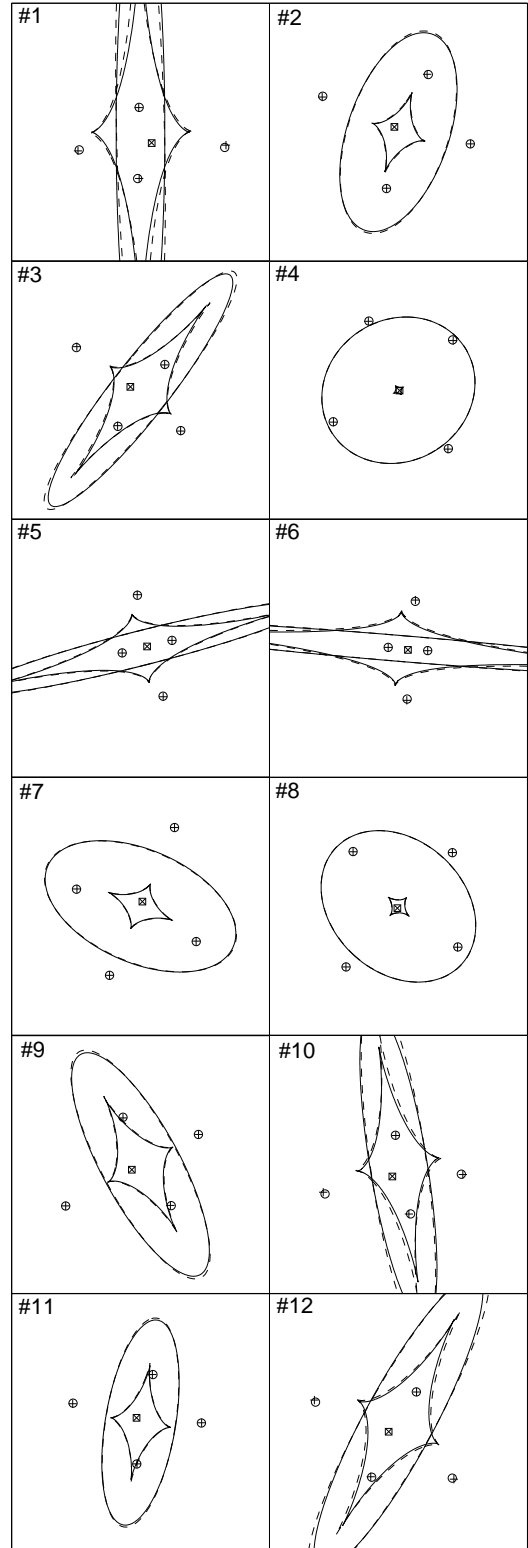


**Figure 6.** Illustration of different lensed image configurations corresponding to the SIE lens model (open circles  $\circ$ ) and the SIE first order one (crosses  $\times$ ). The source positions associated with the SIE lens model (open square  $\square$ ) and the SIE first order one (cross  $\times$ ) are also represented. The lens model parameters were randomly chosen such as  $\theta_s/d(f) \in [0.25, 0.50]$ . The solid lines correspond to the tangential critical and caustic curves deduced from the SIE lens model, whereas the dashed lines correspond to the SIE first order ones.

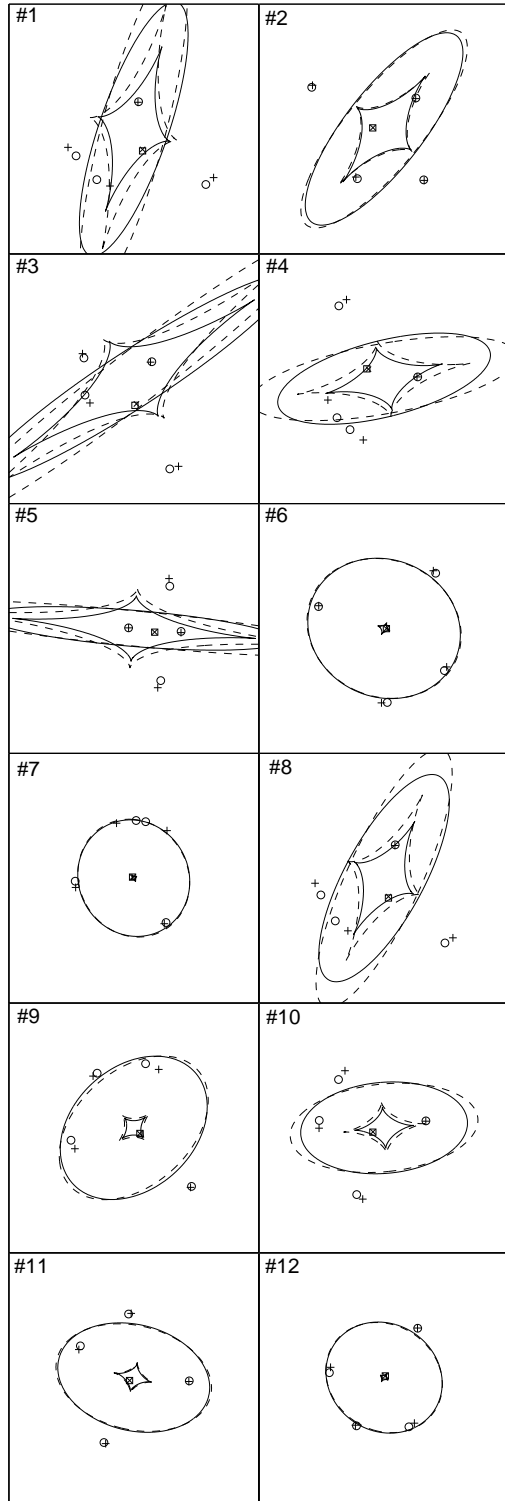


**Figure 7.** Illustration of different lensed image configurations corresponding to the SIE lens model (open circles  $\circ$ ) and the SIE first order one (crosses  $+$ ). The source positions associated with the SIE lens model (open square  $\square$ ) and the SIE first order one (cross  $\times$ ) are also represented. The lens model parameters were randomly chosen such as  $\theta_s/d(f) \in [0.50, 1.25]$ . The solid lines correspond to the tangential critical and caustic curves deduced from the SIE lens model, whereas the dashed lines correspond to the SIE first order ones.

**Table 3.** Real and first order lens parameters for the twelve SIE models represented respectively in Fig. 7. For each lens model denoted by #  $i$ , we have reported the real model parameters (first line) and the retrieved first order ones (second line).

	Real	$f$	$\varpi$	$\theta_s$	$\theta$	$\theta_E$	$\theta_s/d$
First order							
#1	0.2578	0.3307	0.3797	5.0953	1.0881	0.9326	
	0.1858	0.2560	0.3560	5.1187	1.1923		
#2	0.3317	0.6614	0.1831	3.0445	1.0887	0.5194	
	0.3090	0.6805	0.1803	3.0279	1.0997		
#3	0.1522	0.9921	0.4275	4.7548	1.1511	0.8349	
	0.1102	0.9129	0.4068	4.8169	1.2520		
#4	0.3480	1.3228	0.3183	2.6204	1.0330	0.9847	
	0.2588	1.3930	0.2941	2.5930	1.1025		
#5	0.1217	1.6535	0.3406	6.1059	0.8283	0.8909	
	0.0780	1.6678	0.3401	6.1076	1.0078		
#6	0.8842	1.9842	0.0373	6.2076	1.1691	0.7792	
	0.8672	1.9807	0.0367	6.1899	1.1725		
#7	0.9300	2.6456	0.0248	2.4434	0.9144	1.1221	
	0.9066	2.6410	0.0236	2.3989	0.9173		
#8	0.3424	3.6376	0.3250	4.9287	1.0863	0.9449	
	0.2614	0.4324	0.3040	4.9469	1.1578		
#9	0.7360	3.9683	0.1326	5.5470	1.1356	1.1544	
	0.6634	0.8327	0.1321	5.5258	1.1241		
#10	0.5449	4.6297	0.1924	3.5078	0.9882	1.0013	
	0.4648	1.4665	0.1888	3.4897	1.0290		
#11	0.6862	4.9604	0.0829	3.7628	1.0243	0.6551	
	0.6577	1.8069	0.0805	3.7732	1.0266		
#12	0.8936	5.2911	0.0337	0.9354	0.9076	0.9904	
	0.8692	2.1485	0.0337	0.9435	0.9040		

Keeton et al. 1997; Keeton & Kochanek 1998) or multi-parametric models (e.g. a de Vaucouleurs law and King profile, Ken & Falco 1988; singular isothermal sphere and point mass along with external shear, Kochanek 1991; a singular power-law axially symmetric deflector with an external shear, Wambsganss & Paczyński 1994; a non-singular power-law density for the distribution of mass, Chae et al. 1998). The astrometric positions of the four lensed images of Q2237+0305, which come from the CASTLES<sup>1</sup> survey, are listed in Table 7.

For the case of a singular power-law axially symmetric model with external shear, the so-called  $\varepsilon - \gamma$  model, Wertz, Pelgrims & Surdej (2012) have already derived first order equations which link the lensed image positions to the model parameters. As a consequence, we may determine which set of first order equations, between SIE and  $\varepsilon - \gamma$ , leads to the best agreement with the observed lensed images. Furthermore, we have performed numerical modeling in order to independently determine the lens model parameters, for both the  $\varepsilon - \gamma$  and SIE lens models. In addition, we have performed another numerical modeling for the case of the non-singular isothermal ellipsoid with external shear (NSIE +  $\gamma$ ) which constitutes a much more detailed model for the deflector. For this pur-

<sup>1</sup> <http://cfa-www.harvard.edu/castles/>

**Table 4.** Comparison between the values of the time delays derived from the first order equations and the real SIE model. The corresponding lensed image configurations are represented in Fig. 5. The time delays are expressed in days.

Model index	$z_s$	$z_l$		Time delays (real)	Time delays (to first order)
# 1	1.695	0.039	$\Delta t_{01}$	1.95	1.97
			$\Delta t_{02}$	0.76	0.76
			$\Delta t_{03}$	1.97	1.99
# 2	1.695	0.217	$\Delta t_{01}$	3.44	3.47
			$\Delta t_{02}$	0.70	0.70
			$\Delta t_{03}$	2.98	3.01
# 3	1.695	0.54	$\Delta t_{01}$	29.47	29.68
			$\Delta t_{02}$	8.59	8.59
			$\Delta t_{03}$	30.34	30.55
# 4	1.695	0.97	$\Delta t_{01}$	47.91	48.32
			$\Delta t_{02}$	14.14	14.14
			$\Delta t_{03}$	45.19	45.60
# 5	2.350	0.039	$\Delta t_{01}$	0.29	0.30
			$\Delta t_{02}$	-0.002	-0.002
			$\Delta t_{03}$	0.37	0.38
# 6	2.350	0.263	$\Delta t_{01}$	8.37	8.37
			$\Delta t_{02}$	-0.25	-0.25
			$\Delta t_{03}$	8.15	8.15
# 7	2.350	0.66	$\Delta t_{01}$	6.32	6.40
			$\Delta t_{02}$	2.04	2.04
			$\Delta t_{03}$	6.55	6.63
# 8	2.350	1.294	$\Delta t_{01}$	35.11	36.03
			$\Delta t_{02}$	14.47	14.47
			$\Delta t_{03}$	42.55	43.47
# 9	3.260	0.039	$\Delta t_{01}$	1.01	1.01
			$\Delta t_{02}$	-0.12	-0.12
			$\Delta t_{03}$	0.88	0.88
# 10	3.260	0.297	$\Delta t_{01}$	4.01	4.16
			$\Delta t_{02}$	-0.11	-0.11
			$\Delta t_{03}$	3.16	3.30
# 11	3.260	0.76	$\Delta t_{01}$	2.13	2.13
			$\Delta t_{02}$	-0.11	-0.11
			$\Delta t_{03}$	1.80	1.80
# 12	3.260	1.578	$\Delta t_{01}$	2.39	2.46
			$\Delta t_{02}$	-1.18	-1.18
			$\Delta t_{03}$	1.99	2.05

**Table 5.** Comparison between the values of the time delays derived from the first order equations and the real SIE model. The corresponding lensed image configurations are represented in Fig. 6. The time delays are expressed in days.

Model index	$z_s$	$z_l$		Time delays (real)	Time delays (to first order)
# 1	1.695	0.039	$\Delta t_{01}$	1.11	1.33
			$\Delta t_{02}$	-1.89	-1.89
			$\Delta t_{03}$	2.00	2.23
# 2	1.695	0.217	$\Delta t_{01}$	3.27	3.79
			$\Delta t_{02}$	-5.12	-5.12
			$\Delta t_{03}$	5.96	6.48
# 3	1.695	0.54	$\Delta t_{01}$	13.63	15.00
			$\Delta t_{02}$	-18.32	-18.32
			$\Delta t_{03}$	9.81	11.18
# 4	1.695	0.97	$\Delta t_{01}$	5.28	5.68
			$\Delta t_{02}$	2.99	2.99
			$\Delta t_{03}$	8.03	8.43
# 5	2.350	0.039	$\Delta t_{01}$	1.00	1.06
			$\Delta t_{02}$	-0.01	-0.01
			$\Delta t_{03}$	1.40	1.46
# 6	2.350	0.263	$\Delta t_{01}$	6.02	6.54
			$\Delta t_{02}$	0.55	0.55
			$\Delta t_{03}$	8.57	9.09
# 7	2.350	0.66	$\Delta t_{01}$	9.40	10.26
			$\Delta t_{02}$	-11.46	-11.46
			$\Delta t_{03}$	9.11	9.97
# 8	2.350	1.294	$\Delta t_{01}$	13.39	13.87
			$\Delta t_{02}$	6.62	6.62
			$\Delta t_{03}$	14.75	15.23
# 9	3.260	0.039	$\Delta t_{01}$	2.64	2.77
			$\Delta t_{02}$	1.72	1.72
			$\Delta t_{03}$	2.69	2.82
# 10	3.260	0.297	$\Delta t_{01}$	11.85	13.02
			$\Delta t_{02}$	7.12	7.12
			$\Delta t_{03}$	17.46	18.63
# 11	3.260	0.76	$\Delta t_{01}$	7.00	7.60
			$\Delta t_{02}$	-6.85	-6.85
			$\Delta t_{03}$	11.10	11.70
# 12	3.260	1.578	$\Delta t_{01}$	32.60	35.52
			$\Delta t_{02}$	-9.04	-9.04
			$\Delta t_{03}$	15.75	18.67

pose, the function of merit to be minimized is the following :

$$\chi_r^2 = \frac{1}{N} \sum_{j=0}^3 \left( \frac{x_1^{(j)} - \underline{x}_1^{(j)}}{\sigma_1^{(j)}} \right)^2 + \frac{1}{N} \sum_{j=0}^3 \left( \frac{x_2^{(j)} - \underline{x}_2^{(j)}}{\sigma_2^{(j)}} \right)^2, \quad (42)$$

where  $N$  represents the number of degrees of freedom,  $\sigma_1^{(j)}$  (resp.  $\sigma_2^{(j)}$ ) the measured uncertainties affecting the observed positions  $x_1^{(j)}$  (resp.  $x_2^{(j)}$ ), and  $\underline{x}_i^{(j)}$  the image positions derived from the numerical inversion of the lens equation characterized by the deduced model parameters. For the case of the SIE (resp.  $\varepsilon - \gamma$  and NSIE +  $\gamma$ ) model, the number of independent parameters equals 3 (resp. 4 and 6). Therefore, the corresponding number of degrees of freedom is  $N_{\text{SIE}} = 5$  (resp.  $N_{\varepsilon-\gamma} = 4$  and  $N_{\text{NSIE}+\gamma} = 2$ ). The global

optimization has been performed using a sophisticated genetic algorithm, called *Ferret* (Fiege et al. 2004), which is a component of the Qubist Global Optimization Toolbox (Fiege 2010). The best sets of parameters for both the SIE and  $\varepsilon - \gamma$  models, as well as first order lens parameters are summarized in Table 8.

We have assumed that the errors are described by a normal distribution and are uncorrelated. Therefore, the probability that the error of a single measurement lies in the interval  $[-a, a]$  is given by  $p = \text{erf}(a/(\sigma\sqrt{2}))$  where  $\text{erf}(\cdot)$  represents the error function. As a consequence, the corresponding inverse of the  $\chi^2$  cumulative distribution function with the number of degrees of freedom specified by  $N_{\text{SIE}} = 5$  is given by  $\chi_{\text{cutoff}}^2 = F^{-1}(p|N_{\text{SIE}}) = \{\chi_{\text{cutoff}}^2 : F(\chi_{\text{cutoff}}^2|N_{\text{SIE}}) =$

**Table 6.** Comparison between the values of time delays derived from the first order equations and the real SIE model. The corresponding lensed image configurations are represented in Fig. 7. The time delays are expressed in days.

Model index	$z_s$	$z_l$		Time delays (real)	Time delays (to first order)
# 1	1.695	0.039	$\Delta t_{01}$	4.66	5.32
			$\Delta t_{02}$	2.62	2.62
			$\Delta t_{03}$	2.69	3.35
# 2	1.695	0.217	$\Delta t_{01}$	6.99	8.04
			$\Delta t_{02}$	-8.98	-8.98
			$\Delta t_{03}$	3.09	4.14
# 3	1.695	0.54	$\Delta t_{01}$	64.40	71.77
			$\Delta t_{02}$	47.63	47.63
			$\Delta t_{03}$	49.56	56.93
# 4	1.695	0.97	$\Delta t_{01}$	33.93	44.81
			$\Delta t_{02}$	-46.41	-46.41
			$\Delta t_{03}$	0.21	11.09
# 5	2.350	0.039	$\Delta t_{01}$	0.74	1.26
			$\Delta t_{02}$	0.23	0.23
			$\Delta t_{03}$	2.11	2.63
# 6	2.350	0.263	$\Delta t_{01}$	0.31	0.71
			$\Delta t_{02}$	-0.77	-0.77
			$\Delta t_{03}$	2.54	2.94
# 7	2.350	0.66	$\Delta t_{01}$	3.13	3.62
			$\Delta t_{02}$	0.81	0.81
			$\Delta t_{03}$	0.82	1.31
# 8	2.350	1.294	$\Delta t_{01}$	77.74	88.43
			$\Delta t_{02}$	42.18	42.18
			$\Delta t_{03}$	43.04	53.73
# 9	3.260	0.039	$\Delta t_{01}$	1.51	1.80
			$\Delta t_{02}$	1.46	1.46
			$\Delta t_{03}$	1.61	1.89
# 10	3.260	0.297	$\Delta t_{01}$	11.80	13.91
			$\Delta t_{02}$	2.73	2.73
			$\Delta t_{03}$	3.27	5.39
# 11	3.260	0.76	$\Delta t_{01}$	12.11	13.19
			$\Delta t_{02}$	6.23	6.23
			$\Delta t_{03}$	7.51	8.60
# 12	3.260	1.578	$\Delta t_{01}$	0.35	1.03
			$\Delta t_{02}$	-3.56	-3.56
			$\Delta t_{03}$	0.52	1.20

**Table 7.** The lensed image positions for the Q2237+0305 system from the CASTLES<sup>1</sup> survey.

	$-\Delta\alpha$ (in arcsec)	$\Delta\delta$ (in arcsec)
A	0.0	0.0
B	$0.673 \pm 0.003$	$1.697 \pm 0.003$
C	$-0.635 \pm 0.003$	$1.210 \pm 0.003$
D	$0.866 \pm 0.003$	$0.528 \pm 0.003$
G	$0.075 \pm 0.004$	$0.939 \pm 0.003$

**Table 8.** Optimal SIE and  $\varepsilon$ - $\gamma$  lens parameters for the Q2237+0305 system, derived by the *Ferret* sophisticated genetic algorithm which is a component of the Qubist Global Optimization Toolbox.

	SIE	SIE First order	$\varepsilon - \gamma$	$\varepsilon - \gamma$ First order	NSIE + $\gamma$
$\chi_r^2$	1.5466	12.204	18.165	-	0.01342
$f$	$0.6649^{+0.0100}_{-0.0094}$	$0.6479^{+0.0097}_{-0.0097}$	-	-	$0.6634^{+0.0110}_{-0.0096}$
$\varpi$	$1.9720^{+0.0028}_{-0.0029}$	$1.9686^{+0.0024}_{-0.0024}$	-	-	$2.0111^{+0.0023}_{-0.0023}$
$\varepsilon$	-	-	$0.6653^{+0.0100}_{-0.0094}$	1.5949	-
$\gamma$	-	-	$0.1047^{+0.0100}_{-0.0094}$	-0.0292	$0.0138^{+0.00012}_{-0.00012}$
$\omega$	-	-	$2.7437^{+0.0100}_{-0.0094}$	1.1729	$2.7107^{+0.0010}_{-0.0010}$
$\theta_s$	$0.0652^{+0.0021}_{-0.0021}$	$0.0669^{+0.0035}_{-0.0035}$	$0.0595^{+0.0100}_{-0.0094}$	-0.0166	$0.0632^{+0.0012}_{-0.0011}$
$\theta$	$6.1261^{+0.0150}_{-0.0146}$	$6.0629^{+0.0408}_{-0.0408}$	$6.0589^{+0.0100}_{-0.0094}$	6.0524	$6.1236^{+0.0119}_{-0.0118}$
$\theta_E$	$0.8974^{+0.0023}_{-0.0023}$	$0.9024^{+0.0021}_{-0.0021}$	$0.8812^{+0.0100}_{-0.0094}$	0.8865	$0.9396^{+0.0019}_{-0.0019}$
$\rho_c$	-	-	-	-	$0.0332^{+0.0013}_{-0.0013}$
$\Delta x_A$	0.0031	0.0163	0.0064	-	0.0028
$\Delta x_B$	0.0087	0.0097	0.0082	-	0.0020
$\Delta x_C$	0.0082	0.0006	0.0210	-	0.0030
$\Delta x_D$	0.0036	0.0268	0.0335	-	0.0027

**Notes.** The parameters  $\varepsilon$  represents the slope of the power-law mass distribution,  $\gamma$  the magnitude of the external shear,  $\omega$  the orientation of the external shear and  $\rho_c$  the size of the core radius in arcsec. The lower and upper limits correspond to the range of the lens parameters used by the genetic algorithm routine. The distances between the lensed images and the modelled images are represented by  $\Delta x$ .

$p$ ) where :

$$F(\chi_{\text{cutoff}}^2 | N_{\text{SIE}}) = \int_0^{\chi_{\text{cutoff}}^2} \frac{t^{(N_{\text{SIE}}-2)} e^{-t/2}}{2^{N_{\text{SIE}}/2} \Gamma(N_{\text{SIE}}/2)} dt. \quad (43)$$

For a 1- $\sigma$  error calculation, we have found  $\chi_{\text{cutoff}}^2 = 5.8876$  which leads to the reduced value  $\chi_{r,\text{cutoff}}^2 = 1.1775$ . Finally, we have separately constructed 1-D paraboloid-like curves of best  $\chi_r^2$  as a function of each lens model parameter. The  $\chi_{r,\text{cutoff}}^2$  associated with these curves gives the value of the error bars (see Table 8, columns 1 and 3). Concerning the uncertainties of the first order lens parameters, we have derived them by means of the Monte Carlo method.

The SIE lens model shows the best agreement with the observed image positions in comparison with the  $\varepsilon - \gamma$  model :  $\langle \Delta x_{\text{SIE}} \rangle = 0.0059$  arcsec whereas  $\langle \Delta x_{\varepsilon-\gamma} \rangle = 0.0173$  arcsec. Therefore, this is what convinces us to use the SIE first order equations instead of the  $\varepsilon - \gamma$  ones. Furthermore, for the case of the  $\varepsilon - \gamma$  model, the first order values of  $\gamma$  and  $\theta_s$  appear to be non physical. However, we note that the determined value of  $\theta_E$  is similar for both lens models which seems to indicate that the determination of the Einstein angular radius very slightly depends on the choice of the deflector's family of models. We notice that both sets of lens parameters (SIE and first order SIE) are quite similar, which leads to the conclusion that the use of the first order astrometric equations is justified here. For both SIE and first order SIE models, we have derived the value of  $\theta_s/d$  and  $D/d$  from the parameters found in Table 8. For the case of SIE, one finds  $\theta_s/d = 0.5438$ ,  $D/d = 0.5649$ , and for the case of first order SIE,  $\theta_s/d = 0.5231$  and  $D/d = 0.6054$ .

The NSIE +  $\gamma$  model shows the best agreement with the observed lensed image positions in comparison with the SIE model :

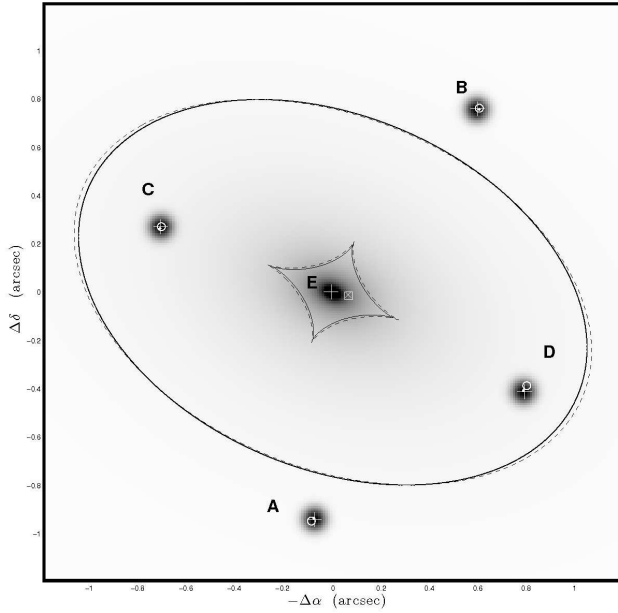


**Figure 8.** Illustration of the Q2237+0305 gravitational lens system. We have represented the corresponding surface mass density  $\kappa(\rho)$  characterized by the model parameters  $f$  and  $\varpi$ , as derived from the first order equations. We have both represented the lensed image positions and the source position, all of them from the model derived by the numerical SIE fitting (see the dots  $\bullet$ ), the NSIE +  $\gamma$  (see the crosses  $+$ ) and the first order equations (see the open circles  $\circ$ ). The diamond-shape and ellipse-shape solide lines represent the numerically derived tangential caustic and critical curves, respectively. The diamond-shape and ellipse-shape dashed lines represent the corresponding first order tangential caustic and critical curves, respectively.

$\langle \Delta x_{\text{NSIE}+\gamma} \rangle \approx 0.0026$  arcsec, which is smaller than the precision of the observed image positions (see Table 7). The large number of independent parameters ( $N_{\text{NSIE}+\gamma} = 6$ ) and the very high precision on the modeled image positions explain why we have found  $\chi_r^2 \ll 1$ . We note that the parameters  $f, \varpi, \theta_s$  and  $\theta$  between the SIE and NSIE +  $\gamma$  models are very similar, which seems to indicate that the NSIE +  $\gamma$  derived numerical solution is the best for this model, i.e. not a local minimum. The addition of a core leads to the appearance of a fifth lensed image, denoted by  $E$ , located very close to the gravity center of the deflector:  $-\Delta\alpha = -0.0069$  arcsec and  $\Delta\delta = 0.0018$  arcsec. The observational existence of a fifth lensed image has first been reported by Racine (1991), but it has never been independently confirmed. For the case of the SIE, the first order SIE and the NSIE +  $\gamma$  models, we have derived the values of the time delays (in hours) and amplification ratio between the lensed image A and the other ones. We have summarized all these informations in Table 9. As expected, the comparison between the values of the time delay  $\Delta t_{AB}$  (resp.  $\Delta t_{CD}$ ) for the case of the SIE and the first order SIE models are extremely close. Indeed, we have shown that the first order time delay expression (Eq. (38)) is identical to the one derived by Witt et al. (2000). Since Eq. (38) remains valid without any approximation for any pairs of lensed images, Eq. (35) seems to be useless. However, the SIE (resp.  $\varepsilon - \gamma$ ) first order Eqs. (20), (23), (24), (27) and (28) have the advantage to test straightforwardly, and without any numerical simulations, to what extent the SIE (resp.  $\varepsilon - \gamma$ ) family of models constitutes a good choice and therefore whether the derived values for the time delays and amplification ratios are trustworthy. Without using these first order equations, Eq. (38) could still be applied to any symmet-

**Table 9.** Comparison between the values of the time delays (in hours) and amplification ratios between two lensed images derived from the first order equations and the real SIE and NSIE +  $\gamma$  models for Q2237+0305.

	SIE	SIE First order	NSIE + $\gamma$
$\Delta t_{AD}/h$	$-5.3821 \pm 0.6841$	$-7.2966 \pm 0.5278$	$-5.4112 \pm 0.4291$
$\Delta t_{AB}/h$	$2.5992 \pm 0.7172$	$2.5983 \pm 0.6152$	$2.5080 \pm 0.5192$
$\Delta t_{AC}/h$	$-17.969 \pm 0.6969$	$-19.877 \pm 0.7448$	$-18.009 \pm 0.6192$
$\Delta t_{CD}/h$	$12.587 \pm 0.6849$	$12.580 \pm 0.6541$	$12.597 \pm 0.5812$
$\mu_B/\mu_A$	0.797172	-	0.84483
$\mu_C/\mu_A$	-0.184621	-	-0.29492
$\mu_D/\mu_A$	-0.305474	-	-0.49083
$\mu_E/\mu_A$	-	-	0.0012186

**Notes.** We have fixed the value of the Hubble parameter to  $67.3 \pm 1.2$  km  $s^{-1} \text{Mpc}^{-1}$  and the matter density parameter  $\Omega_m = 0.315 \pm 0.017$  (Planck Collaboration 2013).

**Table 10.** Model predictions for the time delays (in hours)  $\Delta t_{AB}$ ,  $\Delta t_{AC}$  and  $\Delta t_{AD}$  for Q2237+0305.

Reference	Lens model	$\Delta t_{AB}/h$	$\Delta t_{AC}/h$	$\Delta t_{AD}/h$
Schneider et al. (1988)	Constant mass-to-light ratio	2.4	29.5	26.6
	Best fit	0.54	-6.48	-6.12
Rix et al. (1992)	Model 1	-2.1	-11	-7.1
	Model 2	-1.5	-10.1	-6.1
	Model 2a	1.7	-9.8	-3.7
	Best fit	1.3	-7.4	-2.8
Wambsganss and Paczyński (1994)	Point lens	2.97	-17.41	-4.87
	SIS	1.51	-8.91	-2.46
	Best fit	0.44	-2.54	-0.7
Schmidt et al. (1996)	Bar accounted	2.0	-16.2	-4.9
Chae et al. (1998)	Triaxial model	[0.13,3.4]	[-16.6,-0.77]	[-5.5,-0.22]

**Notes.** The model 1 by Rix et al. (1992) refers to a  $R^{1/4}$  profile, model 2,  $R^{1/4}$  with unresolved nucleus and model 2a is identical to model 2 with only image positions fitted. The model in Schmidt et al. (1996) takes into account the central galaxy bar.

ric quadruply imaged quasar but without the immediate confidence that the SIE family of models constitutes a good approximation to represent the mass distribution. For Q2237+0305, we have shown that the  $\varepsilon - \gamma$  family of models did not properly fit the lensed image positions while the SIE family of models does.

The values of the estimated time delay listed in Table 9 can be compared with those in Table 10 which constitutes a summary of the model predictions for Q2237+0305. A description of the corresponding lens models may be found in Vakulik et al. (2006). We note that the determination of the time delays depends on the considered models. Unfortunately, the possibility of measuring very accurate time delays between two lensed images from their light curves seems to be very difficult. Different attempts have already been performed (see e.g. Koptelova et al. 2006 and Vakulik et al. 2006) but none of them allows the authors to definitely conclude. The uncertainties obtained, which correspond to a 95 % confidence

level, exceed 100%. Therefore, we are not able to compare the measured and the predicted time delays. In order to estimate the value of the Hubble parameter with, at least, the same precision as the Planck collaboration (2013), we have calculated that the uncertainties on  $\Delta t_{AB}$  and  $\Delta t_{CD}$  should be respectively smaller than  $\sigma_{AB} \leq 0.0465$  hours (i.e. 2.8 minutes) and  $\sigma_{CD} \leq 0.225$  hours (i.e. 13.5 minutes).

## 5 CONCLUSIONS

Use of the first order equations leads to a straightforward method of determining whether the deflector's mass distribution can be modeled with the SIE or  $\varepsilon - \gamma$  family of models, without the need of any precise model fitting. We have retrieved the same expression for the time delays between pairs of opposite lensed images as already published by Witt & al. (2000). However, combined with the first order equations, we could easily estimate the validity of these time delay estimates and the relevance of the use of such a family of models. In order to obtain a mean astrometric error  $\leq 0.003$  arcsec, the validity range of the first order equations has been estimated to be  $\theta_s < 0.13 d(f)$  which is similar to the one already deduced for the  $\varepsilon - \gamma$  family of models (see Wertz & al. 2012).

Application to the quadruply imaged quasar Q2237+0305 constitutes a very interesting way of comparing the results of accurate SIE modeling with those derived from the first order equations. We have noticed that the model parameters deduced from the first order equations and the numerical fit are very closed. This leads to the conclusion that the numerical fit, besides being time consuming, does not bring any significant improvement in this case. The degree of misalignment has been evaluated to  $\theta_s/d = 0.5438 > 0.13$ . This latter value allows to understand why the mean astrometric error  $< \Delta x_{1st\ order} > = 0.0134$  arcsec is larger than the 0.003 arcsec which corresponds to the error on the observed positions.

Unfortunately, the uncertainties obtained for the observed time delays between the light curves of pairs of lensed images make any comparison very risky. However, we have shown that in order to derive the Hubble parameter with a high precision requires very accurate values for the time delays. Therefore, we suggest that monitoring the gravitational lens system Q2237+0305 with a very high time sampling should constitute a promising way of determining accurate values of the time delays and a precise determination of the Hubble parameter based upon gravitational lensing.

## ACKNOWLEDGMENTS

We thank J. Fiege for gratefully providing his very performing Qubist Global Optimization Toolbox. OW thanks the Belgian National Fund for Scientific Research (FNRS). JS and OW acknowledge support from the Communauté française de Belgique - Actions de recherche concertées - Académie universitaire Wallonie-Europe, from the ESA PRODEX Programme "GAIA", and from the Belgian Federal Science Policy Office.

## REFERENCES

- Alard C., 2007, MNRAS, 382, L58-L62  
 Bourassa R. R., Kantowski R., 1973, ApJ, 185, 747  
 Bourassa R. R., Kantowski R., 1975, ApJ, 195, 13  
 Brai I., 1984, MNRAS, 208, 511-516  
 Chae K-H., Khersonsky V., Turnshek D., 1998, AJ, 506, 80-92

- Fiege J., Johnstone D., Redman R., Feldman P., 2010, AJ, 616, 925-942  
 Fiege J., 2010, AJ, Qubist Users Guide: Optimization, Data Modeling, and Visualization with the Qubist Optimization Toolbox for MATLAB (Winnipeg, Canada: nQube Technical Computing)  
 Finet F., PhD Thesis, 2013, <http://hdl.handle.net/2268/146860>  
 Huchra J., Gorenstein M., Kent S., Shapiro I., Smith G., Horine E., Perley R., 1985, AJ, 90, 691-696  
 Keeton C. R., Kochanek C. S., 1998, ApJ, 495, 157  
 Keeton C. R., Kochanek C. S., Seljak U., 1997, ApJ, 482, 604  
 Kent S. M., Falco E. E., 1988, AJ, 96, 1570  
 Kochanek C. S., 1991, ApJ, 373, 354  
 Koptelova E., Oknyanskij V., Shimanovskaya, E., 2006, A&A, 452, 37-46  
 Kormann R., Schneider P., Bartelmann M., 1994, A&A, 284, 285-299  
 Planck Collaboration, 2013, eprint arXiv:1303.5076  
 Racine R., 1991, AJ, 102, 454-460  
 Refsdal S., 1964a, MNRAS, 128, 295  
 Refsdal S., 1964b, MNRAS, 128, 307  
 Rix H. W., Schneider D. P., Bahcall J. N., 1992, AJ, 104, 959  
 Schmidt R., Webster R., Lewis Geraint F., 1998, MNRAS, 295, 488  
 Schneider D. P., Turner E. L., Gunn J. E., Hewitt J. N., Schmidt M., Lawrence C. R., 1988, AJ, 95, 1619; Erratum, 1988, AJ, 96, 1755  
 Vakulik V., Schild R., Dudinov V., Nuritdinov S., Tsvetkova V., Burkhanov O., Akhunov T., 2006, A&A, 447, 905-913  
 Wambsgans J., Paczyński B., 1994, AJ, 108, 1156  
 Wertz O., Pelgrims V., Surdej J., 2012, MNRAS, 424 : 1543-1555  
 Witt H., Mao S., Keeton C., 2000, AJ, 544, 98-103

This paper has been typeset from a  $\text{\TeX}/\text{\LaTeX}$  file prepared by the author.

# 3

## USE OF THE FOURIER TRANSFORM TO DERIVE SIMPLE EXPRESSIONS FOR THE GRAVITATIONAL LENS DEFLECTION ANGLE

---

### **3.1** Introduction

---

Since the deflection angle is directly related to the lensing mass distribution, using its explicit expression constitutes a real advantage in order to deeply investigate the associated lens mapping. For the case of axially symmetric mass distributions, the expression of the deflection angle  $\hat{\alpha}(\mathbf{x})$  reduces to a very simple form (see Eq. (1.148)) which constitutes a great simplification of the general form appearing in Eq. (1.111). Unfortunately, for the case of more complicated mass distributions, the derivation of the explicit expression of the deflection angle turns out to be very difficult, or even not possible. In such a case, two ways can be investigated : to adopt alternative analytical methods or to make use of numerical calculations. In the first case, let us mention the use of the Green functions in order to determine the SIE deflection potential (see Kormann & al., 1994), or the complex representation of the lensing theory introduced by Bourassa & Kantowski (1975), corrected by Bray (1984). For more details, see Section 1.11 or the related papers. Furthermore, even if the use of Eq. (1.111) leads to the determination of the explicit expression of  $\hat{\alpha}(\mathbf{x})$ , the results obtained are sometimes so complicated that it may cause strong limitations on further analytical treatments. Let us mention the case of the non-singular isothermal ellipsoid (NSIE) studied by Kormann & al. (1994).

The deflection angle can always be deduced from the deflection potential  $\hat{\psi}(\mathbf{x})$  defined by Eq. (1.112). However, if the explicit expression of  $\hat{\alpha}(\mathbf{x})$  may not be obtained from Eq. (1.111), the expression of  $\hat{\psi}(\mathbf{x})$  may neither, in general, be explicitly deduced from Eq. (1.112). As a

consequence, since the expression of the time delays between pairs of lensed images is a function of  $\hat{\psi}(\mathbf{x})$ , their determinations require also alternative methods.

In the second case, numerical calculations can always be used to derive, from Eq. (1.111), the deflection angle which affects a light ray characterized by the impact parameter  $\mathbf{x}$ . Such an approach has the disadvantages, in addition to be time consuming, to remove the possibility of deeply understanding the characteristics of the lens mapping. In addition, due to its non-linearity, the lens equation (see Eq. (1.110)) can only be analytically inverted for very particular types of deflectors, e.g. black holes, SIS or an infinite sheet with a constant surface mass density. For the majority of deflector models, the use of the numerical techniques is then mandatory. For instance, in the framework of the statistical approach of the gravitational lensing phenomenon, a huge amount of lens equation inversions is required. As a consequence, using the explicit expression of the deflection angle constitutes a real advantage. However, let us note that for the case of galaxy clusters and large-scale structure lensing, numerical techniques constitute a better way to obtain detailed models. More details about numerical techniques can be found in the excellent proceedings contribution "*Numerical Methods in Gravitational Lensing*" by M. Bartelmann (2003). To this end, the deflection angle can be expressed as the convolution of the surface mass density with a kernel. This allows the use of the Fourier theory which is already implemented in very robust algorithms.

According to this, we have investigated the possibility of elaborating a general method to analytically derive expressions of  $\hat{\alpha}(\mathbf{x})$  in the strong lensing regime by making use of the Fourier theory. To this end, we have expressed the deflection angle in terms of Fourier transforms of the dimensionless surface mass density. Then, we have applied this method to the case of homoeoidal symmetric mass distributions which englobe a large variety of already known deflectors, e.g. SIS, SIE or NSIE. Such a family of models has already been investigated by Bourassa & Kantowski (1973, 1975), but without having obtained separate expressions for each component of  $\hat{\alpha}(\mathbf{x})$  (see Eq. (1.191)). Making use of the Fourier approach, we have derived the expressions of the two components of the deflection angle for the case of homoeoidal symmetric mass distributions. The latter result has been summarized in the paper entitled "*Use of the Fourier transform to derive simple expressions for the gravitational lens deflection angle*" published in the peer reviewed journal Monthly Notices of the Royal Astronomical Society (MNRAS) 437, 1051-1055, 2014 (advance access publication 2013 November 26). The full content of this paper, referred in the remainder as to Paper III, is presented in Section 3.2. Several additional calculations are presented respectively in Sections 3.3, 3.4, 3.5 and 3.6.



As an application of the Fourier approach, we have investigated the NSIE family of models. The derived expression for the deflection angle turns out to be more simple than the one already presented by Kormann & al. (1994). These results have allowed us to derive the expression of the deflection potential, in agreement with the one presented by Keeton & Kochanek (1998). Nevertheless, we have performed a complete and original analysis of the critical and caustic curves for which we have derived a complete analytical solution. The latter result has been summarized in the paper entitled "*The non-singular isothermal ellipsoid lens model : a complete analytical solution*" and submitted to the peer reviewed journal MNRAS on 3rd February, 2014. The full content of this paper, referred in the remainder as to Paper IV, is presented in Section 3.7. Several illustrations of such a model are presented in Section 3.8.



**3.2** Paper III

---

# Use of the Fourier transform to derive simple expressions for the gravitational lens deflection angle

O. Wertz and J. Surdej

*Monthly Notices of the Royal Astronomical Society*, 2014, **437**, 1051-1055.



# Use of the Fourier transform to derive simple expressions for the gravitational lens deflection angle

O. Wertz<sup>★†</sup> and J. Surdej<sup>‡</sup>

*Institut d'Astrophysique et de Géophysique, Liège University, Bât. B5c, Allée du 6 Août 17, Sart Tilman, B-4000 Liège, Belgium*

Accepted 2013 September 24. Received 2013 September 24; in original form 2013 July 8

## ABSTRACT

Knowing that the gravitational lens deflection angle can be expressed as the convolution product between the dimensionless surface mass density  $\kappa(\mathbf{x})$  and a simple function of the scaled impact parameter vector  $\mathbf{x}$ , we make use of the Fourier transform to derive its analytical expression for the case of mass distributions presenting a homoeoidal symmetry. For this family of models, we obtain the expression of the two components of the deflection angle in the form of integrals performed over the radial coordinate  $\rho$ . In the limiting case of axially symmetric lenses, we obviously retrieve the well-known relation  $\hat{\alpha}(\mathbf{x}) \propto M(\leq |\mathbf{x}|)\mathbf{x}/|\mathbf{x}|^2$ . Furthermore, we derive explicit solutions for the deflection angle characterized by dimensionless surface mass density profiles such as  $\kappa \propto (\rho_c^2 + \rho^2)^{-\nu}$ ; corresponding to the non-singular isothermal ellipsoid model for the particular case  $\nu = 1/2$ . Let us insist that all these results are obtained without using the complex formalism introduced by Bourassa and Kantowski. Further straightforward applications of this Fourier approach are suggested in the conclusions of this work.

**Key words:** gravitational lensing: strong – methods: analytical.

## 1 INTRODUCTION

Gravitational lens effects consist in the bending of light rays from a background source, under the influence of a foreground mass distribution along the line of sight (e.g. stars, galaxies, clusters of galaxies, etc.). The study of this phenomenon requires realistic lens models which fully account for the observed lensed image configurations, lensed image amplifications and/or time delays between lensed images. From observation, we know that an appreciable fraction of galaxies shows elliptical isophotes which suggest an elliptical mass distribution. First, axially symmetric lenses perturbed by an external large-scale gravitational field, the external shear, were studied in detail by Chang & Refsdal (1984), Kochanek (1991), Wambsganss & Paczyński (1994) and An & Evans (2006), etc. Those types of models have the advantage to be mathematically simple to use. For instance, for the case of a nearly perfect alignment among a point-like source, a power-law mass distribution perturbed by an external shear and an observer, all lens model parameters can be directly derived from the first-order astrometric equations (Wertz, Pelgrims & Surdej 2012). Another approach consists in considering lenses characterized by an elliptical symmetry, i.e. with isodensity contours represented by concentric ellipses (so-called homoeoidal

symmetry). Although the parameters of the elliptical isophotes may vary with the major axis, the isophotes may as well turn out to be ‘twisted’. An elliptical lens is considered to be an adequate model to represent observed gravitational lens systems (Schramm 1990). We note that elliptical potentials may also be used as lens models and these are mathematically easier to handle than elliptical mass distributions. But for large ellipticities (e.g.  $\epsilon \gtrsim 0.5$ ), the corresponding mass distributions turn out to be unphysical (Kassiola & Kovner 1993).

Whether considering the determination of the image positions, image amplification ratios and/or time delays between observed lensed images, the expression of the deflection angle (or deflection potential) needs to be calculated for any given model. According to the complexity of the expression for the dimensionless surface mass density  $\kappa(\mathbf{x})$ , the determination of the deflection angle may turn out to be very complicated. For the case of elliptical mass distributions, Bourassa, Kantowski & Norton (1973) first derived the expression of the deflection angle using a complex formalism (Bourassa & Kantowski 1975; corrected by Bray 1984) which is rather difficult to apply. According to this formalism, the lens equation is given by

$$y_c = x_c + I_c^*(x_c), \quad (1)$$

with the complex deflection angle (the scattering function)

$$I_c(x_c) = -2 \operatorname{sign}(x_c) \cos(\beta) \int_0^\rho \frac{\rho' \kappa(\rho')}{\sqrt{x_c^2 - \rho'^2 \sin^2(\beta)}} d\rho', \quad (2)$$

<sup>★</sup> E-mail: wertz@astro.ulg.ac.be

<sup>†</sup> Aspirant du F.R.S. - FNRS.

<sup>‡</sup> Also Directeur de Recherche honoraire du F.R.S. -FNRS.

where  $y_c = y_1 + \iota y_2$  represents the complex source position,  $x_c = x_1 + \iota x_2$  the complex image positions,  $\rho$ , the radial coordinate and  $1/\cos(\beta) = (1 - \epsilon)$  with  $\epsilon$  the ellipticity of the mass distribution.

It turns out that separating the two components of the deflection angle (equation (2)) is extremely difficult (Schneider, Ehlers & Falco 1992). An alternative equivalent formulation has been derived by Schramm (1990) from results of the classical three-dimensional potential and ellipse theories. However, analytical solutions occur only for very special or simple surface mass density expressions. Let us however note that for numerical evaluation, their formulation represents a very efficient tool.

In this paper, we propose to use the well-known fact that the deflection angle can be expressed as a convolution product (e.g. Bartelmann 2003), in order to analytically derive, with the help of Fourier analysis, the expression of the two components of the deflection angle (Section 2) without the need of invoking complex expressions.

We first apply this new approach to the case of elliptical lenses and derive the explicit expression of the deflection components for mass distributions obeying the law  $\kappa \propto (\rho_c^2 + \rho^2)^{-\nu}$ , in particular for the cases of the non-singular isothermal ellipsoid (NSIE;  $\nu = 1/2$ ) and axially symmetric lenses ( $f = 1$ , see Section 3). Some general conclusions form the last section.

## 2 DEFLECTION ANGLE AND FOURIER ANALYSIS

### 2.1 Basic equations and definitions

Since we adopt the thin lens approximation, a general mass distribution  $\rho(\xi_x, \xi_y, \xi_z)$  is represented by its projected surface mass density  $\Sigma(\xi) = \int_{\mathbb{R}} \rho(\xi, \xi_z) d\xi_z$ , where  $\xi = (\xi_x, \xi_y)$  corresponds to the impact parameter vector defined in the lens plane, perpendicular to the line of sight ( $\xi_z$  direction). Moreover, for a given light ray characterized by a normalized impact parameter  $\mathbf{x} = \xi/\xi_0$ , where  $\xi_0$  represents a scaled factor which is dependent on the lens model,<sup>1</sup> the scaled deflection angle is defined by (Schneider et al. 1992)

$$\hat{\alpha}(\mathbf{x}) = -\frac{1}{\pi} \iint_{\mathbb{R}^2} \kappa(\mathbf{x}') \frac{\mathbf{x} - \mathbf{x}'}{|\mathbf{x} - \mathbf{x}'|^2} d\mathbf{x}', \quad (3)$$

where  $\kappa(\mathbf{x}) = \Sigma(\xi_0 \mathbf{x})/\Sigma_{\text{cri}}$  represents the dimensionless surface mass density (also called convergence) with  $\Sigma_{\text{cri}}$ , the critical surface mass density defined by

$$\Sigma_{\text{cri}} = \frac{c^2 D_{\text{OS}}}{4 G D_{\text{LS}} D_{\text{OL}}}. \quad (4)$$

For the case of simple lens models (e.g. axially symmetric lens models), the expression of  $\hat{\alpha}(\mathbf{x})$  may be derived straightforwardly from equation (3). However, it turns out to be generally more complicated.

### 2.2 Deflection angle as a convolution product

Considering  $\kappa(\mathbf{x})$  which either has a sufficiently rapid decay at infinity or is locally integrable, the expression of the deflection

angle, equation (3), can be expressed as a convolution product (e.g. Bartelmann 2003):

$$\hat{\alpha}(\mathbf{x}) = -\frac{1}{\pi} \kappa(\mathbf{x}) \otimes \frac{\mathbf{x}}{|\mathbf{x}|^2}. \quad (5)$$

Making use of the *Fourier convolution theorem* which states that the Fourier transform of a convolution product is equal to the pointwise product of the Fourier transforms of the functions to be convolved (Bracewell 1999), the expression of the deflection angle can be expressed as

$$\hat{\alpha}(\mathbf{x}) = -2 \mathcal{F}^+ \left[ \mathcal{F}^- [\kappa(\mathbf{x})] \mathcal{F}^- \left[ \frac{\mathbf{x}}{|\mathbf{x}|^2} \right] \right], \quad (6)$$

where

$$\mathcal{F}^\mp[f] = \frac{1}{2\pi} \iint_{\mathbb{R}^2} f(\mathbf{x}) e^{\mp i \mathbf{x} \cdot \mathbf{z}} d\mathbf{x}. \quad (7)$$

In equation (6), the Fourier transform  $\mathcal{F}^- [x/|x|^2]$  is independent of the lens model and only needs to be calculated once. Its expression is simply given by

$$\mathcal{F}^- \left[ \frac{\mathbf{x}}{|\mathbf{x}|^2} \right] = -\frac{\iota \mathbf{z}}{|\mathbf{z}|^2}, \quad (8)$$

where  $\mathbf{z} = (z_1, z_2)$  represents the conjugate variables of  $(x_1, x_2)$  in the Fourier space. As a consequence, equation (6) becomes

$$\hat{\alpha}(\mathbf{x}) = 2 \iota \mathcal{F}^+ \left[ \mathcal{F}^- [\kappa(\mathbf{x})] \frac{\mathbf{z}}{|\mathbf{z}|^2} \right], \quad (9)$$

which remains valid for any expression of the dimensionless surface mass density  $\kappa(\mathbf{x})$ .

## 3 HOMOEOIDAL SYMMETRIC LENSES

For the case of homoeoidal symmetric mass distributions, the first step now consists in explicitly expressing the Fourier transform of the dimensionless surface mass density  $\kappa(\mathbf{x})$ . Since the shape of the isodensity contours consists of concentric ellipses,  $\kappa$  can be expressed in terms of the coordinates  $(\rho, \phi)$  defined such as

$$\begin{cases} x_1 = \rho \cos(\phi) \\ x_2 = \frac{\rho}{f} \sin(\phi), \end{cases} \quad (10)$$

where  $0 < f \leq 1$  represents the axis ratio of the ellipses and is related to the ellipticity  $\epsilon$  by

$$f = 1 - \epsilon. \quad (11)$$

Under such conditions, we have  $\kappa(\mathbf{x}) = \kappa(\rho)$ . Therefore, the expression of the Fourier transform of  $\kappa(\rho)$  becomes

$$\begin{aligned} \mathcal{F}^- [\kappa(\rho)] &= \frac{1}{2\pi f} \int_0^{+\infty} \rho' \kappa(\rho') \left\{ \int_0^{2\pi} e^{-i \rho' z \cos(\phi' - \theta)/f} d\phi' \right\} d\rho', \\ &= \frac{1}{f} \int_0^{+\infty} \rho' \kappa(\rho') J_0 \left( \frac{\rho' z}{f} \right) d\rho', \end{aligned} \quad (12)$$

where  $J_0(\rho' z/f)$  represents the zero-order Bessel function of the first kind and  $(z, \theta)$ , the conjugate coordinates of  $(\rho, \phi)$  in the Fourier space defined such as

$$\begin{cases} z_1 = \frac{z}{f} \cos(\theta) \\ z_2 = z \sin(\theta). \end{cases} \quad (13)$$

<sup>1</sup> In the case of axially symmetric lens models, the scaled factor equals the *Einstein radius*  $\xi_E$ . Furthermore, the value of the *Einstein ring angular radius* is given by  $\theta_E = \xi_E/D_{\text{OL}}$ .

By substituting equation (12) into equation (9), the  $i$ th component of the deflection angle reduces to

$$\hat{\alpha}_i = -\frac{1}{\pi f} \iint_I \left\{ \int_0^{+\infty} \rho' \kappa(\rho') J_0 \left( \frac{\rho' z}{f} \right) d\rho' \right\} \times \frac{F_i(\theta) \sin \left( \frac{\rho z}{f} \cos(\theta - \phi) \right)}{\cos^2(\theta) + f^2 \sin^2(\theta)} dz d\theta, \quad (14)$$

where  $I = [0, +\infty[ \times [0, 2]$ ,  $i \in \{1, 2\}$  and  $F_i(\theta)$  is simply defined by

$$F_i(\theta) = \begin{cases} \cos(\theta) & \text{if } i = 1 \\ f \sin(\theta) & \text{if } i = 2. \end{cases} \quad (15)$$

In the remainder part of this demonstration, we will focus our calculation on the 1st component. Let us apply the Fubini's theorem<sup>2</sup> in order to first calculate the  $z$ -integral. It turns out that, for  $\rho' \geq \rho \cos(\theta - \phi)$ , the  $z$ -integral vanishes. Then, for  $0 < \rho' < \rho \cos(\theta - \phi)$ , one finds (Gradshteyn & Ryzhik 2007, 6.671, p. 718)

$$\int_0^{+\infty} J_0 \left( \frac{\rho' z}{f} \right) \sin \left( \frac{\rho z}{f} \cos(\theta - \phi) \right) dz = \frac{f}{\sqrt{\rho^2 \cos^2(\theta - \phi) - \rho'^2}}. \quad (16)$$

After substituting equation (16) into equation (14), the latter equation can be reduced to

$$\hat{\alpha}_1 = -\frac{1}{\pi} \int_0^2 \frac{\cos(\theta)}{\cos^2(\theta) + f^2 \sin^2(\theta)} \times \left\{ \int_0^{\rho \cos(\theta - \phi)} \frac{\rho' \kappa(\rho') d\rho'}{\sqrt{\rho^2 \cos^2(\theta - \phi) - \rho'^2}} \right\} d\theta. \quad (17)$$

After applying the Fubini's theorem once again, substituting  $\theta - \phi$  by  $\Theta$  and calculating the adequate upper and lower limits, equation (17) reduces to

$$\hat{\alpha}_1 = -\frac{2}{\pi} \int_0^\rho \rho' \kappa(\rho') I(\rho') d\rho', \quad (18)$$

where the integral  $I(\rho')$  is given by

$$I(\rho') = \int_{-l}^l \frac{\cos(\Theta + \phi)}{(\cos^2(\Theta + \phi) + f^2 \sin^2(\Theta + \phi)) \sqrt{\rho^2 \cos^2(\Theta) - \rho'^2}} d\Theta, \quad (19)$$

with  $l = \arccos(\rho'/\rho)$ . The resolution of the  $\Theta$ -integral is not trivial. This integral can be expressed as the difference between two integrals by developing  $\cos(\Theta + \phi) = \cos(\Theta)\cos(\phi) - \sin(\Theta)\sin(\phi)$ . We note that for the 2nd component of the deflection angle, the term to be developed is  $\sin(\Theta + \phi) = \sin(\Theta)\cos(\phi) + \cos(\Theta)\sin(\phi)$  which leads to the sum of the two same integrals over  $\Theta$  but multiplied by  $\sin(\phi)$  (resp.  $\cos(\phi)$ ) instead of  $\cos(\phi)$  (resp.  $\sin(\phi)$ ). After

some mathematical developments, the  $\Theta$ -integral takes the form

$$I(\rho') = \frac{\pi\sqrt{2}}{2} \text{sign}(\cos(\phi)) \left( \frac{1}{\sqrt{\lambda^2 \rho'^2 + \omega_1^2}} + \frac{1}{\sqrt{\lambda^2 \rho'^2 + \omega_2^2}} \right), \quad (20)$$

where the expressions of  $\lambda$ ,  $\omega_1$  and  $\omega_2$  are given by

$$\lambda = \sqrt{2}\sqrt{1 - f^2}, \quad (21)$$

$$\omega_1 = \sqrt{2} \rho (f \cos(\phi) + \iota \sin(\phi)), \quad (22)$$

and

$$\omega_2 = \sqrt{2} \rho (f \cos(\phi) - \iota \sin(\phi)). \quad (23)$$

Here, we note that because  $\omega_2 = \omega_1^*$ , the term in brackets is real, and therefore we have  $I(\rho') \in \mathbb{R}$ , for any values of  $0 < f \leq 1$ ,  $\phi \in [0, 2]$  and  $\rho \in [0, +\infty[$ . As a consequence, even if equation (20) contains imaginary terms, the whole expression is a real valued function of the real variable  $\rho' \in [0, \rho]$ . The 2nd component can be similarly derived. In fact, the  $\Theta$ -integral reduces, in this case, to

$$I(\rho') = \frac{\iota\pi\sqrt{2}}{2} \text{sign}(\cos(\phi)) \left( \frac{1}{\sqrt{\lambda^2 \rho'^2 + \omega_1^2}} - \frac{1}{\sqrt{\lambda^2 \rho'^2 + \omega_2^2}} \right). \quad (24)$$

The term in brackets is a purely imaginary quantity. But since the whole expression is multiplied by the imaginary unit  $\iota$ , the former is a real valued function of the real variable  $\rho'$ . Finally, the expressions of the two components of the deflection angle reduce to

$$\hat{\alpha}_1(\rho, \phi) = -\sqrt{2} \text{sign}(\cos(\phi)) \times \left\{ \int_0^\rho \frac{\rho' \kappa(\rho') d\rho'}{\sqrt{\lambda^2 \rho'^2 + \omega_1^2}} + \int_0^\rho \frac{\rho' \kappa(\rho') d\rho'}{\sqrt{\lambda^2 \rho'^2 + \omega_2^2}} \right\}, \quad (25)$$

and

$$\hat{\alpha}_2(\rho, \phi) = -\iota \sqrt{2} \text{sign}(\cos(\phi)) \times \left\{ \int_0^\rho \frac{\rho' \kappa(\rho') d\rho'}{\sqrt{\lambda^2 \rho'^2 + \omega_1^2}} - \int_0^\rho \frac{\rho' \kappa(\rho') d\rho'}{\sqrt{\lambda^2 \rho'^2 + \omega_2^2}} \right\}. \quad (26)$$

Furthermore, in order to demonstrate that  $\hat{\alpha}_1 = \text{Re}(I_c^*(x_c))$  and  $\hat{\alpha}_2 = \text{Im}(I_c^*(x_c))$  with  $I_c(x_c)$  defined by equation (2), we simply calculate  $\hat{\alpha}_1 + \iota \hat{\alpha}_2$  using equations (10), (25) and (26)

$$\begin{aligned} \hat{\alpha}_1 + \iota \hat{\alpha}_2 &= -2\sqrt{2} \text{sign}(\cos(\phi)) \int_0^\rho \frac{\rho' \kappa(\rho') d\rho'}{\sqrt{\lambda^2 \rho'^2 + \omega_2^2}}, \\ &= -2 \text{sign}(x_c) \frac{1}{f} \int_0^\rho \frac{\rho' \kappa(\rho') d\rho'}{\sqrt{-(1 - \frac{1}{f^2})\rho'^2 + x_c^{*2}}}, \\ &= -2 \text{sign}(x_c) \cos(\beta) \int_0^\rho \frac{\rho' \kappa(\rho') d\rho'}{\sqrt{x_c^{*2} - \rho'^2 \sin^2(\beta)}}, \\ &= I_c^*(x_c), \end{aligned} \quad (27)$$

where  $\cos(\beta) = 1/f$ . Finally, we have succeeded in demonstrating that  $\hat{\alpha}_1$  and  $\hat{\alpha}_2$  constitute the real and imaginary parts of the complex deflection angle defined by Bourassa & Kantowski (1975).

<sup>2</sup> The Fubini's theorem sets conditions which allows the order of integration to be changed in iterated integrals.

For practical purposes, equations (25) and (26) can be used to derive the analytical expression of the two deflection angle components.

Let us first consider the family of models characterized by the dimensionless surface mass density having the form

$$\kappa(\rho) = \frac{\kappa_0}{(\rho_c^2 + \rho^2)^\nu}, \quad (28)$$

with  $\kappa_0$  being a constant,  $\rho_c$  the core scale and  $\nu$  a positive real number. The latter dimensionless surface mass density includes a large class of elliptical lens models. The expressions of the components of the deflection angle deduced from equations (25) and (26) reduce to

$$\hat{\alpha}_1(\rho, \phi) = \kappa_0 \lambda^{2\nu-2} \sqrt{2} (\Omega(\rho, \phi, \omega_1) + \Omega(\rho, \phi, \omega_2)), \quad (29)$$

and

$$\hat{\alpha}_2(\rho, \phi) = \iota \kappa_0 \lambda^{2\nu-2} \sqrt{2} (\Omega(\rho, \phi, \omega_1) - \Omega(\rho, \phi, \omega_2)), \quad (30)$$

where  $\Omega(\rho, \phi, \omega_i)$  is defined by

$$\begin{aligned} \Omega(\rho, \phi, \omega_i) &= \frac{\omega_i}{(\lambda^2 \rho_c^2 - \omega_i^2)^\nu} \\ &\times \left( -\sqrt{1 + \frac{\lambda^2 \rho^2}{\omega_i^2}} {}_2F_1 \left[ \frac{1}{2}, \frac{3}{2}; -\frac{\lambda^2 \rho^2 + \omega_i^2}{\lambda^2 \rho_c^2 - \omega_i^2} \right] \right. \\ &\quad \left. + {}_2F_1 \left[ \frac{1}{2}, \frac{3}{2}; -\frac{\omega_i^2}{\lambda^2 \rho_c^2 - \omega_i^2} \right] \right), \quad (31) \end{aligned}$$

with  ${}_2F_1(a, b, c, z)$  representing the Gauss hypergeometric function and  $\omega_i$  is defined by equations (22) and (23). We note that since  $\omega_2 = \omega_1^*$ , we have  $\Omega(\rho, \phi, \omega_2) = \Omega^*(\rho, \phi, \omega_1)$ .

Let us now consider the so-called NSIE lens model, in which dimensionless surface mass density is obtained from (28) with  $\kappa_0 = \sqrt{f}/2$  and  $\nu = 1/2$ :

$$\kappa(\rho) = \frac{\sqrt{f}}{2 \sqrt{\rho_c^2 + \rho^2}}, \quad (32)$$

where  $\rho_c$  still represents the dimensionless core radius. With the help of equations (29) and (30), we directly deduce the analytical expressions for the two components of the deflection angle, without having to use the complex representation of the lens theory altogether with the results of Bourassa & Kantowski (1975) and Bray (1984). Therefore, since we have

$$\operatorname{arcsinh}(x) = \log \left( x + \sqrt{x^2 + 1} \right) \quad (33)$$

and

$$\operatorname{arctan}(q) = -\frac{i}{2} \log \left( \frac{1 + iq}{1 - iq} \right), \quad (34)$$

the components of the deflection angle can be expressed as

$$\hat{\alpha}_1(\rho, \phi) = \frac{\sqrt{f}}{f'} \operatorname{sign}(\cos(\phi)) \log \left[ \frac{A}{B} \right], \quad (35)$$

and

$$\hat{\alpha}_2(\rho, \phi) = \frac{\sqrt{f}}{2f'} \operatorname{sign}(\cos(\phi)) \operatorname{arctan} \left( \frac{C}{D} \right), \quad (36)$$

where  $f' = \sqrt{1 - f^2}$  and

$$A = \left( 1 + \frac{\rho_c^2}{\rho^2} \right) - \left( f \frac{\rho_c}{\rho} - f' \cos(\phi) \operatorname{sign}(\cos(\phi)) \right)^2, \quad (37)$$

$$B = -f^2 \frac{\rho_c^2}{\rho^2} + \left( \sqrt{1 + \frac{\rho_c^2}{\rho^2}} + f' \cos(\phi) \operatorname{sign}(\cos(\phi)) \right)^2, \quad (38)$$

$$\begin{aligned} C &= f \rho^2 + f'^2 \rho_c \sqrt{\rho^2 + \rho_c^2} \\ &\quad + f' \rho \left( \rho_c + f \sqrt{\rho^2 + \rho_c^2} \cos(\phi) \operatorname{sign}(\cos(\phi)) \right), \quad (39) \end{aligned}$$

and

$$\begin{aligned} D &= \rho \sin(\phi) \left[ -f'^2 \rho \cos(\phi) \right. \\ &\quad \left. + f' \left( f \rho_c - \sqrt{\rho^2 + \rho_c^2} \right) \operatorname{sign}(\cos(\phi)) \right]. \quad (40) \end{aligned}$$

We note that equations (35) and (36) are not identical to the expressions derived by Kormann, Schneider & Bartelmann (1994, equations 62a–e) but remain rigorously equivalent. However, our derived expressions of the deflection angle do not involve complex quantities, unlike those derived by Kormann et al. (1994). Once more, the reader may thus perceive the real interest of using the Fourier approach developed in this work. Of course, for the case of  $\rho_c = 0$ , the latter equations reduce to those for the singular isothermal ellipsoid (SIE) case. In fact, for the singular case  $\rho_c = 0$ , equations (29) and (30) take the simple form

$$\begin{aligned} \hat{\alpha}_1(\rho, \phi) &= -\sqrt{2} \kappa_0 \frac{\rho^{2-\nu}}{(2-\nu)} \\ &\times \left( \frac{1}{\omega_1} {}_2F_1 \left[ \frac{1}{2}, 1 - \frac{\nu}{2}, 2 - \frac{\nu}{2}; -\frac{\lambda^2}{\omega_1^2} \rho^2 \right] \right. \\ &\quad \left. + \frac{1}{\omega_2} {}_2F_1 \left[ \frac{1}{2}, 1 - \frac{\nu}{2}, 2 - \frac{\nu}{2}; -\frac{\lambda^2}{\omega_2^2} \rho^2 \right] \right), \quad (41) \end{aligned}$$

and

$$\begin{aligned} \hat{\alpha}_2(\rho, \phi) &= -\iota \sqrt{2} \kappa_0 \frac{\rho^{2-\nu}}{(2-\nu)} \\ &\times \left( \frac{1}{\omega_1} {}_2F_1 \left[ \frac{1}{2}, 1 - \frac{\nu}{2}, 2 - \frac{\nu}{2}; -\frac{\lambda^2}{\omega_1^2} \rho^2 \right] \right. \\ &\quad \left. - \frac{1}{\omega_2} {}_2F_1 \left[ \frac{1}{2}, 1 - \frac{\nu}{2}, 2 - \frac{\nu}{2}; -\frac{\lambda^2}{\omega_2^2} \rho^2 \right] \right). \quad (42) \end{aligned}$$

We note that the latter equations only remain valid for  $\nu \in \mathbb{R}^+ \setminus \mathbb{Z} \cup \{1\}$ . For the case  $\nu = 1$  and  $\kappa_0 = \sqrt{f}/2$ , i.e. the SIE model, the two components of the deflection angle take the form

$$\begin{aligned} \hat{\alpha}_1(\rho, \phi) &= -\frac{\sqrt{f}}{2f'} \left( \operatorname{arcsinh} \left( \frac{f'}{f \cos(\phi) + \iota \sin(\phi)} \right) \right. \\ &\quad \left. + \operatorname{arcsinh} \left( \frac{f'}{f \cos(\phi) - \iota \sin(\phi)} \right) \right) \quad (43) \end{aligned}$$

and

$$\begin{aligned} \hat{\alpha}_2(\rho, \phi) &= -\frac{\iota \sqrt{f}}{2f'} \left( \operatorname{arcsinh} \left( \frac{f'}{f \cos(\phi) + \iota \sin(\phi)} \right) \right. \\ &\quad \left. - \operatorname{arcsinh} \left( \frac{f'}{f \cos(\phi) - \iota \sin(\phi)} \right) \right). \quad (44) \end{aligned}$$



Using the fact that  $\sinh x = -\iota \sin(\iota x)$  and the addition properties of the logarithmic functions, we straightforwardly retrieve the expected expression for the deflection angle introduced by Kormann et al. (1994)

$$\hat{\alpha}(\mathbf{x}) = -\frac{\sqrt{f}}{f'} \left[ \operatorname{arcsinh} \left( \frac{f'}{f} \cos(\varphi) \right) \mathbf{e}_1 + \arcsin(f' \sin(\varphi)) \mathbf{e}_2 \right], \quad (45)$$

where  $\varphi$  represents the angular coordinate defined in the polar coordinate system and  $\mathbf{e}_1$  (resp.  $\mathbf{e}_2$ ) represents the unit vector along the direction  $x_1$  (resp.  $x_2$ ).

Finally, for the case  $f = 1$ , i.e. for axially symmetric lenses, we note that  $\lambda = 0$ . Therefore, in equations (25) and (26), we deduce that  $\sqrt{\lambda^2 \rho'^2 + \omega_i^2} = \sqrt{2} \rho (\cos(\phi) \pm \iota \sin(\phi)) \operatorname{sign}(\cos(\phi))$  is no longer a function of  $\rho'$ . As a result, the expressions for the two components of the deflection angle take the expected form

$$\hat{\alpha}_1(\rho) = -\frac{\cos(\phi)}{\pi\rho} M(\leq \rho) \quad (46)$$

and

$$\hat{\alpha}_2(\pi\rho) = -\frac{\sin(\phi)}{\pi\rho} M(\leq \rho), \quad (47)$$

where  $M(\leq \rho) = 2\pi \int_0^\rho \rho' \kappa(\rho') d\rho'$ . From these two last equations, we may retrieve the components of the deflection angle for any axially symmetric lenses, e.g. the singular isothermal sphere or spherical NFW lensing models.

#### 4 CONCLUSIONS

Although it is a well-known fact that the deflection angle can be expressed as a convolution product between the dimensionless surface mass density and the simple kernel  $\mathbf{x}/|\mathbf{x}|^2$ , its analytical derivation using the Fourier analysis in a systematic way proves to be a very efficient and appropriate alternative method. For this purpose, we have presented the derivation of the expression for the two components of the deflection angle using the Fourier formalism. From basic theorems of the Fourier and integrals analysis, we have derived the expression of the two components of the deflection angle for the case of homoeoidal symmetric lenses. This result is consistent with the one already derived by Bourassa & Kantowski (1975) but, in our case, we have obtained the expression of the two components separately instead of a unique equation expressed in the complex formalism. As a consequence, equations (25) and (26) turn out to be

very simple and useful in order to calculate the components of the deflection angle. Indeed, for the case of the NSIE, we have derived more simple expressions for the two components of the deflection angle than those previously derived by Kormann et al. (1994). More generally speaking, it should also be straightforward to derive the expression of the deflection angle for the case of a pixelated lens mass distribution such that each pixel in the lens plane represents a constant area with a fixed surface mass density. Following such an analytical approach, it should be easy and convenient to model any unknown gravitational lens mass distribution. By means of such an expression for the deflection angle, it should also be straightforward to analytically determine the values of the expected time delays between pairs of lensed images.

#### ACKNOWLEDGEMENTS

OW thanks the Belgian National Fund for Scientific Research (FNRS). JS and OW acknowledge support from the Communauté française de Belgique – Actions de recherche concertées – Académie universitaire Wallonie-Europe, from the ESA PRODEX Programme ‘GAIA’, and from the Belgian Federal Science Policy Office.

#### REFERENCES

- An J. H., Evans N. W., 2006, MNRAS, 369, 317  
 Bartelmann M., 2003, preprint (astro-ph/0304162)  
 Bourassa R. R., Kantowski R., Norton T. D., 1973, ApJ, 185, 747  
 Bourassa R. R., Kantowski R., 1975, ApJ, 195, 13  
 Bracewell R., 1999, The Fourier Transform and Its Applications, 3rd edn. McGraw-Hill, New York, p. 108  
 Bray I., 1984, MNRAS, 208, 511  
 Chang K., Refsdal S., 1984, A&A, 132, 168  
 Gradshteyn I. S., Ryzhik I. M., 2007, in Jeffrey A., ed., Table of Integrals, Series and Products, 7th edn., Academic Press, New York  
 Kassiola A., Kovner I., 1993, ApJ, 417, 450  
 Kochanek C. S., 1991, ApJ, 373, 354  
 Kormann R., Schneider P., Bartelmann M., 1994, A&A, 284, 285  
 Schneider P., Ehlers J., Falco E. E., 1992, Gravitational Lenses. Springer-Verlag, Berlin  
 Schramm T., 1990, A&A, 231, 19  
 Wambsgans J., Paczyński B., 1994, AJ, 108, 1156  
 Wertz O., Pelgrims V., Surdej J., 2012, MNRAS, 424, 1543

This paper has been typeset from a  $\text{\TeX}/\text{\LaTeX}$  file prepared by the author.



### 3.3 Deflection angle as the sum of two contributions

For the case of homoeoidal symmetric mass distributions, we illustrate hereafter, as an application of the Fourier approach, how the deflection angle can be rigorously expressed as the sum of two contributions, one isotropic, and an anisotropic one. In the remainder, we focus our calculation on the 1st-component. Let us first recall the following expression of the deflection angle  $\hat{\alpha}_i$  derived in Paper II (see Eq. (14)) :

$$\hat{\alpha}_i = -\frac{1}{\pi f} \iint_I \left\{ \int_0^{+\infty} \rho' \kappa(\rho') J_0\left(\frac{\rho' z}{f}\right) d\rho' \right\} \frac{F_i(\theta) \sin\left(\frac{\rho z}{f} \cos(\theta - \phi)\right)}{\cos^2(\theta) + f^2 \sin^2(\theta)} dz d\theta,$$

where  $I = [0, +\infty[ \times ]0, 2\pi]$ ,  $i \in \{1, 2\}$  and  $F_i(\theta)$  is simply defined by :

$$F_i(\theta) = \begin{cases} \cos(\theta) & \text{if } i = 1 \\ f \sin(\theta) & \text{if } i = 2 \end{cases}, \quad (3.1)$$

Let us isolate in Eq. (3.1) the  $\theta$ -integral given by :

$$I(z) = \int_0^{2\pi} \frac{\cos(\theta) \sin\left(\frac{\rho z}{f} \cos(\theta - \phi)\right)}{\cos^2(\theta) + f^2 \sin^2(\theta)} d\theta. \quad (3.2)$$

Let us then apply, to this  $\theta$ -integral, the second mean value theorem for integration (Dixon 1929) which states that if  $g : [a, b] \rightarrow \mathbb{R}$  is a monotonic function and  $h : [a, b] \rightarrow \mathbb{R}$  is an integrable function, then there exists a number  $\zeta \in ]a, b[$  such that :

$$\int_a^b g(t) h(t) dt = \lim_{t' \rightarrow a^+} g(t') \int_a^\zeta h(t) dt + \lim_{t' \rightarrow b^-} g(t') \int_\zeta^b h(t) dt. \quad (3.3)$$

Therefore, we define the functions  $h_1(\theta, z)$  and  $g(\theta)$  :

$$h_1(\theta, z) = \cos(\theta) \sin\left(\frac{\rho z}{f} \cos(\theta - \phi)\right), \quad (3.4)$$

and

$$g(\theta) = \frac{1}{\cos^2(\theta) + f^2 \sin^2(\theta)}, \quad (3.5)$$

the latter being monotonic in the intervals  $[k\pi/2, (k+1)\pi/2]$  with  $k \in \{0, 1, 2, 3\}$ . After applying the second mean value theorem of integration, the  $\theta$ -integral (Eq. (3.2)) takes the form :

$$\begin{aligned} I(z) = & \sum_{k=0}^3 \left( \lim_{\theta' \rightarrow k\pi/2^+} g(\theta') \int_{k\pi/2}^{\zeta_k} h_1(\theta, z) d\theta \right. \\ & \left. + \lim_{\theta' \rightarrow (k+1)\pi/2^-} g(\theta') \int_{\zeta_k}^{(k+1)\pi/2} h_1(\theta, z) d\theta \right), \end{aligned} \quad (3.6)$$

where  $\zeta_k \in ]k\pi/2, (k+1)\pi/2[$ , which depends on the parameters  $\rho, z, f$  and  $\phi$ , may not be unique. Furthermore, we note that

$$\lim_{\theta \rightarrow k\pi/2^+} g(\theta) = \begin{cases} 1 & \text{if } k = 0, 2, \\ \frac{1}{f^2} & \text{if } k = 1, 3, \end{cases} \quad (3.7)$$

and

$$\lim_{\theta \rightarrow (k+1)\pi/2^-} g(\theta) = \begin{cases} 1 & \text{if } k = 1, 3, \\ \frac{1}{f^2} & \text{if } k = 0, 2. \end{cases} \quad (3.8)$$

Therefore, Eq. (3.6) simply reduces to :

$$\begin{aligned} I(z) = & \int_0^{2\pi} h_1(\theta, z) d\theta + \frac{(1-f^2)}{f^2} \left( \int_{\zeta_0}^{\zeta_1} h_1(\theta, z) d\theta + \int_{\zeta_2}^{\zeta_3} h_1(\theta, z) d\theta \right), \\ = & 2\pi \cos(\phi) J_1\left(\frac{\rho z}{f}\right) + 2 \frac{(1-f^2)}{f^2} \int_{\zeta_0}^{\zeta_1} h_1(\theta, z) d\theta, \end{aligned} \quad (3.9)$$

where the second equality holds because  $h_1(\theta, z)$  is a  $\pi$ -periodic function and therefore  $\zeta_2 = \zeta_0 + \pi$  and  $\zeta_3 = \zeta_1 + \pi$ . After substituting Eq. (3.9) into Eq. (3.1), the expression of the deflection angle takes the form :

$$\begin{aligned} \hat{\alpha}_1 = & -\frac{1}{\pi f} \int_0^{+\infty} \left\{ \int_0^{+\infty} \rho' \kappa(\rho') J_0\left(\frac{\rho' z}{f}\right) d\rho' \right\} 2\pi \cos \phi J_1\left(\frac{\rho z}{f}\right) dz \\ & - \frac{1}{\pi f} \int_0^{+\infty} \left\{ \int_0^{+\infty} \rho' \kappa(\rho') J_0\left(\frac{\rho' z}{f}\right) d\rho' \right\} 2 \frac{(1-f^2)}{f^2} \int_{\zeta_0}^{\zeta_1} h_1(\theta, z) d\theta dz. \end{aligned} \quad (3.10)$$

After applying the Fubini's theorem in order to calculate the  $z$ -integral in the first term of the

latter equation, we find :

$$\hat{\alpha}_1 = -\frac{2 \cos \phi}{f} \int_0^{+\infty} \rho' \kappa(\rho') \left\{ \int_0^{+\infty} J_0\left(\frac{\rho' z}{f}\right) J_1\left(\frac{\rho z}{f}\right) dz \right\} d\rho' - \frac{2(1-f^2)}{\pi f^3} \int_0^{+\infty} \left\{ \int_0^{+\infty} \rho' \kappa(\rho') J_0\left(\frac{\rho' z}{f}\right) d\rho' \right\} \int_{\zeta_0}^{\zeta_1} h_1(\theta, z) d\theta dz. \quad (3.11)$$

It turns out that, for  $\rho' > \rho$ , the  $z$ -integral of the first term in the latter equation vanishes, and for  $\rho' < \rho$ , equals  $f/\rho$  (Gradshteyn & Ryzhik 2007, 6.512.3, p. 660). As a result, Eq. (3.11) reduces to :

$$\hat{\alpha}_1 = -\frac{\cos \phi}{\pi \rho} M(\leq \rho) - \frac{2(1-f^2)}{\pi f^3} \int_0^{+\infty} \left\{ \int_0^{+\infty} \rho' \kappa(\rho') J_0\left(\frac{\rho' z}{f}\right) d\rho' \right\} \int_{\zeta_0}^{\zeta_1} h_1(\theta, z) d\theta dz. \quad (3.12)$$

The 2nd-component can be similarly derived :

$$\hat{\alpha}_2 = -\frac{\sin \phi}{\pi \rho} M(\leq \rho) - \frac{2(1-f^2)}{\pi f^3} \int_0^{+\infty} \left\{ \int_0^{+\infty} \rho' \kappa(\rho') J_0\left(\frac{\rho' z}{f}\right) d\rho' \right\} \int_{\zeta_0}^{\zeta_1} h_2(\theta, z) d\theta dz, \quad (3.13)$$

where  $h_2(\theta, z)$  is defined by :

$$h_2(\theta, z) = f \sin(\theta) \sin\left(\frac{\rho z}{f} \cos(\theta - \phi)\right). \quad (3.14)$$

For the case of axially symmetric lenses, i.e.  $f = 1$ , we obviously retrieve the expected expressions of the deflection angle (see Eqs. (46) and (47) in Paper II). As a consequence, for the case of mass distributions with homoeoidal symmetry, the two components of the deflection angle can be expressed as the sum of two contributions. The first one is proportional to the scaled mass of the deflector located inside the ellipse characterized by the semi major axis  $\rho$ , divided by  $\rho$ . The second one represents the contribution of the asymmetrical part of the mass distribution.

## 3.4 The singular isothermal ellipsoid (SIE) lens models

As already mentioned, the determination of the deflection angle for the case of the SIE family of models making use of Eq. (1.111) turns out to be quite difficult. Besides, Kormann & al.

(1994) have chosen to derive  $\hat{\alpha}(\mathbf{x})$  from the Poisson equation  $\Delta\psi(\mathbf{x}) = 2\kappa(\mathbf{x})$  and making use of the Green's function method. In Paper III, we have derived the expression of  $\hat{\alpha}(\mathbf{x})$  after having specified the general result appearing in Eqs. (41) and (42) (from Paper III) for the case of the SIE models. Of course, the determination of the latter general result is not mandatory to obtain  $\hat{\alpha}(\mathbf{x})$  for that particular case. In this section, we present in details the usefulness of the Fourier approach in order to derive  $\hat{\alpha}(\mathbf{x})$  for the case of SIE from Eq. (9) (see Paper III).

First, let us recall the expression of the SIE dimensionless surface mass density :

$$\kappa(x_1, x_2) = \frac{\sqrt{f}}{2\sqrt{x_1^2 + f^2x_2^2}}, \quad (3.15)$$

where  $0 < f \leq 1$  represents the axis ratio of the elliptic iso-density contours and  $(x_1, x_2)$  the cartesian system of coordinates. For later purposes, we recall the expression of  $f' = \sqrt{1 - f^2}$ . Due to the lens model symmetry, we introduce the coordinates  $(\rho, \phi)$  defined such as (see Eq. (10) from Paper III) :

$$\begin{cases} x_1 = \rho \cos(\phi), \\ x_2 = \frac{\rho}{f} \sin(\phi), \end{cases} \quad (3.16)$$

and the surface mass density simplifies into  $\kappa(\rho, \phi) = \sqrt{f}/(2\rho)$ . From Eq. (12) (see Paper III), the Fourier transform of the surface mass density takes the form :

$$\mathcal{F}^- [\kappa(\rho, \phi)] = \frac{\sqrt{f}}{2f} \int_0^{+\infty} J_0\left(\frac{\rho'z}{f}\right) d\rho', \quad (3.17)$$

where  $J_0(\rho'z/f)$  represents the zero order Bessel function of the first kind and  $(z, \theta)$ , the conjugate coordinates of  $(\rho, \phi)$  in the Fourier space defined such as :

$$\begin{cases} z_1 = \frac{z}{f} \cos(\theta), \\ z_2 = \rho \sin(\theta), \end{cases} \quad (3.18)$$

and  $z = \sqrt{f^2z_1^2 + z_2^2}$ . Since  $z/f > 0$ , the  $\rho'$ -integral can be simply reduced to (Gradshteyn & Ryzhik 2007, 6.511.1, p. 659) :

$$\int_0^{+\infty} J_0\left(\frac{\rho'z}{f}\right) d\rho' = \frac{f}{z}. \quad (3.19)$$

As a result, from Eqs. (3.17) and (3.19), one finds :

$$\mathcal{F}^- [\kappa(\rho, \phi)] = \frac{\sqrt{f}}{2 \sqrt{f^2 z_1^2 + z_2^2}} = \frac{\sqrt{f}}{2z} . \quad (3.20)$$

After inserting Eq. (3.20) into Eq. (9) (from Paper III), we derive the expression of the deflection angle, each component separately. First, we have :

$$\begin{aligned} \hat{\alpha}_i(\rho, \phi) &= \iota \sqrt{f} \mathcal{F}^+ \left[ \frac{z_i}{(z_1^2 + z_2^2) z} \right] , \\ &= \frac{\sqrt{f}}{2\pi} \int_0^{2\pi} G_i(\theta) \left\{ \int_0^{+\infty} \frac{\sin \left[ \frac{z\rho}{f} \cos(\phi - \theta) \right]}{z} dz \right\} d\theta , \end{aligned} \quad (3.21)$$

where the function  $G(\theta)$  is defined by :

$$G_i(\theta) = \begin{cases} \frac{\cos(\theta)}{\cos^2(\theta) + f^2 \sin^2(\theta)} & \text{if } i = 1 , \\ \frac{f \sin(\theta)}{\cos^2(\theta) + f^2 \sin^2(\theta)} & \text{if } i = 2 . \end{cases} \quad (3.22)$$

The  $z$ -integral is simply given by (Gradshteyn & Ryzhik 2007, 3.721.1, p. 423) :

$$\int_0^{+\infty} \frac{\sin \left[ \frac{z\rho}{f} \cos(\phi - \theta) \right]}{z} dz = \frac{\pi}{2} \text{sign}(\cos(\phi - \theta)) . \quad (3.23)$$

Therefore, Eq. (3.21) reduces to :

$$\hat{\alpha}_i(\rho, \phi) = \frac{\sqrt{f}}{4} \int_0^{2\pi} \text{sign}(\cos(\phi - \theta)) G_i(\theta) d\theta , \quad (3.24)$$

$$= \frac{\sqrt{f}}{4} \left[ \int_0^{\pi/2+\phi} G_i(\theta) d\theta - \int_{\pi/2+\phi}^{3\pi/2+\phi} G_i(\theta) d\theta + \int_{3\pi/2+\phi}^{2\pi} G_i(\theta) d\theta \right] . \quad (3.25)$$

For the case of the first component, after making use of the variable change  $\Phi = \sin(\phi)$ , Eq.

(3.25) transforms into :

$$\hat{\alpha}_1(\rho, \phi) = \frac{\sqrt{f}}{4} \left[ \int_0^{\cos(\phi)} \frac{1}{1-f'^2 \Phi^2} d\Phi + \int_{-\cos(\phi)}^{\cos(\phi)} \frac{1}{1-f'^2 \Phi^2} d\Phi + \int_{-\cos(\phi)}^0 \frac{1}{1-f'^2 \Phi^2} d\Phi \right] \quad (3.26)$$

$$= \frac{\sqrt{f}}{2} \int_{-\cos(\phi)}^{\cos(\phi)} \frac{1}{1-f'^2 \Phi^2} d\Phi, \quad (3.27)$$

$$= \frac{\sqrt{f}}{f'} \operatorname{arcsinh} \left( \frac{f' \cos(\phi)}{\sqrt{1-f'^2 \cos^2(\phi)}} \right). \quad (3.28)$$

From the definition of  $f'$ , Eq. (3.16) and making use of the polar system coordinates  $(r, \varphi)$  defined such as :

$$\begin{cases} x_1 = r \cos(\varphi), \\ x_2 = r \sin(\varphi), \end{cases} \quad (3.29)$$

Eq. (3.28) reduces to :

$$\hat{\alpha}_1(r, \varphi) = \frac{\sqrt{f}}{f'} \operatorname{arcsinh} \left( \frac{f'}{f} \cos(\varphi) \right), \quad (3.30)$$

which constitutes the expected expression of the first component of the deflection angle for the case of the SIE family of models. For the case of the second component, after making use of the variable change  $\Phi = \cos(\phi)$ , Eq. (3.25) transforms into :

$$\hat{\alpha}_2(\rho, \phi) = \frac{\sqrt{f}}{4f} \left[ \int_{\sin(\phi)}^1 \frac{1}{1+\left(\frac{f'}{f}\right)^2 \Phi^2} d\Phi - \int_{\sin(\phi)}^1 \frac{1}{1+\left(\frac{f'}{f}\right)^2 \Phi^2} d\Phi + \int_{-\sin(\phi)}^{\sin(\phi)} \frac{1}{1+\left(\frac{f'}{f}\right)^2 \Phi^2} d\Phi \right], \quad (3.31)$$

$$= \frac{\sqrt{f}}{2f} \int_{-\sin(\phi)}^{\sin(\phi)} \frac{1}{1+\left(\frac{f'}{f}\right)^2 \Phi^2} d\Phi, \quad (3.32)$$

$$= \frac{\sqrt{f}}{f'} \operatorname{arcsin} \left( \frac{f'}{f} \frac{\sin(\phi)}{\sqrt{1+\left(\frac{f'}{f}\right)^2 \sin^2(\phi)}} \right). \quad (3.33)$$

From the definition of  $f'$  and making use of the polar system of coordinates  $(r, \varphi)$ , Eq. (3.33)



reduces to :

$$\hat{\alpha}_2(r, \varphi) = \frac{\sqrt{f}}{f'} \arcsin(f' \sin(\varphi)) , \quad (3.34)$$

which constitutes the expected expression of the second component of the deflection angle for the case of the SIE family of models. As a result, we retrieve the expected expression of the deflection angle which is finally given by :

$$\hat{\alpha}(\mathbf{x}) = -\frac{\sqrt{f}}{f'} \left[ \operatorname{arcsinh}\left(\frac{f'}{f} \cos \varphi\right) \mathbf{e}_1 + \arcsin(f' \sin \varphi) \mathbf{e}_2 \right] , \quad (3.35)$$

where  $\mathbf{e}_1$  (resp.  $\mathbf{e}_2$ ) represents the unit vector in the direction  $x_1$  (resp.  $x_2$ ), according to the notation adopted by Kormann & al. (1994).

### 3.5 The uniform disk lens models

As an application of the Fourier method, let us consider a uniform disk characterized by a radius  $R$  and a constant surface mass density  $K$ . For such a lens model, we have  $\kappa(r, \varphi) = K \chi_{[0,R]}(r)$  where  $\chi_I$  represents the indicator function of the set  $I$ . The Fourier method allows to straightforwardly derive the expression of the deflection angle. On one hand, making use of the polar system of coordinates, the Fourier transform of  $\kappa(r, \varphi)$  leads to :

$$\mathcal{F}^{-}[\kappa(r, \varphi)] = \frac{1}{2\pi} \int_0^{+\infty} \int_0^{2\pi} K \chi_{[0,R]}(r) e^{-irz \cos(\varphi-\theta)} r dr d\varphi , \quad (3.36)$$

$$= \frac{K}{2\pi} \int_0^R r J_0(rz) dr , \quad (3.37)$$

$$= \frac{KR}{z} J_1(rz) , \quad (3.38)$$

where  $J_i$  represents the Bessel function of the first kind of the  $i$ -th order. After inserting Eq. (3.38) into Eq. (9) (from Paper III), the expression of the first component of the deflection

angle takes the form :

$$\hat{\alpha}_1(r, \varphi) = 2 \iota R K \mathcal{F}^+ \left[ J_1(Rz) \frac{z_1}{z_1^2 + z_2^2} \right], \quad (3.39)$$

$$= \frac{\iota KR}{\pi} \int_0^{+\infty} \int_0^{2\pi} \frac{\cos(\theta)}{z} J_1(Rz) e^{rz \cos(\varphi - \theta)} d\theta dz, \quad (3.40)$$

$$= -2 K R \cos(\varphi) \int_0^{+\infty} \frac{J_1(Rz) J_1(rz)}{z} dz. \quad (3.41)$$

From Gradshteyn & Ryzhik (2007, 6.576.2, p. 684), the solution of the latter integral takes the form :

$$\int_0^{+\infty} \frac{J_1(Rz) J_1(rz)}{z} dz = \frac{Rr}{2(R+r)^2} {}_2F_1\left(1, \frac{3}{2}, 3; \frac{4rR}{(r+R)^2}\right), \quad (3.42)$$

where  ${}_2F_1(a, b, c; \zeta)$  represents the Gauss hypergeometric function which can be simplified, in the present case, into :

$${}_2F_1\left(1, \frac{3}{2}, 3; \frac{4rR}{(r+R)^2}\right) = \left(\frac{r+R}{\max(r, R)}\right)^2, \quad (3.43)$$

where the function  $\max(r, R)$  is defined by :

$$\max(r, R) = \begin{cases} r & \text{if } r \geq R, \\ R & \text{otherwise.} \end{cases} \quad (3.44)$$

As a result, after inserting Eqs. (3.42) and (3.44) into Eq. (3.41), the expression of the first component of the deflection angle results in :

$$\hat{\alpha}_1(r, \varphi) = -K \frac{R^2 r}{(\max(r, R))^2} \cos(\varphi). \quad (3.45)$$

Making use of the same argument, the expression of the second component of the deflection angle differs from Eq. (3.45) only by the term  $\sin(\varphi)$  instead of  $\cos(\varphi)$  :

$$\hat{\alpha}_2(r, \varphi) = -K \frac{R^2 r}{(\max(r, R))^2} \sin(\varphi). \quad (3.46)$$

Its vectorial form  $\hat{\alpha}(\mathbf{x})$  is finally given by :

$$\hat{\alpha}(\mathbf{x}) = -K \frac{R^2}{(\max(x, R))^2} \mathbf{x}, \quad (3.47)$$

where  $x = |\mathbf{x}| \equiv r$  in agreement with the notation introduced in Section 1.10. As expected, the amplitude of  $\hat{\alpha}(\mathbf{x})$  is independent of  $\varphi$ , due to the symmetry.

For particular values of the radius  $R$ , the uniform disk lens model tends respectively towards the point-like ( $R \ll r$ ) or the infinite sheet with a constant surface mass density ( $R \gg r$ ) lens models. For the case of the point-like lens models, we have  $R \rightarrow 0$ ,  $K \rightarrow \delta(\mathbf{x})$  and Eq. (3.47) transforms into :

$$\hat{\alpha}(\mathbf{x}) = -K \left(\frac{R}{r}\right)^2 \mathbf{x}, \quad (3.48)$$

$$\simeq -\frac{\mathbf{x}}{x^2}. \quad (3.49)$$

For the case of the infinite sheet with a constant surface mass density, we have  $R \rightarrow +\infty$  and Eq. (3.47) transforms into :

$$\hat{\alpha}(\mathbf{x}) \simeq -\kappa \mathbf{x}, \quad (3.50)$$

where  $\kappa \equiv K$  represents the so-called convergence. Let us note that the present determination of  $\hat{\alpha}(\mathbf{x})$  for the case of the uniform disk lens model has been obtained without having used the simplification  $\varphi = 0$ . Indeed, such a simplification has been used in Section 1.10 in order to determine Eq. (1.148) from Eq. (9) (from Paper III).

## 3.6 Regular grid composed of square pixels

In the previous sections, we have highlighted the usefulness of the Fourier method concerning the determination of the deflection angle for the case of parametric lens models. In the present section, we consider a non-parametric lens model which, in principle, fully accounts for any type of mass distribution.

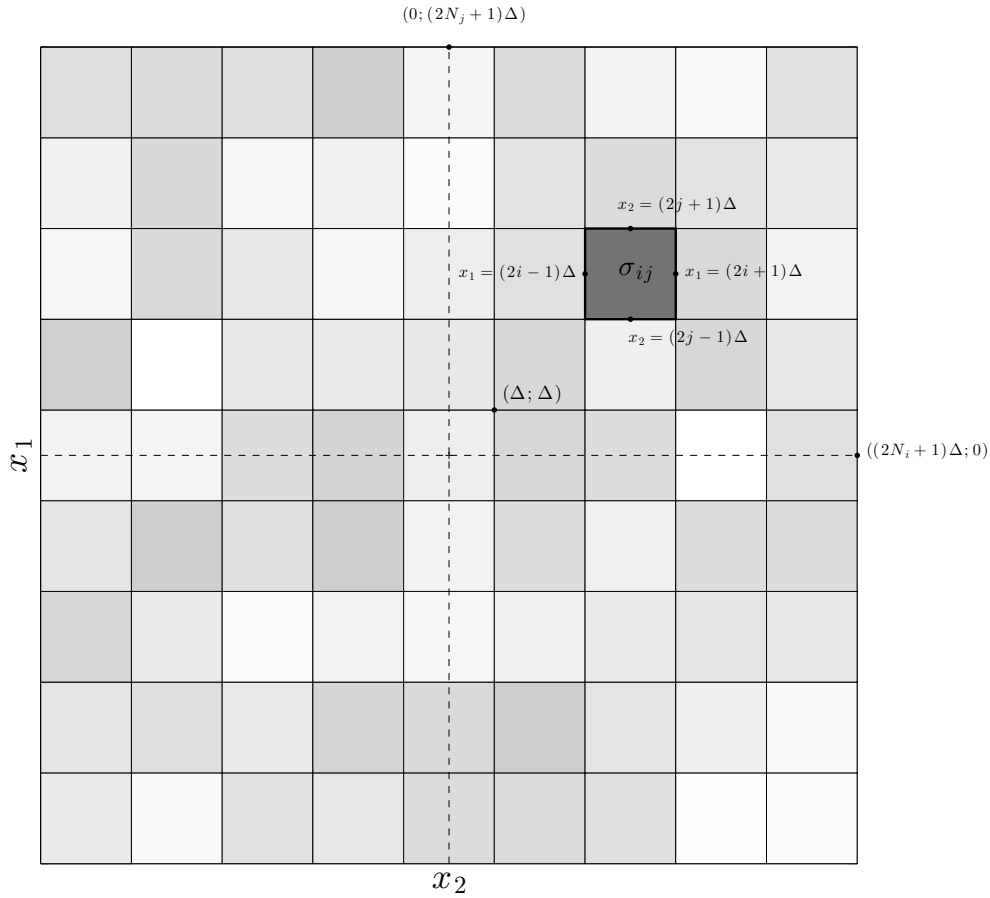


**Figure 3.1:** Illustration of the  $(2N_{(i)} + 1) \times (2N_{(j)} + 1)$  regular grid defined in the lens plane. To the pixel  $p_{ij}$  defined by the interval  $[(2i - 1)\Delta, (2i + 1)\Delta] \cup [(2j - 1)\Delta, (2j + 1)\Delta]$ , we associate a constant surface mass density  $\sigma_{ij}$ . Each of the pixels contributes to the bending of a light ray characterized by an impact parameter  $\mathbf{x}$ .

### 3.6.1 Determination of the expression of the deflection angle

Let us consider a general lens mass distribution which surface mass density defined in the lens plane may be tessellated into  $2\Delta$  by  $2\Delta$  squares, the so-called pixels. For each of them, we associate a constant surface mass density  $\sigma_{ij}$ . The whole grid contains  $(2N_{(i)} + 1) \times (2N_{(j)} + 1)$  pixels where  $N_{(k)} \in \mathbb{N}$  with  $k \equiv i$  or  $j$ . Furthermore, we define an arbitrarily oriented cartesian coordinate system centered on the deflector's gravity center. The origin of the latter coordinate system is set at the center of the indexed pixel  $(0, 0)$  (see Fig. 3.1). Therefore, we

characterize the total surface mass density by

$$\kappa(\mathbf{x}) = \sum_{i=-N_{(i)}}^{N_{(i)}} \sum_{j=-N_{(j)}}^{N_{(j)}} \sigma_{ij} \chi_{I_i}(x_1) \chi_{I_j}(x_2), \quad (3.51)$$

where  $i \in [-N_{(i)}, N_{(i)}]$ ,  $j \in [-N_{(j)}, N_{(j)}]$ ,  $I_k = [(2k - 1)\Delta ; (2k + 1)\Delta]$  and  $\chi_{I_k}(x_l)$  represents the indicator function defined by :

$$\chi_{I_k}(x_l) = \begin{cases} 1 & \text{if } x_l \in I_k \\ 0 & \text{otherwise} \end{cases}, \quad (3.52)$$

where  $l = 1$  or  $2$ . The surface mass density appearing in Eq. (3.51) allows to approximate any general mass distribution. Of course, larger the number of pixels and smaller their size, better the approximation. However, a realistic representation of a mass distribution requires a finite number of pixels characterized by a small, but non zero, size. In the remainder, we adopt the following notation :

$$\sum_{i=-N_{(i)}}^{N_{(i)}} \sum_{j=-N_{(j)}}^{N_{(j)}} = \sum_{\substack{-N_{(i)} \leq i \leq N_{(i)} \\ -N_{(j)} \leq j \leq N_{(j)}}}. \quad (3.53)$$

For a light-ray characterized by an impact parameter  $\mathbf{x} = (x_1; x_2)$  in the lens plane, the deflection angle is given by Eq. (9) (from Paper III). First, we derive the expression of the Fourier transform of  $\kappa(\mathbf{x})$ .

$$\begin{aligned} \mathcal{F}^{-}[\kappa(\mathbf{x})] &= \frac{1}{2\pi} \sum_{\substack{-N_{(i)} \leq i \leq N_{(i)} \\ -N_{(j)} \leq j \leq N_{(j)}}} \sigma_{ij} \int_{(2i-1)\Delta}^{(2i+1)\Delta} \int_{(2j-1)\Delta}^{(2j+1)\Delta} e^{-ix \cdot z} dx_1 dx_2, \\ &= \frac{2}{\pi} \frac{\sin(z_1 \Delta)}{z_1} \frac{\sin(z_2 \Delta)}{z_2} \sum_{\substack{-N_{(i)} \leq i \leq N_{(i)} \\ -N_{(j)} \leq j \leq N_{(j)}}} \sigma_{ij} e^{-2i\Delta(iz_1 + jz_2)}. \end{aligned} \quad (3.54)$$

For the case  $N_{(i)} = 0 = N_{(j)}$ , i.e. for a mass distribution composed of a unique square centered at  $(0, 0)$ , the sum equals 1. In addition, the terms  $e^{-2i\Delta(iz_1 + jz_2)}$ , which represents rotations in the Fourier space, can be simply understood as translations of each pixel from the position  $(0, 0)$  to  $(2i\Delta, 2j\Delta)$ , weighed by  $\sigma_{ij}$ . After inserting Eq. (3.54) into Eq. (9) (from Paper III), the deflection angle reduces to :

$$\hat{\alpha}(\mathbf{x}) = \frac{2l}{\pi^2} \sum_{\substack{-N_{(i)} \leq i \leq N_{(i)} \\ -N_{(j)} \leq j \leq N_{(j)}}} \sigma_{ij} \iint_{\mathbb{R}^2} \frac{z \sin(z_1 \Delta) \sin(z_2 \Delta)}{z_1 z_2 (z_1^2 + z_2^2)} e^{i(z_1 \zeta_1^{(i)} + z_2 \zeta_2^{(j)})} dz_1 dz_2, \quad (3.55)$$

where  $\zeta_1^{(i)} = x_1 - 2i\Delta$  and  $\zeta_2^{(j)} = x_2 - 2j\Delta$ . In the remainder, we will perform the calculus for the first component  $\hat{\alpha}_1(\mathbf{x})$  of the deflection angle :

$$\hat{\alpha}_1(\mathbf{x}) = \frac{2\iota}{\pi^2} \sum_{\substack{-N_{(i)} \leq i \leq N_{(i)} \\ -N_{(j)} \leq j \leq N_{(j)}}} \sigma_{ij} \iint_{\mathbb{R}^2} \frac{\sin(z_1\Delta) \sin(z_2\Delta)}{z_2(z_1^2 + z_2^2)} e^{\iota(z_1\zeta_1^{(i)} + z_2\zeta_2^{(j)})} dz_1 dz_2. \quad (3.56)$$

Let us transform the exponential function in terms of sine and cosine functions :

$$e^{\iota(z_1\zeta_1^{(i)} + z_2\zeta_2^{(j)})} = \cos(z_1\zeta_1^{(i)} + z_2\zeta_2^{(j)}) + \iota \sin(z_1\zeta_1^{(i)} + z_2\zeta_2^{(j)}). \quad (3.57)$$

After inserting the latter equation into Eq. (3.56) and according to the parity of the integrand, both integrals reduce to :

$$\hat{\alpha}_1(\mathbf{x}) = -\frac{8}{\pi^2} \sum_{\substack{-N_{(i)} \leq i \leq N_{(i)} \\ -N_{(j)} \leq j \leq N_{(j)}}} \sigma_{ij} \int_0^{+\infty} \frac{\sin(z_2\Delta) \cos(z_2\zeta_2^{(j)})}{z_2} \left\{ \int_0^{+\infty} \frac{\sin(z_1\Delta) \sin(z_1\zeta_1^{(i)})}{z_1^2 + z_2^2} dz_1 \right\} dz_2 \quad (3.58)$$

The solution of the  $z_1$ -integral is given by (Gradshteyn & Ryzhik 2007, 3.742.1, p. 432) :

$$I_{z_1} \equiv \int_0^{+\infty} \frac{\sin(z_1\Delta) \sin(z_1\zeta_1^{(i)})}{z_1^2 + z_2^2} dz_1 = \frac{\pi}{4|z_2|} \left( e^{-|z_2|\Delta - \zeta_1^{(i)}} - e^{-|z_2|\Delta + \zeta_1^{(i)}} \right). \quad (3.59)$$

Inserting the latter equation into Eq. (3.58) leads to :

$$\hat{\alpha}_1(\mathbf{x}) = -\frac{2}{\pi} \sum_{\substack{-N_{(i)} \leq i \leq N_{(i)} \\ -N_{(j)} \leq j \leq N_{(j)}}} \sigma_{ij} \int_0^{+\infty} \frac{\sin(z_2\Delta) \cos(z_2\zeta_2^{(j)})}{z_2 |z_2|} \left( e^{-|z_2|\Delta - \zeta_1^{(i)}} - e^{-|z_2|\Delta + \zeta_1^{(i)}} \right) dz_2. \quad (3.60)$$

The latter equation can be simplified once we consider separately the two cases  $0 \leq |\zeta_1^{(i)}| \leq \Delta$  and  $|\zeta_1^{(i)}| > \Delta$  :

$$\hat{\alpha}_1(\mathbf{x}) = \begin{cases} -\frac{4}{\pi} \sum_{\substack{-N_{(i)} \leq i \leq N_{(i)} \\ -N_{(j)} \leq j \leq N_{(j)}}} \sigma_{ij} \int_0^{+\infty} \frac{\sin(z_2\Delta) \cos(z_2\zeta_2^{(j)})}{z_2^2} \text{sign}(\zeta_1^{(i)}) e^{-z_2\Delta} \sinh(z_2 |\zeta_1^{(i)}|) dz_2 & \text{if } 0 \leq |\zeta_1^{(i)}| \leq \Delta, \\ -\frac{4}{\pi} \sum_{\substack{-N_{(i)} \leq i \leq N_{(i)} \\ -N_{(j)} \leq j \leq N_{(j)}}} \sigma_{ij} \int_0^{+\infty} \frac{\sin(z_2\Delta) \cos(z_2\zeta_2^{(j)})}{z_2^2} \text{sign}(\zeta_1^{(i)}) e^{-z_2|\zeta_1^{(i)}|} \sinh(z_2\Delta) dz_2 & \text{if } 0 \leq \Delta \leq |\zeta_1^{(i)}|. \end{cases} \quad (3.61)$$

Finally, from the latter equation, the expression of the first component of the deflection angle can be expressed as :

$$\hat{\alpha}_1(\mathbf{x}) = -\frac{1}{\pi} \sum_{\substack{-N_{(i)} \leq i \leq N_{(i)} \\ -N_{(j)} \leq j \leq N_{(j)}}} \sigma_{ij} \left\{ \left( \mathcal{G}[(2j+1)\Delta; (2i+1)\Delta] - \mathcal{G}[(2j+1)\Delta; (2i-1)\Delta] \right) \right. \\ \left. - \left( \mathcal{G}[(2j-1)\Delta; (2i+1)\Delta] - \mathcal{G}[(2j-1)\Delta; (2i-1)\Delta] \right) + 2\pi x_1 \chi_{I_i}(x_1) \chi_{I_j}(x_2) \right\}, \quad (3.62)$$

where  $I_k$  is already defined by Eq. (3.51), and the function  $\mathcal{G}(a; b)$  is given by :

$$\mathcal{G}[a; b] = b \arctan\left(\frac{a-x_2}{x_1-b}\right) + x_1 \arctan\left(\frac{x_1-b}{a-x_2}\right) - \left(\frac{a-x_2}{2}\right) \ln\left((x_1-b)^2 + (a-x_2)^2\right) \quad (3.63)$$

The term  $(\pi/2)x_1 \chi_{I_i}(x_1) \chi_{I_j}(x_2)$  vanishes for all values of  $i$  and  $j$  excepted the ones corresponding to the pixel which contains the impact parameter. The expression of  $\hat{\alpha}_2(\mathbf{x})$  is simply given by inverting the role between  $x_1$  and  $x_2$  in Eqs. (3.62) and (3.63). We note that we recover the case of an infinite sheet with a constant surface mass density by assuming that  $N_{(i)} = N_{(j)} = 0$  and  $\Delta \rightarrow +\infty$ . Indeed, under these assumptions and from Eqs. (3.62) and (3.63), one simply finds :

$$\lim_{\Delta \rightarrow +\infty} \left[ \Delta \arctan\left(\frac{\Delta \pm x_2}{x_1 + \Delta}\right) + \Delta \arctan\left(\frac{\Delta \pm x_2}{x_1 - \Delta}\right) \right] = -x_1, \quad (3.64)$$

$$\lim_{\Delta \rightarrow +\infty} \left[ x_1 \arctan\left(\frac{\pm x_1 - \Delta}{\Delta - x_2}\right) + x_1 \arctan\left(\frac{\pm x_1 - \Delta}{\Delta + x_2}\right) \right] = -l x_1 \ln\left(\frac{1-l}{1+l}\right), \\ = -\frac{\pi}{2} x_1, \quad (3.65)$$

and

$$\lim_{\Delta \rightarrow +\infty} \left[ \frac{\Delta \pm x_2}{2} \ln\left(\frac{(x_1 + \Delta)^2 + (x_2 \pm \Delta)^2}{(x_1 - \Delta)^2 + (x_2 \pm \Delta)^2}\right) \right] = x_1. \quad (3.66)$$

After inserting Eqs. (3.64), (3.65) and (3.66) into Eq. (3.62), the expression of the first component of the deflection angle reduces to :

$$\hat{\alpha}_1(x_1) = -\frac{\kappa}{\pi} (2\pi x_1 - 2x_1 - \pi x_1 + 2x_1), \\ = -\kappa x_1, \quad (3.67)$$

where we have adopted the notation  $\kappa = \sigma_{00}$ . The same procedure can be performed for the second component. As a result, we obtain :

$$\hat{\alpha}(\mathbf{x}) = -\kappa \mathbf{x} , \quad (3.68)$$

which constitutes, of course, the expected result.

### 3.6.2 Test of Eq. (3.62) for the case of the NSIS lens model

In the present section, we propose to illustrate the validity of Eq. (3.62) for the case of the well-known non-singular isothermal sphere (NSIS). Such a model is defined by an axially symmetric mass distribution characterized by the following surface mass density (see Kormann & al., 1994) :

$$\kappa(\mathbf{x}) = \frac{1}{2 \sqrt{x_1^2 + x_2^2 + \rho_c^2}} , \quad (3.69)$$

where  $\rho_c$  represents the core radius. The expression of the associated deflection angle is given by :

$$\hat{\alpha}(\mathbf{x}) = -\frac{\sqrt{x_1^2 + x_2^2 + \rho_c^2} - \rho_c}{x_1^2 + x_2^2} \mathbf{x} . \quad (3.70)$$

First, we compare the components of the deflection angle for an arbitrary value of the impact parameter. On one hand, for a fixed value of the impact parameter, for instance  $\mathbf{x} = (3.57, 1.41)$ , expressed in dimensionless units, we compare the values of  $\hat{\alpha}(\mathbf{x})$  obtained with three constant dimensioned grids characterized by the different pixel sizes  $\Delta = 2$ ,  $\Delta = 2/5$ , and  $\Delta = 1/10$ , also expressed in dimensionless units (see Fig. 3.2). For each grid, we have represented both the surface mass density profile associated with the grid and the real one given by Eq. (3.69). A summary of the corresponding values of  $\hat{\alpha}(\mathbf{x})$  may be found in Table 3.1. As expected, the value of  $\hat{\alpha}(\mathbf{x})$ , derived from the grid model, tends towards the real one as the resolution increases. On the other hand, for a fixed value of the impact parameter, for instance  $\mathbf{x} = (10.74, 12.41)$ , and grid resolution  $\Delta = 2/3$ , both expressed in dimensionless units, we compare the values of  $\hat{\alpha}(\mathbf{x})$  obtained with three grids characterized by the different dimensions  $L = 19\Delta$ ,  $L = 31\Delta$  and  $L = 121\Delta$  (see Fig. 3.3). For each grid, we have also represented both the surface mass density profile associated with the grid



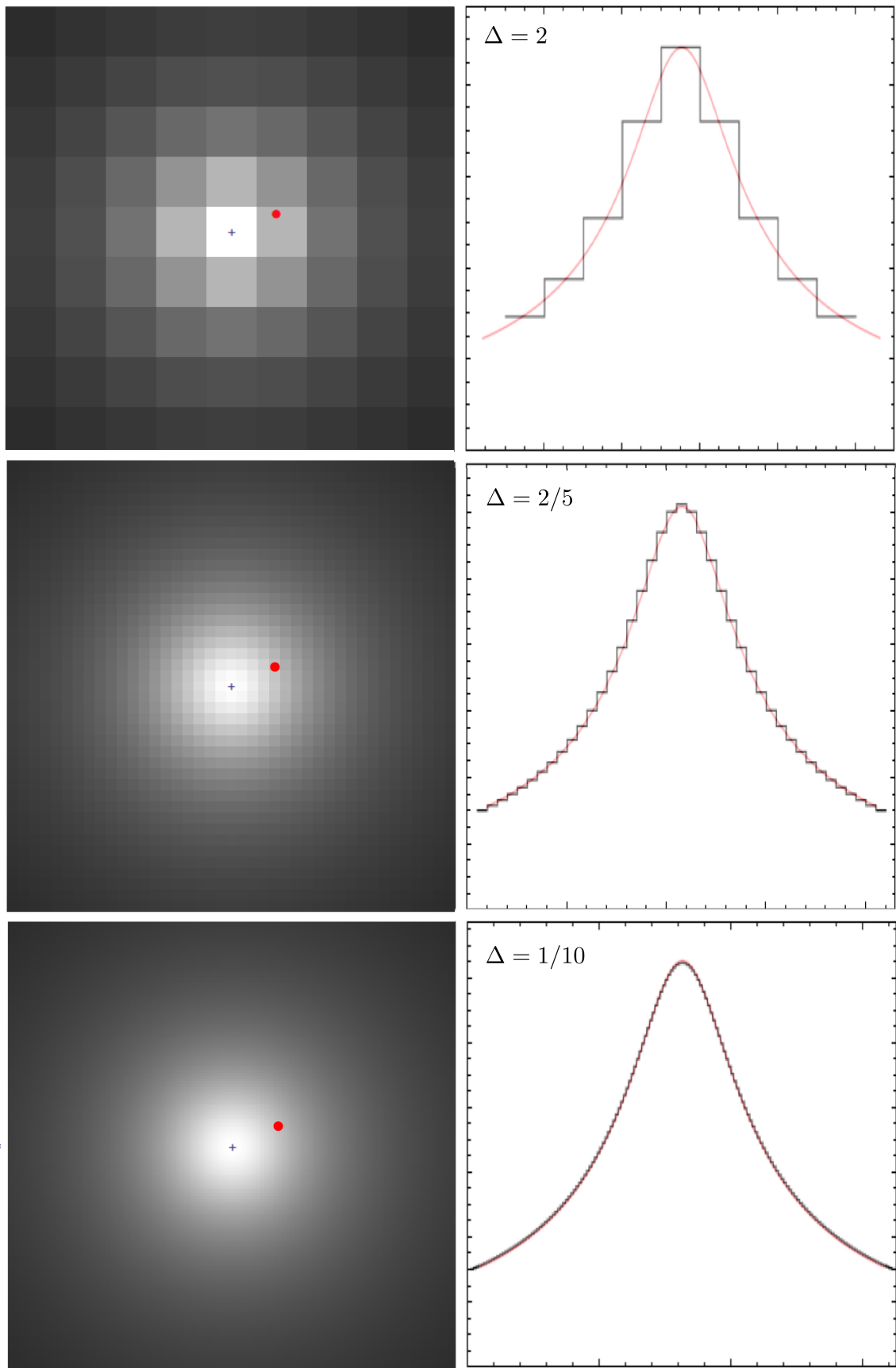


**Figure 3.2:** Illustration of three grid models having the same size ( $L = 18$ ) but characterized by different pixel sizes in order to represent an NSIS model. The red dot and the black cross (left panels) represent the impact parameter and the grid center positions, respectively. The black and red curves (right panels) represent the surface mass density profile associated with the grid and the real lens models, respectively.

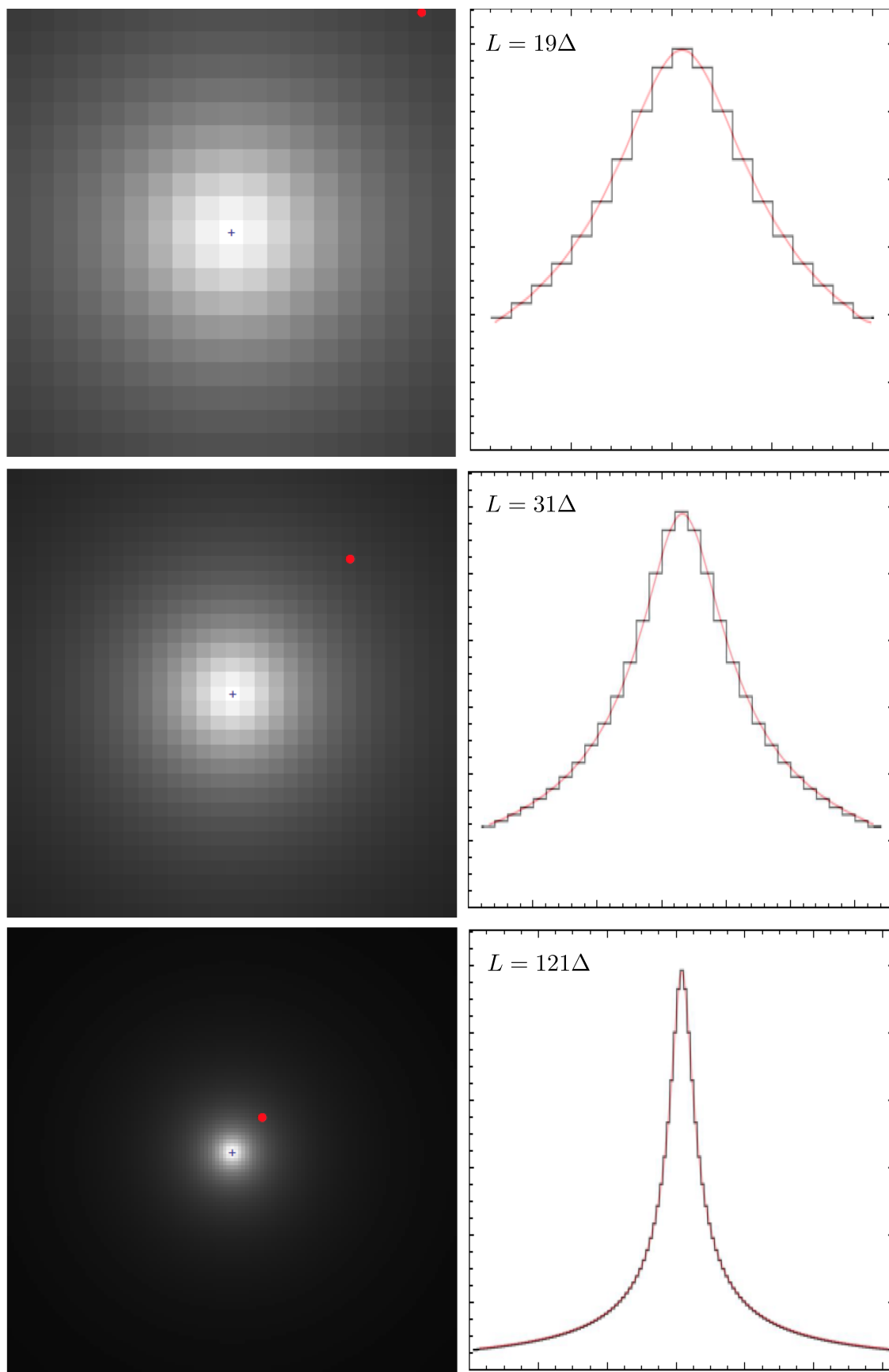


**Figure 3.3:** Illustration of three fixed resolution ( $\Delta = 2/3$ ) grid models characterized by different sizes in order to represent an NSIS model. The red dot and the black cross (left panels) represent the impact parameter and the grid center positions, respectively. The black and red curves (right panels) represent the surface mass density profile associated with the grid and the real lens models, respectively.

**Table 3.1:** Comparison between the components of the deflection angle derived from the grid models and the NSIS one. The resolution, characterized by the size  $\Delta$  of the pixels, increases from one model to another. The dimension of the grid is fixed to  $L = 18$ .

	$\hat{\alpha}_1(\mathbf{x})$	$\hat{\alpha}_2(\mathbf{x})$	$\Delta\hat{\alpha}_1$	$\Delta\hat{\alpha}_2$
NSIS	-0.374067	-0.147741	–	–
$\Delta = 2$	-0.351322	-0.149219	-0.022745	0.001478
$\Delta = 2/5$	-0.374606	-0.146881	0.000539	-0.000860
$\Delta = 1/10$	-0.374274	-0.147150	0.000207	-0.000591

**Table 3.2:** Comparison between the components of the deflection angle derived from the grid models and the NSIS one. The dimension of the grid, characterized by  $L$ , increases from one model to another. The size of a pixel is fixed to  $\Delta = 2/3$ .

	$\hat{\alpha}_1(\mathbf{x})$	$\hat{\alpha}_2(\mathbf{x})$	$\Delta\hat{\alpha}_1$	$\Delta\hat{\alpha}_2$
NSIS	-0.514061	-0.593994	–	–
$L = 19\Delta$	-0.423368	-0.540215	-0.090693	-0.053779
$L = 31\Delta$	-0.494017	-0.581257	0.020044	-0.127370
$L = 121\Delta$	-0.513403	-0.593611	0.000658	-0.000383

and the real one given by Eq. (3.69). A summary of the corresponding values of  $\hat{\alpha}(\mathbf{x})$  may be found in Table 3.2. Once again, the value of  $\hat{\alpha}(\mathbf{x})$ , derived from the grid model, tends towards the real one as the grid dimension increases.

Secondly, we compare the lensed images produced by the NSIS lens model and the NSIS successively modeled with two grids characterized by different resolutions. To this end, we have selected a circular 2-D gaussian image for the source and set the core radius of the NSIS equal to half the FWHM of the source. The lensed images obtained with the analytical lens model are shown in Fig. 3.4. The lensed images produced by means of the two grids, their representations and residual maps obtained by comparison (in terms of absolute value) between the grid and the analytical lens models are shown in Figs. 3.5 and 3.6. For the case of the first grid (see Fig. 3.5), the dimensionless size of the pixels has been set equal to  $\Delta = 25$  and  $N_i = N_j = 4$ . For the case of the second grid (see Fig. 3.6), the dimensionless size of the pixels has been set equal to  $\Delta = 5$  and  $N_i = N_j = 20$ . Let us note that the total size of the grid is equivalent in both cases ( $L = 100$ ). As expected, the highest resolution shows the best agreement with the lensed images produced by the analytical NSIS lens model.

The analytical expressions obtained in this section might constitute a very useful result, particularly for the lens modeling. Indeed, together with a sophisticated genetic algorithm, called *Ferret*, which allows to perform global optimization, we project to investigate the modeling of well-known gravitational lens systems. As any non-parametric lens model, the lens modeling can be approached without any preconception about the mass distribution of

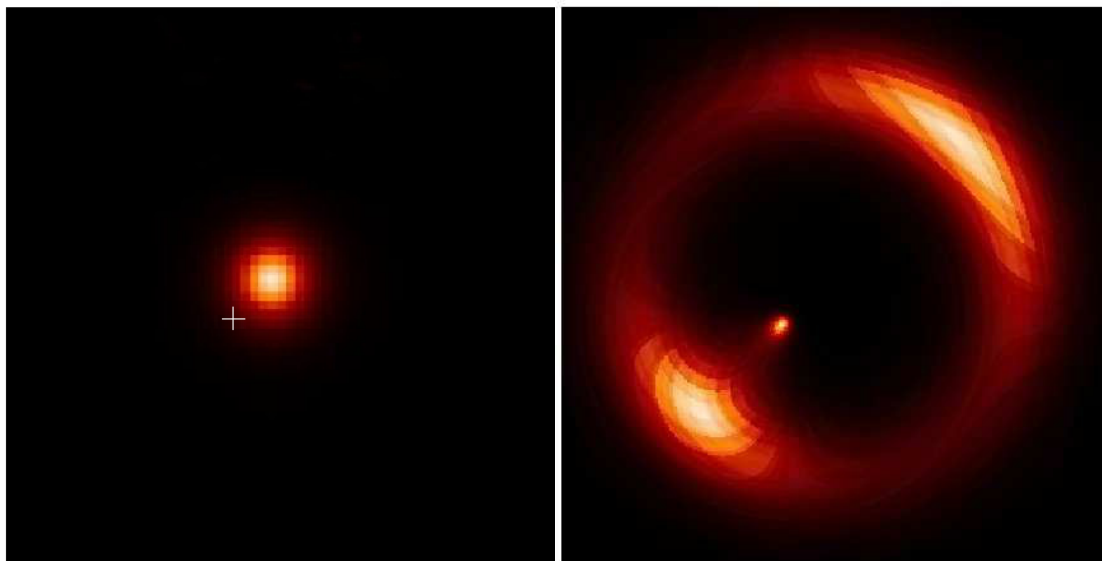


**Figure 3.4:** Left panel : the circular 2-D gaussian source. The white cross locates the center of the deflector. Right panel : the lensed images produced by the NSIS model

the deflector. In addition, having analytical expressions for  $\hat{a}(\mathbf{x})$  may lead to very efficient numerical calculations which are, up to now, essential in order to invert the lens equation.

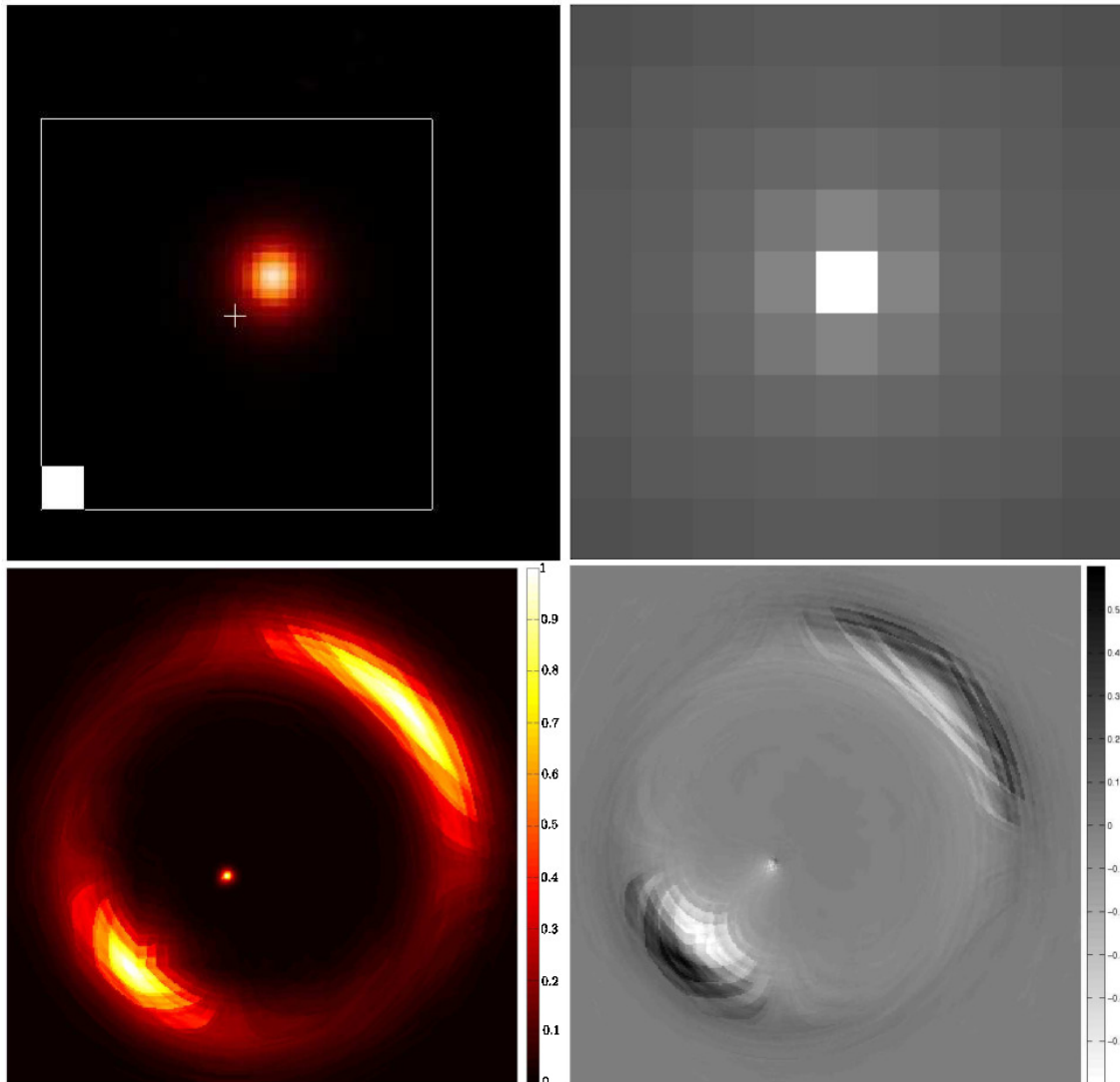


**Figure 3.5:** Illustration of the lensed images produced by a grid lens model characterized by  $\Delta = 20$  and  $N_i = N_j = 5$  and which approximates the analytical NSIS lens model. The top left panel represents the source plane. The small filled square represents the size of a single pixel adopted to characterize the NSIS mass distribution, while the big white square represents the total grid, both in comparison with the source size. The top right panel represents the pixellated mass distribution in the lens plane. The bottom panels represent the lensed images and the residual map, respectively.

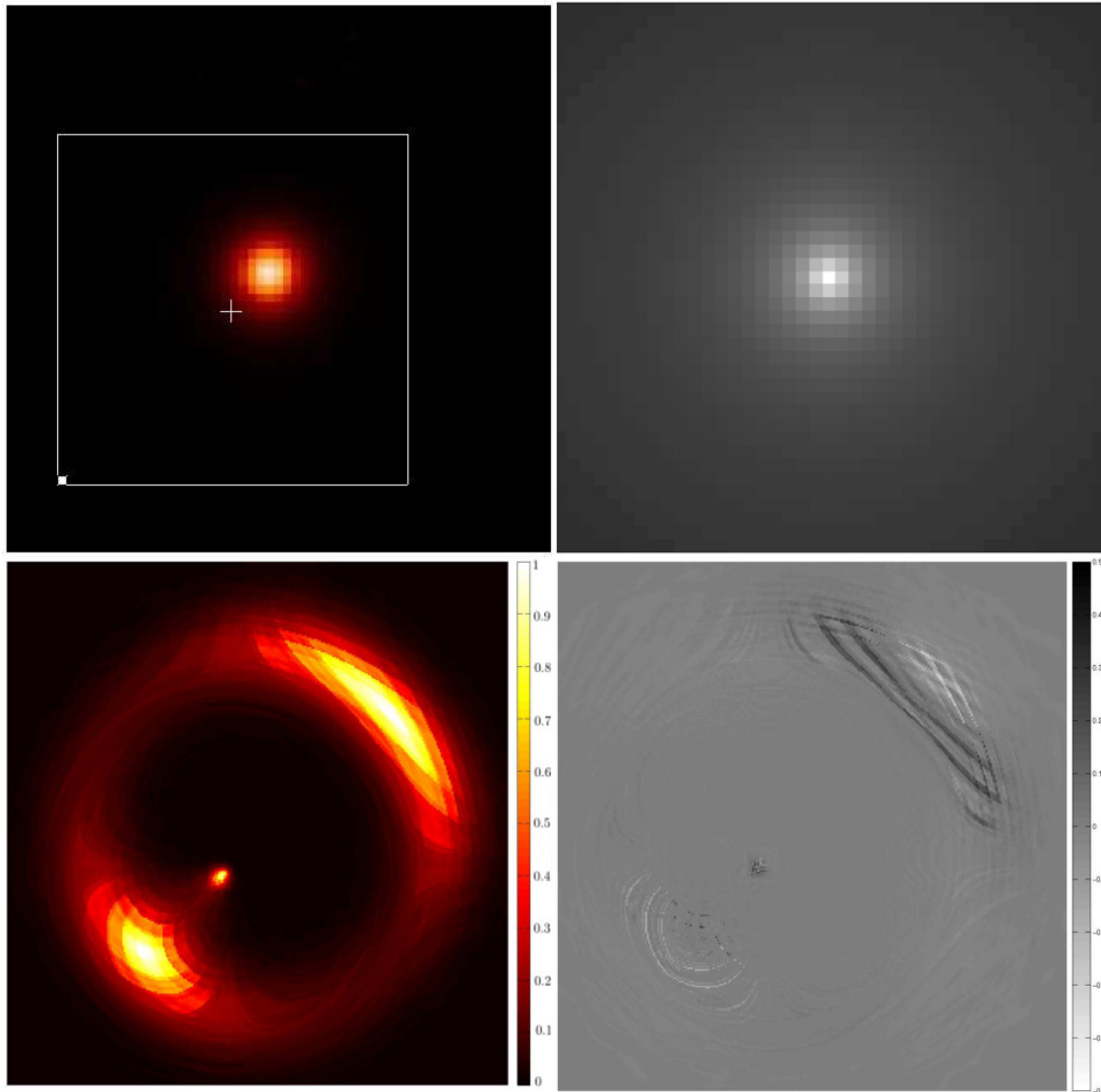


**Figure 3.6:** Illustration of the lensed images produced by a grid lens model characterized by  $\Delta = 5$  and  $N_i = N_j = 20$  and which approximates the analytical NSIS lens model. The top left panel represents the source plane. The small filled square represents the size of a single pixel adopted to characterize the NSIS mass distribution, while the big white square represents the total grid, both in comparison with the source size. The top right panel represents the pixellated mass distribution in the lens plane. The bottom panels represent the lensed images and the residual map, respectively.







**3.7** Paper IV

---

# **The non-singular isothermal ellipsoid lens model revisited : a complete analytical solution**

**O. Wertz and J. Surdej**

*Monthly Notices of the Royal Astronomical Society*, 2014, submitted.

**The non-singular isothermal ellipsoid lens model revisited :  
a complete analytical solution**

Journal:	<i>Monthly Notices of the Royal Astronomical Society</i>
Manuscript ID:	Draft
Manuscript type:	Main Journal
Date Submitted by the Author:	n/a
Complete List of Authors:	Wertz, Olivier; Université de Liège, Extragalactic Astrophysics and Space Observations Surdej, Jean; Université de Liège, Extragalactic Astrophysics and Space Observations
Keywords:	gravitational lensing: strong < Physical Data and Processes

# The non-singular isothermal ellipsoid lens model revisited : a complete analytical solution

O. Wertz<sup>1\*</sup> and J. Surdej<sup>1\*†</sup>

<sup>1</sup>*Institut d'Astrophysique et de Géophysique, Université de Liège, Allée du 6 Août 17, Sart Tilman, Bât. B5c, 4000 Liège, Belgique*

Accepted — Received —; in original form —

## ABSTRACT

The non-singular isothermal ellipsoid (NSIE) represents a realistic class of deflector models leading to the formation of up to five lensed images. The first analytical approach of the NSIE has been proposed by Kormann & al. 1994. Unfortunately, the complicated expression derived for the deflection angle causes strong limitations for a proper analytical treatment of this model. In the present paper, we propose a new expression for the NSIE deflection angle based upon the Fourier approach (Wertz & Surdej 2014). Furthermore, we derive a complete analytical expression for the normalized deflection potential  $\hat{\psi}$  as well as for the critical and caustic curves, even off the axis.

**Key words:** gravitational lensing : strong – cosmology : cosmological parameters.

## 1 INTRODUCTION

The complete analytical treatment of a family of deflector models presents the advantage to lead to rigorous expressions for the deflection angle, the deflection potential, the time delays and amplification ratios between pairs of lensed images, as well as the shape of the critical curves and their associated caustic curves. For the case of the NSIE family of models, an expression of the deflection angle has first been proposed by Kormann & al. (1994, hereafter KSB). Unfortunately, the complicated expression derived for the deflection angle by KSB implies strong limitations for a complete analytical treatment of this family of models. Their approach consists in using the complex formalism together with the results introduced by Bourassa & Kantowski (1973, 1975), corrected by Bray (1984). This elegant representation of the lens theory allows KSB to obtain analytical expressions for the deflection angle and the internal shear. From these results, KSB were able to derive analytical expressions for the intersection points between the critical (resp. caustic) curves and the axes of the orthogonal coordinate system, which restricted the analytic treatment to only a few particular points. However, they have constructed complete critical and caustic curves from an unfactorizable third order polynomial in  $\kappa$ , the dimensionless surface mass density.

In the present paper, we apply the Fourier approach, developed by the authors (Wertz & Surdej 2014, hereafter WS), to derive the expression of the NSIE deflection angle. Although rigorously equivalent to the one derived by KSB, our expression of the deflection angle is more simple (Section 2). Consequently, this simplification has allowed us to determine analytical expressions for the deflection potential (Section 3) and a complete analytical treat-

ment of the critical and caustic curves, even off the axes (Section 4). Some conclusions form the last section.

## 2 THE DEFLECTION ANGLE FROM THE FOURIER APPROACH

We have recently proposed the use of the Fourier transform in order to analytically derive simple expressions of the gravitational lens deflection angle (see WS). As a reminder, the deflection angle can always be expressed as a convolution product:

$$\hat{\alpha}(\mathbf{x}) = -\frac{1}{\pi} \kappa(\mathbf{x}) \otimes \frac{\mathbf{x}}{|\mathbf{x}|^2}, \quad (1)$$

where  $\mathbf{x} = (x_1, x_2)$  corresponds to the normalized impact parameter vector defined in the lens plane, perpendicular to the line-of-sight, and  $\kappa(\mathbf{x})$  represents the dimensionless surface mass density, also called convergence. Making use of the Fourier convolution theorem and after some simplifications, the expression of the deflection angle becomes

$$\hat{\alpha}(\mathbf{x}) = 2 \iota \mathcal{F}^+ \left[ \mathcal{F}^- [\kappa(\mathbf{x})] \frac{\mathbf{z}}{|\mathbf{z}|^2} \right], \quad (2)$$

where

$$\mathcal{F}^\mp[f] = \frac{1}{2\pi} \iint_{\mathbb{R}^2} f(\mathbf{x}) e^{\mp i\mathbf{x}\cdot\mathbf{z}} d\mathbf{x}, \quad (3)$$

denotes the Fourier transform (–) or its inverse (+), and  $\iota$  represents the imaginary unit.

The NSIE models are characterized by the dimensionless surface mass density :

$$\kappa(x_1, x_2) = \frac{\sqrt{f}}{2\sqrt{x_1^2 + f^2 x_2^2 + \rho_c^2}} \equiv \frac{\sqrt{f}}{2\xi}, \quad (4)$$

\* Aspirant du F.R.S. - FNRS.

† Also Directeur de Recherche honoraire du F.R.S. -FNRS.

## 2 *O. Wertz and J. Surdej*

where  $\rho_c$  represents the dimensionless core radius and  $\xi$  is defined by  $\xi = \sqrt{x_1^2 + f^2 x_2^2 + \rho_c^2}$ . The NSIE models constitute a special case of a more general family of models characterized by the dimensionless surface mass density having the form

$$\kappa(x_1; x_2) = \frac{\kappa_0}{(\rho_c^2 + \rho^2)^\nu}, \quad (5)$$

where  $\rho = \sqrt{x_1^2 + f^2 x_2^2}$ , and for which we have already published the expressions of the deflection angle components (see WS, Eqs. (29), (30) and (31)). The NSIE family of models is obtained from Eq. (5) by considering  $\kappa_0 = \sqrt{f}/2$  and  $\nu = 1/2$ . After substituting Eq. (4) into Eq. (2), the deflection angle takes the form:

$$\hat{\alpha}_1(x_1; x_2) = \frac{\sqrt{f}}{2f'} \ln \left( \frac{2ff'x_1\rho_c + \rho_c^2 + f^2(r^2 - \rho_c^2)}{(2 - f^2)x_1^2 + \rho_c^2 + f^2(x_2^2 - \rho_c^2) + 2f'x_1\xi} \right), \quad (6)$$

and

$$\hat{\alpha}_2(x_1; x_2) = \frac{\sqrt{f}}{f'} \arctan \left( \frac{ff'x_2(f\rho_c - f'x_1 - \xi)}{f'x_1(\rho_c + f\xi) + (f\rho^2 + f'^2\rho_c\xi)} \right), \quad (7)$$

where  $r = \sqrt{x_1^2 + x_2^2}$  and  $f' = \sqrt{1 - f^2}$ . These expressions of the deflection angle components constitute a new simplification of the expressions that we have already published for the NSIE (see WS). We note that Eqs. (6) and (7) remain rigorously equivalent to the expressions derived by Kormann et al. (1994, Eqs. (62a-e)) although no complex quantities are here involved.

For  $\rho_c = 0$ , these equations reduce to the singular isothermal ellipsoid (SIE) deflection angle. Furthermore, by taking the limit of Eqs. (6) and (7), as  $f$  tends towards 1, we retrieve the expression of the non-singular isothermal sphere (NSIS) deflection angle.

### 3 THE DEFLECTION POTENTIAL $\hat{\psi}$

The complicated expression of the deflection angle has caused strong limitations on the analytic handling of this family of models. As far as we know, the analytical expression of the deflection potential has never been published yet. Fortunately, the simplification of the deflection angle expressions that we have obtained allows us to derive the analytical expression of  $\hat{\psi}(x_1; x_2)$ .

First, we recall that  $\hat{\alpha}(x) = -\nabla\hat{\psi}(x)$ . Since the deflection potential is defined up to an additive constant, we have :

$$\int \hat{\alpha}_1(x_1; x_2) dx_1 = -\hat{\psi}_1(x_1; x_2) + K_1(x_2) \equiv -\hat{\psi}(x_1; x_2), \quad (8)$$

and

$$\int \hat{\alpha}_2(x_1; x_2) dx_2 = -\hat{\psi}_2(x_1; x_2) + K_2(x_1) \equiv -\hat{\psi}(x_1; x_2), \quad (9)$$

where  $K_1$  (resp.  $K_2$ ) represents an integration constant with respect to  $x_1$  (resp.  $x_2$ ) which could be a function of  $x_2$  (resp.  $x_1$ ). Therefore, by taking the derivative of Eq. (8) with respect to  $x_2$ , we obtain an equation for which only  $dK_1(x_2)/dx_2$  is unknown :

$$\frac{dK_1(x_2)}{dx_2} = \hat{\alpha}_2(x_1; x_2) + \frac{\partial \hat{\psi}_1(x_1; x_2)}{\partial x_2}. \quad (10)$$

We deduce the expression of  $\hat{\psi}_1(x_1; x_2)$  from the undefined integral of Eq. (6) in which we split the logarithm of a ratio into the differ-

ence of two logarithms.

$$\begin{aligned} -\hat{\psi}_1(x_1; x_2) &= \frac{\sqrt{f}}{2f'} \int \ln(f^2 x_1^2 + 2ff'\rho_c x_1 + f^2 x_2^2 + f'^2 \rho_c^2) dx_1 \\ &\quad - \frac{\sqrt{f}}{2f'} \int \ln((2 - f^2)x_1^2 + 2f'\xi x_1 + f^2 x_2^2 + f'^2 \rho_c^2) dx_1. \end{aligned} \quad (11)$$

The two latter undefined integrals can be analytically calculated (see App. A1). After substituting the derivative of Eq. (11) with respect to  $x_2$  into Eq. (10) and some algebraic simplifications, we find the following very simple expression for  $dK_1(x_2)/dx_2$  :

$$\frac{dK_1(x_2)}{dx_2} = -\text{sign}(x_2) \frac{\pi\sqrt{f}}{2f'}, \quad (12)$$

from which we deduce the expression of the function  $K_1(x_2)$  :

$$K_1(x_2) = -|x_2| \frac{\pi\sqrt{f}}{2f'}. \quad (13)$$

After substituting Eq. (13) and the expression of  $\hat{\psi}_1(x_1; x_2)$  into Eq. (8), the expression of the NSIE deflection potential can be expressed as :

$$\begin{aligned} \hat{\psi}(x_1; x_2) &= \frac{\sqrt{f}}{4f'} \left[ 2x_2 \left( \arctan \left( \frac{f^2 r^2 - f'^2 \rho_c^2}{2ff'\rho_c x_2} \right) - \arctan \left( \frac{f^2 f' x_2 \xi}{P_+} \right) \right) \right. \\ &\quad \left. - \arctan \left( \frac{f^2 f' x_2 \xi}{P_-} \right) \right] - \frac{\rho_c f'}{f} \ln \left[ \frac{Q_+}{Q_-} \left( (f^2 r^2 + f'^2 \rho_c^2)^2 - (2ff'\rho_c x_1)^2 \right) \right] \\ &\quad + 2x_1 \ln \left[ \frac{(f'x_1 + \xi)^2 - (f\rho_c)^2}{(fx_1 + f'\rho_c)^2 + (fx_2)^2} \right] + |x_2| \pi \text{sign} \left[ |x_2| - \frac{\sqrt{\rho_c(f\xi - \rho_c)}}{ff'} \right], \end{aligned} \quad (14)$$

where  $P_{\pm} = f^2 f'^2 x_2^2 \pm f\rho_c \xi + \rho_c^2$  and  $Q_{\pm} = f^2(r^2 + \rho_c^2) \pm 2f\rho_c \xi + \rho_c^2$ . We note that the argument of the sign function is real only if  $\rho \geq \rho_c f'/f$ . For  $\rho < \rho_c f'/f$ , we set  $\text{sign}(z) = 1$  with  $z \in \mathbb{C}$ . In addition, the derived expression of  $\hat{\psi}$  satisfies of course the Poisson equation  $\Delta\hat{\psi}(x_1; x_2) = 2\kappa(x_1; x_2)$ .

For the case  $\rho_c = 0$ , i.e. for the SIE models, we retrieve the well-known expression of the deflection potential published in KSB. Indeed, for  $\rho_c = 0$ , we have  $\xi = \rho$ ,  $P_{\pm} = f^2 f'^2 x_2^2$ ,  $Q_{\pm} = f^2 r^2$ , and the deflection angle reduces to :

$$\begin{aligned} \hat{\psi}_{\text{SIE}}(x_1; x_2) &= \frac{\sqrt{f}}{f'} \left[ x_2 \left( \text{sign}(x_2) \frac{\pi}{4} - \arctan \left( \frac{\rho}{f'x_2} \right) \right) \right. \\ &\quad \left. + x_1 \ln \left( \frac{f'x_1 + \rho}{fr} \right) + |x_2| \frac{\pi}{4} \right]. \end{aligned} \quad (15)$$

Furthermore, since  $\rho \geq 0$ ,  $f' \geq 0$  and by definition of the arctangent function, we have :

$$\arctan \left( \frac{\rho}{f'x_2} \right) = \begin{cases} \pi/2 - \arctan \left( \frac{f'x_2}{\rho} \right) & \text{if } x_2 \geq 0 \\ -\pi/2 - \arctan \left( \frac{f'x_2}{\rho} \right) & \text{if } x_2 < 0, \end{cases} \quad (16)$$

which leads to :

$$\hat{\psi}_{\text{SIE}}(x_1; x_2) = \frac{\sqrt{f}}{f'} \left[ x_2 \arctan \left( \frac{f'x_2}{\rho} \right) + x_1 \ln \left( \frac{f'x_1 + \rho}{fr} \right) \right]. \quad (17)$$

$$(18)$$

Finally, making use of the two following identities :

$$\arctan(z) = \arcsin \left( \frac{z}{\sqrt{1+z^2}} \right), \quad (19)$$

and

$$\ln(z) = \text{arcsinh} \left( \frac{z^2 - 1}{2z} \right), \quad (20)$$

we retrieve the expression of the SIE deflection potential :

$$\hat{\psi}_{\text{SIE}}(x_1; x_2) = \frac{\sqrt{f}}{f'} \left[ x_2 \arcsin \left( f' \frac{x_2}{r} \right) + x_1 \operatorname{arcsinh} \left( \frac{f'}{f} \frac{x_1}{r} \right) \right]. \quad (21)$$

## 4 CRITICAL AND CAUSTIC CURVES

### 4.1 Problem statement

The critical curves correspond to the geometrical locus in the lens plane at which the amplification factor  $\mu$  tends towards infinity. We recall that  $\mu$  is defined by :

$$\mu(x_1; x_2) = \frac{1}{(1 - \kappa)^2 - \gamma^2}, \quad (22)$$

where  $\kappa(x_1; x_2)$  is given by Eq. (5),  $\gamma^2 = \gamma_1^2 + \gamma_2^2$ , and the two components of the internal shear by :

$$\begin{aligned} \gamma_1(x_1; x_2) &= \frac{1}{2} (\hat{\psi}_{,11}(x_1; x_2) - \hat{\psi}_{,22}(x_1; x_2)), \\ &= \frac{1}{2} (\hat{\alpha}_{1,1}(x_1; x_2) - \hat{\alpha}_{2,2}(x_1; x_2)) \end{aligned} \quad (23)$$

and

$$\gamma_2(x_1; x_2) = \hat{\psi}_{,12}(x_1; x_2) = \hat{\alpha}_{1,2}(x_1; x_2) = \hat{\alpha}_{2,1}(x_1; x_2), \quad (24)$$

where the derivative with respect to  $x_1$  (resp.  $x_2$ ) is denoted by comma 1 (resp. comma 2). After substituting Eqs. (4), (23) and (24) into Eq. (22), one obtains a third order equation in  $\kappa$  which cannot be factorized off the axes, with respect to  $x_1$  or  $x_2$  (see KSB, Eq. (69 a - e)). However, we propose to modify Eq. (22) into a form which can be factorized, and therefore obtain a complete analytical expression for the critical and caustic curves.

We first note that, from the Poisson equation :

$$\hat{\psi}_{,ii}(x_1; x_2) = 2 \kappa(x_1; x_2) - \hat{\psi}_{,jj}(x_1; x_2), \quad (25)$$

where  $i = 1$  or  $2$  and  $j = 2$  or  $1$ . After substituting Eq. (23) into Eq. (22), and making use of Eq. (25) with  $i = 2$  (hence  $j = 1$ ), the amplification factor transforms into :

$$\mu^{-1}(x_1; x_2) = 1 - 2 \kappa(x_1; x_2) + \hat{\psi}_{,11}(x_1; x_2) \hat{\psi}_{,22}(x_1; x_2) - \gamma_2^2(x_1; x_2). \quad (26)$$

Our interest in this expression of the amplification factor lies in the fact that the terms  $\kappa$ ,  $\hat{\psi}_{,11}$  and  $\hat{\psi}_{,22}$  are no longer squared, which simplify the further calculations. The explicit expressions of  $\hat{\psi}_{,11}(x_1; x_2)$  and  $\hat{\psi}_{,22}(x_1; x_2)$  may be found in App. A2. The expressions of  $\gamma_1^2(x_1; x_2)$  and  $\gamma_2^2(x_1; x_2)$  have been first derived by KSB (see Eqs. (63 a - c)).

Since we are searching the solutions of the equation  $\mu^{-1} = 0$  in terms of  $x_1$  (or  $x_2$ ) and the parameters  $f$  and  $\rho_c$ , we gather all the explicit terms in  $\xi$  and obtain :

$$\mu^{-1}(x_1; x_2) = F_2(x_1; x_2) \xi + F_1(x_1; x_2) = 0, \quad (27)$$

where the functions  $F_i(x_1; x_2)$ , given in App. A3, do not depend explicitly on  $\xi$ . Furthermore, all solutions of Eq. (27) are necessarily solutions of the following equation :

$$F_2^2(x_1; x_2) \xi^2 - F_1^2(x_1; x_2) = 0, \quad (28)$$

even though the reciprocal is not true. Eq. (28) has the advantage to be expressed in terms of  $x_1$ ,  $x_2$  and their whole power. Therefore, Eq. (28) may be considered as a polynomial with respect to  $x_1$  or  $x_2$ , and can then be simplified to obtain the following equation to resolve :

$$(\xi^3 + p_2 \xi^2 + p_1 \xi + p_0) G_1(x_1; x_2) G_2(x_1; x_2) = 0, \quad (29)$$

where  $\xi = x_1^2$ ,  $p_i$  representing real functions of  $x_2$ ,  $f$ ,  $\rho_c$ , and are defined by :

$$p_2 = \left[ x_2^2 (2 + f^2) - (2 - 3f^2) \frac{\rho_c^2}{f^2} - f \right], \quad (30)$$

$$\begin{aligned} p_1 &= \left[ x_2^4 (1 + 2f^2) + x_2^2 \frac{2}{f^2} \left( (1 - f^2 + f^4) \rho_c^2 - f^3 \right) \right. \\ &\quad \left. + \frac{\rho_c}{f^4} (2f^{9/2} - 2f^3 (1 + f^2) \rho_c + (1 - 4f^2 + 3f^4) \rho_c^3) \right], \end{aligned} \quad (31)$$

and

$$\begin{aligned} p_0 &= x_2^6 f^2 + x_2^4 \left[ (3 - 2f^2) \rho_c^2 - f \right] \\ &\quad + x_2^2 \frac{\rho_c}{f^2} \left[ 2f^{5/2} - 2f (1 + f^2) \rho_c + (3 - 4f^2 + f^4) \rho_c^3 \right] \\ &\quad + \frac{\rho_c^2}{f^4} \left[ -f^4 + 2f^{5/2} (1 + f^2) \rho_c - f (1 + f^2)^2 \rho_c^2 + f'^4 \rho_c^4 \right]. \end{aligned} \quad (32)$$

Since they only lead to imaginary solutions, the functions  $G_1(x_1; x_2)$  and  $G_2(x_1; x_2)$  are without any real interest. Therefore, the squared value of the critical curve point abscissae are solutions of the equation  $\xi^3 + p_2 \xi^2 + p_1 \xi + p_0 = 0$ . The resolution of the latter equation leads to six solutions for  $x_1$  in terms of  $x_2$ ,  $f$  and  $\rho_c$  :

$$x_1^{(1)} = \pm \frac{\sqrt{3}}{3} \sqrt{-p_2 + \frac{1}{2^{1/3} f^2} \left( 4^{1/3} \frac{S_1}{S_2} + S_2 \right)}, \quad (33)$$

$$x_1^{(2)} = \pm \frac{\sqrt{3}}{3} \sqrt{-p_2 + \frac{1}{2^{1/3} f^2} \left( 4^{1/3} J \frac{S_1}{S_2} + J^* S_2 \right)}, \quad (34)$$

and

$$x_1^{(3)} = \pm \frac{\sqrt{3}}{3} \sqrt{-p_2 + \frac{1}{2^{1/3} f^2} \left( 4^{1/3} J^* \frac{S_1}{S_2} + J S_2 \right)}, \quad (35)$$

where  $J = (-1 + i\sqrt{3})/2$  represents the first complex root of the unity,  $J^*$  its complex conjugate,  $S_1$  is given by :

$$\begin{aligned} S_1 &= f^4 f'^4 x_2^4 + x_2^2 (2f^2 f'^2 (f^3 - 7\rho_c^2)) \\ &\quad + (f^6 - 6f^{9/2} \rho_c + 10f^3 \rho_c^2 + \rho_c^4), \end{aligned} \quad (36)$$

and  $S_2$  is defined by :

$$S_2 = (A_1 + R \sqrt{A_2})^{1/3}, \quad (37)$$

where  $A_1$  and  $A_2$  both represent third order polynomials with respect to  $x_2^2$  and are given by :

$$\begin{aligned} A_1 &= x_2^6 2 f^6 f'^6 + x_2^4 6 f^4 f'^4 (f^3 + 11\rho_c^2) \\ &\quad + x_2^2 6 f^2 f'^2 (f^6 - 3f^{9/2} \rho_c - 2f^3 \rho_c^2 - 11\rho_c^4) \\ &\quad + 2 f^9 - 18f^{15/2} \rho_c + 57f^6 \rho_c^2 - 90f^{9/2} \rho_c^3 + 78f^3 \rho_c^4 - 2\rho_c^6, \end{aligned} \quad (38)$$

and

$$\begin{aligned} A_2 &= 12f^4 f'^6 x_2^6 + 24x_2^4 f^2 f'^4 (f^{3/2} + \rho_c)^2 \\ &\quad + 12x_2^2 f'^2 (f^{3/2} + \rho_c) (f^{9/2} - 6f^3 \rho_c + 3f^{3/2} \rho_c^2 + \rho_c^3) \\ &\quad - 3f \rho_c (f^{3/2} - 2\rho_c)^2 (4f^{3/2} + \rho_c), \end{aligned} \quad (39)$$

and, finally,  $R$  is given by :

$$R = 3f \rho_c \left[ f^3 + 2f^2 f'^2 x_2^2 - 4f^{3/2} \rho_c + 2\rho_c^2 \right]. \quad (40)$$

We note that for  $\rho_c > \sqrt{f}/(1+f) \equiv \rho_{c,\text{max}}$ , we have  $x_1^{(i)} \in \mathbb{C}$  for any

## 4 *O. Wertz and J. Surdej*

values of  $x_2$ , which implies that there are no critical curves. This particular value of  $\rho$  has first been deduced by KSB. In the remainder, we will only consider the three "+" solutions for the mathematical treatment. Indeed, the "-" solutions are exactly similar due to the symmetry of the deflection potential.

### 4.2 Validity range of Eqs. (33) - (35)

According to the values of  $f$ ,  $\rho_c$  and  $x_2$ , the values of the critical point abscissae are given by the solutions  $x_1^{(1)}$ ,  $x_1^{(2)}$  or  $x_1^{(3)}$ . In order to obtain the validity range of each solution, we have to verify under which conditions these solutions are real and verify Eq. (27). The solutions  $x_1^{(i)}$  are real only if their radicands, denoted by  $\Gamma^{(i)}$  in Eqs. (41) to (43), are real and positive. We will investigate separately these two cases in the following sections.

$$\Gamma^{(1)} = -p_2 + \frac{1}{2^{1/3} f^2} \left( 4^{1/3} \frac{S_1}{S_2} + S_2 \right), \quad (41)$$

$$\Gamma^{(2)} = -p_2 + \frac{1}{2^{1/3} f^2} \left( 4^{1/3} J \frac{S_1}{S_2} + J^* S_2 \right), \quad (42)$$

and

$$\Gamma^{(3)} = -p_2 + \frac{1}{2^{1/3} f^2} \left( 4^{1/3} J^* \frac{S_1}{S_2} + J S_2 \right). \quad (43)$$

#### 4.2.1 Conditions under which $\Gamma^{(i)} \in \mathbb{R}$

We note that for any value of  $0 \leq f \leq 1$ ,  $\rho_c \geq 0$  and  $x_2 \in \mathbb{R}$ , we have  $S_1 \in \mathbb{R}$ ,  $A_1 \in \mathbb{R}$  and  $R \in \mathbb{R}$ , whereas  $S_2$  might not be real, which may lead to  $x_1^{(i)} \in \mathbb{C}$ . From Eq. (37), we deduce that  $S_2$  lies in the complex field when  $A_2 < 0$  with  $R \neq 0$  or  $A^\dagger = A_1 + R \sqrt{A_2} < 0$ . The first condition is fulfilled for  $R \neq 0$  and  $|x_2| < X_2^{(2)}$  where  $X_2^{(2)}$ , a function of  $f$  and  $\rho_c$ , is defined in App. A4. Furthermore, from Eq. (40), we deduce that  $R = 0$  if  $x_2 = X_2^{(1)}$  where the expression of  $X_2^{(1)}$  is given by :

$$X_2^{(1)} = \frac{\sqrt{2}}{2 f f'} \sqrt{-2\rho_c^2 + 4f^{3/2}\rho_c - f^3}. \quad (44)$$

We note that  $X_2^{(1)}$  is real only for  $\rho_c^{(1-)} \leq \rho_c \leq \rho_c^{(1+)}$ , where  $\rho_c^{(1\pm)}$  is defined by :

$$\rho_c^{(1\pm)} = \frac{\sqrt{2}}{2} \sqrt{3 \pm 2\sqrt{2}} f^{3/2}. \quad (45)$$

The second condition requires more attention. The study of the function  $A^\dagger$  with respect to  $x_2$  leads to the conclusion that a necessary condition (but not sufficient) to obtain  $A^\dagger$  negative is  $X_2^{(2)} < |x_2| < X_2^{(3)}$  where  $X_2^{(3)}$  is defined by:

$$X_2^{(3)} = \frac{1}{f f'} \sqrt{7\rho_c^2 - f^3 - \sqrt{6\rho_c} \sqrt{8\rho_c^3 - 4f^3\rho_c + f^{9/2}}}. \quad (46)$$

We note that  $X_2^{(3)}$  is real only for  $\rho_c \geq f^{3/2}/2$ , which indicates that for  $\rho_c < f^{3/2}/2$ , the function  $A^\dagger$  is positive for any value  $|x_2| > X_2^{(2)}$ . Furthermore, for the case  $X_2^{(2)} < |x_2| < X_2^{(3)}$  and for a fixed value of  $f$ , we note that decreasing values of  $\rho_c$  implies increasing values of  $A^\dagger$ , and, for fixed values of  $f$  and  $\rho_c$ , the sign of  $A^\dagger$  remains unchanged. In other words, if we find a value of  $\rho_c$ , denoted for instance by  $\tilde{\rho}_c$ , for which  $A^\dagger > 0$ , then, for any real value  $\rho_c < \tilde{\rho}_c$  and  $X_2^{(2)} < |x_2| < X_2^{(3)}$ , we have  $A^\dagger > 0$ . Therefore, the change in sign of  $A^\dagger$  essentially depends on the values of  $f$  and  $\rho_c$ . By taking account of these two latter observations, we may solve the

**Table 1.** Summary of the real or complex nature and the sign study of the function  $A^\dagger$

		$\rho_c > f^{3/2}/2$			
		$ x_2  < X_2^{(2)}$	$X_2^{(2)} <  x_2  < X_2^{(3)}$	$ x_2  > X_2^{(3)}$	
		$f > f^\dagger$		$0 < f < f^\dagger$	
				$f^{3/2}/2 < \rho_c < \rho_c^\dagger$	$\rho_c > \rho_c^\dagger$
$A^\dagger$	$\in \mathbb{C}$	$> 0$	$> 0$	$< 0$	$> 0$
$S_2$	$\in \mathbb{C}$	$\in \mathbb{R}$	$\in \mathbb{R}$	$\in \mathbb{C}$	$\in \mathbb{R}$
$\Gamma^{(1)}$	$\in \mathbb{R}$	$\in \mathbb{R}$	$\in \mathbb{R}$	$\in \mathbb{C}$	$\in \mathbb{R}$
$\Gamma^{(2)}$	$\in \mathbb{R}$	$\in \mathbb{C}$	$\in \mathbb{C}$	$\in \mathbb{C}$	$\in \mathbb{C}$
$\Gamma^{(3)}$	$\in \mathbb{R}$	$\in \mathbb{C}$	$\in \mathbb{C}$	$\in \mathbb{R}$	$\in \mathbb{C}$
		$\rho_c < f^{3/2}/2$			
		$ x_2  < X_2^{(2)}$	$ x_2  > X_2^{(2)}$		
$A^\dagger$	$\in \mathbb{C}$		$> 0$		
$S_2$	$\in \mathbb{C}$		$\in \mathbb{R}$		
$\Gamma^{(1)}$	$\in \mathbb{R}$		$\in \mathbb{R}$		
$\Gamma^{(2)}$	$\in \mathbb{R}$		$\in \mathbb{C}$		
$\Gamma^{(3)}$	$\in \mathbb{R}$		$\in \mathbb{C}$		

inequation  $A^\dagger > 0$  with respect to  $f$  for the particular values  $\rho_c = \rho_{c,\max}$  and  $x_2 = X_2^{(3)}$ . By denoting  $f^\dagger$  the value of  $f$  for which  $A^\dagger > 0$  for these particular values of  $\rho_c$  and  $|x_2|$ , then  $A^\dagger$  remains positive for any value of  $\rho_c < \rho_{c,\max}$  and  $X_2^{(2)} < |x_2| < X_2^{(3)}$ . As a result, we deduce that  $A^\dagger > 0$  for any value of  $\rho_c$  when  $f > f^\dagger$ , where the derived value of  $f^\dagger$  is given by :

$$f^\dagger = \frac{-1 + \sqrt{17 - 8\sqrt{2}}}{2} \approx 0.6923. \quad (47)$$

For the case  $f \leq f^\dagger$ , there remains one possibility to obtain  $A^\dagger < 0$ . After considering  $A^\dagger$  as a function of  $\rho_c$  and  $x_2 = X_2^{(3)}$ , we deduce that  $A^\dagger < 0$  when  $\rho_c > \rho_c^\dagger$ , where  $\rho_c^\dagger$  is given by :

$$\rho_c^\dagger = \frac{f^{3/2}}{2} \left( 1 + \frac{\sqrt{2}}{2} \right). \quad (48)$$

We have summarized the real or complex nature of the function  $A^\dagger$ , its sign study and the impact on the nature of the function  $S_2$  in Table 1. We note that  $S_2 \in \mathbb{C}$  does not necessarily imply  $x_1^{(i)} \in \mathbb{C}$ . Indeed, for the case  $X_2^{(2)} < |x_2| < X_2^{(3)}$ ,  $0 < f < f^\dagger$  and  $\rho_c > \rho_c^\dagger$ , we have deduced that :

$$4^{1/3} J^* \frac{S_1}{S_2} \in \mathbb{R} \quad \text{and} \quad J S_2 \in \mathbb{R}. \quad (49)$$

Furthermore, for the case  $|x_2| < X_2^{(2)}$ , we have deduced that :

$$4^{1/3} \frac{S_1}{S_2} = (S_2)^*, \quad (50)$$

$$4^{1/3} J \frac{S_1}{S_2} = (J^* S_2)^*, \quad (51)$$

and

$$4^{1/3} J^* \frac{S_1}{S_2} = (J S_2)^*. \quad (52)$$

Therefore, even if  $S_2 \in \mathbb{C}$ , we note that  $\Gamma^{(1)}$  remains real, which implies that  $x_1^{(1)} \in \mathbb{C}$  only if  $\Gamma^{(1)} < 0$ . In addition, for the case

$|x_2| < X_2^{(2)}$  and after substituting Eqs. (50), (51) and (52) into Eqs. (33), (34) and (35), the latter equations can be reduced to:

$$x_1^{(1)} = \pm \frac{\sqrt{3}}{3} \sqrt{-p_2 + \frac{1}{2^{1/3} f^2} (\chi + \chi^*)}, \quad (53)$$

$$x_1^{(2)} = \pm \frac{\sqrt{3}}{3} \sqrt{-p_2 + \frac{1}{2^{1/3} f^2} (J\chi + J^* \chi^*)}, \quad (54)$$

and

$$x_1^{(3)} = \pm \frac{\sqrt{3}}{3} \sqrt{-p_2 + \frac{1}{2^{1/3} f^2} (J^* \chi + J\chi^*)}, \quad (55)$$

where  $\chi = (A_1 - \iota R \sqrt{-A_2})^{1/3}$ . As a consequence, the latter equation leads to the fact that, for  $|x_2| < X_2^{(2)}$ ,  $\Gamma^{(i)}$  remain real, for any value of  $f$  and  $\rho_c$ , which implies that  $x_1^{(i)} \in \mathbb{C}$  only if  $\Gamma^{(i)} < 0$ . A summary of the real or complex nature of  $\Gamma^{(i)}$  may be found in Table 1.

#### 4.2.2 Conditions under which $\Gamma^{(i)} > 0$

In order to go further in the nature study of  $x_1^{(i)}$ , we need to determine, for a given set of parameters  $f$  and  $\rho_c$ , for which values of  $x_2$  the real value of  $\Gamma^{(i)}$  is positive. We first notice that for any value of  $f$  and  $\rho_c$  for which  $\Gamma^{(1)} \in \mathbb{R}$ , we have  $\Gamma^{(1)} > 0$  when  $|x_2| < |x_{2,\max_1}^{(\pm)}|$  and  $\Gamma^{(1)} < 0$  when  $|x_2| > |x_{2,\max_1}^{(\pm)}|$  where  $x_{2,\max_1}^{(\pm)}$  is defined by :

$$x_{2,\max_1}^{(\pm)} = \pm \frac{1}{f} \sqrt{f - 2f^{3/2} \rho_c - f^2 \rho_c^2}. \quad (56)$$

These special values of  $x_2$  correspond to the y-intercept of one of the critical line, i.e. the top (resp. bottom) part. Furthermore, since the values of  $x_{2,\max_1}^{(\pm)}$  have to be real, we obtain a condition for the existence of the critical lines, with respect to  $\rho_c$ . Indeed, from Eq. (56), we deduce that  $x_{2,\max_1}^{(\pm)} \in \mathbb{R}$  only for  $\rho_c \leq \sqrt{f}/(1+f)$ . In the same way, for any value of  $f$  and  $\rho_c$  for which  $\Gamma^{(3)} \in \mathbb{R}$ , we have  $\Gamma^{(3)} > 0$  when  $|x_2| < |x_{2,\max_2}^{(\pm)}|$  and  $\Gamma^{(3)} < 0$  when  $|x_2| > |x_{2,\max_2}^{(\pm)}|$  where  $x_{2,\max_2}^{(\pm)}$  is defined by :

$$x_{2,\max_2}^{(\pm)} = \pm \frac{\sqrt{2\rho_c}}{2f} \sqrt{2f^{3/2} - \rho_c \left( 2 - f^2 \left( 1 - \sqrt{1 + \frac{4}{\sqrt{f}\rho_c}} \right) \right)}. \quad (57)$$

These special values of  $x_2$  correspond to the y-intercept of the other critical line, i.e. the top (resp. bottom) part. Furthermore, since the values of  $x_{2,\max_2}^{(\pm)}$  have to be real, we obtain a condition for the existence of two critical lines, with respect to  $\rho_c$ . Indeed, from Eq. (57), we deduce that  $x_{2,\max_2}^{(\pm)} \in \mathbb{R}$  only for  $\rho_c \leq f^{3/2}/(1+f)$ . In order to organise all the particular values of  $\rho_c$ , let us note that for the case  $f > \tilde{f}$ , we have  $\rho_c^{(1+)} > \sqrt{f}/(1+f)$ , while for the case  $f \leq \tilde{f}$ ,  $\rho_c^{(1+)} \leq \sqrt{f}/(1+f)$ , where  $\tilde{f}$  is given by :

$$\tilde{f} = \frac{-1 + \sqrt{9 - 4\sqrt{2}}}{2} \approx 0.4142. \quad (58)$$

Therefore, we can put in order all the particular values of  $\rho_c$  :

$$0 < \rho_c^{1-} < \frac{f^{3/2}}{2} < \frac{f^{3/2}}{1+f} < \frac{\sqrt{f}}{1+f}, \quad (59)$$

if  $f > \tilde{f}$ , and :

$$0 < \rho_c^{1-} < \frac{f^{3/2}}{2} < \frac{f^{3/2}}{1+f} < \rho_c^{1+} \leq \frac{\sqrt{f}}{1+f}, \quad (60)$$

if  $f \leq \tilde{f}$ . For all particular ranges of the  $\rho_c$  values defined by Eqs. (59) and (60), we have studied the sign of the functions  $\Gamma^{(i)}$  with respect to  $x_2$ . It is interesting to note that the particular values of  $x_2$  for which we observe a sign change for  $\Gamma^{(i)}$  are simply given by  $X_2^{(1)}$ ,  $X_2^{(3)}$ ,  $x_{2,\max_1}^{(\pm)}$ ,  $x_{2,\max_2}^{(\pm)}$ , respectively defined by Eqs. (44), (46), (56) and (57), and  $X_2^{(2)}$  for which the complicated analytical expression can be found in App. A4. We have summarized the sign study of the functions  $\Gamma^{(i)}$  in Table B1.

### 4.3 Analytical expressions of the critical and caustic lines

The last step in determining the validity range of the solutions  $x_1^{(i)}$  consists in testing which values of  $x_1^{(i)}$ , derived from  $\Gamma^{(i)} \in \mathbb{R}^+$  given in Table B1, verify Eq. (27). We note that only a few cases for which  $\Gamma^{(i)} > 0$  do not correspond to a solution of Eq. (27). We have summarized the validity range of the solutions  $x_1^{(i)}$  in Table 2. Making use of this table, we are able to analytically derive the critical curves for any set of NSIE model parameters. In order to obtain the corresponding caustic curves, we substitute the solutions  $x_2$  and  $x_1^{(i)}$  into the lens equation. Therefore, the analytical expressions of the two components of the caustic curves are expressed by :

$$y_1 = x_1^{(i)} - \hat{\alpha}_1(x_1^{(i)}, x_2), \quad (61)$$

and

$$y_2 = x_2 - \hat{\alpha}_2(x_1^{(i)}, x_2), \quad (62)$$

where the ranges of values of  $x_1^{(i)}$  are given in Table 2, for a fixed set of model parameters. In App. B, we have illustrated the critical curves and their corresponding caustic curves for different sets of model parameters. In Figs. 1 to 6, for a given set of the model parameters  $f$ ,  $\rho_c$  and for a given point-like source position  $(y_1, y_2)$ , we have represented the lensed image positions, the critical and caustic curves, and the Fermat potential,  $\tau(x_1; x_2) = (x - y)^2/2 - \hat{\psi}(x_1; x_2)$  where  $\hat{\psi}$  is derived from Eq. (14).

## 5 CONCLUSIONS

The adopted Fourier approach has allowed us to derive simple expressions for the deflection angle of the NSIE gravitational lens model. Although the latter remains rigorously equivalent to the one already published by KSB, the expressions derived in the present work are significantly more simple. Consequently, we have been able to perform a complete analytical development of the NSIE family of models. As far as we know, the expression of the deflection potential, as well as those for the critical and caustic curves, have never been published before. Furthermore, the proposed analytical treatment avoids numerical calculations of the time delays and amplification ratios. As a consequence, any further model fitting should be much more efficient and less time consuming. However, since the lens equation is highly non linear, the lensed image positions still remain to be numerically derived.

Our results provide an additional proof of the relevance of the Fourier approach in order to determine the expression of the deflection angle for the case of more complex gravitational lens models (see WS). We are convinced that such a method constitutes a promising alternative to the complex formalism introduced by Bourassa & Kantowski (1973, 1975), corrected by Bray (1984).

6 *O. Wertz and J. Surdej***Table 2.** Validity ranges of the functions  $x_1^{(i)}$  with respect to  $x_2$ ,  $f$  and  $\rho_c$ 

	$0 \leq \rho_c < \rho_c^{(1-)}$	$\rho_c^{(1-)} \leq \rho_c < \frac{f^{3/2}}{2}$	$\frac{f^{3/2}}{2} \leq \rho_c < \frac{f^{3/2}}{1+f}$	$\frac{f^{3/2}}{1+f} \leq \rho_c < \rho_c^{(1+)}$	$\rho_c^{(1+)} \leq \rho_c \leq \frac{\sqrt{f}}{1+f}$
$0 \leq  x_2  < X_2^{(1)}$	$x_1^{(1)}$ $x_1^{(3)}$ if $ x_2  < x_{2,\max_2}^{(+)}$	$x_1^{(2)}$ $x_1^{(3)}$ if $ x_2  < x_{2,\max_2}^{(+)}$	$x_1^{(2)}$ $x_1^{(3)}$ if $ x_2  < x_{2,\max_2}^{(+)}$	$x_1^{(2)}$	$x_1^{(3)}$
$X_2^{(1)} \leq  x_2  < X_2^{(2)}$	$x_1^{(1)}$ $x_1^{(3)}$ if $ x_2  < x_{2,\max_2}^{(+)}$	$x_1^{(1)}$ $x_1^{(3)}$ if $ x_2  < x_{2,\max_2}^{(+)}$	$x_1^{(1)}$	$\begin{cases} x_1^{(3)} & \text{if } 0 < f < f^\dagger \\ & \text{and } \rho_c > \rho_c^\dagger \\ x_1^{(1)} & \text{otherwise} \end{cases}$	$x_1^{(3)}$
$X_2^{(2)} \leq  x_2  < X_2^{(3)}$	$x_1^{(1)}$	$x_1^{(1)}$	$\begin{cases} x_1^{(3)} & \text{if } 0 < f < f^\dagger \\ & \text{and } \rho_c > \rho_c^\dagger \\ x_1^{(1)} & \text{otherwise} \end{cases}$	$\begin{cases} x_1^{(3)} & \text{if } 0 < f < f^\dagger \\ & \text{and } \rho_c > \rho_c^\dagger \\ x_1^{(1)} & \text{otherwise} \end{cases}$	$x_1^{(3)}$
$X_2^{(3)} \leq  x_2  \leq X_2^{(3+)}$	$x_1^{(1)}$	$x_1^{(1)}$	$x_1^{(1)}$	$x_1^{(1)}$	$x_1^{(1)}$
Particular values of $X_2^{(i)}$ with respect to $\rho_c$	$X_2^{(1)} \in \mathbb{C}$ $X_2^{(3)} \in \mathbb{C}$	$X_2^{(3)} \in \mathbb{C}$			$X_2^{(1)} \in \mathbb{C}$

We note that for  $f > \bar{f}$ , we have  $\sqrt{\bar{f}}/(1+f) < \rho_c^{(1+)}$ . Therefore, for this particular case, the last column can be omitted and the penultimate is valid for  $\frac{f^{3/2}}{1+f} \leq \rho_c < \sqrt{\bar{f}}/(1+f)$  instead of  $\frac{f^{3/2}}{1+f} \leq \rho_c < \rho_c^{(1+)}$

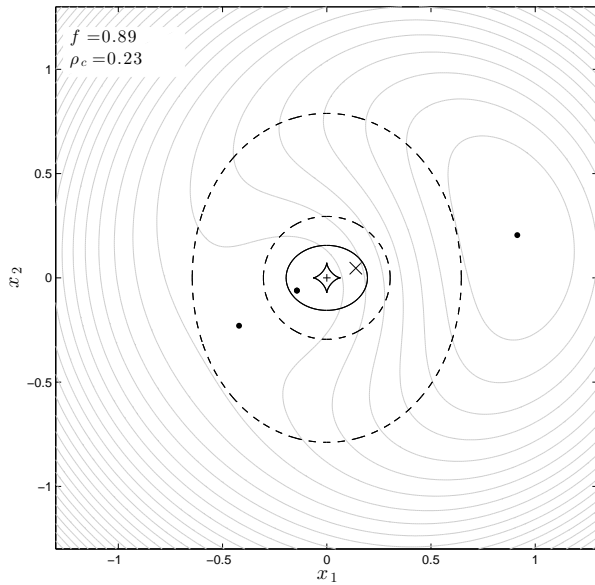


**Figure 1.** For the lens parameters  $f = 0.89$  and  $\rho_c = 0.23$ , we have represented the position of a point-like source (cross  $\times$ ), the associated lensed images (dots  $\bullet$ ), the critical curves (dashed lines), the caustic curves (solid black lines) and the iso-contours of the Fermat potential (gray solid lines). The cross  $+$  denotes the central position of the deflector

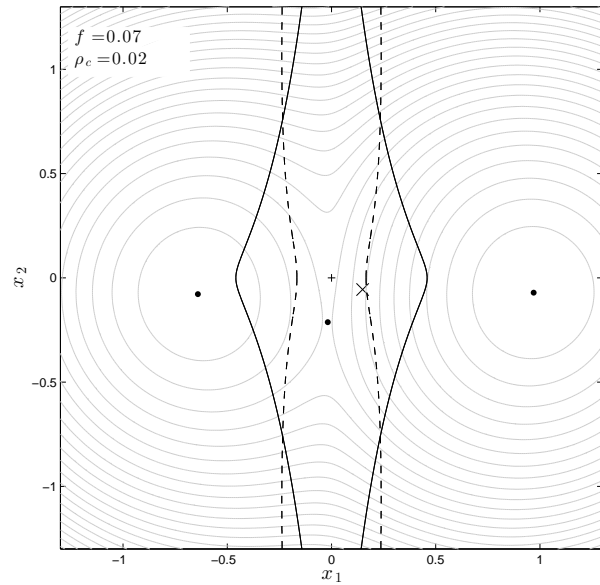


**Figure 2.** For the lens parameters  $f = 0.07$  and  $\rho_c = 0.02$ , we have represented the position of a point-like source (cross  $\times$ ), the associated lensed images (dots  $\bullet$ ), the critical curves (dashed lines), the caustic curves (solid black lines) and the iso-contours of the Fermat potential (gray solid lines). The cross  $+$  denotes the central position of the deflector

**ACKNOWLEDGMENTS**

OW thanks the Belgian National Fund for Scientific Research (FNRS). JS and OW acknowledge support from the Communauté française de Belgique - Actions de recherche concertées - Académie universitaire Wallonie-Europe, from the ESA PRODEX Programme "GAIA", and from the Belgian Federal Science Policy Office.

**REFERENCES**

- Bourassa R. R., Kantowski R., 1973, ApJ, 185, 747  
 Bourassa R. R., Kantowski R., 1975, ApJ, 195, 13  
 Bray I., 1984, MNRAS, 208 : 511-516  
 Gradshteyn I. S., Ryzhik I. M., 2007, A. Jeffrey (Ed.), Table of Integrals, Series and Products (7th ed.), Academic Press, New York.  
 Kormann R., Schneider P., Bartelmann M., 1994, MNRAS, 284 : 285-299 (KSB)



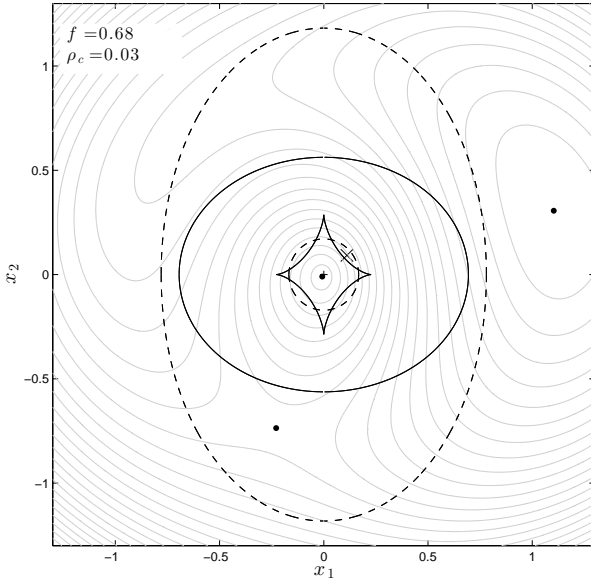


**Figure 3.** For the lens parameters  $f = 0.68$  and  $\rho_c = 0.03$ , we have represented the position of a point-like source (cross  $\times$ ), the associated lensed images (dots  $\bullet$ ), the critical curves (dashed lines), the caustic curves (solid black lines) and the iso-contours of the Fermat potential (gray solid lines). The cross  $+$  denotes the central position of the deflector

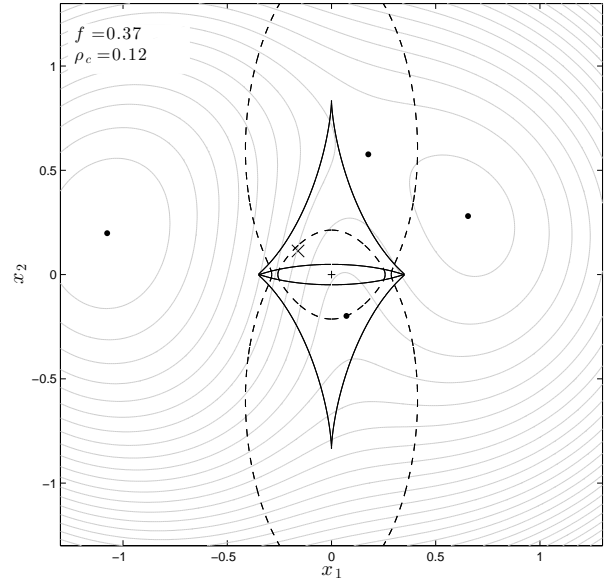


**Figure 4.** For the lens parameters  $f = 0.37$  and  $\rho_c = 0.12$ , we have represented the position of a point-like source (cross  $\times$ ), the associated lensed images (dots  $\bullet$ ), the critical curves (dashed lines), the caustic curves (solid black lines) and the iso-contours of the Fermat potential (gray solid lines). The cross  $+$  denotes the central position of the deflector

Wertz O., Surdej J., 2014, MNRAS, 437 : 1051-1055 (WS)

## APPENDIX A: INTERMEDIATE RESULTS

In this appendix, we present some intermediate analytical results which are used in the present paper.

### A1 Undefined integrals

We first propose to express the solutions of the two undefined integrals appearing in Eq. (11). Whereas the first undefined integral can be straightforwardly derived from results established in Gradshteyn & Ryzhik (2007, Eq. (2.731), p. 239), the second one is more difficult, especially because of  $\xi$ , which is a function of  $x_1$  :

$$\int \ln(f^2 x_1^2 + 2ff'\rho_c x_1 + f^2 x_2^2 + f'^2 \rho_c^2) dx_1 = -2x_1 + 2x_2 \arctan\left(\frac{fx_1 + f'\rho_c}{fx_2}\right) + \left(x_1 + \frac{f'\rho_c}{f}\right) \ln(f^2 r^2 + 2ff'x_1\rho_c + f'^2 \rho_c^2), \quad (\text{A1})$$

$$\begin{aligned} \int \ln[(2 - f^2)x_1^2 + 2f'\xi x_1 + f^2 x_2^2 + f'^2 \rho_c^2] dx_1 = & -2x_1 \\ & + x_1 \ln\left[(2 - f^2)x_1^2 + \rho_c^2 + f^2(x_2^2 - \rho_c^2) + 2x_1 f' \xi\right] \\ & + \frac{1}{f}(fx_2 - if'\rho_c) \arctan\left(\frac{f\xi}{ff'x_2 - if'\rho_c}\right) \\ & + \frac{1}{f}(fx_2 + if'\rho_c) \arctan\left(\frac{f\xi}{ff'x_2 + if'\rho_c}\right) \\ & + \frac{1}{f}(-fx_2 + if'\rho_c) \arctan\left(\frac{fx_1}{fx_2 - if'\rho_c}\right) \\ & - \frac{1}{f}(fx_2 - if'\rho_c) \arctan\left(\frac{fx_1}{fx_2 + if'\rho_c}\right). \end{aligned} \quad (\text{A2})$$

We note that the result of Eq. (A2) is real. Indeed, the imaginary parts pairwise vanish.

### A2 Expression of the NSIE internal shear

In order to derive the expressions for the two components of the internal shear ( $\gamma_1$  and  $\gamma_2$ ), we give the expressions of  $\hat{\psi}_{,11}$  and  $\hat{\psi}_{,22}$  in terms of  $x_1$  and  $x_2$  :

$$\hat{\psi}_{,11}(x_1; x_2) = \frac{\sqrt{f}}{\xi} \frac{\Psi_1(x_1, x_2)}{f^4 r^4 - 2f^2 f'^2 \rho_c^2 (x_1^2 - x_2^2) + f'^4 \rho_c^4}, \quad (\text{A3})$$

where  $\Psi_1$  is defined by :

$$\Psi_1(x_1, x_2) = \rho_c^4 + f^4 x_2^2 (r^2 - \rho_c^2) - f^2 \rho_c^2 (x_1^2 - 2x_2^2 + \rho_c^2) + \xi f \rho_c (f^2 (x_1^2 - x_2^2) - \rho_c^2 f^2), \quad (\text{A4})$$

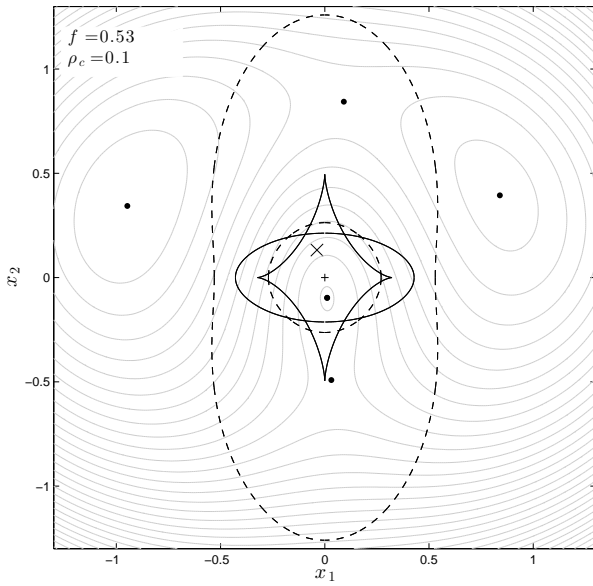


**Figure 5.** For the lens parameters  $f = 0.53$  and  $\rho_c = 0.10$ , we have represented the position of a point-like source (cross  $\times$ ), the associated lensed images (dots  $\bullet$ ), the critical curves (dashed lines), the caustic curves (solid black lines) and the iso-contours of the Fermat potential (gray solid lines). The cross  $+$  denotes the central position of the deflector

and

$$\hat{\psi}_{,22}(x_1, x_2) = \frac{f^{3/2}}{\xi} \frac{\Psi_2(x_1, x_2)}{f^4 r^4 - 2f^2 f'^2 \rho_c^2 (x_1^2 - x_2^2) + f^4 \rho_c^4}, \quad (\text{A5})$$

where  $\Psi_2$  is defined by :

$$\Psi_2(x_1, x_2) = \xi \rho_c (\rho_c^2 - f^2 (x_1^2 - x_2^2 + \rho_c^2)) + f^3 (x_1^2 r^2 + (2x_1^2 - x_2^2) \rho_c^2 + \rho_c^4) - f \rho_c^2 (x_1^2 + \rho_c^2). \quad (\text{A6})$$

The expression of  $\gamma_2$  is given by :

$$\gamma_2(x_1, x_2) = \frac{f^{5/2} x_1 x_2 (f' (\xi^2 + (f' x_1 - f \rho_c)^2) + 2f' \xi (f' x_1 - f \rho_c))}{f' \xi (2f f' x_1 \rho_c + \rho_c^2 + f^2 (r^2 - \rho_c^2)) T(x_1, x_2)}, \quad (\text{A7})$$

where

$$T(x_1, x_2) = 2x_1^2 + \rho_c^2 - f^2 (x_1^2 - x_2^2 + \rho_c^2) + 2f' x_1 \xi. \quad (\text{A8})$$

### A3 Expressions of the function $F_i(x_1, x_2)$

The expressions of the functions  $F_1(x_1, x_2)$  and  $F_2(x_1, x_2)$  are rather long. However, the expression  $F_2^2(x_1, x_2) \xi^2 - F_1^2(x_1, x_2)$  takes a surprisingly simple form (see Eq. (28)). First, the function  $F_1(x_1, x_2)$  can be expressed as a polynomial of the 9th degree with respect to  $x_1$ :

$$F_1(x_1, x_2) = s_9 x_1^9 + s_8 x_1^8 + 4f^2 f' s_7 x_1^7 + s_6 x_1^6 + s_5 x_1^5 + s_4 x_1^4 + 4f' s_3 x_1^3 + s_2 x_1^2 + s_1 x_1 + s_0, \quad (\text{A9})$$

where the coefficients  $s_i$  are given by :

$$s_9 = 4f^4 f' (1 + f'^2), \quad (\text{A10})$$

$$s_8 = -f^{9/2} (8 - 8f^2 + f^4) + 16f^3 (2 - 3f^2 + f^4) \rho_c, \quad (\text{A11})$$

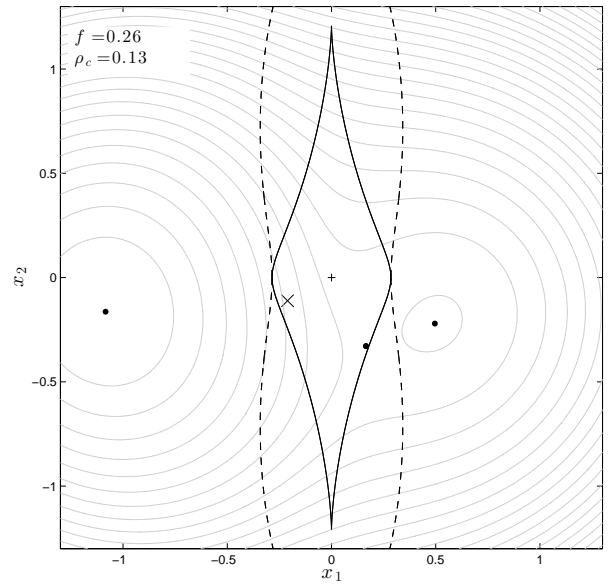


**Figure 6.** For the lens parameters  $f = 0.26$  and  $\rho_c = 0.13$ , we have represented the position of a point-like source (cross  $\times$ ), the associated lensed images (dots  $\bullet$ ), the critical curves (dashed lines), the caustic curves (solid black lines) and the iso-contours of the Fermat potential (gray solid lines). The cross  $+$  denotes the central position of the deflector

$$s_7 = f^2 (4 + f^2 - f^4) x_2^2 - f^{3/2} (8 - 8f^2 + f^4) \rho_c + (12 - 15f^2 + 4f^4) \rho_c^2, \quad (\text{A12})$$

$$s_6 = x_2^2 (4f^{9/2} (-4 + 2f^2 + f^4) + 16f^3 (2 - 3f^4 + f^6) \rho_c) + f^4 (8 - 8f^2 + f^4) \rho_c + 4f^{5/2} (-12 + 22f^2 - 11f^4 + f^6) \rho_c^2 + 16f'^2 f (2 - f^4) \rho_c^3, \quad (\text{A13})$$

$$s_5 = (4f^4 f' (2 + 5f^2 - f^4)) x_2^4 + 4f' x_2^2 (f^{7/2} (-8 + 5f^4) \rho_c + f^2 (4 + 18f^2 - 24f^4 + 5f^6) \rho_c^2) + 4f' (f^3 (4 - 6f^2 + f^4) \rho_c^2 - f'^2 f^{3/2} (8 - f^4) \rho_c^3 + (2 + 13f^2 - 25f^4 + 10f^6) \rho_c^4), \quad (\text{A14})$$

$$s_4 = x_2^4 (2f^{9/2} (-4 - 4f^2 + 5f^4) + 48f^5 f'^2 \rho_c) + x_2^2 ((8f^4 - 5f^8) \rho_c - 4f^{5/2} (4 + 8f^2 - 21f^4 + 9f^6) \rho_c^2 + 32f^3 (3 - 5f^2 + 2f^4) \rho_c^3) + (f^2 (8 - 24f^2 + 23f^4 - 5f^6) \rho_c^3 + 2\sqrt{f} (-4 - 20f^2 + 5f^4) f'^4 \rho_c^4 - 16f (-3 + f^2) f'^4 \rho_c^5), \quad (\text{A15})$$

$$s_3 = x_2^6 f^6 (3 + f^2) + x_2^4 f^4 \rho_c (-f^{3/2} (8 - 5f^2) + 9\rho_c - 6f^4 \rho_c) + x_2^2 f^2 \rho_c^2 [2f^3 (1 - 2f^2) - 2f^{3/2} \rho_c (8 - 11f^2 + 3f^4) + f'^2 \rho_c^2 (9 + 6f^2 - 5f^4)] + f'^2 \rho_c^4 [2f^3 - f^{3/2} f'^2 \rho_c (7 + f'^2) + f'^2 \rho_c^2 (3 + 4f^2)], \quad (\text{A16})$$

$$\begin{aligned}
s_2 = & x_2^6 \left( -4f^{13/2} (1 + f'^2) + 16f^7 f'^2 \rho_c \right) \\
& + x_2^4 \left[ 8f^6 \rho_c - 5f^8 \rho_c - 4f^{9/2} (6 - 7f^2 + f^4) \rho_c^2 \right. \\
& \quad \left. + 16f^5 (3 - 5f^2 + 2f^4) \rho_c^3 \right] \\
& + x_2^2 \left[ 16f^4 \rho_c^3 - 30f^6 \rho_c^3 + 18f^8 \rho_c^3 - 4f^{5/2} (6 + f^2) f'^4 \rho_c^4 \right. \\
& \quad \left. + 16f^3 (3 - 4f^2 + f^4) f'^2 \rho_c^5 \right] + f^2 (8 - 17f^2 + 5f^4) f'^2 \rho_c^5 \\
& \quad - 4\sqrt{f} (2 + f^2) f'^6 \rho_c^6 + 16ff'^6 \rho_c^7, \tag{A17}
\end{aligned}$$

$$\begin{aligned}
s_1 = & 4f' (f'^2 \rho_c^2 + f^2 x_2^2)^2 \left[ f^4 x_2^4 + x_2^2 (-f^{7/2} \rho_c + f^2 (1 + f'^2) \rho_c^2) \right. \\
& \quad \left. + \rho_c^2 (-f^3 - f^{3/2} f'^2 \rho_c + f'^2 \rho_c^2) \right], \tag{A18}
\end{aligned}$$

$$\begin{aligned}
s_0 = & \sqrt{f} (f' 2\rho_c^2 + f^2 x_2^2)^2 \left[ (-f^{3/2} + \rho_c) \rho_c^3 + 2f^2 (x_2^2 - \rho_c^2) \rho_c^2 \right. \\
& \quad \left. + f^4 (x_2^2 - \rho_c^2)^2 - f^{7/2} \rho_c (x_2^2 + \rho_c^2) \right]. \tag{A19}
\end{aligned}$$

Secondly, the function  $F_2(x_1, x_2)$  can be expressed as a polynomial of the 8th degree with respect to  $x_1$  :

$$\begin{aligned}
F_2(x_1, x_2) = & f^4 u_8 x_1^8 + 4f^3 f' u_7 x_1^7 + u_6 x_1^6 + 4ff' u_5 x_1^5 \\
& + 2u_4 x_1^4 + u_3 x_1^3 + 4u_2 x_1^2 + 4\sqrt{f} f' u_1 x_1 + u_0, \tag{A20}
\end{aligned}$$

where the coefficients  $u_i$  are given by :

$$u_8 = 8 - 8f^2 + f^4, \tag{A21}$$

$$u_7 = -f^{3/2} (1 + f'^2) + (8 - 8f^2 + f^4) \rho_c, \tag{A22}$$

$$\begin{aligned}
u_6 = & -4f^4 (-4 + 2f^2 + f^4) x_2^2 \\
& + 4f^2 f'^2 \rho_c [-4f^{3/2} (1 + f'^2) + (12 - 10f^2 + f^4) \rho_c], \tag{A23}
\end{aligned}$$

$$\begin{aligned}
u_5 = & \rho_c \left[ f^3 (1 + f'^2) + f^{3/2} (-12 + 17f^2 - 5f^4) \rho_c + (8 - f^4) f'^2 \rho_c^2 \right. \\
& \quad \left. + x_2^2 [-f^{7/2} (3 + f'^2) + f^2 \rho_c (8 - 5f^4)] \right], \tag{A24}
\end{aligned}$$

$$\begin{aligned}
u_4 = & x_2^4 f^4 (4 + 4f^2 - 5f^4) \\
& + 2x_2^2 f^2 \rho_c [-4f^{3/2} (2 + f^4 + f^2 (-3 + f'^2) \\
& \quad + (4 + 8f^2 - 21f^4 + 9f^6) \rho_c) + \rho_c^2 (f^3 (8 - 16f^2 + 7f^4) \\
& \quad - 16f^{3/2} f'^4 \rho_c + (4 + 16f^2 - 25f^4 + 5f^6) f'^2 \rho_c^2)], \tag{A25}
\end{aligned}$$

$$\begin{aligned}
u_3 = & -x_2^4 4f^{9/2} f' (2 + f^2 + \sqrt{f} (-8 + 5f^2) \rho_c) \\
& + x_2^2 \left[ 4f^4 f' (1 + f^2 + f'^2) \rho_c + 8f^{5/2} (-2 - f^2 + 3f^4) f' \rho_c^2 \right. \\
& \quad \left. + 8f^3 (8 - 3f^2) f'^3 \rho_c^3 + 4\sqrt{f} f'^3 \rho_c^3 [-2\rho_c + \sqrt{f} (2f (1 - 2f^2) \right. \\
& \quad \left. + f^{3/2} (-3 + 5f^2) \rho_c + f'^2 (7 + f'^2) \rho_c^2) \right], \tag{A26}
\end{aligned}$$

$$\begin{aligned}
u_2 = & f^6 (1 + f'^2) x_2^6 + x_2^4 f^4 \rho_c (-4f^{3/2} f'^2 + (6 - 7f^2 + f^4) \rho_c) \\
& + x_2^2 f^2 \rho_c^2 (-f^5 - 8f^{3/2} f'^4 \rho_c - (-6 + 5f^2 + f^4) f'^2 \rho_c^2) \\
& + f'^2 \rho_c^4 (f^5 - 4f^{3/2} f'^4 \rho_c - (-2 + f^2 + f^4) f'^2 \rho_c^2), \tag{A27}
\end{aligned}$$

$$\begin{aligned}
u_1 = & x_2^6 f^6 (-1 + \sqrt{f} \rho_c) + x_2^4 f^4 \rho_c [-3f'^2 \rho_c + \sqrt{f} (f + 3f'^2 \rho_c^2)] \\
& + x_2^2 f^2 f'^2 \rho_c^3 [-3f'^2 \rho_c + \sqrt{f} (2f + 3f'^2 \rho_c^2)] \\
& + f'^4 \rho_c^5 [-f'^2 \rho_c + \sqrt{f} (f + f'^2 \rho_c^2)], \tag{A28}
\end{aligned}$$

$$u_0 = (f^2 x_2^2 + f'^2 \rho_c^2)^2 (f^4 x_2^4 - 2f^2 (f - f'^2 x_2^2) \rho_c^2 + f'^4 \rho_c^4). \tag{A29}$$

#### A4 Expression of the function $X_2^{(2)}$

The values of  $X_2^{(2)}$  corresponds to particular values of  $|x_2|$  which lead to  $A_2 < 0$  with  $R \neq 0$ , where  $A_2$  is defined to Eq. (39) and  $R$  to Eq. (40). The expression of  $X_2^{(2)}$  is then given by :

$$\begin{aligned}
X_2^{(2)} = & \frac{\sqrt{3}}{3} \left[ -\frac{2(f^{3/2} + \rho_c)^2}{f^2 f'^2} - \frac{(1 - \iota \sqrt{3}) R_2}{2^{2/3} R_1} \right. \\
& \left. - \frac{(1 + \iota \sqrt{3})}{R_1 R_2} \left[ 16f^4 f'^8 (f^{3/2} + \rho_c) (\rho_c^3 + 3f^{3/2} \rho_c^2 + 30f^3 \rho_c + f^{9/2}) \right] \right]^{1/2}, \tag{A30}
\end{aligned}$$

where  $R_1$  is defined by :

$$R_1 = 4 f^4 2^{2/3} (f^6 - 4f^4 + 3f^2 - 1), \tag{A31}$$

and  $R_2$  by :

$$\begin{aligned}
R_2 = & [-16f^6 f'^{12} (8f^9 - 492f^{15/2} \rho_c - 2229f^6 \rho_c^2 - 1460f^{9/2} \rho_c^3 \\
& \quad - 420f^3 \rho_c^4 + 48f^{3/2} \rho_c^5 + 8\rho_c^6) + 48\sqrt{3} \rho_c f^{15/2} f'^{12} \\
& \quad \times (-8f^{9/2} + 3f^3 \rho_c - 24f^{3/2} \rho_c^2 - 8\rho_c^3)^{2/3}]^{1/3}. \tag{A32}
\end{aligned}$$

#### APPENDIX B: ADDITIONAL ILLUSTRATIONS AND TABLES

We present additional illustrations (Figs. B1, B2 and B3) of the critical curves and the corresponding caustic curves, for different values of the model parameters  $f$  and  $\rho_c$ . We also present in Table B1 the complete sign study of the functions  $\Gamma^{(i)}$ .

1  
2  
3  
4  
5  
6  
7  
8  
9  
10  
11  
12  
13  
14  
15  
16  
17  
18  
19  
20  
21  
22  
23  
24  
25  
26  
27  
28  
29  
30  
31  
32  
33  
34  
35  
36  
37  
38  
39  
40  
41  
42  
43  
44  
45  
46  
47  
48  
49  
50  
51  
52  
53  
54  
55  
56  
57  
58  
59  
60

10 *O. Wertz and J. Surdej*

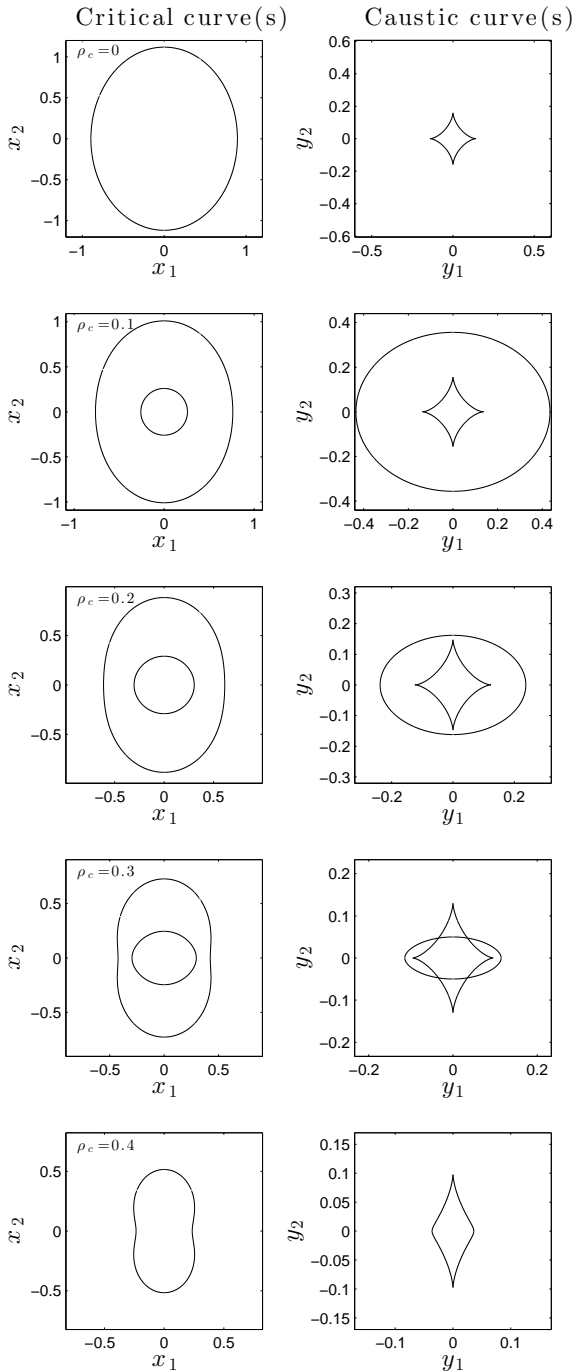


**Figure B1.** Illustration of the critical and caustic curves for the NSIE lens model parameters  $f = 0.8$  and  $\rho_c \in [0, 0.4]$ .

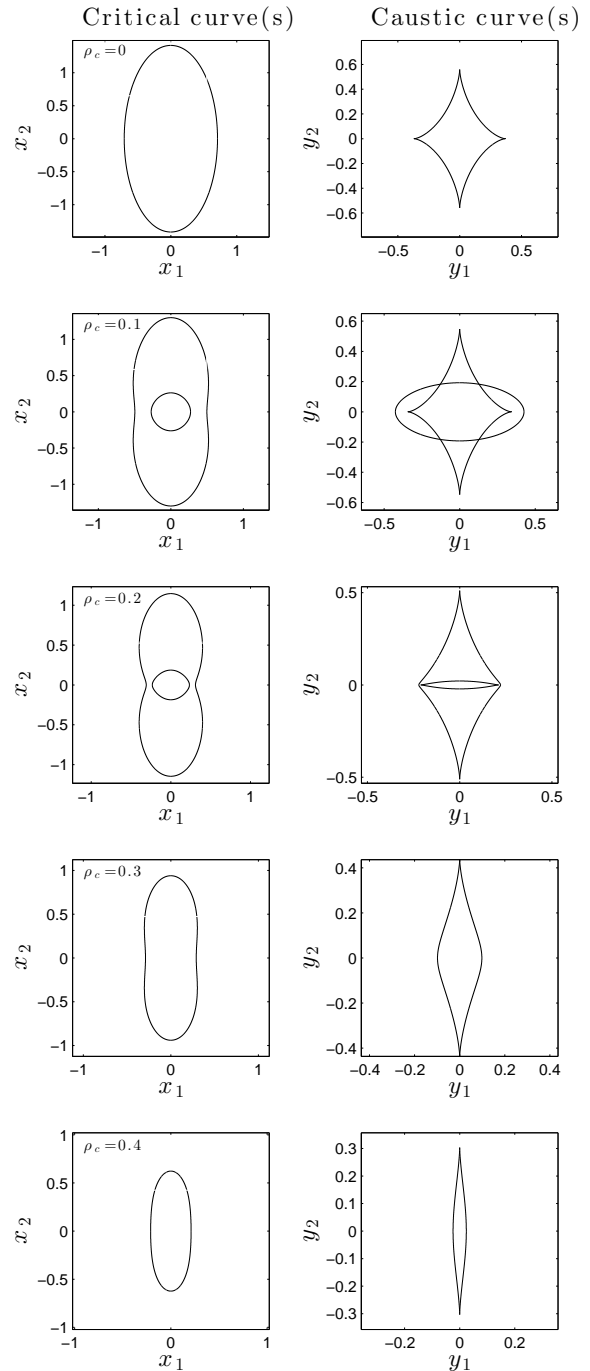


**Figure B2.** Illustration of the critical and caustic curves for the NSIE lens model parameters  $f = 0.5$  and  $\rho_c \in [0, 0.4]$ .

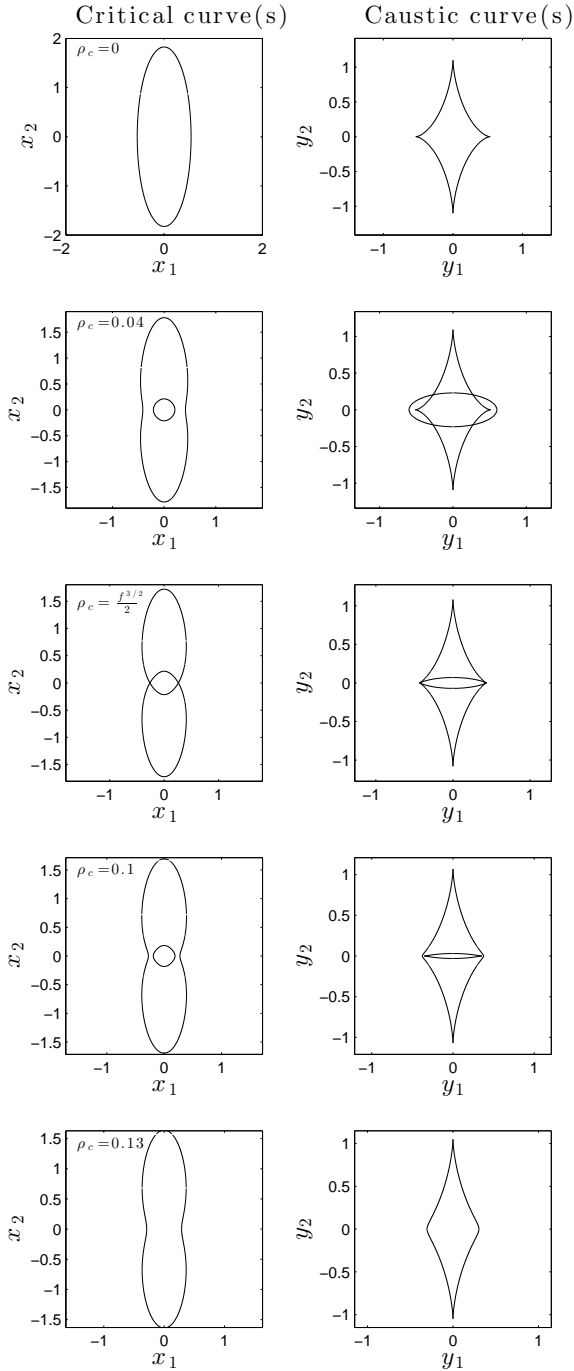


**Figure B3.** Illustration of the critical and caustic curves for the NSIE lens model parameters  $f = 0.3$  and  $\rho_c \in [0, 0.13]$ .

	$0 \leq \rho_c < \rho_c^{(1-)}$	$\rho_c^{(1-)} \leq \rho_c < \frac{f^{3/2}}{2}$	$\frac{f^{3/2}}{2} \leq \rho_c < \frac{f^{3/2}}{1+f}$	$\frac{f^{3/2}}{1+f} \leq \rho_c < \rho_c^{(1+)}$	$\rho_c^{(1+)} \leq \rho_c \leq \frac{\sqrt{f}}{1+f}$
$0 \leq  x_2  < X_2^{(1)}$	$\Gamma^{(1)} > 0$ $\Gamma^{(2)} > 0$ $\begin{cases} \Gamma^{(3)} < 0 \text{ if }  x_2  > x_{2,\max_2}^{(+)} \\ \Gamma^{(3)} > 0 \text{ if }  x_2  < x_{2,\max_2}^{(+)} \end{cases}$	$\Gamma^{(1)} > 0$ $\Gamma^{(2)} > 0$ $\begin{cases} \Gamma^{(3)} < 0 \text{ if }  x_2  > x_{2,\max_2}^{(+)} \\ \Gamma^{(3)} > 0 \text{ if }  x_2  < x_{2,\max_2}^{(+)} \end{cases}$	$\Gamma^{(1)} > 0$ $\Gamma^{(2)} > 0$ $\begin{cases} \Gamma^{(3)} < 0 \text{ if }  x_2  > x_{2,\max_2}^{(+)} \\ \Gamma^{(3)} > 0 \text{ if }  x_2  < x_{2,\max_2}^{(+)} \end{cases}$	$\Gamma^{(1)} > 0$ $\Gamma^{(2)} > 0$ $\Gamma^{(3)} < 0$	$\Gamma^{(1)} \in \mathbb{C}$ $\Gamma^{(2)} \in \mathbb{C}$ $\Gamma^{(3)} > 0$
$X_2^{(1)} \leq  x_2  < X_2^{(2)}$	$\Gamma^{(1)} > 0$ $\Gamma^{(2)} > 0$ $\begin{cases} \Gamma^{(3)} < 0 \text{ if }  x_2  > x_{2,\max_2}^{(+)} \\ \Gamma^{(3)} > 0 \text{ if }  x_2  < x_{2,\max_2}^{(+)} \end{cases}$	$\Gamma^{(1)} > 0$ $\Gamma^{(2)} > 0$ $\begin{cases} \Gamma^{(3)} < 0 \text{ if }  x_2  > x_{2,\max_2}^{(+)} \\ \Gamma^{(3)} > 0 \text{ if }  x_2  < x_{2,\max_2}^{(+)} \end{cases}$	$\Gamma^{(1)} > 0$ $\Gamma^{(2)} > 0$ $\Gamma^{(3)} < 0$	$\Gamma^{(1)} > 0$ $\Gamma^{(2)} > 0$ $\Gamma^{(3)} > 0$	$\Gamma^{(1)} \in \mathbb{C}$ $\Gamma^{(2)} \in \mathbb{C}$ $\Gamma^{(3)} > 0$
$X_2^{(2)} \leq  x_2  < X_2^{(3)}$	$\Gamma^{(1)} > 0$ $\Gamma^{(2)} < 0$ $\Gamma^{(3)} < 0$	$\Gamma^{(1)} > 0$ $\Gamma^{(2)} \in \mathbb{C}$ $\Gamma^{(3)} \in \mathbb{C}$	$\begin{cases} \Gamma^{(1)} \in \mathbb{C} \text{ if } 0 < f < f^\dagger \text{ and } \rho_c > \rho_c^\dagger \\ \Gamma^{(1)} > 0 \text{ otherwise} \end{cases}$ $\Gamma^{(2)} \in \mathbb{C}$ $\begin{cases} \Gamma^{(3)} > 0 \text{ if } 0 < f < f^\dagger \text{ and } \rho_c > \rho_c^\dagger \\ \Gamma^{(3)} \in \mathbb{C} \text{ otherwise} \end{cases}$	$\begin{cases} \Gamma^{(1)} \in \mathbb{C} \text{ if } 0 < f < f^\dagger \text{ and } \rho_c > \rho_c^\dagger \\ \Gamma^{(1)} > 0 \text{ otherwise} \end{cases}$ $\Gamma^{(2)} \in \mathbb{C}$ $\begin{cases} \Gamma^{(3)} > 0 \text{ if } 0 < f < f^\dagger \text{ and } \rho_c > \rho_c^\dagger \\ \Gamma^{(3)} \in \mathbb{C} \text{ otherwise} \end{cases}$	$\Gamma^{(1)} \in \mathbb{C}$ $\Gamma^{(2)} \in \mathbb{C}$ $\Gamma^{(3)} > 0$
$X_2^{(3)} \leq  x_2  \leq x_{2,\max_1}^{(+)}$	$\Gamma^{(1)} \geq 0$ $\Gamma^{(2)} \in \mathbb{C}$ $\Gamma^{(3)} \in \mathbb{C}$	$\Gamma^{(1)} \geq 0$ $\Gamma^{(2)} \in \mathbb{C}$ $\Gamma^{(3)} \in \mathbb{C}$	$\Gamma^{(1)} \geq 0$ $\Gamma^{(2)} \in \mathbb{C}$ $\Gamma^{(3)} \in \mathbb{C}$	$\Gamma^{(1)} \geq 0$ $\Gamma^{(2)} \in \mathbb{C}$ $\Gamma^{(3)} \in \mathbb{C}$	$\Gamma^{(1)} \geq 0$ $\Gamma^{(2)} \in \mathbb{C}$ $\Gamma^{(3)} \in \mathbb{C}$
$x_{2,\max_1}^{(+)} <  x_2 $	$\Gamma^{(1)} < 0$ $\Gamma^{(2)} \in \mathbb{C}$ $\Gamma^{(3)} \in \mathbb{C}$	$\Gamma^{(1)} < 0$ $\Gamma^{(2)} \in \mathbb{C}$ $\Gamma^{(3)} \in \mathbb{C}$	$\Gamma^{(1)} < 0$ $\Gamma^{(2)} \in \mathbb{C}$ $\Gamma^{(3)} \in \mathbb{C}$	$\Gamma^{(1)} < 0$ $\Gamma^{(2)} \in \mathbb{C}$ $\Gamma^{(3)} \in \mathbb{C}$	$\Gamma^{(1)} < 0$ $\Gamma^{(2)} \in \mathbb{C}$ $\Gamma^{(3)} \in \mathbb{C}$
Particular values of $X_2^{(i)}$ with respect to $\rho_c$	$X_2^{(1)} \in \mathbb{C}$ $X_2^{(3)} \in \mathbb{C}$	$X_2^{(3)} \in \mathbb{C}$			$X_2^{(1)} \in \mathbb{C}$

**Table B1.** Summary of the sign study of the functions  $\Gamma^{(i)}$  with respect to  $x_2$ , for the full validity ranges of  $f$  and  $\rho_c$ . We note that for  $f > \bar{f}$ , we have  $\sqrt{\bar{f}}/(1+f) < \rho_c^{(1+)}$ . Therefore, for this particular case, the last column can be omitted and the penultimate is valid for  $\frac{f^{3/2}}{1+f} \leq \rho_c < \sqrt{\bar{f}}/(1+f)$  instead of  $\frac{f^{3/2}}{1+f} \leq \rho_c < \rho_c^{(1+)}$ .

**Table 3.3:** Summary of the core radius values for the different NSIE lens models represented in Fig. 3.7 - 3.13.

Figure label	$\rho_c$	Number of caustic (resp. critic) curves	Remarks
Fig. 3.7	0	1	The case of the SIE model
Fig. 3.8	0.03	2	The fifth lensed image appears
Fig. 3.9	0.08	2	
Fig. 3.10	0.13	2	
Fig. 3.11	0.23	1	Since we have $\rho_c > f^{3/2}/(1+f)$ , one caustic (resp. critical) curve vanishes. At most, we have 3 lensed images
Fig. 3.12	0.38	1	
Fig. 3.13	0.47	0	Since we have $\rho_c > \sqrt{f}/(1+f)$ , the caustic (resp. critical) curves no longer exist

## 3.8 Illustration of the NSIE lens mapping

In the present section, we illustrate the gravitational lensing deformation due to the NSIE model for several values of the lens parameters. To this end, we have chosen the same source as the one already used for the case of the SIE model, i.e. the Homer Simpson picture (see Section 1.11). In all the figures, the green lines correspond respectively to the caustic curves (left panel) and their associated critical lines (right panel). Of course, all these curves have been analytically derived from Eqs. (33), (34), (35) and Table 2 (from Paper IV). The axis ratio  $f$  of the elliptical iso-density contours is fixed to  $f = 0.4$  and the dimensionless core radius  $\rho_c$  is set equal to the following values  $\rho_c = [0, 0.03, 0.08, 0.13, 0.23, 0.38, 0.47]$  (see Table 3.3).

For the case  $\rho_c = 0$  (see Fig. 3.7), we retrieve of course the SIE lens model with only one non-degenerate caustic curve, the tangential one, and its associated critical curve. For the case  $\rho_c > 0$ , the presence of the fifth lensed image becomes more obvious as the core radius increases (see Figs. 3.8, 3.9, 3.10). For the case  $\rho_c \geq f^{3/2}/(1+f) \simeq 0.1807$ , one of the caustic curves vanishes, as well as its associated critical one (see Figs. 3.11 and 3.12). As a consequence, any parts of the source surrounded by the remaining caustic curve produce only three lensed images, while the others produce a unique lensed image. While the core radius continues to increase, the cross section of the second caustic curve decreases. For the case  $\rho_c \geq \sqrt{f}/(1+f) \simeq 0.4517$ , the caustic curves no longer exist, as well as the corresponding

critical ones (see Fig. 3.13). For such a case, any parts of the source produce one and only one lensed image, even though the resulting lensed image plane is still altered. For the case of large values of the core radius in comparison with the impact parameter, the NSIE lens model tends first towards the uniform disk lens model, and finally, towards the infinite sheet with a constant surface mass density.



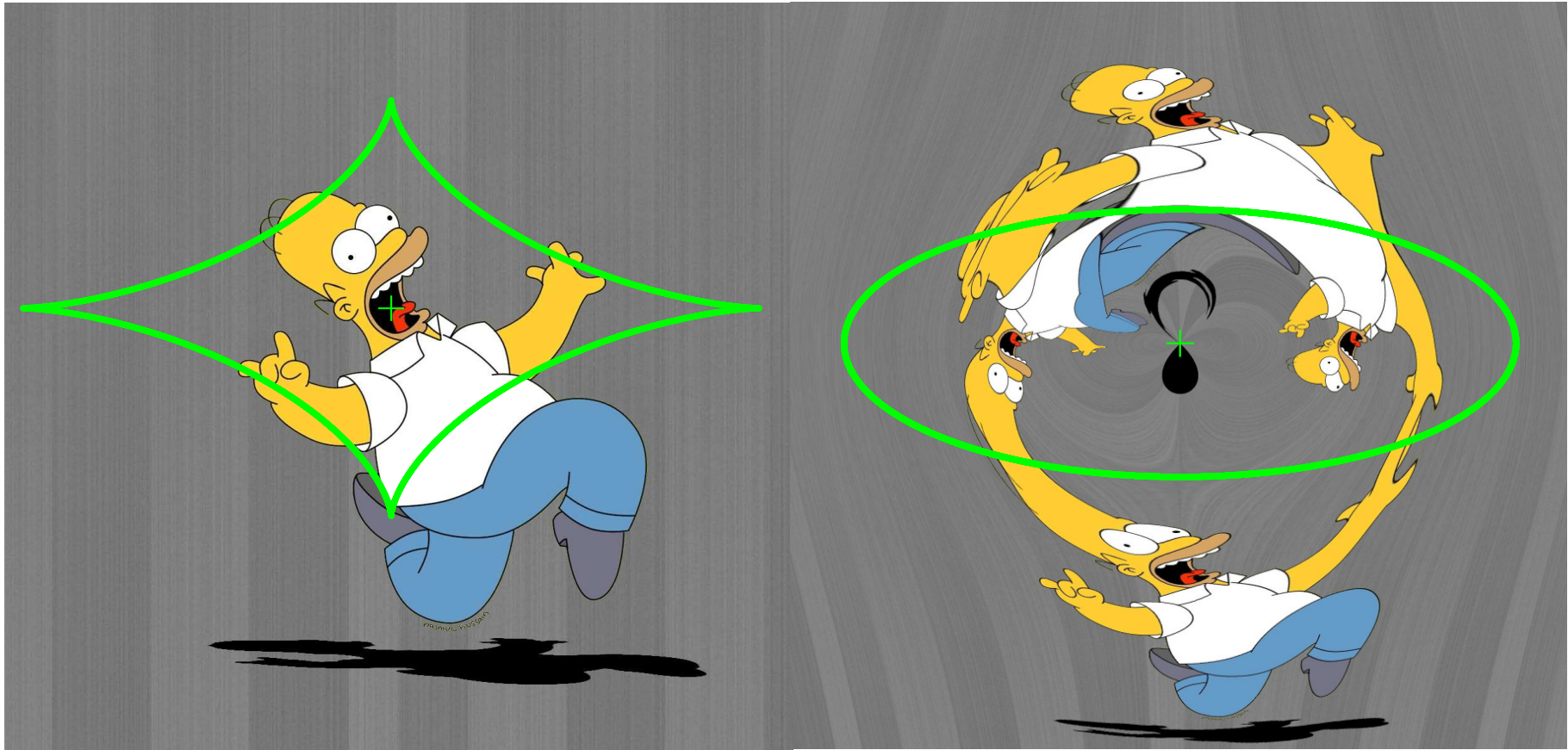


**Figure 3.7:** Illustration of the source, the lensed images, the caustic curves (green lines, left panel) and their associated critical ones (green lines, right panel), for the case of the NSIE with  $f = 0.4$  and  $\rho_c = 0$

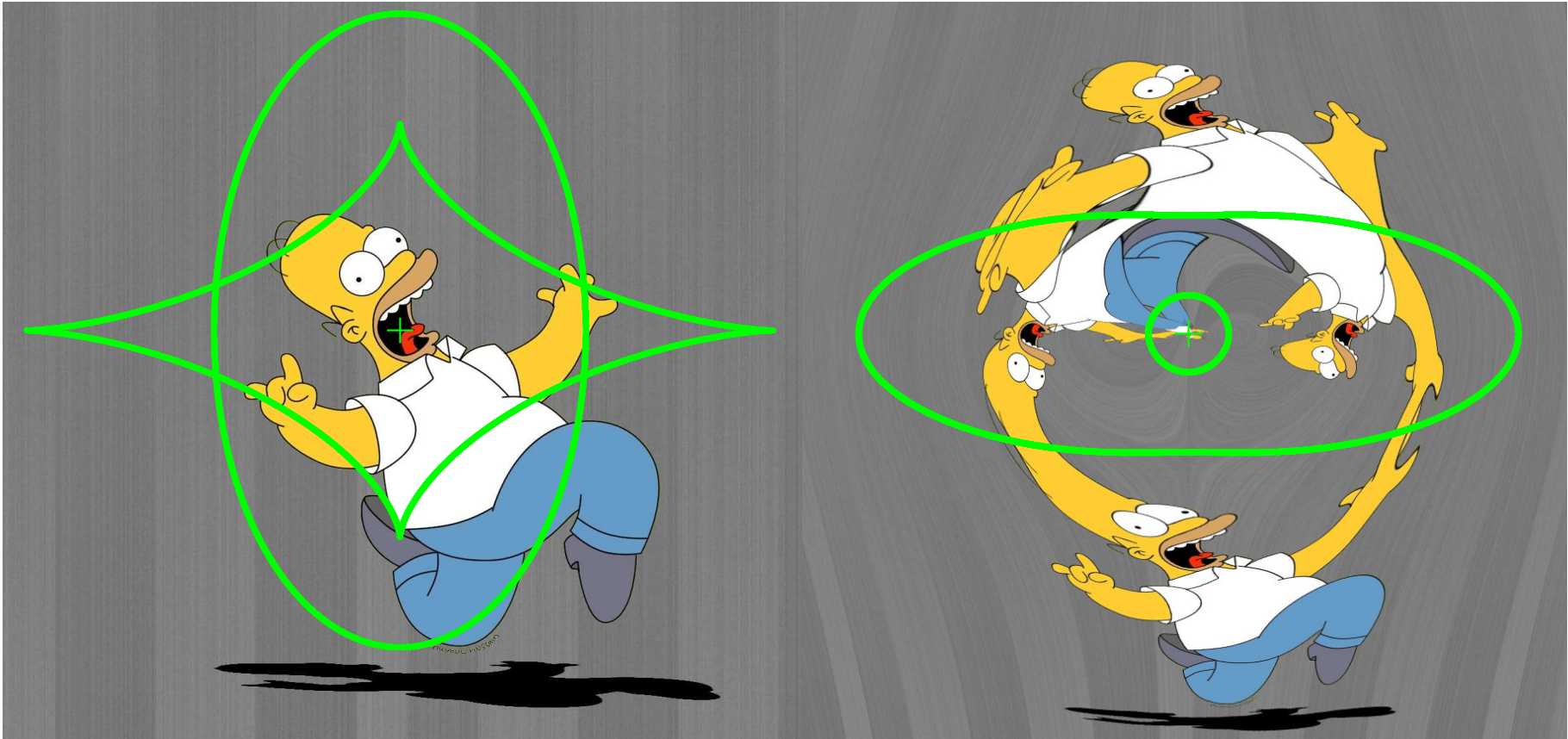


**Figure 3.8:** Illustration of the source, the lensed images, the caustic curves (green lines, left panel) and their associated critical ones (green lines, right panel), for the case of the NSIE with  $f = 0.4$  and  $\rho_c = 0.03$

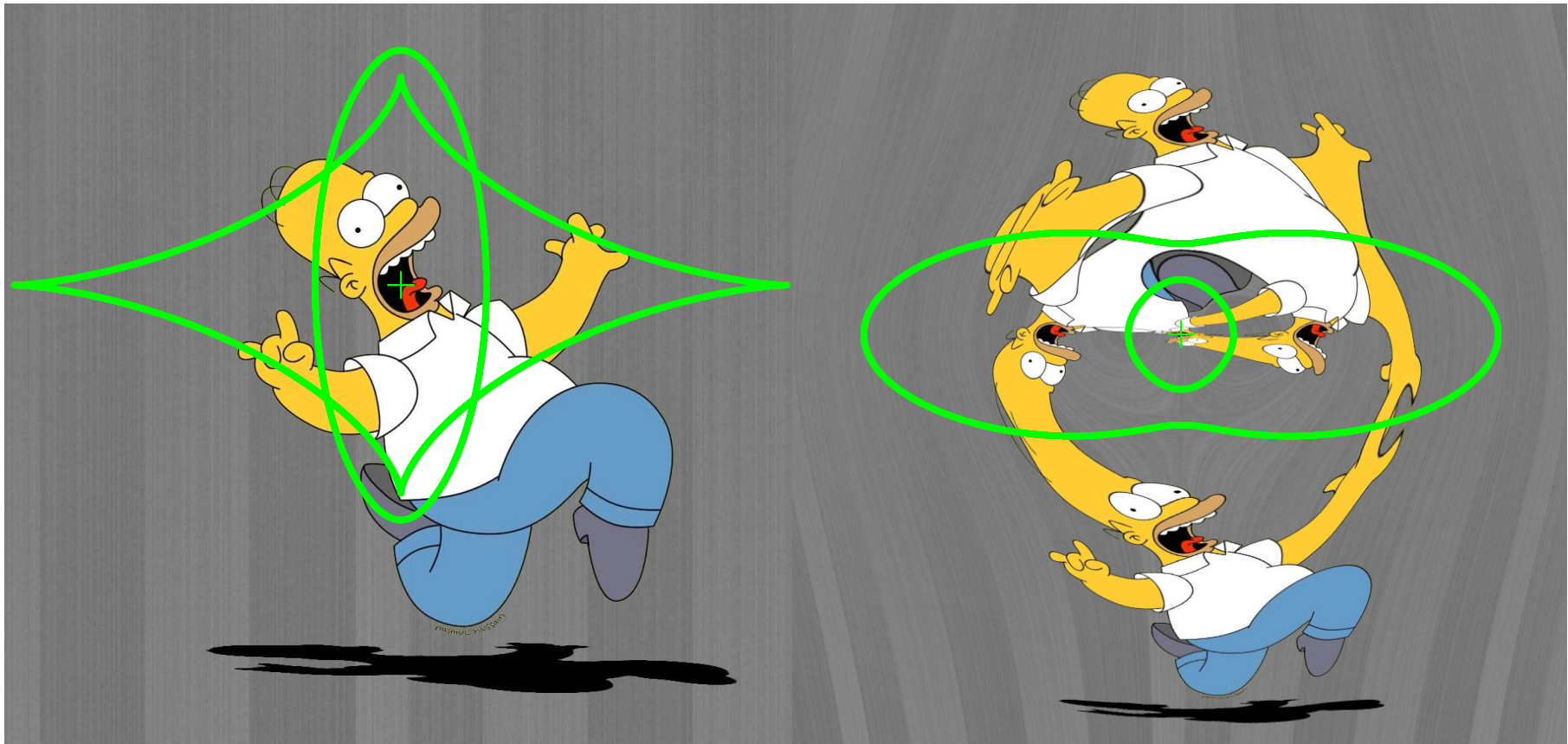


**Figure 3.9:** Illustration of the source, the lensed images, the caustic curves (green lines, left panel) and their associated critical ones (green lines, right panel), for the case of the NSIE with  $f = 0.4$  and  $\rho_c = 0.08$



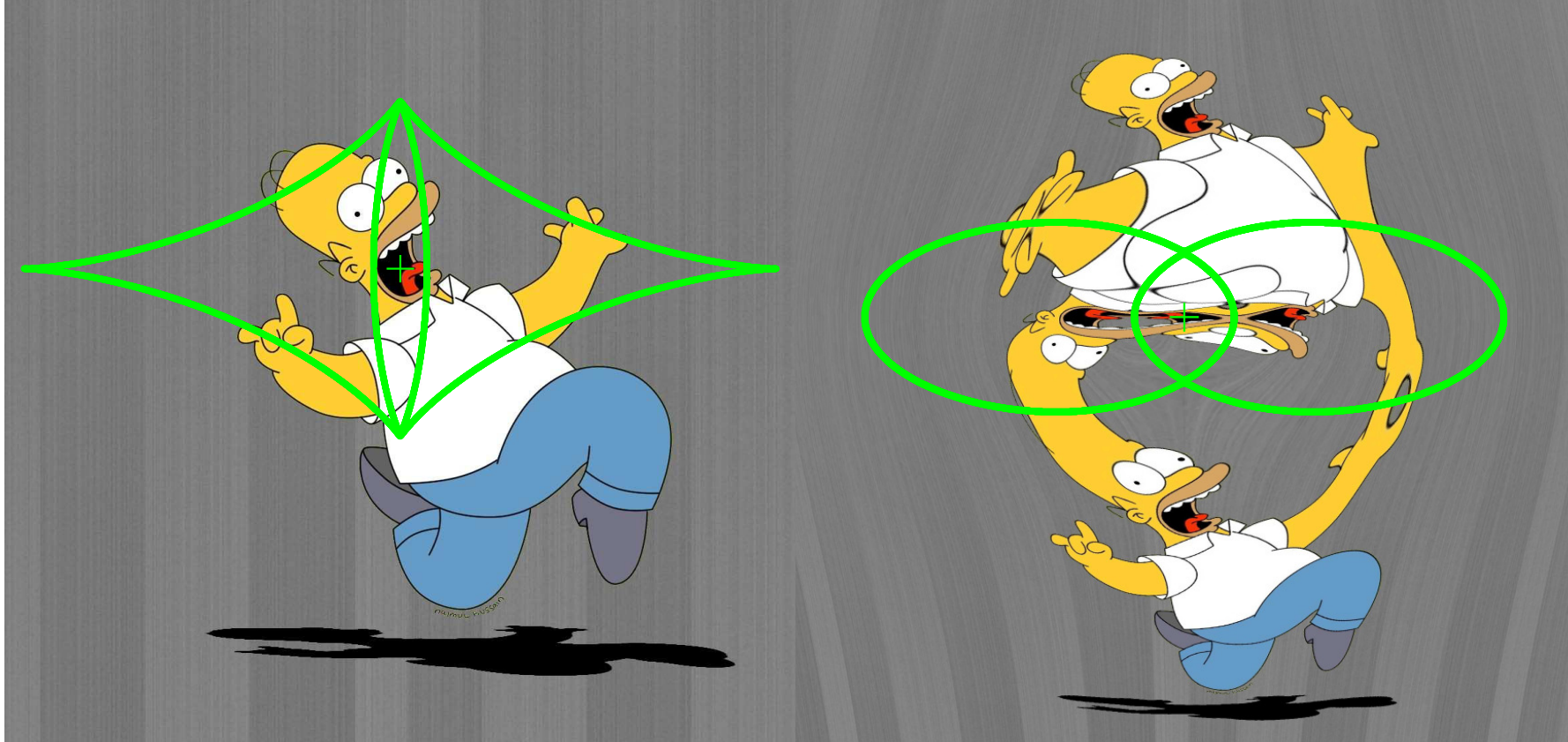


**Figure 3.10:** Illustration of the source, the lensed images, the caustic curves (green lines, left panel) and their associated critical ones (green lines, right panel), for the case of the NSIE with  $f = 0.4$  and  $\rho_c = 0.13$

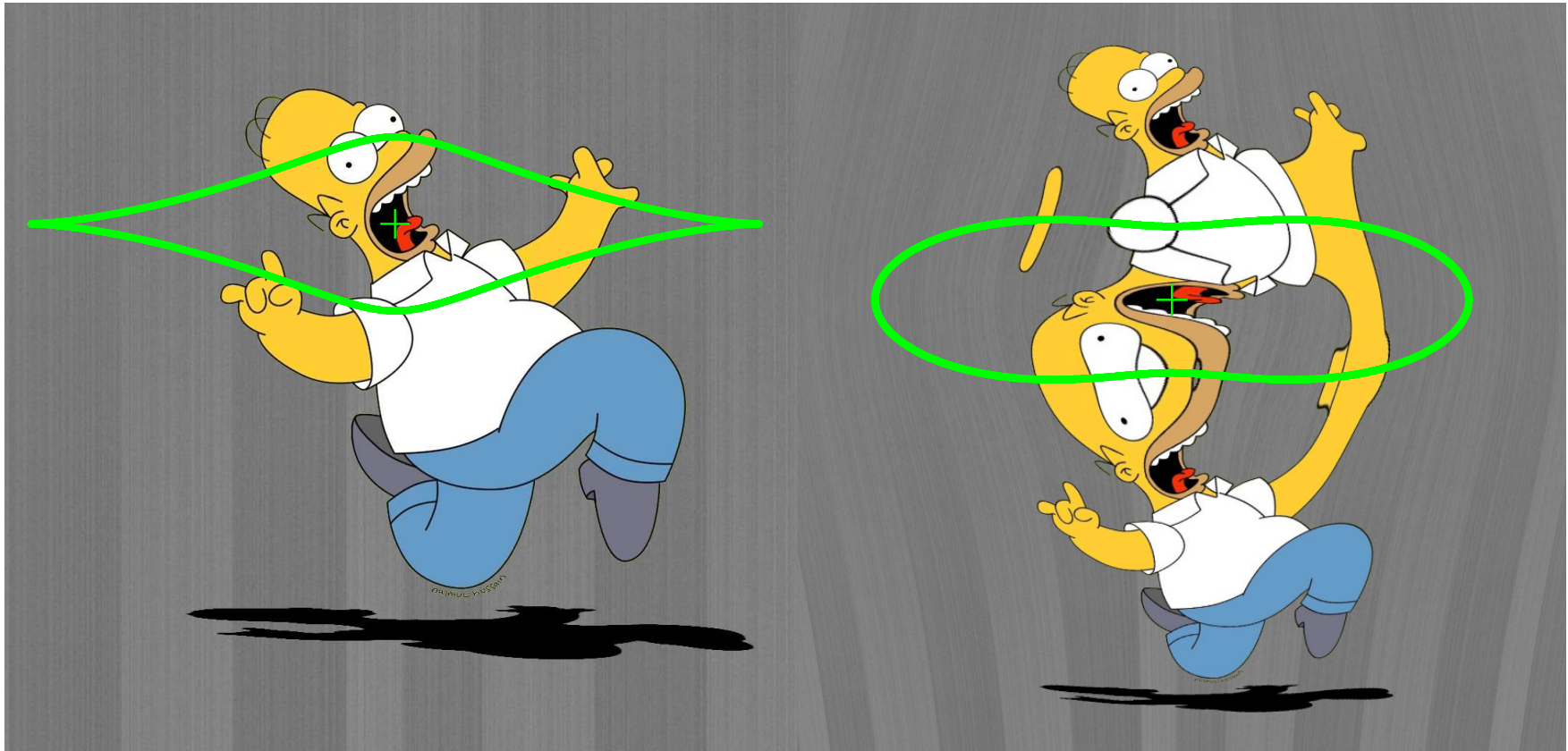


**Figure 3.11:** Illustration of the source, the lensed images, the caustic curves (green lines, left panel) and their associated critical curves (green lines, right panel), for the case of the NSIE with  $f = 0.4$  and  $\rho_c = 0.23$

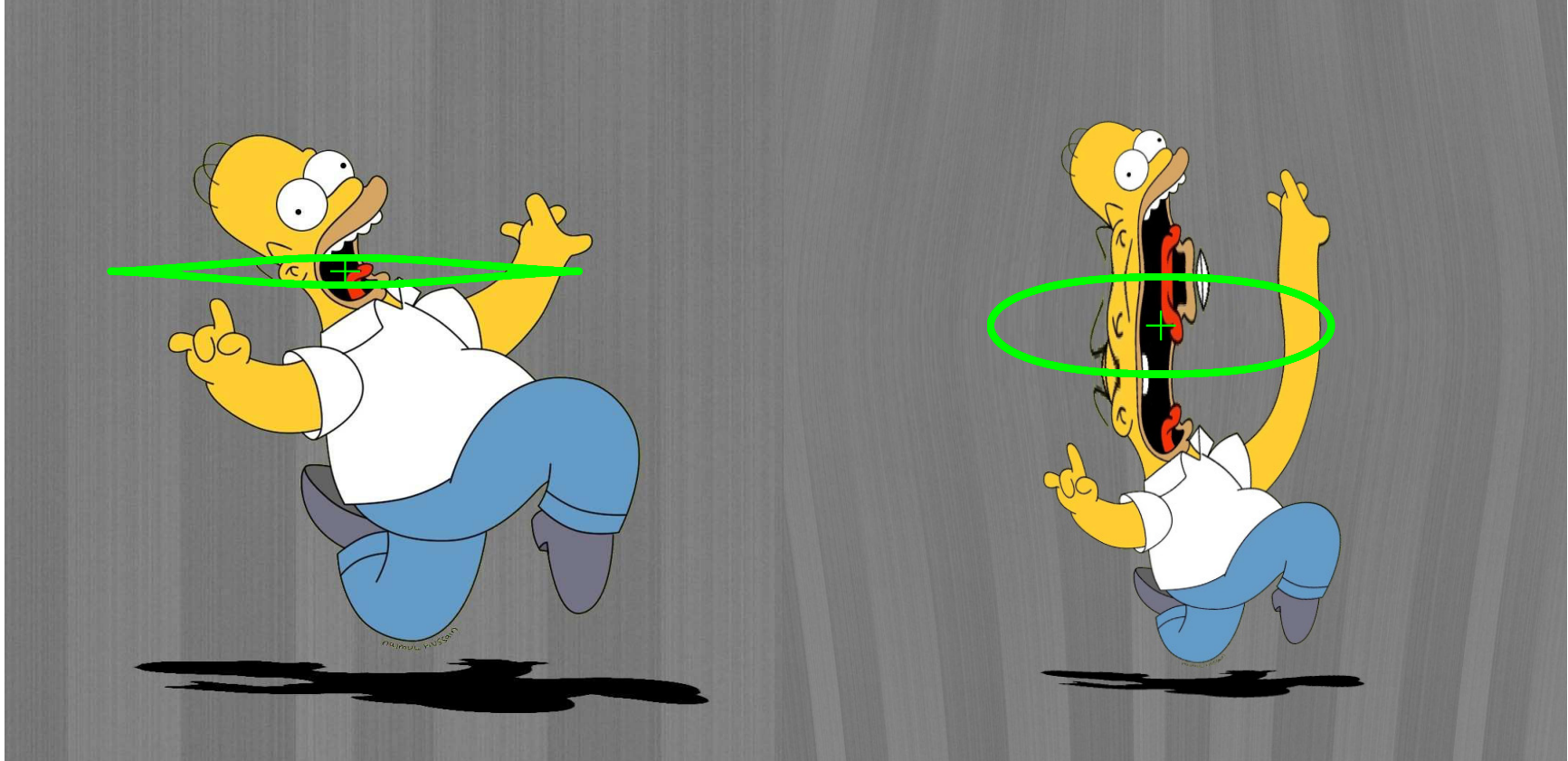


**Figure 3.12:** Illustration of the source, the lensed images, the caustic curves (green lines, left panel) and their associated critical curves (green lines, right panel), for the case of the NSIE with  $f = 0.4$  and  $\rho_c = 0.38$



**Figure 3.13:** Illustration of the source and the lensed images, the caustic curves and their associated critical ones do not exist, for the case of the NSIE with  $f = 0.4$  and  $\rho_c = 0.47$





# 4

## CONCLUSIONS

---

*“The probability that nebulae which act as gravitational lenses will be found becomes practically a certainty.”*

FRITZ ZWICKY, 1937.

Since its publication by A. Einstein in 1916, General Relativity has been the incubator of many elegant theories, the modern GL theory being one of them. During almost half a century, no well-established observational evidence was spotted, until 1979, year of the discovery of the first lensing effect outside our solar system. From that moment, the GL phenomenon has become a key actor in cosmology. Along with observational investigations, theoretical in-depth studies have been the source of significant prospects. To cite but one example, let us mention the work of S. Refsdal on the possibility of deriving the value of the Hubble parameter  $H_0$  from the time delays based on the light curves observed between multiple lensed images of a distant source (Refsdal 1964a, b). Due to the need of realistic models to characterize the mass distribution behind the lensing effects, theoretical investigations of the lens mapping have always been the center of major interests. Although much has been achieved, there always exists a way to contribute. It is with this in mind that we have decided to investigate two sides of the GL theory : the determination of the value of  $H_0$ , and, analytical methods in order to derive the expression of the deflection angle.

In Chapter 2, we have investigated the possibility of determining  $H_0$  irrespective of the lens models. Let us consider what we mean by “lens models”. Mass distribution of the deflector can be apprehended according to two different ways : the non-parametric lens models or the parametric ones. The parametric family of models, often constructed from physical considerations, allows to describe the mass distributions making use of simple analytical functions depending on several parameters. A given family of models may include a large (or infinite) number of distinct models, all characterized by a unique canonical function for the mass distribution and a few parameters. For instance, the SIS family of models, which is appropriate to describe mass distributions with flat galaxy rotation curves, leads to

a unique model only for a given set of parameters. Therefore, there exist two levels of model independence : the one relative to the models defined within a given family, and, the global one in relation with the family of models. In Chapter 2, we referred to the first one.

To this end, the case of a small misalignment between the source, the deflector and the observer turns out to be particularly appropriate. Indeed, for such a case, the lensed image positions are very close to the ones obtained in the case of a perfect alignment. For the case of a power-law axially symmetric mass distribution characterized by  $M(\leq |\mathbf{x}|) = |\mathbf{x}|^\varepsilon$  and affected by an external shear, the so-called  $\varepsilon - \gamma$  family of models, the lensed image positions have been analytically derived in the case of perfect alignment. As a consequence, making use of the perturbative theory, we have analytically derived an approximate expression for  $H_0$  based only on observable quantities, and which is valid irrespective of the  $\varepsilon - \gamma$  models and to first order for a small misalignment between the source, the deflector and the observer. Of course, such a result can only be applied for a symmetric lens system which can be adequately modeled by the  $\varepsilon - \gamma$  family of models. In order to straightforwardly test whether such a family of models is appropriate, we have demonstrated the possibility of expressing all the model parameters as a function of the lensed image positions only. As a consequence, we can retrieve, to first order, all these parameters without any numerical simulations. The major results of this study have been summarized in the paper entitled "*Asymptotic solutions for the case of nearly symmetric gravitational lens systems*" and published in the peer reviewed journal MNRAS 424, 1543-1555, 2012.

In order to expand the possibilities proposed by such an approach, we have investigated the singular isothermal ellipsoid (SIE) family of models. For the case of a small misalignment between the source, the deflector and the observer, we have once again demonstrated the possibility of determining  $H_0$  irrespective of the models. Furthermore, we have also derived expressions which link the model parameters to the lensed image positions only. The next step naturally consisted in applying these results to a real gravitational lens system which fulfilled the required conditions : Q2237+0305. Making use of the analytical expressions of the model parameters in terms of astrometry, we have concluded that the SIE family of models was more appropriate than the  $\varepsilon - \gamma$  one. Indeed, while the obtained  $\varepsilon - \gamma$  parameters led to unphysical values of some parameters, e.g. a negative shear intensity, the SIE ones allowed to constrain the lensed image positions with a mean precision  $\langle \Delta \mathbf{x} \rangle = 0.0134$  arcsec, without any numerical simulations. In order to test the validity of these results obtained to first order, we have performed precise numerical fitting of the deflector using the  $\varepsilon - \gamma$ , SIE and non-singular isothermal ellipsoid (NSIE) + shear lens models. On one hand, the astrometric constraints obtained with the  $\varepsilon - \gamma$  family of models are of less good quality

than the ones obtained with the SIE to first order. On the other hand, the model parameters derived for the SIE and NSIE + shear are in very good agreement with the SIE first order ones. Since the time delays for Q2237+0305 are, up to now, not very well constrained, we have been unable to propose an estimate for  $H_0$ . Consequently, after having adopted the value of  $H_0$  recently proposed by the PLANCK collaboration, we have deduced the expected values of the time delays between pairs of lensed images. The major results of this study have been summarized in the paper entitled "*Asymptotic solutions for the case of SIE lens models and application to the quadruply imaged quasar Q2237+0305*", recently submitted to the peer reviewed journal MNRAS for publication.

Different perspectives can be considered. On one hand, we may test the first order equations for a large sample of well-known gravitational lens systems, both for the  $\varepsilon - \gamma$  and SIE lens models. For those which succeed to be represented by one of these lens models, we could directly estimate the value of  $H_0$ . For those gravitational lens systems having no well constrained time delays, alike Q2237+0305, we shall adopt the best actual determination of  $H_0$  in agreement with recent works and deduce the expected values of those time delays between pairs of lensed images. Depending on the symmetry of the considered gravitational lens systems, the associated time delays can be very small. As a consequence, it should be of great interest to observe these systems, not during long periods but with a very good time sampling. On the other hand, we may investigate, to first order, other lens models, for instance the NSIE lens models. Since the first order approach provides interesting results for the case of the  $\varepsilon - \gamma$  and *SIE* lens models, we can reasonably assume that such a method should also be promising for other families of models.

In Chapter 3, we have presented a new approach in order to determine the explicit expression of the deflection angle based on the well-known fact that the latter can be expressed as a convolution product between the dimensionless surface mass density and the simple kernel  $\mathbf{x}/|\mathbf{x}|^2$ . Although this property has already found some utility in numerical applications, it has never been adopted, as far as we know, to model strong gravitational lensing. Of course, the Fourier approach allows to retrieve expressions of the deflection angle for the case of well-known deflectors such as axially symmetric lens models. In addition, we are convinced that such a method constitutes a real alternative to the complex formalism introduced by Bourassa & Kantowski (1973, 1975), corrected by Bray (1984). In order to test the interest of this method, we have considered the case of homoeoidal symmetric mass distributions which englobe a large variety of already known deflector models. Contrary to Bourassa & Kantowski (1975), we have succeeded to separately derive the expressions of both components of the deflection angle. In that, the Fourier approach constitutes a real progress. The latter result

has been summarized in the paper entitled "*Use of the Fourier transform to derive simple expressions for the gravitational lens deflection angle*" and published in the peer reviewed journal MNRAS 437, 1051-1055, 2014 (advance access publication 2013 November 26).

A particular case of homoeoidal symmetric lenses lies among the NSIE models. Such a family of models has first been investigated by Kovner (1987), Kormann & al. (1994) and improved by Keeton & Kochanek (1998). These studies were limited to the determination of the expressions for the deflection angle and the deflection potential. Making use of the Fourier approach, we have derived different but equivalent expressions for these quantities. In addition, we have proposed a complete analytical study of the caustic curves and their corresponding critical ones. Such analytical results should achieve real relevance in the framework of statistical studies of the gravitational lensing phenomena. Indeed, the probability for a quasar to be multiply imaged requires the determination of the cross-section associated to a lens model, which is directly correlated with the shape of the caustic and critical curves. Having analytical expressions for these curves constitutes of course a real advantage. The latter results have been summarized in the paper entitled "*The non-singular isothermal ellipsoid lens model : a complete analytical solution*" and submitted to the peer reviewed journal MNRAS on 3rd of February, 2014.

The usefulness of the Fourier approach also appears in the treatment of non-parametric lens models. To this end, we have derived the expression of the deflection angle for the case of a mass distribution represented by a tessellated plane with square pixels characterized by a constant surface mass density. The obtained expressions may be easily generalized for an adaptive grid of different size pixels. In principle, this non-parametric lens model has the ability to represent any mass distribution, without any preconception. We have tested the analytical expressions of the deflection angle for the case of the pixellated non-singular isothermal sphere (NSIS) and compared the lensed images with those provided by the ones produced by the analytical NSIS family of models. Even for the case of a rough grid, the positions of the lensed images are found to be in good agreement with the analytical models. The real interest in such a modeling method lies, among others, in the deflector reconstruction. Indeed, for a given gravitational lens system, it turns out to be possible to retrieve the mass distribution which causes the formation of lensed images by combining the use of an adaptive grid as described and numerical techniques. We may also consider such a method for cluster lensing which requires numerical treatments. Finally, let us recall that all these modeling methods aim at constraining the cosmological parameters of the Universe.

To conclude this work, let us mention the fact that the gravitational lensing theory has still a lot to offer. It is up to us to disclose all its secrets.

## BIBLIOGRAPHY

---

- [1] J. H. An and N. W. Evans, “The Chang-Refsdal lens revisited,” *MNRAS*, vol. 369, pp. 317–334, June 2006.
- [2] M. Bartelmann, “Numerical Methods in Gravitational Lensing,” *ArXiv Astrophysics e-prints*, *arXiv:astro-ph/0304162*, Apr. 2003.
- [3] M. Bartelmann and P. Schneider, “Weak gravitational lensing,” *Physics Reports*, vol. 340, pp. 291–472, Jan. 2001.
- [4] E. Borra, P. Hickson, and J. Surdej, “The international liquid mirror telescope,” *Optics and Photonics News*, vol. 20, no. 4, pp. 28–33, 2009.
- [5] R. R. Bourassa, R. Kantowski, and T. D. Norton, “The Spheroidal Gravitational Lens,” *ApJ*, vol. 185, pp. 747–756, Nov. 1973.
- [6] R. R. Bourassa and R. Kantowski, “The theory of transparent gravitational lenses,” *ApJ*, vol. 195, pp. 13–21, Jan. 1975.
- [7] I. Bray, “Spheroidal gravitational lenses,” *MNRAS*, vol. 208, pp. 511–516, June 1984.
- [8] V. Chantry, D. Sluse, and P. Magain, “COSMOGRAIL: the COSmological MONitoring of GRAVItational Lenses. VIII. Deconvolution of high resolution near-IR images and simple mass models for 7 gravitationally lensed quasars,” *A&A*, vol. 522, p. A95, Nov. 2010.
- [9] K. Chang and S. Refsdal, “Star disturbances in gravitational lens galaxies,” *A&A*, vol. 132, pp. 168–178, Mar. 1984.
- [10] J. F. Claeskens, *Aspects statistiques du phénomène de lentille gravitationnelle dans un échantillon de quasars très lumineux*. PhD thesis, Université de Liège, 1998.
- [11] F. Courbin, V. Chantry, Y. Revaz, D. Sluse, C. Faure, M. Tewes, E. Eulaers, M. Koleva, I. Asfandiyarov, S. Dye, P. Magain, H. van Winckel, J. Coles, P. Saha, M. Ibrahimov, and G. Meylan, “COSMOGRAIL: the COSmological MONitoring of GRAVItational Lenses. IX. Time delays, lens dynamics and baryonic fraction in HE 0435-1223,” *A&A*, vol. 536, p. A53, Dec. 2011.
- [12] Dixon, A. C., “The second Mean Value Theorem in the Integral Calculus,” *Mathematical Proceedings of the Cambridge Philosophical Society*, vol. 25, pp. 282–284, 1929.

- [13] A. Eigenbrod, F. Courbin, C. Vuissoz, G. Meylan, P. Saha, and S. Dye, “COSMOGRAIL: The COSmological MONitoring of GRAvItational Lenses. I. How to sample the light curves of gravitationally lensed quasars to measure accurate time delays,” *A&A*, vol. 436, pp. 25–35, June 2005.
- [14] A. Eigenbrod, F. Courbin, S. Dye, G. Meylan, D. Sluse, C. Vuissoz, and P. Magain, “COSMOGRAIL: the COSmological MONitoring of GRAvItational Lenses. II. SDSS J0924+0219: the redshift of the lensing galaxy, the quasar spectral variability and the Einstein rings,” *A&A*, vol. 451, pp. 747–757, June 2006.
- [15] A. Eigenbrod, F. Courbin, G. Meylan, C. Vuissoz, and P. Magain, “COSMOGRAIL: the COSmological MONitoring of GRAvItational Lenses. III. Redshift of the lensing galaxy in eight gravitationally lensed quasars,” *A&A*, vol. 451, pp. 759–766, June 2006.
- [16] A. Eigenbrod, F. Courbin, and G. Meylan, “COSMOGRAIL: the COSmological MONitoring of GRAvItational Lenses. VI. Redshift of the lensing galaxy in seven gravitationally lensed quasars,” *A&A*, vol. 465, pp. 51–56, Apr. 2007.
- [17] A. Einstein, “Die Grundlage der allgemeinen Relativitätstheorie,” *Annalen der Physik*, vol. 354, pp. 769–822, 1916.
- [18] I. M. H. Etherington, “On the Definition of Distance in General Relativity.,” *Philosophical Magazine*, vol. 15, p. 761, 1933.
- [19] E. Eulaers, M. Tewes, P. Magain, F. Courbin, I. Asfandiyarov, S. Ehgamberdiev, S. Rathna Kumar, C. S. Stalin, T. P. Prabhu, G. Meylan, and H. Van Winckel, “COSMOGRAIL: the COSmological MONitoring of GRAvItational Lenses. XII. Time delays of the doubly lensed quasars SDSS J1206+4332 and HS 2209+1914,” *A&A*, vol. 553, p. A121, May 2013.
- [20] E. E. Falco, M. V. Gorenstein, and I. I. Shapiro, “On model-dependent bounds on  $H_0$  from gravitational images Application of Q0957 + 561A,B,” *ApJ*, vol. 289, pp. L1–L4, Feb. 1985.
- [21] M. Fukugita, T. Futamase, and M. Kasai, “A Possible Test for the Cosmological Constant with Gravitational Lenses,” *MNRAS*, vol. 246, p. 24P, Oct. 1990.
- [22] J. R. Gott, III, M.-G. Park, and H. M. Lee, “Setting limits on  $q_0$  from gravitational lensing,” *ApJ*, vol. 338, pp. 1–12, Mar. 1989.
- [23] I. S. Gradshteyn, I. M. Ryzhik, A. Jeffrey, and D. Zwillinger, *Table of Integrals, Series, and Products*. Academic Press, 2007.

- [24] C. R. Keeton and C. S. Kochanek, “Gravitational Lensing by Spiral Galaxies,” *ApJ*, vol. 495, p. 157, Mar. 1998.
- [25] R. Kormann, P. Schneider, and M. Bartelmann, “Isothermal elliptical gravitational lens models,” *A&A*, vol. 284, pp. 285–299, Apr. 1994.
- [26] I. Kovner, “The quadrupole gravitational lens,” *ApJ*, vol. 312, pp. 22–44, Jan. 1987.
- [27] S. Liebes, “Gravitational Lenses,” *Physical Review*, vol. 133, pp. 835–844, Feb. 1964.
- [28] C. W. Misner, K. S. Thorne, and J. A. Wheeler, *Gravitation*. W. H. Freeman, 1973.
- [29] M. Oguri, N. Inada, M. A. Strauss, C. S. Kochanek, I. Kayo, M.-S. Shin, T. Morokuma, G. T. Richards, C. E. Rusu, J. A. Frieman, M. Fukugita, D. P. Schneider, D. G. York, N. A. Bahcall, and R. L. White, “The Sloan Digital Sky Survey Quasar Lens Search. VI. Constraints on Dark Energy and the Evolution of Massive Galaxies,” *AJ*, vol. 143, p. 120, May 2012.
- [30] A. O. Petters, H. Levine, and J. Wambsganss, *Singularity theory and gravitational lensing*. Birkhäuser, 2001.
- [31] Planck Collaboration, P. A. R. Ade, N. Aghanim, C. Armitage-Caplan, M. Arnaud, M. Ashdown, F. Atrio-Barandela, J. Aumont, C. Baccigalupi, A. J. Banday, and et al., “Planck 2013 results. XVI. Cosmological parameters,” *ArXiv e-prints*, Mar. 2013.
- [32] S. Rathna Kumar, M. Tewes, C. S. Stalin, F. Courbin, I. Asfandiyarov, G. Meylan, E. Eulaers, T. P. Prabhu, P. Magain, H. Van Winckel, and S. Eghamberdiev, “COSMOGRAIL: the COSmological MONitoring of GRAVItational Lenses. XIV. Time delay of the doubly lensed quasar SDSS J1001+5027,” *A&A*, vol. 557, p. A44, Sept. 2013.
- [33] S. Refsdal and J. Surdej, “Gravitational lenses,” *Reports on Progress in Physics*, vol. 57, pp. 117–185, Feb. 1994.
- [34] S. Refsdal, “On the possibility of determining Hubble’s parameter and the masses of galaxies from the gravitational lens effect,” *MNRAS*, vol. 128, p. 307, 1964.
- [35] S. Refsdal, “The gravitational lens effect,” *MNRAS*, vol. 128, p. 295, 1964.
- [36] P. Saha, F. Courbin, D. Sluse, S. Dye, and G. Meylan, “COSMOGRAIL: the COSmological MONitoring of GRAVItational Lenses. IV. Models of prospective time-delay lenses,” *A&A*, vol. 450, pp. 461–469, May 2006.
- [37] P. Schneider, J. Ehlers, and E. E. Falco, *Gravitational Lenses*. Springer-Verlag, 1992.



- [38] P. Schneider, “The amplification caused by gravitational bending of light,” *A&A*, vol. 140, pp. 119–124, Nov. 1984.
- [39] B. F. Schutz, *A First Course in General Relativity*. Cambridge University Press, Feb. 1985.
- [40] D. Sluse, V. Chantry, P. Magain, F. Courbin, and G. Meylan, “COSMOGRAIL: the COSmological MONitoring of GRAvItational Lenses. X. Modeling based on high-precision astrometry of a sample of 25 lensed quasars: consequences for ellipticity, shear, and astrometric anomalies,” *A&A*, vol. 538, p. A99, Feb. 2012.
- [41] J. Surdej, J. F. Claeskens, D. Crampton, A. V. Filippenko, D. Hutsemekers, P. Magain, B. Pirenne, C. Vanderriest, and H. K. C. Yee, “Gravitational lensing statistics based on a large sample of highly luminous quasars,” *AJ*, vol. 105, pp. 2064–2078, June 1993.
- [42] M. Tewes, F. Courbin, and G. Meylan, “COSMOGRAIL: the COSmological MONitoring of GRAvItational Lenses. XI. Techniques for time delay measurement in presence of microlensing,” *A&A*, vol. 553, p. A120, May 2013.
- [43] M. Tewes, F. Courbin, G. Meylan, C. S. Kochanek, E. Eulaers, N. Cantale, A. M. Mosquera, P. Magain, H. Van Winckel, D. Sluse, G. Cataldi, D. Vörös, and S. Dye, “COSMOGRAIL: the COSmological MONitoring of GRAvItational Lenses. XIII. Time delays and 9-yr optical monitoring of the lensed quasar RX J1131-1231,” *A&A*, vol. 556, p. A22, Aug. 2013.
- [44] E. L. Turner, J. P. Ostriker, and J. R. Gott, III, “The statistics of gravitational lenses - The distributions of image angular separations and lens redshifts,” *ApJ*, vol. 284, pp. 1–22, Sept. 1984.
- [45] E. Van Drom, “Aspects théoriques du phénomène "mirage gravitationnel",” Master’s thesis, Université de Liège, 1989.
- [46] C. Vuissoz, F. Courbin, D. Sluse, G. Meylan, M. Ibrahimov, I. Asfandiyarov, E. Stoops, A. Eigenbrod, L. Le Guillou, H. van Winckel, and P. Magain, “COSMOGRAIL: the COSmological MONitoring of GRAvItational Lenses. V. The time delay in SDSS J1650+4251,” *A&A*, vol. 464, pp. 845–851, Mar. 2007.
- [47] C. Vuissoz, F. Courbin, D. Sluse, G. Meylan, V. Chantry, E. Eulaers, C. Morgan, M. E. Eyler, C. S. Kochanek, J. Coles, P. Saha, P. Magain, and E. E. Falco, “COSMOGRAIL: the COSmological MONitoring of GRAvItational Lenses. VII. Time delays and the Hubble constant from WFI J2033-4723,” *A&A*, vol. 488, pp. 481–490, Sept. 2008.



- 
- [48] D. Walsh, R. F. Carswell, and R. J. Weymann, “0957 + 561 A, B - Twin quasistellar objects or gravitational lens,” *Nature*, vol. 279, pp. 381–384, May 1979.
- [49] O. Wertz, V. Pelgrims, and J. Surdej, “Asymptotic solutions for the case of nearly symmetric gravitational lens systems,” *MNRAS*, vol. 424, pp. 1543–1555, Aug. 2012.
- [50] O. Wertz and J. Surdej, “Asymptotic solutions for the case of SIE lens models and application to the quadruply imaged quasar Q2237+0305,” *MNRAS*, 2014, submitted.
- [51] O. Wertz and J. Surdej, “The non-singular isothermal ellipsoid lens model revisited : a complete analytical solution,” *MNRAS*, 2014, submitted on 3rd of February 2014.
- [52] O. Wertz and J. Surdej, “Use of the Fourier transform to derive simple expressions for the gravitational lens deflection angle,” *MNRAS*, vol. 437, pp. 1051–1055, Jan. 2014.
- [53] H. J. Witt, S. Mao, and C. R. Keeton, “Analytic Time Delays and  $H_0$  Estimates for Gravitational Lenses,” *ApJ*, vol. 544, pp. 98–103, Nov. 2000.

## List of publications

### Legend


**Bibliometric indicators linked to the journal** (for those whose ISSN has been indicated by the author)


- **IF = Impact factor Thomson ISI.** Are indicated : IF of the year of publication and IF of the last edition of JCR (**last**), « ? » if not known by ORBi yet ; « - » if non-existent.
- **IF5** : idem as IF but for a 5 year period (new indicator since 2009).
- **EigenF = EigenFactor** (see : <http://www.eigenfactor.org/>).
- **Article Infl. = Article Influence** : EigenFactor divided by the number of articles published in the journal.  
→ More information ? <http://orbi.ulg.ac.be/rpt#rev>

**Bibliometric indicators linked to the article**

- **ORBi viewed** = total number of visualizations of a reference on ORBi (of which X internally within the ULg).
- **ORBi downloaded** = total number of downloads of the full text via ORBi, including requests copy.
- **SCOPUS®** = number of citations picked up by SCOPUS®.  
→ More information ? <http://orbi.ulg.ac.be/rpt#art>

(Warning : According to disciplines, some bibliometric indicators may not be relevant)





 etc: full text of the document available in Open Access






 etc: full text of the document available in restricted access





### 1. Published books, as author, co-author or editor


### 2. Books chapters, as author or co-author

### 3. Articles accepted in journals with committee (peer reviewed)

- 1) **Wertz, O.**, & Surdej, J. (2013). Use of the Fourier transform to derive the gravitational lens deflection angle. *Monthly Notices of the Royal Astronomical Society*, 437, 1051-1055.  
 <http://hdl.handle.net/2268/161851>  
ORBi viewed: **10** (2 ULg) ; downloaded: **0** — SCOPUS®: **0**  
IF 2013: ?; last: **5.521**; IF5: **5.009** — EigenF 2013: ?; last: **0.2488** — Article Infl. 2013: ?; last: **1.6034**
- 2) **Wertz, O.**, Pelgrims, V., & Surdej, J. (2012). Asymptotic solutions for the case of nearly symmetric gravitational lens systems. *Monthly Notices of the Royal Astronomical Society*, 424, 1543-1555.  
 <http://hdl.handle.net/2268/126775>  
ORBi viewed: **55** (24 ULg) ; downloaded: **10** (10 ULg) — SCOPUS®: **1**  
IF 2012: **5.521**; last: **5.521**; IF5: **5.009** — EigenF 2012: ?; last: **0.2630** — Article Infl. 2012: ?; last: **1.7504**
- 3) Southworth, J., Mancini, L., Browne, P., Burgdorf, M., Calchi Novati, S., Dominik, M., Gerner, T., Hinse, T. C., Jørgensen, U. G., Kains, N., Ricci, D., Schäfer, S., Schönebeck, F., Tregloan-Reed, J., Alsubai, K. A., Bozza, V., Chen, G., Dodds, P., Dreizler, S., Fang, X.-S., Finet, F., Gu, S.-H., Hardis, S., Harpsøe, K., Henning, T., Hundertmark, M., Jessen-Hansen, J., Kerins, E., Kjeldsen, H., Liebig, C., Lund, M. N., Lundkvist, M., Mathiasen, M., Nikolov, N., Penny, M. T., Proft, S., Rahvar, S., Sahu, K., Scarpetta, G., Skottfelt, J., Snodgrass, C., Surdej, J., & **Wertz, O.** (2013). High-precision photometry by telescope defocusing - V. WASP-15 and WASP-16. *Monthly Notices of the Royal Astronomical Society*, 434, 1300-1308.  
 <http://hdl.handle.net/2268/163473>  
ORBi viewed: **0** ; downloaded: **0**
- 4) Southworth, J., Hinse, T. C., Dominik, M., Fang, X.-S., Harpsøe, K., Jørgensen, U. G., Kerins, E., Liebig, C., Mancini, L., Skottfelt, J., Anderson, D. R., Smalley, B., Tregloan-Reed, J., **Wertz, O.**, Alsubai, K. A., Bozza, V., Calchi Novati, S., Dreizler, S., Gu, S.-H., Hundertmark, M., Jessen-Hansen, J., Kains, N., Kjeldsen, H., Lund, M. N., Lundkvist, M., Mathiasen, M., Penny, M. T., Rahvar, S., Ricci, D., Scarpetta, G., Snodgrass, C., & Surdej, J. (2012). High-precision photometry by telescope defocusing - IV. Confirmation of the huge radius of WASP-17 b. *Monthly Notices of the Royal Astronomical Society*, 426, 1338-1348.  
 <http://hdl.handle.net/2268/142589>  
ORBi viewed: **15** (7 ULg) ; downloaded: **4** — SCOPUS®: **6**  
IF 2012: **5.521**; last: **5.521**; IF5: **5.009** — EigenF 2012: ?; last: **0.2630** — Article Infl. 2012: ?; last: **1.7504**

- 5)  Shin, I.-G., Han, C., Gould, A., Udalski, A., Sumi, T., Dominik, M., Beaulieu, J.-P., Tsapras, Y., Bozza, V., Szymański, M. K., Kubiak, M., Nagaya, M., Nishimoto, K., Ohnishi, K., Okumura, T., Omori, K., Perrott, Y. C., Rattenbury, N., Saito, T., Skuljan, L., Sullivan, D. J., Dreizler, S., Suzuki, D., Sweatman, W. L., Tristram, P. J., Wada, K., Yock, P. C. M., The MOA Collaboration, Christie, G. W., Depoy, D. L., Dong, S., Gal-Yam, A., Fang, X.-S., Gaudi, B. S., Hung, L.-W., Janczak, J., Kaspi, S., Maoz, D., McCormick, J., McGregor, D., Moorhouse, D., Muñoz, J. A., Natusch, T., Grundahl, F., Nelson, C., Pogge, R. W., Tan, T.-G., Polishook, D., Shvartzvald, Y., Shporer, A., Thornley, G., Malamud, U., Yee, J. C., Choi, J.-Y., Gu, C.-H., Jung, Y.-K., Park, H., Lee, C.-U., Park, B.-G., Koo, J.-R., The  $\mu$ FUN Collaboration, Bajek, D., Bramich, D. M., Browne, P., Horne, K., Hardis, S., Ipatov, S., Snodgrass, C., Steele, I., Street, R., Alsubai, K. A., Burgdorf, M. J., Calchi Novati, S., Dodds, P., Harpsøe, K., Hinse, T. C., Hundertmark, M., Jessen-Hansen, J., Jørgensen, U. G., Soszyński, I., Kains, N., Kerins, E., Liebig, C., Lund, M., Lundkvist, M., Mancini, L., Mathiasen, M., Hornstrup, A., Penny, M. T., Proft, S., Pietrzyński, G., Rahvar, S., Ricci, D., Scarpetta, G., Skottfelt, J., Southworth, J., Surdej, J., Tregloan-Reed, J., **Wertz, O.**, Zimmer, F., Albrow, M. D., Poleski, R., Batista, V., Brilliant, S., Caldwell, J. A. R., Calitz, J. J., Cassan, A., Cole, A., Cook, K. H., Corrales, E., Coutures, C., Dieters, S., Ulaczyk, K., Dominis Prester, D., Donatowicz, J., Fouqué, P., Greenhill, J., Hill, K., Hoffman, M., Kane, S. R., Kubas, D., Marquette, J.-B., Martin, R., Pietrukowicz, P., Meintjes, P., Menzies, J., Pollard, K. R., Sahu, K. C., Wambsganss, J., Williams, A., Vinter, C., Zub, M., Kozłowski, S., Skowron, J., Wyrzkowski, Ł., The OGLE Collaboration, Abe, F., Bennett, D. P., Bond, I. A., Botzler, C. S., Freeman, M., Fukui, A., Furusawa, K., Hayashi, F., Hearnshaw, J. B., Hosaka, S., Itow, Y., Kamiya, K., Kilmartin, P. M., Kobara, S., Korpela, A., Lin, W., Ling, C. H., Makita, S., Masuda, K., Matsubara, Y., Miyake, N., & Muraki, Y. (2012). Microlensing Binaries with Candidate Brown Dwarf Companions. *Astrophysical Journal*, 760, 116.  
<http://hdl.handle.net/2268/142586>  
ORBi viewed: 31 (6 ULg) ; downloaded: 6 (1 ULg) — SCOPUS®: 2  
IF 2012: 6.733; last: 6.733; IF5: 5.945 — EigenF 2012: ?; last: 0.4871 — Article Infl. 2012: ?; last: 1.9055
- 6)  Shin, I.-G., Han, C., Choi, J.-Y., Udalski, A., Sumi, T., Gould, A., Bozza, V., Dominik, M., Fouqué, P., Horne, K., Szymański, M. K., Liebig, C., Lund, M., Lunkkvist, M., Mancini, L., Mathiasen, M., Penny, M. T., Rahvar, S., Ricci, D., Scarpetta, G., Skottfelt, J., Moorhouse, D., Southworth, J., Surdej, J., Tregloan-Reed, J., Wambsganss, J., **Wertz, O.**, MiNDSTEp Consortium, T., Almeida, L. A., Batista, V., Christie, G., DePoy, D. L., Natusch, T., Dong, S., Gaudi, B. S., Henderson, C., Jablonski, F., Lee, C.-U., McCormick, J., McGregor, D., Ngan, H., Park, S.-Y., Pogge, R. W., Tan, T.-G., Thornley, G., Yee, J. C., The  $\mu$ FUN Collaboration, Albrow, M. D., Kubiak, M., Bachelet, E., Beaulieu, J.-P., Brilliant, S., Cassan, A., Cole, A. A., Corrales, E., Coutures, C., Dieters, S., Dominis Prester, D., Donatowicz, J., Soszyński, I., Greenhill, J., Kubas, D., Marquette, J.-B., Menzies, J. W., Sahu, K. C., Zub, M., The PLANET Collaboration, Pietrzyński, G., Poleski, R., Ulaczyk, K., Pietrukowicz, P., Kozłowski, S., Skowron, J., Wyrzkowski, Ł., The OGLE Collaboration, Abe, F., Bennett, D. P., Bond, I. A., Botzler, C. S., Chote, P., Freeman, M., Fukui, A., Furusawa, K., Itow, Y., Kobara, S., Ling, C. H., Masuda, K., Matsubara, Y., Miyake, N., Muraki, Y., Ohmori, K., Ohnishi, K., Rattenbury, N. J., Saito, T., Sullivan, D. J., Suzuki, D., Suzuki, K., Sweatman, W. L., Takino, S., Tristram, P. J., Wada, K., Yock, P. C. M., The MOA Collaboration, Bramich, D. M., Snodgrass, C., Steele, I. A., Street, R. A., Tsapras, Y., The RoboNet Collaboration, Alsubai, K. A., Browne, P., Burgdorf, M. J., Calchi Novati, S., Dodds, P., Dreizler, S., Fang, X.-S., Grundahl, F., Gu, C.-H., Hardis, S., Harpsøe, K., Hinse, T. C., Hornstrup, A., Hundertmark, M., Jessen-Hansen, J., Jørgensen, U. G., Kains, N., & Kerins, E. (2012). Characterizing Low-mass Binaries from Observation of Long-timescale Caustic-crossing Gravitational Microlensing Events. *Astrophysical Journal*, 755, 91.  
<http://hdl.handle.net/2268/142597>  
ORBi viewed: 12 (5 ULg) ; downloaded: 1 (1 ULg) — SCOPUS®: 1  
IF 2012: 6.733; last: 6.733; IF5: 5.945 — EigenF 2012: ?; last: 0.4871 — Article Infl. 2012: ?; last: 1.9055
- 7)  Ricci, D., Elyiv, A., Finet, F., **Wertz, O.**, Alsubai, K., Anguita, T., Bozza, V., Browne, P., Burgdorf, M., Calchi Novati, S., Dodds, P., Dominik, M., Dreizler, S., Gerner, T., Glittrup, M., Grundahl, F., Hardis, S., Harpsøe, K., Hinse, T. C., Hornstrup, A., Hundertmark, M., Jørgensen, U. G., Kains, N., Kerins, E., Liebig, C., Maier, G., Mancini, L., Masi, G., Mathiasen, M., Penny, M., Proft, S., Rahvar, S., Scarpetta, G., Sahu, K., Schäfer, S., Schönebeck, F., Schmidt, R., Skottfelt, J., Snodgrass, C., Southworth, J., Thöne, C. C., Wambsganss, J., Zimmer, F., Zub, M., & Surdej, J. (2013). Flux and color variations of the doubly imaged quasar UM673. *Astronomy and Astrophysics*, 551, 104-110.  
<http://hdl.handle.net/2268/142573>  
ORBi viewed: 28 (13 ULg) ; downloaded: 5 (3 ULg) — SCOPUS®: 1  
IF 2013: ?; last: 5.084; IF5: 4.422 — EigenF 2013: ?; last: 0.2542 — Article Infl. 2013: ?; last: 1.4742
- 8)  Mancini, L., Southworth, J., Ciceri, S., Dominik, M., Henning, T., Jørgensen, U. G., Lanza, A. F., Rabus, M., Snodgrass, C., Vilela, C., Alsubai, K. A., Bozza, V., Calchi Novati, S., D'Ago, G., Galianni, P., Gu, S.-H., Harpsøe, K., Hinse, T., Hundertmark, M., Jaimes, R. J. F., Juncher, D., Kains, N., Korhonen, H., Popovas, A., Rahvar, S., Skottfelt, J., Street, R., Surdej, J., Tsapras, Y., Wambsganss, J., Wang, X.-B., & **Wertz, O.** (2013). Physical properties and transmission spectrum of the WASP-80 planetary system from multi-colour photometry. *Astronomy and Astrophysics*, 1312, 4982.  
<http://hdl.handle.net/2268/162006>  
ORBi viewed: 6 ; downloaded: 0 — SCOPUS®: -  
IF 2013: ?; last: 5.084; IF5: 4.422 — EigenF 2013: ?; last: 0.2542 — Article Infl. 2013: ?; last: 1.4742
- 9)  Mancini, L., Ciceri, S., Chen, G., Tregloan-Reed, J., Fortney, J. J., Southworth, J., Tan, T. G., Burgdorf, M., Calchi Novati, S., Dominik, M., Fang, X.-S., Finet, F., Gerner, T., Hardis, S., Hinse, T. C., Jørgensen, U. G., Liebig, C., Nikolov, N., Ricci, D., Schäfer, S., Schönebeck, F., Skottfelt, J., **Wertz, O.**, Alsubai, K. A., Bozza, V., Browne, P., Dodds, P., Gu, S.-H., Harpsøe, K., Henning, T., Hundertmark, M., Jessen-Hansen, J., Kains, N., Kerins, E., Kjeldsen, H., Lund, M. N., Lundkvist, M., Madhusudhan, N., Mathiasen, M., Penny, M. T., Prof, S., Rahvar, S., Sahu, K., Scarpetta, G., Snodgrass, C., & Surdej, J. (2013). Physical properties, transmission and emission spectra of the WASP-19 planetary system from multi-colour photometry. *Monthly Notices of the Royal Astronomical Society*, 436, 2-18.  
<http://hdl.handle.net/2268/158518>  
ORBi viewed: 14 (7 ULg) ; downloaded: 1 (1 ULg) — SCOPUS®: 0

- 10)  Kains, N., Street, R. A., Choi, J.-Y., Han, C., Udalski, A., Almeida, L. A., Jablonski, F., Tristram, P. J., Jørgensen, U. G., Szymański, M. K., Kubiak, M., Muraki, Y., Bennett, D. P., Koziowski, S., Gu, C.-H., Liebig, C., Batista, V., Dodds, P., Surdej, J., Abe, F., Browne, P., Masuda, K., Mancini, L., Caldwell, J. A. R., Natusch, T., Bramich, D. M., Lee, C.-U., Yock, P. C. M., Sumi, T., Freeman, M., Bötzler, C. S., Dreizler, S., Allen, W., Jessen-Hansen, J., Skottfelt, J., Beaulieu, J.-P., **Wertz, O.**, Jung, Y.-K., Cassan, A., Furusawa, K., Martin, R., Fang, X.-S., Ulaczyk, K., Kubas, D., Christie, G., Drummond, J., Zub, M., Brilliant, S., Dieters, S., Shin, I.-G., Skowron, J., Suzuki, D., Dominis Prester, D., Tregloan-Reed, J., Lundkvist, M., Marquette, J.-B., Sahu, K. C., Bond, I. A., Menzies, J., Henderson, C., Dominik, M., Williams, A., Kane, S. R., Rahvar, S., Takino, S., Calchi Novati, S., Gould, A., Bozza, V., McGregor, D., Burgdorf, M. J., Southworth, J., Hardis, S., Wada, K., Hessman, F. V., Itow, Y., Ipatov, S., Hundertmark, M., Wambsganss, J., Ricci, D., Harpsøe, K., Greenhill, J., Meintjes, P., Matsubara, Y., Tsapras, Y., Koo, J.-R., Hornstrup, A., Ngan, H., Sweatman, W. L., Ling, C. H., Pietrukowicz, P., Pogge, R. W., Pietrzyński, G., Chung, S.-J., Poleski, R., Sullivan, D. J., Miyake, N., Saito, T., Coutures, C., Ohnishi, K., Suzuki, K., Penny, M. T., Scarpetta, G., Bachelet, E., Snodgrass, C., DePoy, D. L., Gaudi, B. S., Wouters, D., Park, H., Pollard, K. R., Alsubai, K. A., Donatowicz, J., Albrow, M. D., Yee, J., Soszyński, I., Fouqué, P., Bajek, D., Kerins, E., Horne, K., Cole, A., McCormick, J., Wyrzykowski, Ł., Muñoz, J. A., Steele, I. A., Hinse, T. C., Fukui, A., Corrales, E., Rattenbury, N., Grundahl, F., Chote, P., Lund, M., & Mathiasen, M. (2013). A giant planet beyond the snow line in microlensing event OGLE-2011-BLG-0251. *Astronomy and Astrophysics*, 552, 70.  
<http://hdl.handle.net/2268/162022>  
 ORBi viewed: 24 (15 ULg) ; downloaded: 3 (3 ULg) — SCOPUS®: 3
- 11)  Kains, N., Bramich, D. M., Arellano Ferro, A., Figuera Jaimes, R., Jørgensen, U. G., Giridhar, S., Penny, M. T., Alsubai, K. A., Andersen, J. M., Bozza, V., Browne, P., Burgdorf, M., Calchi Novati, S., Damerdjy, Y., Diehl, C., Dodds, P., Dominik, M., Elyiv, A., Fang, X.-S., Giannini, E., Gu, S.-H., Hardis, S., Harpsøe, K., Hinse, T. C., Hornstrup, A., Hundertmark, M., Jessen-Hansen, J., Juncher, D., Kerins, E., Kjeldsen, H., Korhonen, H., Liebig, C., Lund, M. N., Lundkvist, M., Mancini, L., Martin, R., Mathiasen, M., Rabus, M., Rahvar, S., Ricci, D., Sahu, K., Scarpetta, G., Skottfelt, J., Snodgrass, C., Southworth, J., Surdej, J., Tregloan-Reed, J., Vilela, C., **Wertz, O.**, & Williams, A. (2013). Estimating the parameters of globular cluster M 30 (NGC 7099) from time-series photometry. *Astronomy and Astrophysics*, 555, 36.  
<http://hdl.handle.net/2268/158514>  
 ORBi viewed: 17 (10 ULg) ; downloaded: 1 (1 ULg) — SCOPUS®: 0
- 12)  Harpsøe, K. B. W., Hardis, S., Hinse, T. C., Jørgensen, U. G., Mancini, L., Southworth, J., Alsubai, K. A., Bozza, V., Browne, P., Burgdorf, M. J., Calchi Novati, S., Dodds, P., Dominik, M., Fang, X.-S., Finet, F., Gerner, T., Gu, S.-H., Hundertmark, M., Jessen-Hansen, J., Kains, N., Kerins, E., Kjeldsen, H., Liebig, C., Lund, M. N., Lundkvist, M., Mathiasen, M., Nesvorný, D., Nikolov, N., Penny, M. T., Proft, S., Rahvar, S., Ricci, D., Sahu, K. C., Scarpetta, G., Schäfer, S., Schönebeck, F., Snodgrass, C., Skottfelt, J., Surdej, J., Tregloan-Reed, J., & **Wertz, O.** (2013). The transiting system GJ1214: high-precision defocused transit observations and a search for evidence of transit timing variation. *Astronomy and Astrophysics*, 549, 10.  
<http://hdl.handle.net/2268/142584>  
 ORBi viewed: 28 (5 ULg) ; downloaded: 6 — SCOPUS®: 3
- 13)  Choi, J.-Y., Shin, I.-G., Han, C., Udalski, A., Sumi, T., Gould, A., Bozza, V., Dominik, M., Fouqué, P., Horne, K., Szymański, M. K., Kubiak, M., Soszyński, I., Pietrzyński, G., Poleski, R., Ulaczyk, K., Pietrukowicz, P., Koziowski, S., Skowron, J., Wyrzykowski, Ł., The OGLE Collaboration, Abe, F., Bennett, D. P., Bond, I. A., Bötzler, C. S., Chote, P., Freeman, M., Fukui, A., Furusawa, K., Itow, Y., Kobara, S., Ling, C. H., Masuda, K., Matsubara, Y., Miyake, N., Muraki, Y., Ohmori, K., Ohnishi, K., Rattenbury, N. J., Saito, T., Sullivan, D. J., Suzuki, D., Suzuki, K., Sweatman, W. L., Takino, S., Tristram, P. J., Wada, K., Yock, P. C. M., The MOA Collaboration, Bramich, D. M., Snodgrass, C., Steele, I. A., Street, R. A., Tsapras, Y., The RoboNet Collaboration, Alsubai, K. A., Browne, P., Burgdorf, M. J., Calchi Novati, S., Dodds, P., Dreizler, S., Fang, X.-S., Grundahl, F., Gu, C.-H., Hardis, S., Harpsøe, K., Hinse, T. C., Hornstrup, A., Hundertmark, M., Jessen-Hansen, J., Jørgensen, U. G., Kains, N., Kerins, E., Liebig, C., Lund, M., Lundkvist, M., Mancini, L., Mathiasen, M., Penny, M. T., Rahvar, S., Ricci, D., Scarpetta, G., Skottfelt, J., Southworth, J., Surdej, J., Tregloan-Reed, J., Wambsganss, J., **Wertz, O.**, MiNDSTeP Consortium, T., Almeida, L. A., Batista, V., Christie, G., DePoy, D. L., Dong, S., Gaudi, B. S., Henderson, C., Jablonski, F., Lee, C.-U., McCormick, J., McGregor, D., Moorhouse, D., Natusch, T., Ngan, H., Pogge, R. W., Tan, T.-G., Thornley, G., Yee, J. C., The  $\mu$ FUN Collaboration, Albrow, M. D., Bachelet, E., Beaulieu, J.-P., Brilliant, S., Cassan, A., Cole, A. A., Corrales, E., Coutures, C., Dieters, S., Dominis Prester, D., Donatowicz, J., Greenhill, J., Kubas, D., Marquette, J.-B., Menzies, J. W., Sahu, K. C., Zub, M., & The PLANET Collaboration. (2012). A New Type of Ambiguity in the Planet and Binary Interpretations of Central Perturbations of High-magnification Gravitational Microlensing Events. *Astrophysical Journal*, 756, 48.  
<http://hdl.handle.net/2268/142593>  
 ORBi viewed: 16 (5 ULg) ; downloaded: 0 — SCOPUS®: 2  
 IF 2012: 6.733; last: 6.733; IF5: 5.945 — EigenF 2012: ?; last: 0.4871 — Article Infl. 2012: ?; last: 1.9055

- 14)  Choi, J.-Y., Han, C., Udalski, A., Sumi, T., Gaudi, B. S., Gould, A., Bennett, D. P., Dominik, M., Beaulieu, J.-P., Tsapras, Y., Bozza, V., Scarpetta, G., Skottfelt, J., Snodgrass, C., Tregloan-Reed, J., Wambsganss, J., **Wertz, O.**, Zimmer, F., MiNDSTeP Consortium, T., Albrow, M. D., Bachelet, E., Steele, I. A., Batista, V., Abe, F., Brilliant, S., Cassan, A., Cole, A. A., Coutures, C., Dieters, S., Dominis Prester, D., Donatowicz, J., Fouqué, P., Street, R. A., Greenhill, J., Kubas, D., Bond, I. A., Marquette, J.-B., Menzies, J. W., Sahu, K. C., Zub, M., The PLANET Collaboration, Bramich, D. M., Horne, K., The RoboNet Collaboration, Botzler, C. S., Chote, P., Freeman, M., Fukui, A., Furusawa, K., Itow, Y., Ling, C. H., Skowron, J., Masuda, K., Matsubara, Y., Miyake, N., Muraki, Y., Ohnishi, K., Rattenbury, N. J., Saito, T., Sullivan, D. J., Suzuki, K., Sweatman, W. L., Kozłowski, S., Suzuki, D., Takino, S., Tristram, P. J., Wada, K., Yock, P. C. M., The MOA Collaboration, Szymański, M. K., Kubiak, M., Pietrzyński, G., Soszyński, I., Poleski, R., Ulaczyk, K., Wyrzykowski, Ł., Pietrukowicz, P., The OGLE Collaboration, Almeida, L. A., DePoy, D. L., Dong, S., Browne, P., Gorbikov, E., Jablonski, F., Henderson, C. B., Hwang, K.-H., Janczak, J., Jung, Y.-K., Kaspi, S., Lee, C.-U., Malamud, U., Maoz, D., Burgdorf, M. J., McGregor, D., Muñoz, J. A., Park, B.-G., Park, H., Pogge, R. W., Shvartzvald, Y., Shin, I.-G., Yee, J. C., The  $\mu$ FUN Collaboration, Alsubai, K. A., Calchi Novati, S., Dodds, P., Fang, X.-S., Finet, F., Glittrup, M., Grundahl, F., Gu, S.-H., Hardis, S., Southworth, J., Harpsøe, K., Hinse, T. C., Hornstrup, A., Hundertmark, M., Jessen-Hansen, J., Jørgensen, U. G., Kains, N., Kerins, E., Liebig, C., Lund, M. N., Surdej, J., Lundkvist, M., Maier, G., Mancini, L., Mathiasen, M., Penny, M. T., Rahvar, S., & Ricci, D. (2013). Microlensing Discovery of a Population of Very Tight, Very Low Mass Binary Brown Dwarfs. *Astrophysical Journal*, 768, 129.  
<http://hdl.handle.net/2268/163474>  
ORBi viewed: 0 ; downloaded: 0 — SCOPUS®: 2  
IF: ? — EigenF: ? — Article Infl.: ?
- 15)  Arellano Ferro, A., Bramich, D. M., Figuera Jaimes, R., Giridhar, S., Kains, N., Kuppaswamy, K., Jørgensen, U. G., Alsubai, K. A., Andersen, J. M., Bozza, V., Browne, P., Calchi Novati, S., Damerdjji, Y., Diehl, C., Dominik, M., Dreizler, S., Elyiv, A., Giannini, E., Harpsøe, K., Hessman, F. V., Hinse, T. C., Hundertmark, M., Juncher, D., Kerins, E., Korhonen, H., Liebig, C., Mancini, L., Mathiasen, M., Penny, M. T., Rabus, M., Rahvar, S., Ricci, D., Scarpetta, G., Skottfelt, J., Snodgrass, C., Southworth, J., Surdej, J., Tregloan-Reed, J., Vilela, C., **Wertz, O.**, & Mindstep Consortium. (2013). A detailed census of variable stars in the globular cluster NGC 6333 (M9) from CCD differential photometry. *Monthly Notices of the Royal Astronomical Society*, 434, 1220-1238.  
<http://hdl.handle.net/2268/158517>  
ORBi viewed: 19 (12 ULg) ; downloaded: 4 (2 ULg) — SCOPUS®: 0  
IF 2013: ?; last: 5.521; IF5: 5.009 — EigenF 2013: ?; last: 0.2488 — Article Infl. 2013: ?; last: 1.6034

#### 4. Articles accepted in journals without committee (non-peer reviewed)

---

#### 5. Articles accepted in conference proceedings

---

#### 6. Oral presentations in conferences with scientific selection committee

---

#### 7. Patents

---



# *Acknowledgements*

It would not have been possible to write this doctoral thesis without the help and support of several people around me, to only some of whom it is possible to give particular mention here.

Above all, I owe my deepest gratitude to my supervisor, Prof. Jean Surdej. I would like to thank you for encouraging my research and for allowing me to grow as a research scientist. Your advice on both research as well as human matters have been priceless.

I am also grateful to the members of the jury who have accepted to read this thesis and to devote some of their precious time to examine my work.

Marie-Eve has given me her unequivocal support throughout, as always, for which my mere expression of thanks likewise does not suffice. A special thanks also to my family. Words cannot express how grateful I am for all the sacrifices that you have made on my behalf.

These years would not have been the same without all the people in the institute. I would particularly like to thank Ludovic, François, Olivier, Lorraine, Maxime, Charles, Anthony, and Davide. I am also grateful for the assistance given by Sylvia.

And finally, I would like to offer my special thanks to Jean-Paul, Pierre-Patrick, Laurent, Nathalie and Annie. All those years spent to participate and then organize our astronomy camp will be unforgettable.

For any errors or inadequacies that may remain in this work, of course, the responsibility is entirely mine.